

# THESE

Présentée à

UNIVERSITY OF LILLE 1- SCIENCES AND TECHNOLOGIES

Pour obtenir le grade de

**Doctor of Philosophy in Physics**

Par

**Rakibul ISLAM**

---

## **ELECTRICAL AND THERMAL TRANSPORT PROPERTIES OF POLYMER / CARBONACEOUS NANOSTRUCTURED COMPOSITES**

---

Soutenue le 18 Octobre 2016 devant le jury d'examen

|              |                       |                                    |
|--------------|-----------------------|------------------------------------|
| Rapporteurs: | Pr Olivier CHAUVET    | IMN, Université de Nantes          |
|              | Pr Lionel FLANDIN     | LEPMI, Université de Savoie        |
| Examineurs:  | Pr. Fabrizio CLERI    | IEMN, Université de Lille          |
|              | Pr. Frederic VIDAL    | LPPI, Université de Cergy-Pontoise |
| Directeurs : | Pr. Frederick ROUSSEL | UMET, Université de Lille          |
|              | Pr. Carole GORS       | UMET, Université de Lille          |

## ACKNOWLEDGEMENTS

The late Prof. Frédérick Roussel (supervisor of my thesis) gave me the valuable opportunity to join his research group when I had no credentials or research background and I cannot thank him enough for being compassionate and generous throughout these years. He inspired creativity, nurtured curiosity, and fostered the desire in me towards achieving my goal. Although he is no more with us, I will cherish these memories for the rest of my life.

Also, I express my deep sense of gratitude and indebtedness with full of honour and respect to Prof. Carole Gors (co-supervisor, ), Prof. Roch-Chan-Yu-King (University of Science and Arts of Oklahoma, USA), Dr. Anthony N. Papathanassiou (Assistant professor, National and Kapodistrian University of Athens ), Dr. Jean-François Brun (Maître de conférences, UMET, Université Lille 1 - Sciences et Technologies) and Dr. Corinne Binet (Maître de conférences, UMET, Université Lille 1 - Sciences et Technologies) for their cooperation, inspiring guidance and constant help at all stages of my project. Their constant encouragement and concern during the execution of the present work would be remembered with gratefulness for all times to come. It is only because of the supportive and congenial nature of our research group members that my PhD tenure had been a memorable one. Particularly, I would like to thank Mr. Jean-François Tahon, and Mr. Marc Deleplace for their constant help and guidance.

I extend my special thanks to Dr. Abdelhak Hadj Sahraoui (Professor, UDSMM, Université du Littoral-Côte-d'Opale) and Dr. Michael Depriester (Maître de conférences, UDSMM, Université du Littoral-Côte-d'Opale) for providing access to PTR facilities. I would like to thank to Dr. Ahmed Addad, and Dr. M. Moreau for providing access to the SEM, and TEM, and LASIR Raman facilities respectively.

I would like to thank Prof. Alexandre Legris, Director of the UMET (Unité Matériaux et Transformations - UMR CNRS 8207) for accepting my candidature as well as providing me all the necessary supports during the thesis work. I am very happy and proud to say that I have been a part of this research lab.

My sincere thanks to the board of examiners, Prof. Olivier Chauvet (IMN, Université de Nantes), and Prof. Lionel Flandin (LEPMI, Université de Savoie) as reporters, as well as Prof. Fabrizio

Cleri (IEMN, Université de Lille), and Prof. Frederic Vidal (LPPI, Université de Cergy-Pontoise) as examiners, for their kind acceptance to evaluate this thesis work.

I have been fortunate to had many friends during my research career, all of them coloured my days both in India and Europe. They are Salma Sultana, Samsur Habib, Imran Khan, Anny Ahmed, Moksud Alam Raja, Murshid Alam, Satwik Mukherjee, Tamanna Hussain, Natasha Yasmin, Julia Ashina, Tarun Agrawal, Mauro Kenny, Grecia Romero, Izabel Fernandes, Gustavo Sousa, Klara Babińska, Soukaina Ben Salk, Himani Garg, Fabio Landuzzi, Lyes Alileche, Sricharan Srinath, Srinivasan Mahendran, Sazzad Hossain Khan, Debarun Dhali, Narinder Singla, and all members of Lille cricket club. I enjoyed their friendship, love and care very much.

I am extremely grateful to my family for their unconditional love and support. If there is any place where I get the highest of all- appreciation, love, compassion, support and acceptance, then that is my home. I am undoubtedly fortunate to born as the son of Mr. Raisuddin, and Mrs. Mahabuba Khatun. Without them my life will not go ahead a single step. Because, they educated me, protected me and fulfilled all my basic needs by sacrificing many of their happiness and well-being. Their priceless deeds couldn't be described here and a word of gratitude is just not worthy enough to honour them. I also grateful to my brothers (Rajibul Islam, and Tousif Biswas), my sweet sister (Riya), my uncles and aunts. I indeed feel lucky and proud to be part of my beautiful family.

Last but not the least, I would like to use this opportunity to thank to all of those my well wishers who have supported me to be what I am at present, as a professional and as a person.

Dedicated to my beloved and respected professor  
Frédéric Roussel (2 May 1969 – 21 October 2015)

# TABLE OF CONTENTS

|  |          |
|--|----------|
| <b>Acknowledgement</b>   | <b>i</b> |
| <b>Abstract</b>  | <b>6</b> |
| GENERAL INTRODUCTION.....  | 10       |
| CHAPTER 1 MATERIALS .....  | 19       |
| 1.1. Thermoelectric (TE) materials .....                                     | 19       |
| 1.2. Conducting polymers .....   | 21       |
| 1.2.1. Polyacetylene .....   | 22       |
| 1.2.2. Poly (3,4-ethylenedioxythiophene) (PEDOT) .....                       | 25       |
| 1.2.3. Polyaniline (PANI) .....  | 26       |
| 1.3. Carbonaceous nano-fillers.....  | 31       |
| 1.3.1. 1-D carbonaceous nano-fillers .....                                   | 32       |
| 1.3.1.1 Single wall carbon nanotubes (SWCNT)- structure and properties ..... | 33       |
| 1.3.1.2 Multi wall carbon nanotubes (MWCNT)- structure and properties .....  | 34       |
| 1.3.2. 2-D Carbonaceous nano-objects .....                                   | 36       |
| 1.4. Polymer nanocomposites.....   | 38       |
| 1.4.1. SWCNT-based PANI nanocomposites .....                                 | 39       |
| 1.4.2. MWCNT-based PANI nanocomposites.....                                  | 40       |
| 1.4.3. RGO-based PANI nanocomposites.....                                    | 41       |
| CHAPTER 2 THEORITICAL BACKGRUND .....  | 44       |
| 2.1. Introduction .....  | 44       |
| 2.2. Electrical properties.....  | 44       |
| 2.2.1. Background.....   | 44       |
| 2.2.2. Conduction mechanism.....   | 46       |
| 2.2.3. Electrical conductivity models.....                                   | 48       |
| 2.2.3.1 Filler volume fraction dependent electrical conductivity .....       | 48       |
| 2.2.3.2 Temperature dependent electrical conductivity:.....                  | 51       |
| 2.3. Thermal properties .....  | 53       |

|   |  |     |
|---|--|-----|
| 2.3.1.                                  | Heat capacity (C) .....  | 53  |
| 2.3.2.                                  | Thermal diffusivity ( $\alpha$ ) and thermal effusivity (e) .....            | 53  |
| 2.3.3.                                  | Thermal conductivity (k) .....   | 54  |
| 2.3.3.1                                 | Background.....  | 54  |
| 2.3.3.2                                 | Thermal conductivity models .....  | 58  |
| 2.4.                                    | Thermoelectric (TE).....   | 61  |
| 2.4.1.                                  | Background on thermoelectric .....   | 61  |
| 2.4.2.                                  | Seebeck Coefficient .....  | 66  |
| 2.4.3.                                  | Thermoelectric performance or figure of merit (ZT).....                      | 70  |
| 2.5.                                    | Dielectric properties .....  | 72  |
| CHAPTER 3 EXPERIMENTAL TECHNIQUES ..... |  | 76  |
| 3.1.                                    | Material preparation .....   | 76  |
| 3.1.1.                                  | Synthesis of polyaniline/SWCNT or polyaniline /MWCNT nanocomposites .....    | 77  |
| 3.1.2.                                  | Synthesis of polyaniline/reduced graphene oxide (PANI/RGO) nanocomposites .. | 77  |
| 3.2.                                    | Samples preparation and characterization techniques.....                     | 78  |
| 3.2.1.                                  | Scanning electron microscopy (SEM) .....                                     | 78  |
| 3.2.2.                                  | Transmission electron microscopy (TEM) .....                                 | 79  |
| 3.2.3.                                  | Raman spectroscopy .....   | 80  |
| 3.2.4.                                  | X-Ray diffraction (XRD).....   | 82  |
| 3.2.5.                                  | Four-probe technique .....   | 84  |
| 3.2.6.                                  | Seebeck measurement technique .....  | 88  |
| 3.2.7.                                  | Laser flash method.....  | 89  |
| 3.2.8.                                  | Differential scanning calorimetry (DSC).....                                 | 91  |
| 3.2.9.                                  | Photothermal radiometry .....  | 92  |
| 3.2.10.                                 | Dielectric spectroscopy .....  | 95  |
| CHAPTER 4 RESULTS AND DISCUSSIONS ..... |  | 98  |
| 4.1.                                    | Single wall carbon nanotubes based polymer nanocomposites .....              | 98  |
| 4.1.1.                                  | Density ( $\rho$ ) .....   | 98  |
| 4.1.2.                                  | Morphological and structural characterizations.....                          | 100 |
| 4.1.2.1                                 | SEM investigation .....  | 100 |
| 4.1.2.2                                 | TEM investigation .....  | 101 |

|            |  |     |
|------------|--|-----|
| 4.1.3.     | Electrical properties .....  | 103 |
| 4.1.4.     | Thermal properties .....   | 107 |
| 4.1.4.1    | Thermal diffusivity ( $\alpha$ ) .....                                 | 107 |
| 4.1.4.2    | Volumetric heat capacity ( $\rho C$ ).....                             | 108 |
| 4.1.4.3    | Thermal conductivity (k).....  | 110 |
| 4.1.5.     | Seebeck coefficient (S) and power factor (PF) .....                    | 112 |
| 4.1.6.     | Thermoelectric properties .....  | 116 |
| 4.2.       | Multi wall carbon nanotubes based polymer nanocomposites.....          | 118 |
| 4.2.1.     | Density ( $\rho$ ) .....   | 118 |
| 4.2.2.     | Morphological and structural characterizations.....                    | 119 |
| 4.2.2.1    | SEM investigation .....  | 119 |
| 4.2.2.2    | TEM investigation .....  | 121 |
| 4.2.3.     | Electrical properties .....  | 123 |
| 4.2.4.     | Thermal properties .....   | 128 |
| 4.2.4.1    | Thermal diffusivity ( $\alpha$ ) .....                                 | 128 |
| 4.2.4.2    | Volumetric heat capacity ( $\rho C$ ).....                             | 129 |
| 4.2.4.3    | Thermal conductivity (k).....  | 130 |
| 4.2.5.     | Seebeck coefficient (S) and power factor (PF) .....                    | 132 |
| 4.2.6.     | Thermoelectric properties .....  | 135 |
| 4.3.       | Reduced graphene oxide based polymer nanocomposites .....              | 138 |
| 4.3.1.     | Density .....  | 138 |
| 4.3.2.     | Morphological and structural characterizations.....                    | 139 |
| 4.3.2.1    | SEM Investigation .....  | 139 |
| 4.3.2.2    | TEM investigation .....  | 141 |
| 4.3.2.3    | Raman spectra analysis.....  | 142 |
| 4.3.2.4    | XRD analysis.....  | 144 |
| 4.3.3.     | Electrical properties .....  | 146 |
| 4.3.3.1    | Electrical properties characterized by in plane measurement .....      | 146 |
| 4.3.3.2    | Electrical properties characterized by through plane measurement ..... | 150 |
| 4.3.3.2.1. | Introduction .....   | 150 |
| 4.3.3.2.2. | Investigation of dielectric spectrum .....                             | 151 |

|   |            |
|---|------------|
| 4.3.3.2.3. Conclusion.....  | 160        |
| 4.3.3.3 Temperature dependence of electrical properties characterized by through plane measurement.....           | 161        |
| 4.3.3.3.1. Introduction .....   | 161        |
| 4.3.3.3.2. Investigation of temperature dependence of dielectric spectrum .....                                   | 161        |
| 4.3.3.3.3. Conclusion.....  | 166        |
| 4.3.4. Thermal properties .....   | 167        |
| 4.3.4.1 Thermal properties investigated by laser flash method and DSC .....                                       | 167        |
| 4.3.4.1.1. Thermal diffusivity and Volumetric heat capacity .....   | 167        |
| 4.3.4.1.2. Thermal conductivity .....   | 168        |
| 4.3.4.2 Thermal properties investigated by photothermal radiometry (PTR) .....                                    | 170        |
| 4.3.4.2.1. Thermal diffusivity and thermal effusivity.....  | 170        |
| 4.3.4.2.2. Thermal conductivity .....   | 172        |
| 4.3.4.2.3. Contribution of void fraction in the thermal conductivity.....   | 175        |
| 4.3.4.3 Volumetric heat capacity .....  | 178        |
| 4.3.4.4 Heat absorption capability .....  | 181        |
| 4.3.5. Seebeck coefficient(S) and power factor (PF).....  | 185        |
| 4.3.6. Thermoelectric properties .....  | 188        |
| <b>CHAPTER 5 COMPARATIVE STUDY OF 1-D AND 2-D CARBONACEOUS NANO-FILLERS- BASED NANOSTRUCTURED COMPOSITES.....</b> | <b>190</b> |
| 5.1. Morphological study .....  | 190        |
| 5.2. Electrical properties.....   | 193        |
| 5.3. Thermal properties .....   | 198        |
| 5.4. Seebeck effect .....   | 201        |
| 5.5. Power factor .....   | 204        |
| 5.6. Thermoelectric performance (ZT).....   | 206        |
| <b>GENERAL CONCLUSION .....</b>   | <b>208</b> |
| <b>BIBLIOGRAPHY .....</b>   | <b>215</b> |
| <b>ABSTRACT.....</b>  | <b>227</b> |
| <b>RESUMÉ .....</b>   | <b>228</b> |





# Abstract

Polymer nanocomposites are a combination of polymer matrix and nano-fillers which have at least one dimension in the nanometer range. There are various nano-fillers with different dimensions such as, zero-dimensional (0-D) which include quantum dot, one-dimensional (1-D) including nanotubes and nanofibers, two-dimensional (2-D) including layered like materials, and three-dimensional (3-D) including spherical particles. Over the last decade, the polymer nanocomposites have attracted tremendous interests in both academia and industry research.

This thesis reports the properties of conducting polymers, more specifically polyaniline (PANI) nanostructured composites filled with carbonaceous nano-fillers such as SWCNT (1-D), MWCNT (1-D), and RGO (2-D), as a function of nano-fillers content and presents possible direction to optimize their thermoelectric performance and energy storage capability.

Three series of PANI/SWCNT, PANI/MWCNT, and PANI/RGO composites are synthesized by in situ polymerization of aniline in the presence of varying amount of the nano-fillers ranging from 0 to 21 wt-% in acidic medium. SEM, TEM, X-ray diffraction, and Raman spectroscopy were employed to investigate their structure and morphology. SEM and TEM images exhibit that the fillers are covered by a polymer layer resulting in core-shell structure in which filler as core and polyaniline as shell are presented. These structures indicate good interaction through  $\pi$ - $\pi$  stacking between filler and matrix as evidenced by Raman spectroscopy and X-ray studies.

The electrical conductivities of the samples are measured by 4-probe method. The electrical conductivity of the nanocomposites follows a percolation behavior and electrical transport mechanism takes place through 2-D conductive network. It is observed that a significant enhancement in electrical conductivity is strongly related to tunneling effect in the composites.

Furthermore, laser flash method and DSC are employed to investigate the thermal properties of the composites. The experimental results reveal that thermal diffusivity, volumetric heat capacity, and thermal conductivity increase with the addition of carbonaceous nano-fillers. Unlike electrical conductivity, the thermal conductivity of the composites increases only slightly with the nano-fillers fraction. Effective medium approximation (EMA) model is used to estimate the interfacial resistance ( $R_k$ ) between the filler and the polymer host.

To evaluate the thermoelectric performance, the Seebeck coefficient carried out on homemade Seebeck measurement system is investigated as a function of the nano-fillers content. Compared to that of pure PANI, the thermoelectric performance of the composites exhibits a ZT enhancement.

Moreover, a comparative study on electrical and thermal transport and thermoelectric properties are carried out in order to investigate the dimensionality effect in these properties. It is observed that inclusion of 2-D nano-fillers into matrix makes layers like core-shell structures but addition of 1-D nano-fillers (SWCNT and MWCNT) gives rod-like core-shell structures. The electrical properties show that although nano-fillers have different dimensions, the electrical percolation follows 2-D conduction process. But there is significant dimensionality effect on electrical conductivity enhancement, percolation threshold, and tunneling phenomena. Also thermal conductivity and volumetric heat capacity depend on the dimensions of the fillers. The results show three different signatures of the Seebeck coefficient for three different fillers. It is observed that at lower concentration of MWCNT fillers, the Seebeck coefficient behaves like PANI/SWCNT composites whereas at higher concentration, the behavior of Seebeck coefficient is like PANI/RGO composites. The thermoelectric performance ZT is associated with the dimensions of the fillers.

In addition, for extension of the research on PANI/RGO composites, others properties of same series of chemically synthesized PANI/RGO nanocomposites are investigated. Thermal properties of the composites are analyzed through photothermal radiometry (PTR) at room temperature. The contributions of RGO nano-fillers to various thermal parameters such as thermal diffusivity ( $\alpha$ ), thermal effusivity ( $e$ ), thermal conductivity ( $k$ ) and volumetric heat capacity ( $\rho C$ ) of the nanocomposites are subsequently determined. The analyses indicate that the thermal conductivity barely changes at lower RGO nano-fillers loading (<1 vol-%) but rises sharply beyond that percentage. Likewise, the influence of the nano-filler concentration on the volumetric heat capacity shows significant enhancement. While the thermal conductivity of the nanocomposites shows no percolation behaviour, however, the evolution of volumetric heat capacity displays the opposite phenomenon. This valuable characteristic of the nanocomposites is expected to find potential applications in high heat capacitive materials. To gain further insight

into the thermal properties of the nanocomposites, their heat storage factor or heat absorption per unit area  $Q$  ( $J/m^2$ ) is assessed with a new analytical model proposed for first time in this study.

Also the dielectric properties of PANI/RGO nanohybrids are investigated by Broadband Dielectric Spectroscopy at different temperature. The observed dielectric relaxation peaks are analyzed within the framework of the Kohlrausch-Williams-Watts (KWW) model. At room temperature, it is shown that charge trapping occurs at the PANI/RGO interface. The relaxation dynamics of trapped charges are studied as a function of volume fraction of RGO. This charge trapping process is thermally activated and exhibits an Arrhenius-like behavior. The dielectric relaxation mechanism associated with the interfacial polarization in the nanocomposites is found to shift towards lower frequencies on increasing temperature. The effective activation energy value is negative. Basic concepts of the Sillars dielectric theory of a heterogeneous medium are revisited for a material consisting of conducting platelets dispersed in a semi-insulating matrix in order to explain the negative sign of the relaxation energy. A plausible explanation to this observation involves a thermally activated de-trapping mechanism through the effective potential barrier at the interfaces between RGO and PANI. It results in an enhancement of the density of charge carriers which contributes to DC conductivity at expense of the density of charge carriers that relax within RGO inclusions.



# GENERAL INTRODUCTION

The energy information administration (EIA) of the U.S. department of energy reported yearly basis energy consumption data which is depicted in Figure 1 [1]. For example, in 2007, 495 quadrillion British Thermal Units (BTUs) which is equivalent to an average power of 16.6 Terawatts (TW) were consumed by global civilization [2,3]. The report shows an enhancement of energy consumption up to 49% by 2035 in comparison with energy consumption which was 495 quadrillion British Thermal Units (BTUs) [2,3]. The amount is definitely a cause for alarm because it will be a challenge to supply energy on this scale.

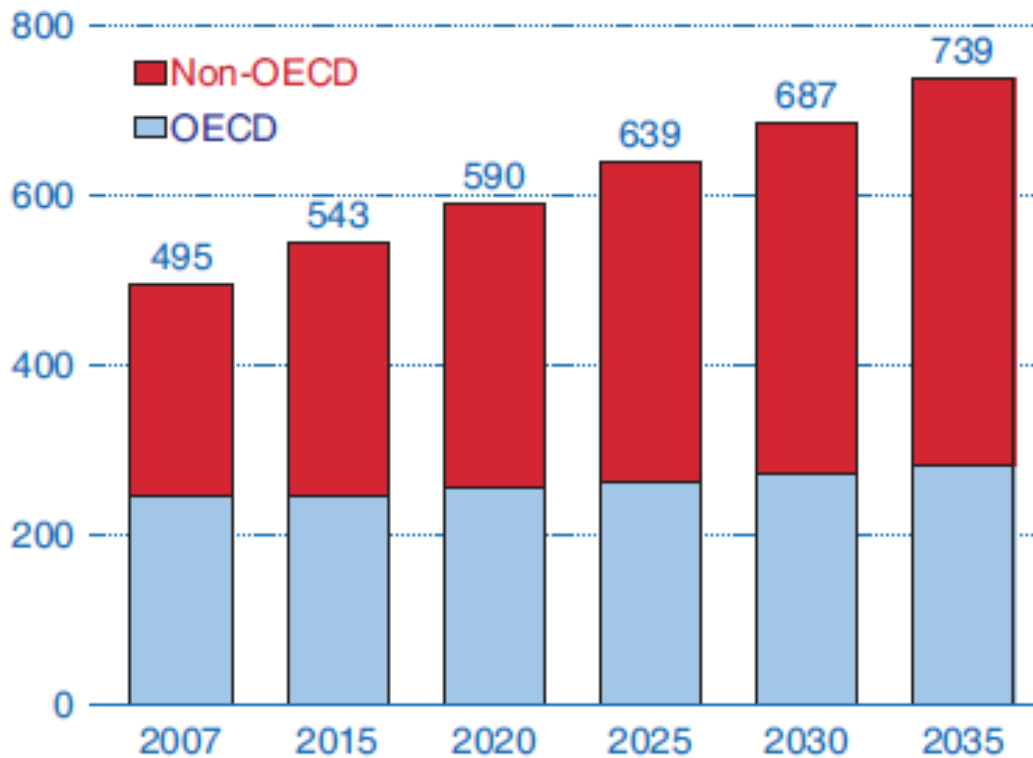


**Figure 1.** World marketed energy consumption, 2007-2035 (quadrillion BTU). Non-OECD stands for nations outside the organization for economic co-operation and development and OECD stands for organization for economic co-operation and development [1].

Also the noticeable point is that almost two third (~66%) of the energy consumed in different ways is lost to the environment as waste heat. Recent time, although the planet is facing the energy resource limitation problem, heat is wasted in daily life. Figure 2 presents the energy statistics which shows that 34% of total energy is used.

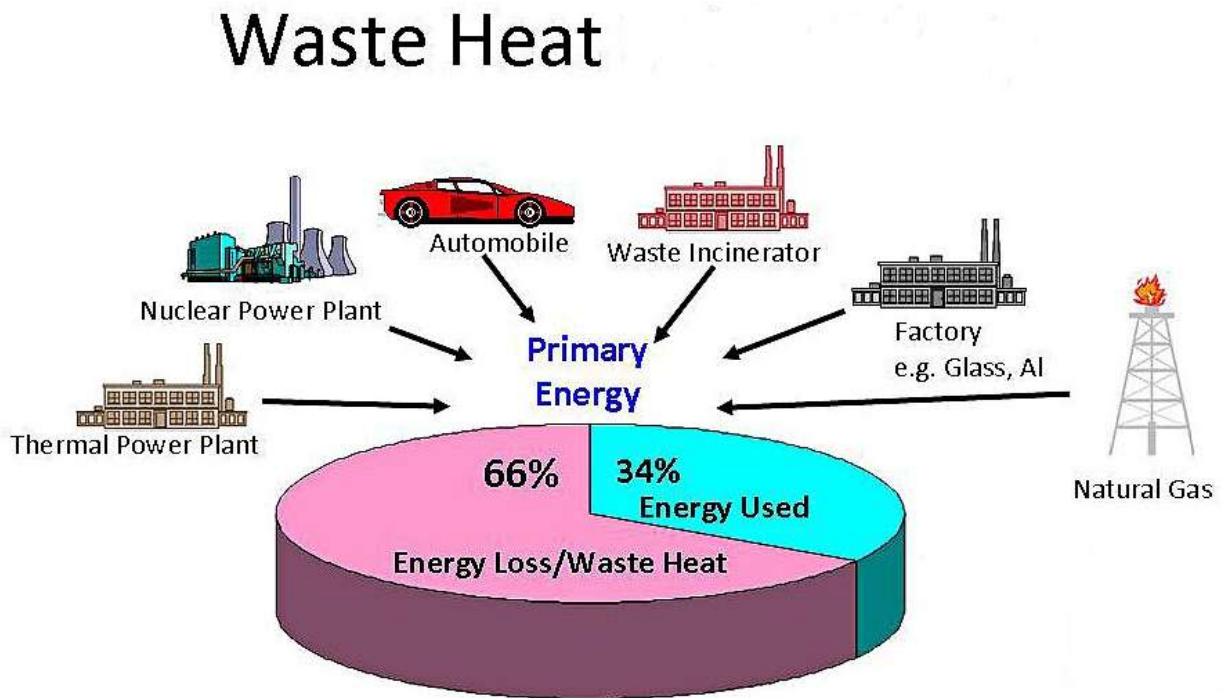


**Figure 2.** Representation of energy statistic

However, during the last two decades, increasing demand for energy and pollutants free environments has led to continuous investigation of leading-edge technological products with high energy efficient performance and low fabrication cost. In order to address these problems, thermoelectric energy conversion could be the best possible solution.

Thermoelectric (TE) possess the capability to capture heat from natural sources or waste heat and convert it into electricity. Figure 3 schematically displays the conversion of waste heat to electricity by the TE device. The major challenge of the conversion system is that how a small gradient of temperature with respect to the environmental temperature can be efficiently

harvested [3]. This energy conversion provides extremely reliable, small in size, light and silent in operation power source with no moving parts and no need for maintenance. But the main disadvantage is the low efficiency of the existing thermoelectric systems. Therefore, improvement of the efficiency is a key issue in this research area. Thus the research on different thermoelectric materials is still being conducting in order to improve the efficiency.

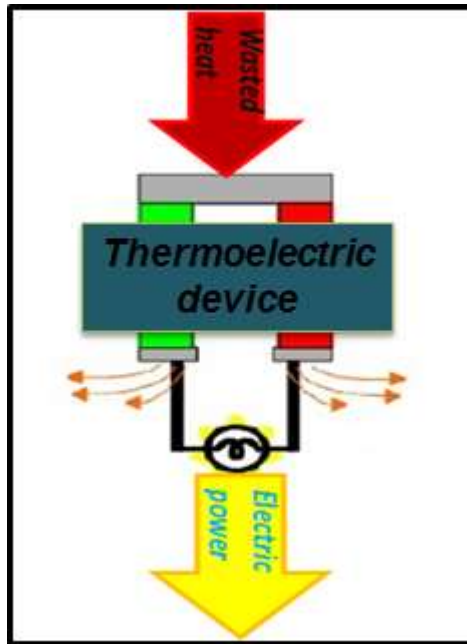


**Figure 3.** Conversion of waste heat to electricity by thermoelectric system.

TE materials are good candidates for the fabrication of energy harvesting systems or heating/cooling devices. The gradual advances realized over the years and further improvement in TE technology could find widespread commercial applications in cost-effective and sustainable energy conversion and recovery. For the maximum efficiency and low cost thermal energy conversion technology, inexpensive and abundant materials are required, which can be easily processable at room temperature, preferably via chemical processing methods. For these reasons, polymer nanocomposites can be an exciting group of materials, which could potentially fulfill most of these requirements. More specifically, conducting polymer nanocomposites lead to a special class of materials which have low thermal conductivity and high electrical



conductivity. Thus, the polymer nanocomposites can be considered as good materials in order to achieve the promising thermoelectric performance or figure of merit ( $ZT$ ) at room temperature. But, the important question is that what factors are responsible for improving their thermoelectric efficiency ( $ZT$ ). In consequence, we need a clear understanding of electrical and thermal properties in these materials.

A combination of a polymer and nano-filler is represented as a typical polymer nanostructured composite which has at least one dimension in the nanometer range. Owing to their relatively ease of syntheses and their unique attributes, polymer nanocomposites have opened up new frontiers in both academia and industrial research over few years. More specifically, progress in the field of material research has taken a new lead since the advent of conducting polymer nanocomposites due to their novel properties such as electrical, thermal, and mechanical properties [4–9]. Due to these outstanding properties, conducting polymer composites are used in a wide variety of industrial applications such as light emitting diode, electrodes, battery and fuel cell, corrosion resistance materials, and antistatic media [6,9]. To avoid a low mechanical strength, a heavy weight and a poor processability when high fillers concentrations are added, a low filler content and good filler dispersion into the host are preferable condition to achieve desirable polymer nanocomposites [10,11]. Reinforcing materials such nano-fillers are often used in order to obtain efficient changes in various properties. Many previous studies have attempted to investigate the contributions of the different fillers in different conducting polymers such as polypyrrole, PEDOT: PSS, and polyaniline composites.

Various inorganic and organic nano-fillers can be dispersed into host materials to change the properties of nanocomposites in large scale range. Under ideal conditions, the incorporation of nano-fillers into the host is conducted without sacrificing the properties of the neat polymer, rather should improve their overall characteristics [12,13]. Central to the enhancement of composite properties are several challenging key factors that remain to be optimized: the method of preparation and subsequent processing which are often dependent on fillers morphology (length, width, thickness, chirality and size/shape), its architectural network and interaction with the host matrix [14]. It is, therefore, not surprising that much intense theoretical and applied research are still being conducted in hope to better understand the synergistic role played by the multi-components of the composite materials.

Especially, carbon based fillers have been tremendous interest in research in the field of polymer composites due to their uses in different potential applications [4,15–17]. Moreover, fillers with different dimensions (0-D, 1-D, 2-D, and 3-D) can play important role in the properties of the composites. Specially, low dimensional (less than three dimensions) carbonaceous nano-fillers (the carbon allotropes) such as SWCNT (1-D), MWCNT (1-D), and graphene and its derivatives (2-D) have emerged in material research due to their extraordinary physical properties [4,15,17]. Till date, many researchers have demonstrated the influences of fillers on different properties such as, electrical [18–20], thermal [21–25], and mechanical properties [26,27] of polymer nanocomposites.

In order to improve the effective electrical conductivity ( $>10$  S/m) as well as to maintain light weight and corrosion resistance, carbonaceous fillers are employed into polymer matrix [28,29]. Till date, within the framework of classical percolation theory and/or the inter-particle tunneling conduction, different polymer composites filled with different dimensional carbonaceous nano-fillers have been investigated to identify the responsible factors for improved electrical properties [9,30–33]. Miyasaka *et al.* [34] reported that electrical conductivity in the carbon-polymer composites enhances by almost 10 orders of magnitude at a critical concentration of fillers designated as the threshold concentration. For appropriate utilization of these novel materials in commercial applications, we need an in-depth understanding and predictive capability of the key structure–property relationships that govern the electrical properties of polymer nanocomposites. Although numerous studies have been taken on electrical properties of polymer composites filled with carbonaceous fillers over past two decades, there are many unresolved questions, especially the specific effect of filler properties and composite structure on the electrical properties of the system. As a consequence, well-defined systems are needed in order to investigate required theoretical and experimental studies on electrical properties.

Thermal performance plays an important role for the applications such as thermal barrier coating, nuclear fuels, and thermoelectric energy conversion and it is also vital for some technologies where primary goal is non-thermal [35]. In general, the many nano-devices require a sophisticated and controlled thermal transport as the nanoscale. Improved thermal stability [36] and thermal conductivity [11] of the related nanohybrid materials are often attributed to the high

aspect ratio of the filler which facilitates its good dispersion into the matrix via its good polymer/filler interactions. While the many physical properties of the polymer/carbonaceous nano-fillers composites have been extensively investigated, there is still room for further understanding of their thermal properties [13,37] and their ability to store thermal energy.

So far most high-performance TE units are based on inorganics/ metalloids [38,39] or their composites [40]. Since the discovery of TE properties of intrinsically conducting polymers (ICPs) such as polyanilines (PANI), polypyrroles (PPY), polythiophenes (PTH, PEDOT:PSS), ICPs or their derivatives are intensively investigated because they possess relatively low thermal conductivity, good electrical conductivity, air stability, light weight, easy preparation, and much less costly in their production compared to their inorganic counterparts [41,42]. Recently, it has been demonstrated that the introduction of low dimensional nanostructures in composites materials such as PANI/Bi<sub>2</sub>Te<sub>3</sub> [43], and PEDOT:PSS/ Ca<sub>3</sub>Co<sub>4</sub>O<sub>9</sub> [44] has significantly improved TE characteristics due to inter-component junctions, thereby leading to phonon scattering and hopping of charge carriers [45,46]. In addition, the use of carbonaceous nanomaterials like carbon nanotubes (CNT) or graphene in polymer-based TE composites have attracted much attention due to their exceptional electrical, thermal and mechanical characteristics [47]. In particular, it has been recently demonstrated that the change in nanotube characteristics (single or multiple-walled carbon nanotubes, oxidized or un-oxidized) allows a better tuning of the TE properties in PANI/CNT composites [7].

We report herein a detailed investigation of the electrical and thermal properties of three series of PANI/SWCNT, PANI/MWCNT, and PANI/RGO nanocomposites which are synthesized by in situ polymerization as a function of nano-fillers content ranging from 0-21 wt-%. More specifically, SEM, TEM, XRD, and Raman spectroscopy are employed to investigate the morphology and structural properties of the prepared samples. Electrical ( $\sigma$ ) and thermal ( $k$ ) conductivities of the composites are characterized by four probes method and laser flash, and DSC techniques respectively. In order to investigate the transport mechanism in these composites, the physical models are used with experimental data. In addition, Seebeck coefficients ( $S$ ) of these composites are also determined by using a homemade setup. The combination of  $\sigma$ ,  $k$ , and  $S$  allows to optimize the thermoelectric performance or figure of merit

(ZT) of these composites. To make an idea on dimensionality effect of the fillers in these proposed properties, a comparative study (1-D filler/ 2-D filler) is discussed in this thesis.

In addition, others properties of same series of PANI/RGO nanocomposites are discussed here. We make use of a photothermal radiometry (PTR) technique to modulate the frequency of a laser beam so as to photothermally excite the composites and detect the subsequent thermal responses emitted from the surface of the materials. The results obtained are analyzed as a function of RGO loading which provide various dynamic thermal parameters such as thermal diffusivity ( $\alpha$ ) and thermal effusivity ( $e$ ) from which the thermal conductivity ( $k$ ) is obtained. Using the thermal diffusivity, thermal effusivity and the thermal conductivity, the volumetric heat capacity ( $\rho C$ ) is computed. The heat storage factor (or heat absorption per unit area factor,  $Q$  ( $J/m^2$ )) of these composites has been determined with a proposed analytical model which, we expect to be quite useful for assessing the  $Q$  values of other nanohybrid materials.

Also, the data obtained with Broadband Dielectric Spectroscopy (BDS) are exploited to investigate the electrical and dielectric properties of the PANI/RGO composites with various RGO loadings. The obtained dielectric permittivity data are analyzed within the framework of Kohlrausch-William-Watts (KWW) model in order to correlate DC-conductivity along the network with capacitance phenomena resulting from electric charge trapping at interfaces. The effect of temperature on the charge relaxation mechanisms taking place at the polarized RGO/PANI interfaces which, unexpectedly, provided negative values for the corresponding relaxation energies is also discussed. In order to explain the negative sign of the relaxation energy, the Sillars dielectric theory of a heterogeneous medium are revisited for a material consisting of conducting platelets dispersed in a semi-insulating matrix.

In this thesis, chapter 1 is focused on some informations of proposed materials such as thermoelectric materials, conducting polymers, carbonaceous nano-fillers, and carbonaceous based polymer nanocomposites. Chapter 2 relates to theoretical background. It includes the electrical, thermal, Seebeck coefficient, thermoelectric performance, and dielectric properties of the materials. In chapter 3, we highlight the experimental techniques. We discuss about material synthesis, SEM, TEM, Raman spectroscopy, X-ray diffraction, 4-probe method, Seebeck coefficient measurement, laser flash method, DSC, photothermal radiometry (PTR), and

broadband dielectric spectroscopy. Chapter 4 is devoted to experimental results on PANI/SWCNT, PANI/MWCNT, PANI/RGO nanocomposites. More specifically, electrical, thermal properties of the studied materials are investigated. In this chapter, dielectric properties of the PANI/RGO nanocomposites are also discussed. Finally, in chapter 5, a comparison between 1-D and 2-D nano-fillers is developed and after that general conclusion is presented.



# CHAPTER 1 MATERIALS

Here, we present a discussion of the different materials which have been used in our study with a focus on their intrinsic properties. The knowledge of these intrinsic properties is important to address their utilizations in different application fields. In this section, a brief introduction on the properties of thermoelectric materials, conducting polymers, carbonaceous nano-fillers, and their nano-composites is presented.

## 1.1. Thermoelectric (TE) materials

Waste heat can be converted to electricity by thermoelectric generators. But the development is hindered by the lack of cheap materials with good thermoelectric properties. In recent years, inorganic materials such as  $\text{Bi}_2\text{Te}_3$ ,  $\text{PbTe}$ ,  $\text{GeTe}$  and  $\text{Sb}_2\text{Te}_3$ , are still the main focus in TE research [48–52]. Figure 4 shows the figure of merit of various inorganic materials as a function of temperature.

Nevertheless, due to the scarcity and expensiveness of their raw materials, the toxicity of the elements and the difficulty of processing, the use of inorganic materials limits the practical application [53–56].

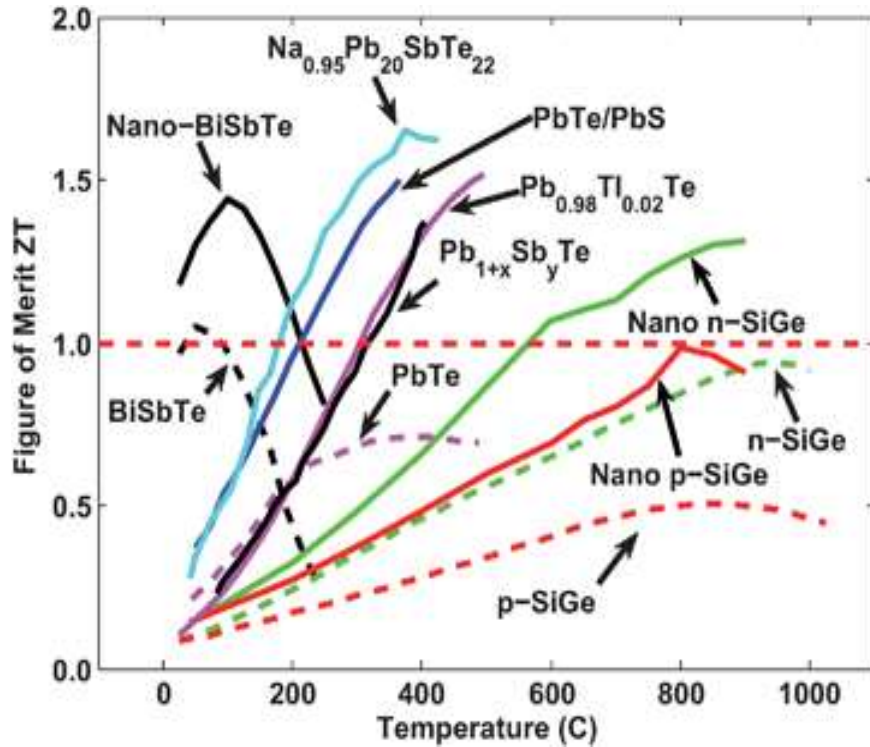


**Figure 4.** Figure of merit ZT of current state of the inorganic thermoelectric materials versus temperature. The dashed lines show the maximum ZT values for bulk state of the art materials, and the solid lines show recently reported ZT values, many of which were obtained in bulk nanostructured materials [40].

In order to overcome this problem, organic semiconductor can be alternative thermoelectric materials. More specifically, organic polymer TE materials can lead the thermoelectric research field due to their unique superiorities, for instance, low thermal conductivity, low density, facile processing into versatile forms and adjustable molecular structures, etc. [53–56]. Organic conducting polymers, such as polyaniline (PANI), poly (3,4-ethylenedioxythiophene) (PEDOT), polythiophene (PTh), polypyrrole (PPy), polyacetylene (PA), polycarbazole (PC) and their derivatives, have exhibited enormous potential for the applications in TE field. In recent time, organic polymer TE materials have achieved significant progress. Although low thermal conductivity of the polymers makes better thermoelectric materials, low electrical conductivity confines the thermoelectric applications. So, to improve the electrical conductivity, inclusion of conducting nano-fillers into polymer matrix can play significant contribution which can improve ZT. Generally, combination of low thermal



conductivity of polymers and high electrical conductivity of nano-fillers can be promising thermoelectric materials. For example, carbon-based materials are shown to have improved electrical conductivity [30]. Thus, a novel class of conducting polymer/carbonaceous TE composites has received increasing attention due to their extremely high electrical conductivities that can remarkably improve TE performance.

## 1.2. Conducting polymers

Conventional polymers such as plastics or rubbers are electrically insulating materials. However, in the past decades, newer types of synthetic polymers capable of conducting electricity have emerged. They are divided into four major categories: (a) conductively-filled polymers made of conventional polymers, e.g. polyvinyl chloride or epoxy resin containing variable amounts of added metallic particles (b) ionically conducting polymers which are also composed of conventional polymers as the insulating matrix (e.g., polyethers) containing electrolytes such as lithium ions (c) charge transfer polymers which combine charge donors (e.g., fullerenes) and acceptors (e.g., tetracyanoquinodimethanes) and (d) intrinsically conducting polymers (ICPs), “synthetic metals” or “organic conducting polymers” such as doped polyanilines (PANI), polypyrroles (PPY), polyacetylenes and 3,4-polyethylenedioxy thiophenes (PEDOT). The discovery of free standing, highly conducting iodine-doped polyacetylene films in the 1970s has spurred extensive research and applications of a number of ICPs which eventually culminated in the award of a Nobel prize in chemistry (in the year of 2000) to A. J. Heeger, A. J. MacDiarmid and Shirakawa [57]. In general, ICPs share a common and critical feature needed for conductivity, i.e., they contain conjugated repeating units as indicated by the presence of alternating double and single bonds (Figure 5). The double bond contains the less strongly localized  $\pi$  bonds which are weaker than the strong localized chemical  $\sigma$  bonds. Electrical conductivity is facilitated in the polymer chains because of the delocalization of  $\pi$  electrons through the extended overlapping p-orbitals. It is to be pointed out that most organic conducting polymers do not have intrinsic charge carriers (i.e., they are insulating) and that the presence of conjugation is only a pre-requisite criterion for conductivity.

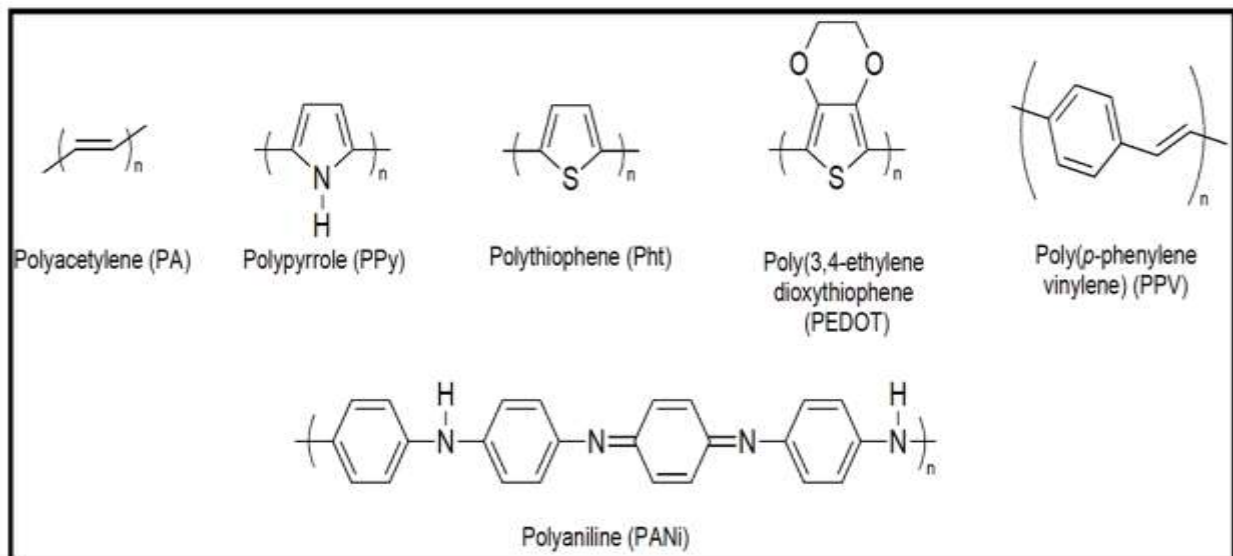


**Figure 5.** Chemical structures of some intrinsically conducting polymers.

So, a doping process is required to introduce the needed charge carriers. Such a process often involves a redox reaction which could be achieved via partial oxidation (p-doping) of the polymer chains in the presence of electron acceptors (oxidizing agents) or partial reduction (n-doping) with electron donors (reducing agents). However, some conducting polymers are discussed below.

### 1.2.1. Polyacetylene

Polyacetylene, a prototype ICP, is insulating and is made of long chains of alternating single and double carbon-carbon bonds in which each carbon holds one hydrogen atom. It can be rendered conducting either through oxidation (p-doping, e.g. with  $I_2$  or  $AsF_5$ ) or reduction (n-doped; e.g. with metallic elements such as Na or K). The latter process is shown below (Figure 6).

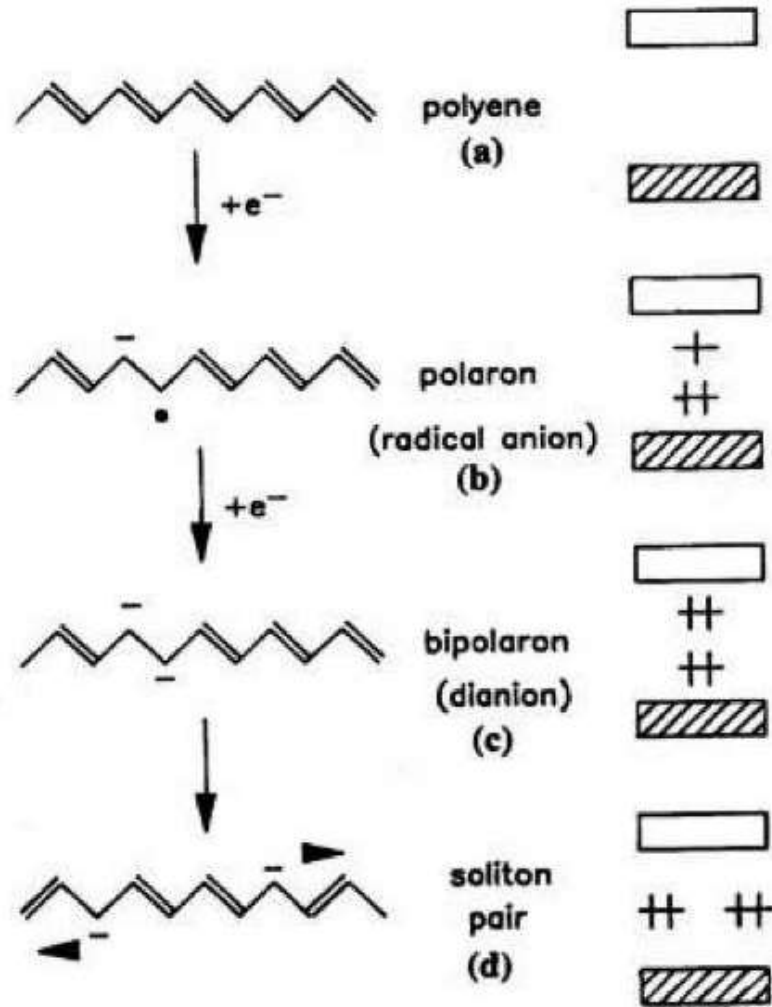


**Figure 6.** A schematic description of the formation of polaron, bipolaron, and soliton pair on a polyacetylene chain by n-doping. At right: shaded and unshaded boxes represent the valence bands and conduction bands, respectively [58].

It can be seen that the addition of an electron from Na or K to the bottom of the conduction band of a polyacetylene chain leads to partially filled conduction band with the formation of a radical anion or polaron (Figure 6(b)). This process creates new energy states in the band gap. A polaron carries both spin ( $1/2$ ) and charge ( $-1e$ ). Addition of a second electron results in the formation of a spinless bipolaron obtained through dimerization of two polarons, which can lower the total energy (Figure 6(c)). In extended conjugated polymers the bipolarons

can further lower their energy by dissociating into two spinless solitons at one-half of the gap energy (Figure 6(d)).

Conversely, the process of oxidative p-doping with e.g.,  $I_2$  or  $AsF_5$  (not shown in the Figure 6), via the removal of an electron from the top energy level of a valence band will create a polaronic radical cation (spin  $\frac{1}{2}$  and  $+1e$  charge). The removal of another electron will lead to a spinless bipolaron which may reorganize into two spinless solitons in a polymer chain.

In general, the population of polarons, bipolarons, and/or solitons increases with higher doping levels, leading to new energy bands between and even overlapping the valence and conduction bands, through which electrons can flow upon application of an electrical potential. Figure 7 provides a simplified explanation of electrical conductivity taking place in a polymer chain matrix in which charged species, obtained from redox doping processes, that may migrate under the influence of an electric field.

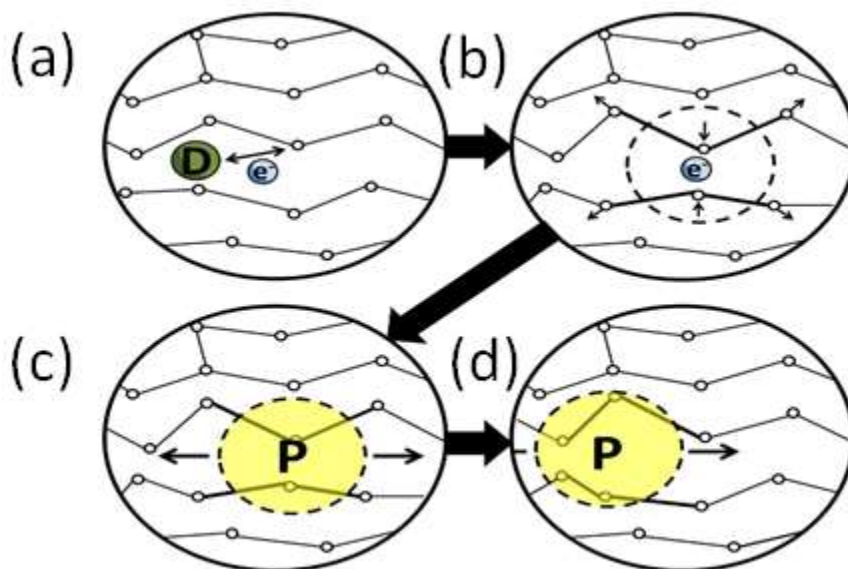


**Figure 7.** A simplified explanation of the electrical conductivity of conducting polymers. (a) The dopant removes or adds an electron from/to the polymer chain, creating a delocalized charge. (b) It is energetically favorable to localize this charge and surround it with a local distortion of the crystal lattice. (c) A charge surrounded by a distortion is known as a polaron (a radical ion associated with a lattice distortion). (d) The polaron can travel along the polymer chain, allowing it to conduct electricity [59].

## 1.2.2. Poly (3,4-ethylenedioxythiophene) (PEDOT)

Poly(3,4-ethylenedioxythiophene) (PEDOT) which is a polythiophene (PTh) derivative is another interesting conjugated and conducting polymer whose structures are shown in Figure 8 . It exhibits optical transparency in its conducting state, moderate band gap, high electrical conductivity (better conductivity and thermal stability than Polypyrroles), good chemical and environmental stabilities. PEDOT and its derivatives have been investigated and found applications in the areas of biosensing, neural electrodes, nerve grafts and heart muscle patches etc. A major disadvantage of PEDOT is its poor solubility in many solvents including water. However, it is possible to prepare an aqueous suspension of PEDOT by complexing it with large dopant counter anions such sodium polystyrene sulfonate (PSSNa) forming PEDOT:PSS Na (Figure 8). The aqueous suspension can be easily processed into, e.g., thin films [60] coated on glass or plastic substrates which can be used in e.g., LCD devices or solar cells [61].

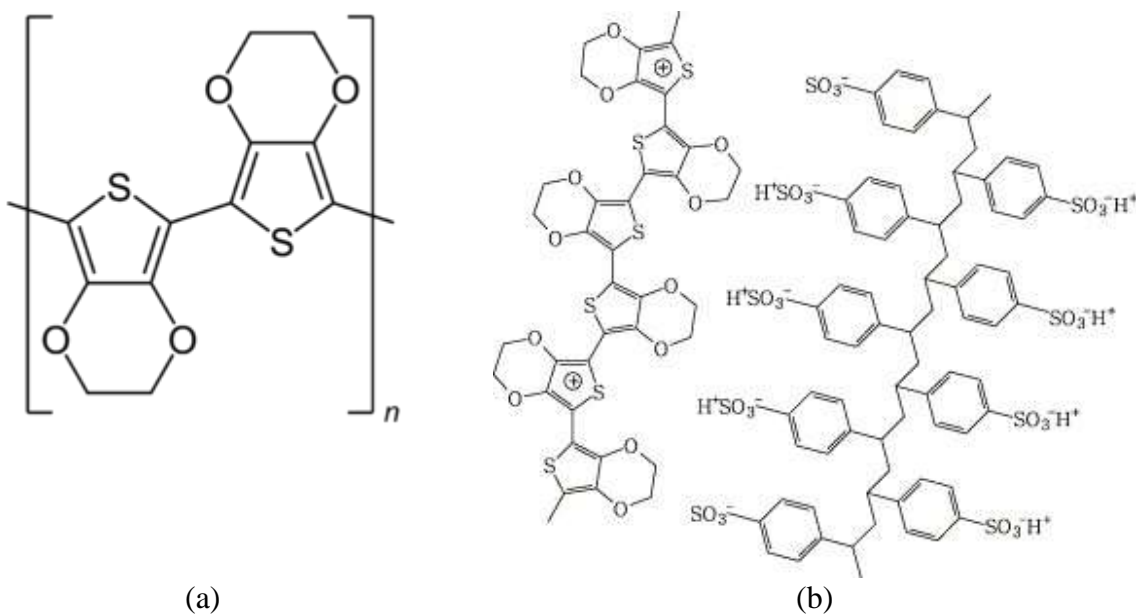


**Figure 8.** The chemical structures of PEDOT: (a) dedoped ; (b) doped in the form of PEDOT:PSSNa.

### 1.2.3. Polyaniline (PANI)

Polyaniline can be defined as a linear chain macromolecule consisting of para-coupled aniline [62,63]. Polyaniline (PANI) is the one of the most studied ICPs because of its ease of synthesis, high environmental stability, light weight and good electrical conductivity. Figure 9 shows the basic chemical structure of PANI. PANI can exist in a variety of forms that differ in physical and chemical properties [64–66]. PANI can be found in different oxidation states: the fully oxidized pernigraniline base (blue/violet  $[C_6H_4N]_n$ ), half-oxidized emeraldine base (green for the emeraldine salt, blue for the emeraldine base  $\{[C_6H_4NH]_2[C_6H_4N]_2\}_n$ ) and fully reduced leucoemeraldine base (white/grayish  $[C_6H_4NH]_n$ ).

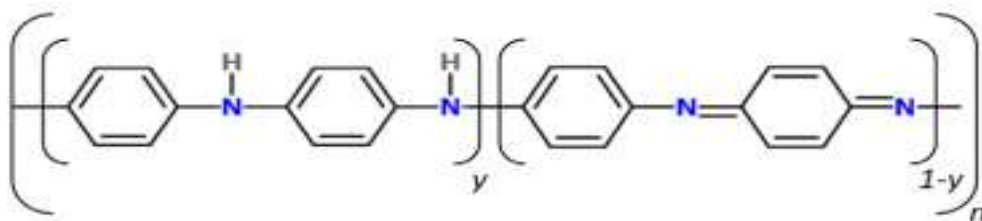
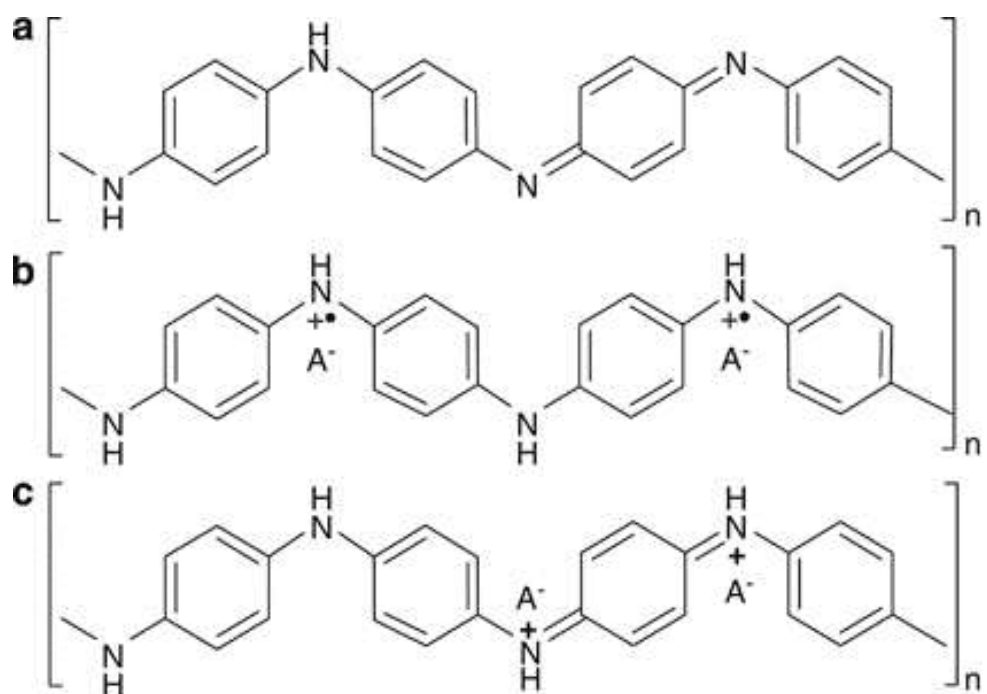


**Figure 9.** The basic structure of polyanilines.

Of all known PANI, emeraldine is the most used form because it can be easily switched between its conductive and resistive states, via doping with an acid (e.g. HCl or  $H_2SO_4$ ) and dedoping with a base (e.g. NaOH or  $NH_3$  (aq.)). Figure 10 shows various forms of PANI emeraldine states: (a) the emeraldine base (blue) in its resistive state (EB), the conductive states (green): emeraldine salt (ES) (b) with separated polarons or (c) with bipolaron.



$A^-$ , the counter ion, can be  $Cl^-$  or  $HSO_4^-$

**Figure 10.** Various forms of PANI emeraldine state: (a) the resistive emeraldine base (EB), the conducting emeraldine salts (ES) (b) with separated polarons and (c) bipolarons.

Moreover, the conducting state in PANI can also depend on the oxidation (loss of electron) and reduction (gain of electron). Since both processes take place at same time in the reaction medium, the terms (oxidation and reduction) are combined in one word which is defined as oxidoreduction or redox reaction. For example, in dedoped PANI (not protonated) which is nonconductive, there are 2 types of N-atoms. One is amine nitrogen and the other one is imine nitrogen (Shown in Figure 11(a)). During reaction the imine N-atoms transfer its electron negative charge to an electron acceptor (oxidizing agent) which is shown in Figure 11(b). As a consequence, the N turned into positive (+) charge and the PANI becomes conducting (shown in Figure 11(c)).

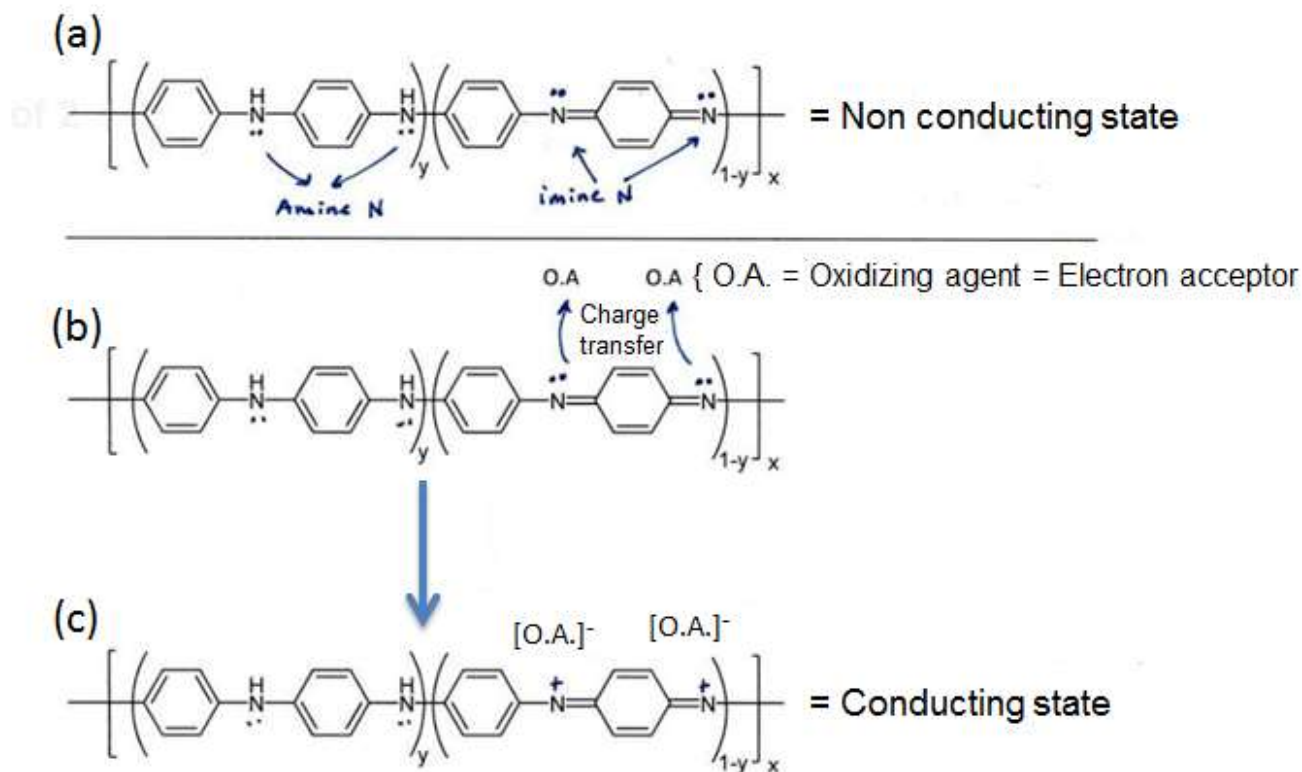


**Figure 11.** (a) Non conducting state of PANI. (b) charge transfer process in PANI during reaction, and (c) conducting state of PANI.

So, in order to improve conducting properties of doped PANI, the conditions of preparation/dopant incorporation is of fundamental importance. Veluru Jagadeesh Babu *et al.* [67] reported that acid doped conducting polymers influence more on conducting properties in comparison with metal oxides. For example, HCl is considered as oxidizing agent here. The reaction process of PANI and HCl is shown in Figure 12(a). The proton or  $H^+$  accepts the electron from N resulting in conducting state of PANI or protonated PANI which is shown in Figure 12(b).



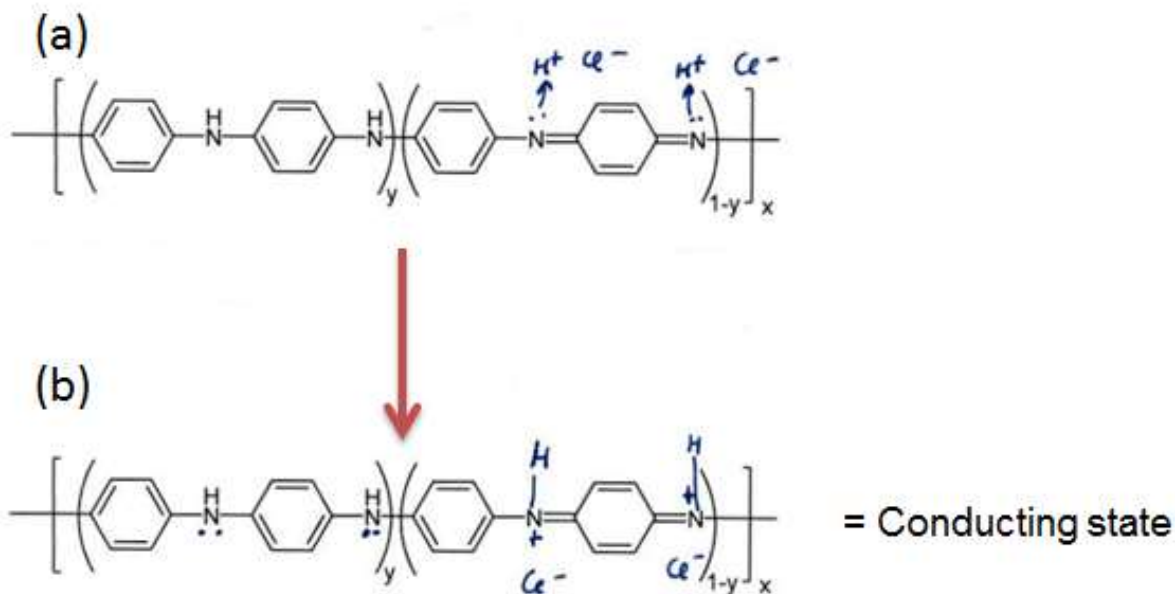


**Figure 12.** (a) The reaction process of PANI and HCl (b) conducting state of PANI after reaction with HCl.

Furthermore, the most common green emeraldine PANI exhibits conductivity on a semiconductor level of the order of 1 S/cm which is many orders of magnitude higher than that of common polymers ( $<10^{-9}$  S/cm) but lower than that of typical metals ( $>10^4$  S/cm). Also protonated PANI, (e.g., PANI hydrochloride) can be converted into a non-conducting blue emeraldine base by using ammonium [66] which is shown in Figure 13.

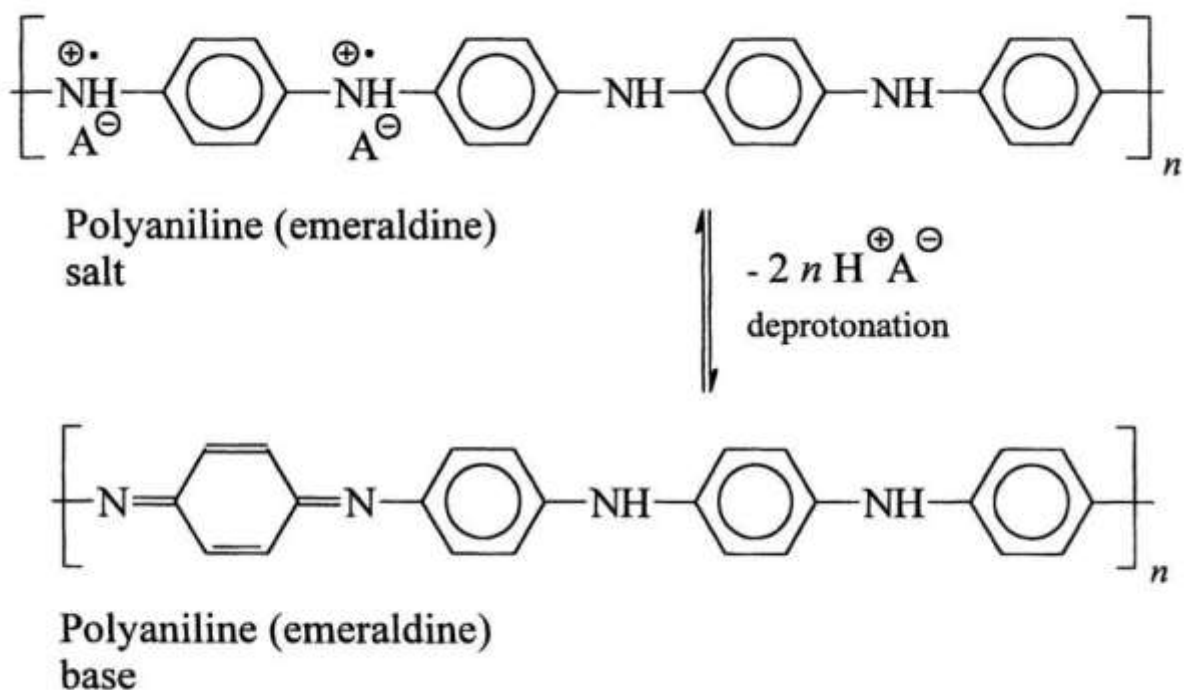


**Figure 13.** Polyaniline (emeraldine) salt is deprotonated in the alkaline medium to polyaniline (emeraldine) base.  $\text{A}^-$  is an arbitrary anion, e.g., chloride [68].

However, the reaction conditions can affect the effective conductivity of PANI [68]. The different reaction temperature, reaction volume, and reaction pressure provides different values of the conductivity of PANI. There are also additional factors which can influence the conductivity of PANI such as palletization effect, temperature during conductivity measurements, and storage etc.

The acid or base induced properties of PANI make it very attractive for many applications in the areas of chemical vapor sensors, actuators, supercapacitors, electrochromics, antistatic coatings, electromagnetic shielding and flexible electrodes. In addition, PANI has also been applied in biology as biosensors, neural probes, controlled drug delivery and tissue engineering applications. The establishment of the physical properties of PANI reflecting the conditions of preparation is thus of fundamental importance.

### 1.3. Carbonaceous nano-fillers

A nano-filler is defined as a material confined in one, two or three dimensions at nanoscale (1-100 nm). Many nanotechnology applications are based on novel as well as conventional materials deliberately engineered to be nanostructured for which the term ‘nano-filler’ is now frequently used. Some nano-fillers exhibit additional features and/or properties as compared to coarser materials with similar chemical composition. These nano-fillers are now used in a wide range of innovative technological applications and products. There are different types of nano-fillers whose names stem from their individual shapes and dimensions. These include nanoparticle, nanofibers and nanoplates. Nanoparticles are the materials in which all three dimensions are within the nanoscale. However, nanofibers have a diameter in the nanoscale but can be several hundred nanometers long or even longer. Further, nanofibres are divided into nanotubes (hollow nanofibres), nanorods (solid nanofibres) and nanowires (solid or hollow electrically conducting or semiconducting nanofibres). Nanoplates are the nano-fillers with one external dimension at nanoscale and the two others external dimensions are usually significantly larger.

Carbonaceous nano-filler is an important family of  $sp^2$  bonded graphitic carbons nanomaterials. In the past two decades, zero-dimensional (fullerenes and their derivatives), one-dimensional (carbon nanotubes), and two-dimensional (graphene and their derivatives) carbonaceous nano-fillers (Figure 14) have attracted significant attention from the scientific community. This is due to their unique electronic, optical, thermal, mechanical, and chemical properties which are strongly dependent on their atomic structures and interactions with other materials. These nano-fillers are experiencing renewed interests as they are the basis of numerous applications which include but are not limited to electronic, optoelectronic, photovoltaic, and sensing devices.

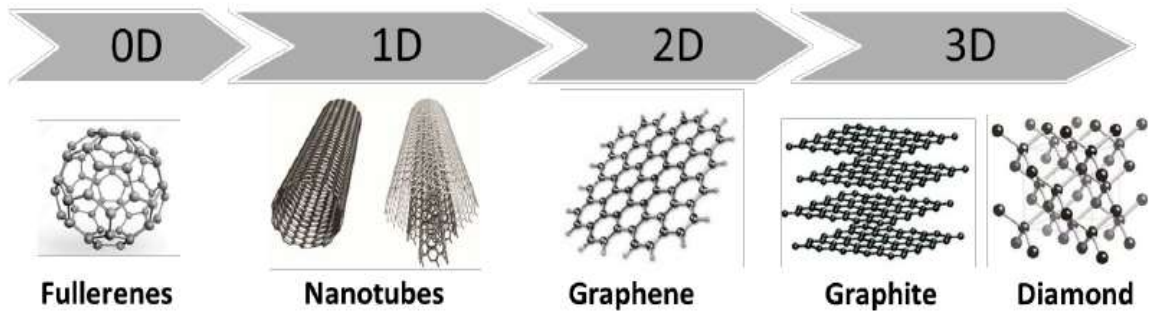


**Figure 14.** Carbonaceous nanomaterials with different dimensions [69].

### 1.3.1. 1-D carbonaceous nano-fillers

As a 1-D carbonaceous nano-filler, carbon nanotubes (CNTs) were first discovered in 1991 by Iijima [70]. These nanomaterials have structures with diameters varying from fractions of a nanometer to several dozen nanometers and length ranging from one micron to several hundred microns or more. CNTs may exist in two forms: single wall carbon nanotubes (SWCNT) and multi wall carbon nanotubes (MWCNT) as shown in Figure 15.

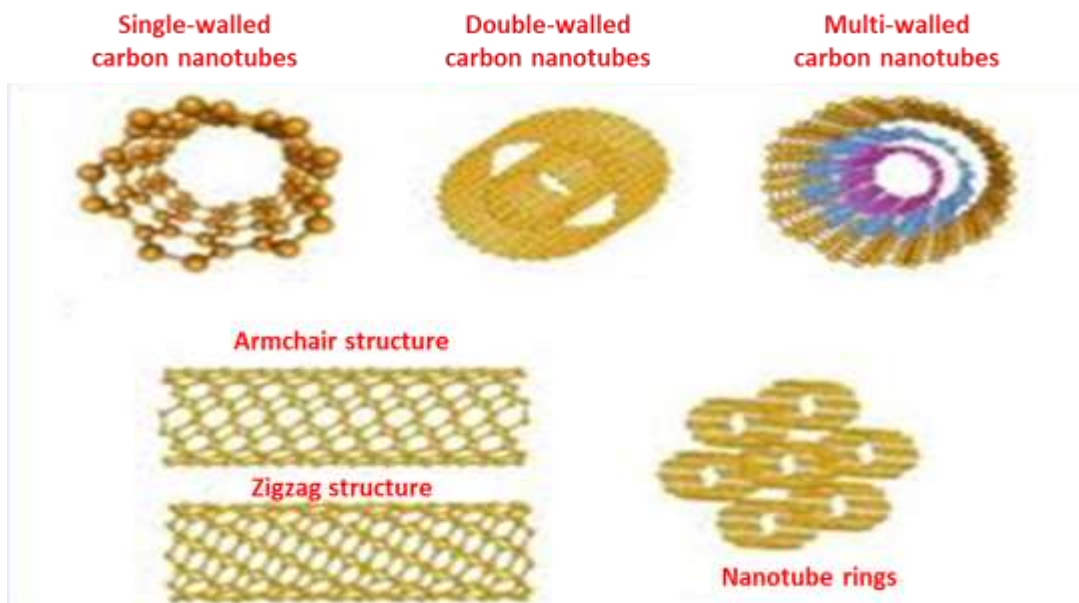


**Figure 15.** Different structural types of carbon nanotubes [71].

They exhibit unique electromagnetic, optical and mechanical properties. For example a) the current density in metallic nanotubes may be several orders greater than in conventional metals and b) they possess high electric and thermal conductivity along the tube axis while in the lateral directions they act as insulators. A number of one dimensional CNTs applications have been reported. They are also used in mechanically enhanced composites, energy and hydrogen storage devices, field emission displays and high performance semiconductor components and interconnects [70]. In addition, CNTs can be used for organic diodes and field effect transistors, needles in scanning tunneling and atomic force microscopy and the development of semiconductor heterostructures.

### 1.3.1.1 Single wall carbon nanotubes (SWCNT)- structure and properties

SWCNT nano-fillers are allotropes of carbon with a cylindrical structure which is consider as a “rolled-up” form of another carbon allotrope called graphene. They consist of  $sp^2$ -hybridized bonds and have a very high aspect ratio. Structurally SWCNT nano-fillers are characterized by the chiral vector  $\vec{Ch} = n\vec{a}_1 + m\vec{a}_2 = (n, m)$ , which links pairs of atoms that coincide upon this imaginary process of wrapping, where  $n$  and  $m$  ( $n \geq m$ ) denote the number of unit vectors along two directions in the honeycomb crystal lattice of graphene sheet at a given carbon atom (Figure 16). The different values of  $n$  and  $m$  give the tubes totally different properties such as nanotubes with  $n-m$  divisible by 3 are metallic (or narrow-gap semiconductors) while the rest of the nanotubes are semiconductors, although their band gap approaches zero with increasing diameters. Further, there are “zigzag” nanotubes, also known as  $(n, 0)$  nanotubes and “armchair”  $(n, n)$  nanotubes. These two classes of nanotubes are optically inactive while all other nanotubes are chiral. The values of  $n$  and  $m$  uniquely define the diameter and band structure of SWCNT. The diameter ( $d_{\text{SWCNT}}$ ) of an individual SWCNT in nanometer is determined as [72]:

$$d_{\text{SWCNT}} = \frac{0.246}{\pi} (\sqrt{n^2 + nm + m^2}) \quad 1$$

Among the CNTs, SWCNT possess the most interesting combination of physical properties. They have been used for various purposes, e.g., photovoltaic devices, nanoelectronics, molecular sensors and anti-cancer agents.

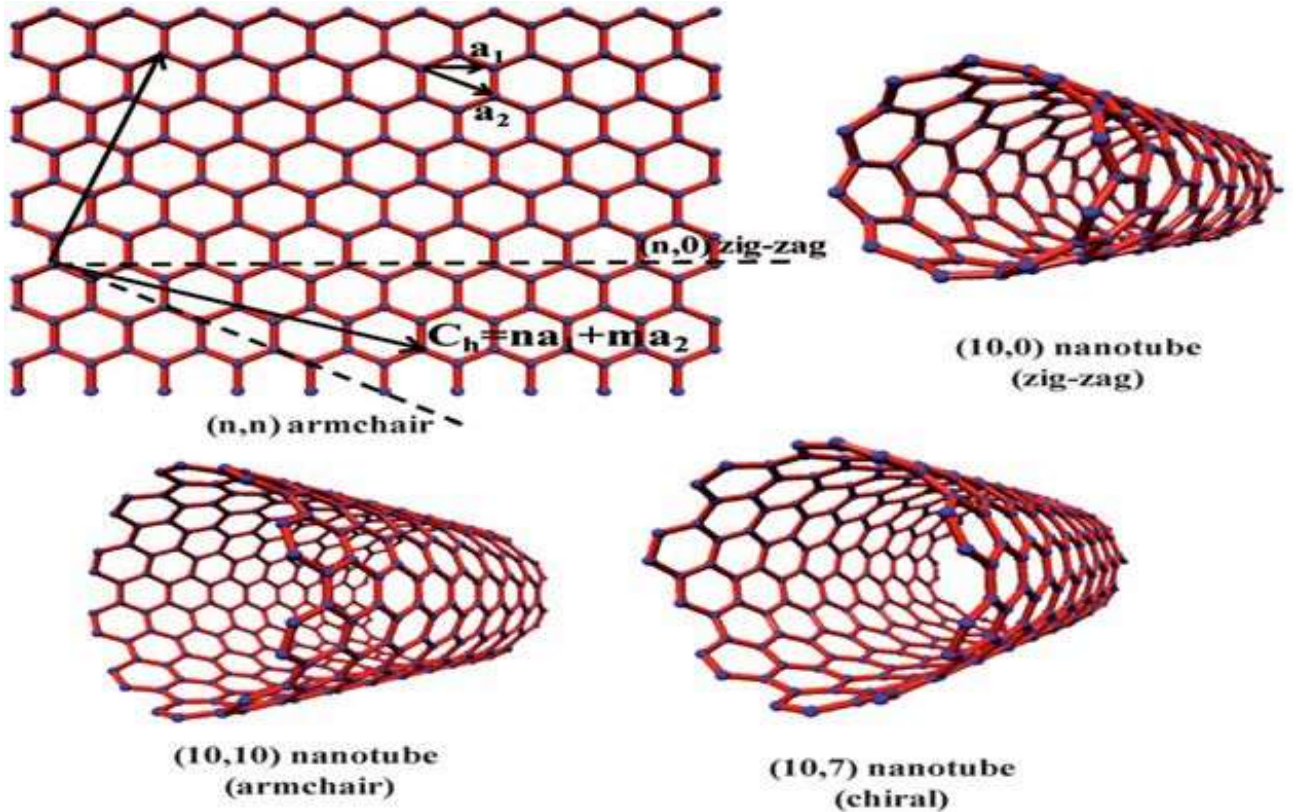


**Figure 16.** Structures of single-walled carbon nanotubes [73].

### 1.3.1.2 Multi wall carbon nanotubes (MWCNT)- structure and properties

Besides SWCNT, multi wall carbon nanotubes (MWCNT) which consist of multiple layers of graphenes rolled up resulting in a cylindrical shape structure are also presented as one-dimensional nano-fillers. This structure can be viewed as a collection of concentric SWCNT



with different diameters, lengths and properties (Figure 17). The distance between each layer is approximately 0.34 nm, slightly larger than the interlayer distance of graphite sheets and the layers are coupled to each other through van der Waals forces [74,75]. The properties of MWCNT resemble those of SWCNT to some extent in that they have high chemical stability, high electrical conductivity, high mechanical properties and a high aspect ratio with lengths typically more than 100 times the diameter, and in certain cases much higher. They have excellent tensile strength and thermal stability (more than 600 °C) depending on the level of defects and the degree of purity. Much like their SWCNTs counterparts, MWCNTs find applications in many areas, e. g. as chemical sensors, or components in reinforced structural composites (aerospace, sporting goods), in energy applications such as lithium ion batteries [76].

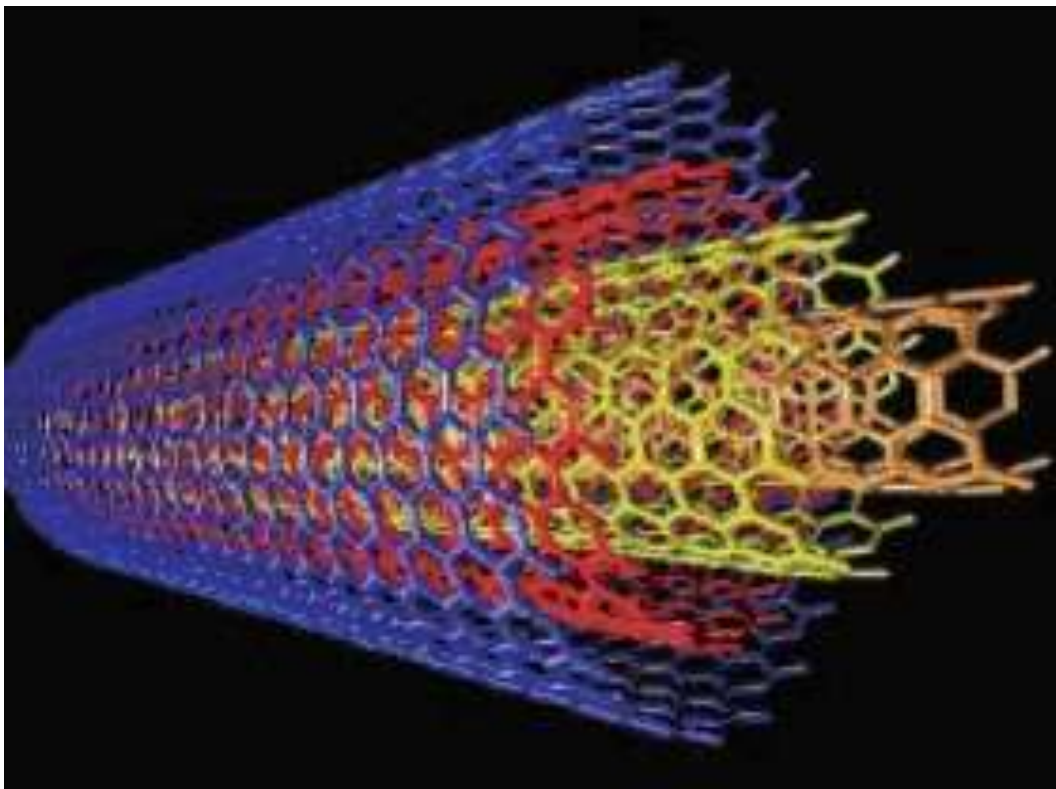


**Figure 17.** Multi-walled carbon nanotubes [77].

### 1.3.2. 2-D Carbonaceous nano-objects

Two dimensional (2-D) carbonaceous nano-fillers (Figure 18) have been the subject of intensive research in recent years since the successful isolation of individual graphene sheets by micromechanical cleavage of highly oriented pyrolytic graphite (HOPG). While one of the dimensions of these nano-fillers is in nanoscale, the others may be significantly larger. Members of these 2-D carbon allotropes may be produced or isolated in the form of graphene sheets, graphene nanoplates, graphene oxide nanoplates, reduced graphene oxide sheets. Out of these, reduced graphene oxide (RGO) is discussed below.

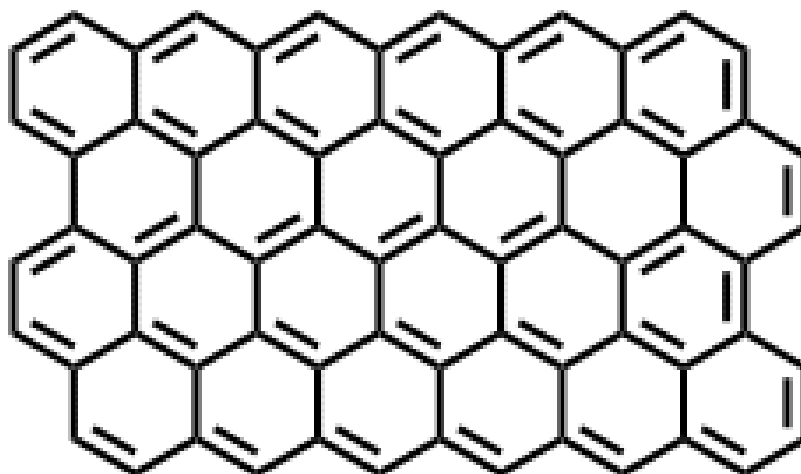


**Figure 18.** The structure of two dimensional (2-D) carbonaceous nano-fillers.

Across the globe, researchers are looking for ways to understand the properties of graphene sheets whose thickness is that of one carbon atom. Attempt to access relatively pure graphene sheets can be achieved by reduction of graphene oxide (GO) either chemically, thermally or electrochemically (Figure 19) [78].



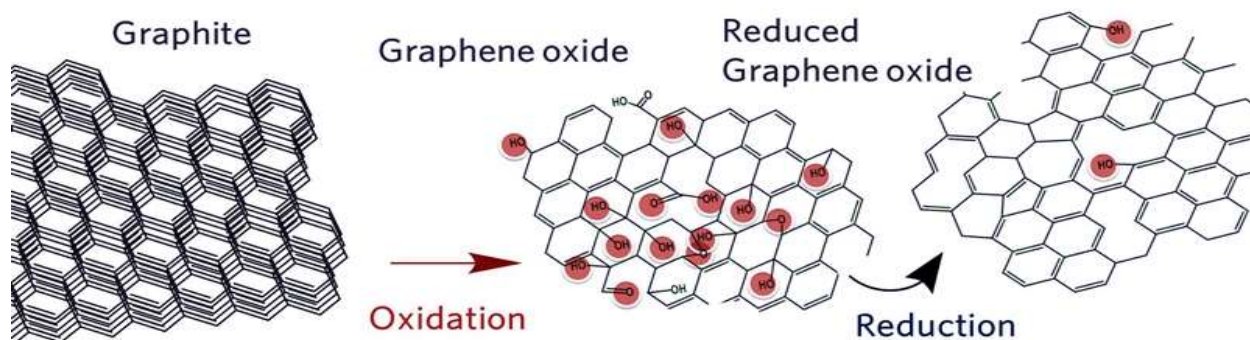


**Figure 19.** The chemical structure of reduced graphene oxide [79].

Though numerous efforts have been made to produce RGO [80], the reduction process is extremely sensitive and has a large impact on the quality of the RGO produced, and therefore determine how close RGO will come, in terms of structure, to pristine graphene [81]. The presence of residual functional groups and defects dramatically alter the structure of the carbon plane, therefore, it is not appropriate to refer the as-prepared materials to “RGO”s. The structure of RGO is usually described by the presence of nanometric  $sp^2$  graphitic islands separated by regions of oxidized graphene in which the tendency of oxygen to agglomerate into highly oxidized domains surrounded by areas of pristine graphene. This feature has been recently demonstrated by first principle approximation and statistical calculations [82]. Because the physical properties of RGO depend on the degree of reduction, they show both insulating and conducting characters, depending on the percentage of oxygen left on the graphene sheet. It has been recently reported that electrochemically produced RGO exhibits a very high carbon to oxygen ratio and excellent electronic conductivity (8500 S/m) higher than that of silver 6300 S/m [81]. RGO also has a high surface area, close to that of pristine graphene. Even in large scale operations where large quantities of graphenes are needed for industrial applications, RGO is most likely the desired substitute for pristine graphene, due to the relative ease for the preparation of sufficient quantities of relatively pure RGO with the desired quality levels. RGO is expected to be exploited in e.g., supercapacitors for energy storage, electrodes in Li-ion batteries or transparent electrodes in solar cells, photoluminescence applications [83–85].

## 1.4. Polymer nanocomposites

Polymer nanocomposites are generally defined as hybrid materials arising from the combination of a polymer matrix and fillers with at least one of its dimensions in the nanoscale range. The structure of the fillers can be three dimensional (such as spherical nanoparticles), two dimensional (which include layered like structures) or one dimensional (examples include nanotubes and nanofibers). Often, these nano-fillers are incorporated into the matrix so as to enhance the overall properties of the composites. The polymer matrix and fillers may be bonded to each other by weak intermolecular forces, while chemical bondings are rarely involved. But, if the fillers are well dispersed at the nanoscale and connected with the matrix by chemical bondings, then significant improvements of the overall characteristics are achieved or unexpected new properties might be realized [86].

Owing to the large surface area of nano-fillers (compared to their micro and macro counterparts), polymer nanocomposites have attracted much interest in science and technological fields since the past few decades. The presence of small amounts of nano-fillers embedded into the nanocomposite gives outstanding overall properties such as mechanical strength, barrier resistance, flame retardancy, water resistance, optical, magnetic and electrical properties [86–89]. These different properties of polymer nanocomposites will determine the application to which it is appropriate.

Carbonaceous nano-filler-based polymer nanocomposites have increasingly attracted much attention over the last few years and scientists set them apart in their own class due to their distinct properties. In order to overcome the limitation of many properties of the host polymers e.g., electrical conductivity and thermal conductivity, carbonaceous nano-fillers such as carbon black, SWCNT, MWCNT, graphene, graphene oxide and reduced graphene oxide are added into the host to produce enhanced properties of the resulting nanocomposites. For example, filler loadings play an important role in 2-D or 3D percolation behavior of electrical and thermal properties [18,90]. Further, interfaces between filler and host control the charge trapping or phonon scattering in the systems [91,92].

On the basis of different applications, carbonaceous nano-objects could be used in conjunction with various conducting polymers (PPy, PANI and PEDOT etc.) to make the final products. The present study focuses on carbonaceous nano-fillers based PANI nanocomposites such as:

1. SWCNT-based PANI nanocomposites (PANI/SWCNT).
2. MWCNT-based PANI nanocomposites (PANI/MWCNT).
3. RGO-based PANI nanocomposites (PANI/RGO).

#### 1.4.1. SWCNT-based PANI nanocomposites

PANI/SWCNT nanocomposites are prepared through several methods described in the literature [7,93–97]. For example, W.K. Msser *et al.* [98] synthesized PANI/SWCNT composites by using “in situ” polymerization process using SWCNT in concentrations ranging from 2 to 50 weight percentage (wt-%) and showed that SWCNT favors the formation of inhomogeneous mixtures rather than of a homogeneous composite materials, independent of the SWNT concentration. Nakamatsu *et al.* (2007) [99] described a unique fabrication technique to control the electrical conductivity of PANI/SWCNT composite by a conventional rubbing technique. A combination of outstanding properties of SWCNT and those of intrinsically conducting polymer (PANI) allows the fabrication of hybrid devices whose properties find wide applicability in various fields such as sensing, energy harvesting and storage, electromagnetic interference shielding, and so on [7,93–95]. Naturally, such hybrid properties critically depend on the PANI–SWCNT interfacial physicochemical and electronic interactions (Figure 20). In particular, a strong coupling between SWCNT and PANI through  $\pi$ - $\pi$ -interaction enhances a set of practically important properties of the nanocomposites such as thermal stability, conductivity, and processability [7,100–102]. Another important characteristic of the PANI/SWCNT composites is the nanoscopic dimension of their components. This dimensionality suggests that the materials can potentially show size-dependent effects and a singularity or nonlinearity in their structure–property relationships [102]. In the present work, core-shell SWCNT-PANI nanocomposites are synthesized via an in-situ polymerization process and their physical properties are exploited in thermoelectric and storage materials.

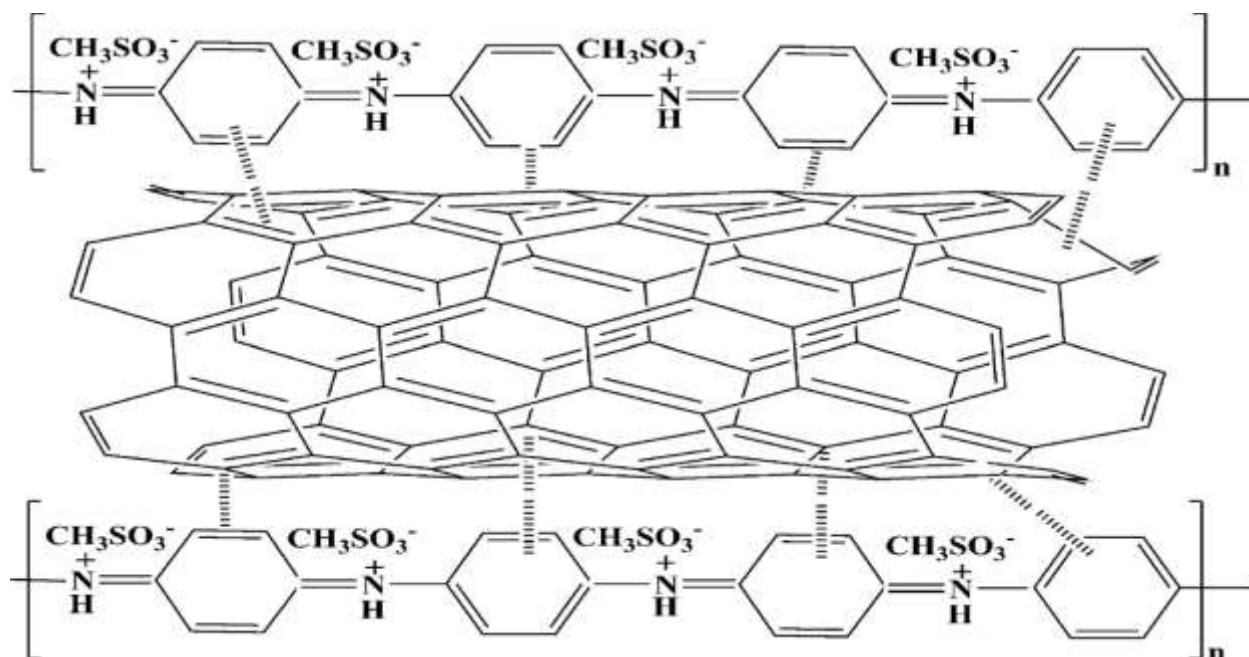


**Figure 20.** Schematic representation of  $\pi$ - $\pi$  interactions between fully protonated PANI chains with the basal walls of un-oxidised carbon nanotubes [7].

#### 1.4.2. MWCNT-based PANI nanocomposites

Much like PANI/SWCNT, reports on the preparation, properties and applications of PANI/MWCNT are found in the literature [7,103–105]. For example, MWCNT/poly(o-anisidine) composite degrades at higher temperature than poly(o-anisidine) alone [106]. The room temperature resistivity of PANI films containing 10% MWCNT decreases by one order of magnitude compared to that of neat PANI [107]. Murielle Cochet *et al.* [108] showed that the synthesis of PANI/MWCNT by an in-situ process leads to effective site-selective interactions between the quinoid ring of the PANI and the MWNTs facilitating charge-transfer processes between the two components. PANI/MWCNT nanocomposites had been used for microwave absorption and EMI shielding [109]. Other applications of PANI/MWCNT composites are found in, e.g., fuel cells, sensors, transistors, actuators photovoltaic cells showing the promising use of these nanostructured hybrid materials [109].

Furthermore, It is shown that the strong interfacial interaction of MWCNT with the PANI through  $\pi$ - $\pi$  interaction significantly contributes to produce core-shell MWCNT-PANI nanocomposites [7,108,110]. Generally, MWCNT based nanocomposites show different behavior in structural order, oxidation state, imperfection of the molecular structure, and thermostability, from the neat PANI. The enhancing influence of the PANI shell on practical properties of the synthesized powder nanocomposites is illustrated by the example of the sharp growth of thermostability of the nanocomposites and the remarkable reduction of the response time for gaseous ammonia sensors [111]. Despite these reports, there is still a lack of understanding of some of the principles and mechanism paths that control the overall characteristics. In this work, we have tried to shed some light on the influence of MWCNT loadings in enhancing the characteristics of the composites via synergistic effects of the MWCNT and PANI. The composite data are also compared separately to those of the pristine MWNT and neat PANI (synthesized under the same conditions).

### 1.4.3. RGO-based PANI nanocomposites

Although SWCNT and MWCNT polymer nanocomposites hold excellent properties for many applications, these can be restricted because they can be commercially expensive. To overcome this problem, researchers are finding new carbonaceous nano-object – based polymer nanocomposites such as graphene and its derivative based polymer nanocomposites, e.g., RGO based PANI nanocomposites may be the alternative materials. The choice of RGO stems partly from their strong electrochemical activity, satisfactory electrochemical stability and advantage of production in large quantities via chemical reduction of GO colloidal dispersion [112]. So far, there are two ways to produce RGO based PANI nanocomposites. One method is in situ growth involving the polymerization of PANI on graphene sheets, and the other is to polymerize anilines on graphene sheets by electrochemical synthesis [112]. Despite the availability of these recent methods, additional theoretical research and applied research are still being conducted in hope to better understand the combined role played by RGO and PANI in the nanocomposites. For example, it has recently been found that electrical transport properties of (modified) reduced graphene-filled PANI nanocomposites invariably exhibit an increasing non-linear trend as a

function of the filler whose quite low % is often sufficient to induce electrical percolation [113,114]. In addition, RGO based nanocomposites have turned out to be able to enhance the thermal conductivity, mechanical strength of the nanocomposites [115–117]. Other applications are found in the areas of thermal management equipments, reinforced mechanical systems, EMI shielding devices, supercapacitors or memory devices for portable electronics [112,118–122]. In this work, we focus on the influence of the loadings of RGO and their interfacial interactions with PANI in tuning the overall properties of the resulting nanocomposites and their potential use as thermoelectric and energy storage materials.



# CHAPTER 2 THEORITICAL BACKGROUND

## 2.1. Introduction

Fillers-based polymer nanocomposites are usually called random heterogeneous materials (RHM) owing to the position and composition disorder of their constituents that characterize them [123]. One type of RHM makes use of polymers that contain various dimensional nano-fillers: zero-dimensional (0-D), one-dimensional (1-D) and two-dimensional (2-D). The behavior of these systems relies on the combination of physical properties of filler and host material. These hybrid properties are controlled through some crucial parameters such as the interactions between filler and host, the quality of the filler dispersion or interfacial space of the nanocomposites. Nevertheless, intense theoretical and applied researches are still being conducted in hope to pinpoint the influences and better understand the roles played by both components of the composites at nanoscale level. In this chapter, we present briefly a theoretical overview on some of the properties of the nanocomposites that govern or dictate their applications.

## 2.2. Electrical properties

### 2.2.1. Background

The Electrical properties of a material determine ability of material to be suitable for the flow of electric current. In order to study the electrical properties of the material, electrical conductivity ( $\sigma$ ) and electrical resistivity ( $\rho$ ) are used. The electrical conductivity measures a material's ability to conduct an electric current. The SI unit of the electrical conductivity is Siemens per meter (S/m). And the electrical resistivity ( $\rho$ ) is the reciprocal of electrical conductivity.



Electrical conductivity of the polymer composites reinforced with conducting nano-fillers shows great technological importance. Generally, conducting polymers have very low electrical conductivity which cannot meet the requirements for many applications. For a practical standpoint, efforts to improve the electrical properties of conducting polymer nanocomposites have sustained continued challenges in the area of theoretical and applied sciences. Figure 21 displays a schematic diagram of electrical characteristics of materials ranging from insulating to the typical metallic conductors. To achieve high electrical conductivity, proper selection of the polymer matrix materials and conducting nano-fillers are very important. The incorporation of conducting nano-fillers into matrix can improve the electrical conductivity of the composites significantly. The effective electrical conductivity of polymer composites can increase by several orders of magnitude. But the effective electrical conductivity can be affected by several factors such as the aspect ratio and type of fillers, functionalization and dispersion of fillers, as well as the conditions of the material processing.

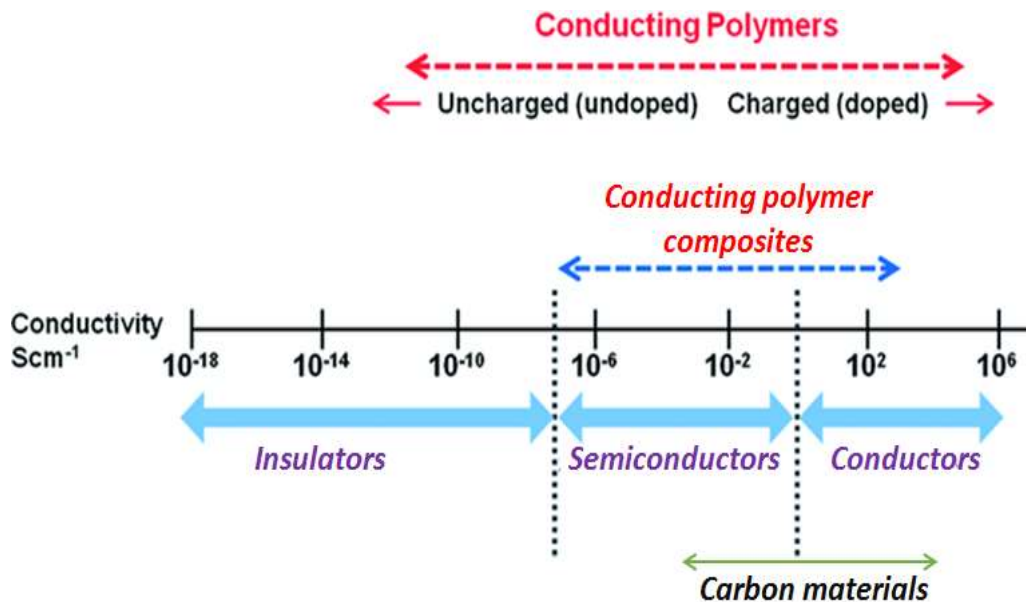


**Figure 21.** Schematic diagram of conductivity range of conducting polymers and carbon materials.

## 2.2.2. Conduction mechanism

In general, the conductive composites are two-phase system with quasi insulating phase (polymer matrix) and conductive phase (nano-fillers). The understanding of the conduction mechanisms that control the electrical conductivity of matrix and nano-fillers helps the material research for future potential applications.

As pointed out in Chapter 1, the key structural feature for conducting polymers is their extensive conjugation. In the absence of charged species, they are essentially insulators. So, to make the materials conducting a doping process is needed which produces, e.g., polaronic species with conduction proceeding via variable range hopping (VRH) of the polarons. Generally, the conductivity and charge mobility of doped materials are low and the bandgap of the systems is approximately 1.5-2.5 eV. The conduction mechanisms of polyaniline doped with oxidizing agent have been described in Chapter 1 (section 1.2.3). However, in some cases (e.g. polyacetylenes) the doping with oxidizing agents such as iodine can make the systems extremely reactive with oxygen [124]. Consequently, the polymers become more unstable. So selection of materials for the doping process could be challenging.

However, this drawback can be circumvented with the use of carbonaceous materials which act as the conducting inclusions and interact with matrix through Van Der Waals attractions resulting in no decrease in the stability of the composites [90]. Carbonaceous materials may be metallic or semiconductor, but sometimes in bulk form, these materials can behave as pseudo metals with conductivity of approximately  $10^5$  S/m. Generally, in the semiconducting carbonaceous materials, electrons and holes can be represented as the charge carriers which are responsible for the electrical conductivity of the materials. The carriers may be scattered strongly by the disordered structures. As a result, the mean free path may sometimes be in the order of the scale of the disorder. So, carbonaceous fillers with different forms exhibit different electrical conductivity because of different conduction mechanism.

From electrical conduction point of view, SWCNT is represented as quasi one-dimensional electronic system [125–127]. SWCNT can be either semiconducting or metallic by changing their spiral structure and diameter [127]. However, the basic electrical properties of the tubes are

controlled through conduction mechanisms in SWCNT. Although many efforts have been done to understand the charge transport mechanism in SWCNT, It is still not fully understood. Fischer et al. [128] reported that SWCNT crystalline ropes exhibit metallic resistivity. Also variable range hopping (VRH) conduction mechanisms can be observed in SWCNT [129–131]. SWCNT can show different dimensional VRH. Y. Yosida *et al.* [129] reported that three-dimensional VRH (3D VRH) conduction can be observed in SWCNT, and that the effect of the Coulomb gap is negligible. And Z.K. Tang et al. reported that one-dimensional VRH (1D VRH) can be observed in SWCNT aligned in 1 nm sized channels of zeolite crystals [130]. In general, 1D VRH is expected in SWCNT because of their quasi-1D structure.

Like SWCNT, MWCNT behaves one-dimensional electronic system. Also MWCNT shows almost same conduction mechanism like SWCNT. But their conduction level is different from SWCNT. As a consequence, both show different electrical conductivity because aspect ratio, diameter of tubes, and length of the tubes affect the overall electrical conductivity.

Also, reduced graphene oxides exhibit two-dimensional electronic systems which favor 2-D conduction mechanism. At room temperature, conduction mechanism of reduced graphene oxide is dominated by two-dimensional (2D) electric field-assisted, thermally-driven variable-range hopping (VRH) through highly disordered regions [132]. Joung *et al.* [133] reported that at low temperature electron transport of chemically reduced graphene oxide (RGO) sheets with different carbon  $sp^2$  fractions of 55 to 80 % follow Efros-Shklovskii variable range hopping (ES-VRH) in in the low bias (Ohmic) regime. At high temperature above 1000°C, the electrical conduction mechanism of the reduced graphene oxide thin-films synthesized from defective graphene oxide shows a band-like transport with small thermal activation energy ( $E_a \sim 10$  meV) that occurs during high carrier mobility ( $\sim 210$  cm<sup>2</sup>/Vs) [134]. origin of the band-like transport can be interpreted by the charge carriers, which are more easily excited into the conduction band due to the decreasing energy gap with the expansion of the conjugated  $\pi$ -electron system in the reduced graphene oxides [134].

## 2.2.3. Electrical conductivity models

Past studies show that depending on the concentration of conducting fillers, the electrical conductivity of the composites can be tailored over many order of magnitude. The activity can be performed for any polymers by using traditional doping resulting in charge carriers. The electrical conductivity of the composites can also vary substantially depending on molecular weight, distributions, defect concentration and purity of both the filler and polymer. To understand the changing of electrical conductivity value, several electrical conductivity models are used. The accurate models simplify the behavior of the materials. Here, few important models are described for filler volume fraction dependent and temperature dependent electrical conductivity.

### 2.2.3.1 Filler volume fraction dependent electrical conductivity

The effective electrical conductivity of the composites depends on the conductivity of matrix and the conductivity of fillers. Thus, the electrical conductivity of polymer composites can be changed as function of filler concentration. So, the electrical conductivity of the composites is characterized by its dependence on volume fraction. The behavior of electrical conductivity as a function of filler volume fraction can be interpreted by using mixing rule which is the simplest models as well as the first step. In general, there are two models. One is One “parallel model” (upper bound) and another one is ”series model”. The parallel model considers that overall property is in the direction parallel to the filler. The model is expressed as below:

$$\sigma = \sigma_{\text{filler}} \cdot \Phi_{\text{filler}} + \sigma_{\text{matrix}} \cdot \Phi_{\text{matrix}} \quad 2$$

where  $\sigma$ ,  $\sigma_{\text{filler}}$ ,  $\sigma_{\text{matrix}}$ ,  $\Phi_{\text{filler}}$  and  $\Phi_{\text{matrix}}$  are the electrical conductivity of the composites, the electrical conductivity of the filler, the electrical conductivity of the matrix, the volume fraction of the filler and the volume fraction of matrix, respectively. Here, each phase contributes to the

overall conductivity. The series model corresponds that the overall property is in the direction perpendicular to the filler. This model is expressed as:

$$\frac{1}{\sigma} = \frac{\Phi_{\text{filler}}}{\sigma_{\text{filler}}} + \frac{\Phi_{\text{matrix}}}{\sigma_{\text{matrix}}} \quad 3$$

In addition, at low filler concentration the electrical conductivity is increased by several orders of magnitude and a quasi-insulator-conductor transition is achieved upon incorporation of the conducting fillers into the matrix. Generally, when filler concentration in the composites is increased, the fillers begin to contact to each other and a continuous path is formed through the volume of the sample for charge carriers to travel. This mechanism can be explained with the percolation theory [135,136] which is based on statistical, geometrical, thermodynamics, structure-oriented or fractal percolation models.

The beginning of percolation theory is attributed to Hammersley and Broadbent in 1957 [137]. The percolation concept is frequently used to describe the movement of fluid flow in porous medium. There are few examples: the passage of water through soil, and the movement of water through coffee beans and filters. Also the percolation theory explains the transition from non-connected to connected state in a randomly disordered system which consists of two different phases. The percolation is a statistical concept in which a connected network formed by particles is presented. The study provides the information about the percolation threshold that results in an abrupt change of properties of the observed medium. This phenomenon is studied for composite materials in which conductive fillers are dispersed in an insulating matrix. More specially, the percolation threshold represents the transition from poorly conductive state to highly conductive state. Here, a continues network which allows to move the charge carriers across the materials, is built with the inclusion of conductive fillers (Figure 22).

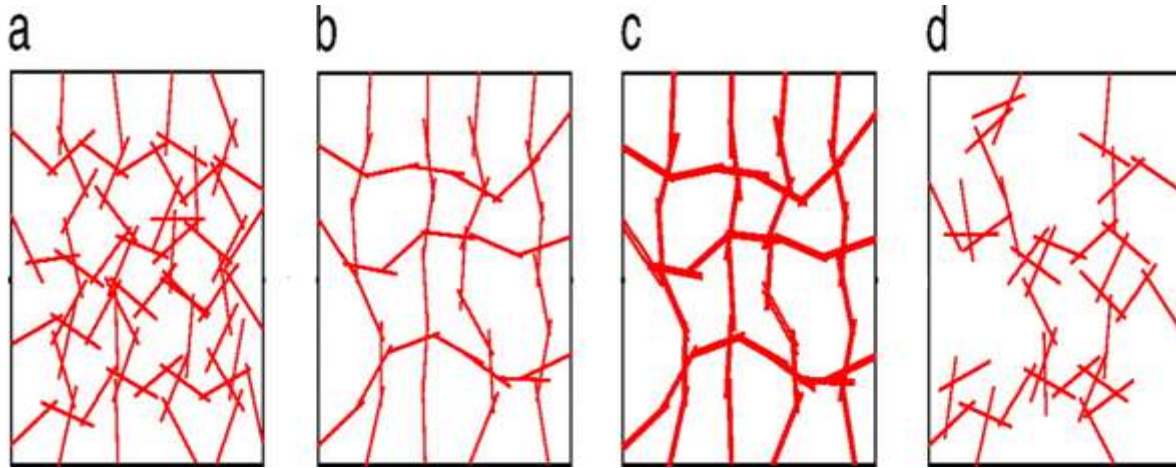


**Figure 22(a)–(d).** The schematic representation of different types continues conductive percolation network in composites.

The physical properties could be understood by investigating the geometrical structure of the percolation network. In these models, a sharp increase of the conductivity is observed with the sufficient fillers which introduce a conductive network also called “infinite cluster” [123]. The variation in electrical conductivity of the composites can be analyzed by the scaling law of percolation theory:

$$\sigma \propto (\Phi_{\text{filler}} - \Phi_c)^t \quad 4$$

where  $\sigma$  (S/m) is the electrical conductivity of the composites,  $\Phi_{\text{filler}}$  is the volume fraction of fillers,  $\Phi_c$  is the volume percolation concentration or percolation threshold, and  $t$  is a critical exponent. The percolation threshold could be influenced by many parameters such as filler/matrix interaction, aspect ratio of fillers, filler shape or filler distribution. The low value of volume percolation concentration could be attributed to the fractal structure of the conducting network. But, the percolation behavior of the composites is not always explained by this scaling law.

### 2.2.3.2 Temperature dependent electrical conductivity:

In addition, the investigation of electrical conductivity of the composites as a function of temperature (T) is also important for a practical standpoint and in order to understand the conduction mechanism. If conduction proceeds by hopping process, the thermally activated electrical conductivity of the materials can be analyzed by the Arrhenius equation:

$$\sigma(T)=\sigma_0 \exp( -E_a/K_B T) \quad 5$$

where  $\sigma_0$  is a constant,  $K_B$  is the Boltzmann constant, and  $E_a$  (eV) is the activation energy for hopping conduction. This model is also known as the nearest-neighbor-hopping (NNH) conduction in which, hopping conduction always occurs through the neighboring sites, and the hopping range and activation energy do not depend on temperature. In this model, the natural logarithm of conductivity changes linearly with inverse temperature. The temperature dependence of electrical conductivity also could be explained by Mott (variable-range hopping) which is a model describing low-temperature conduction in strongly disordered systems with localized charge-carrier states [138]:

$$\sigma(T)=\sigma_0 \exp [-(T_0/T)^{1/(z+1)} ] \quad 6$$

where  $T_0$  is the Mott temperature and in general  $z$  represents the dimension of conduction process. For the homogenous polymer composites, the evolution of  $\log\sigma$  with inverse temperature gives not only linear relationship but at times could be a non-linear behavior in which case the latter phenomenon could be analyzed by the Vogel-Tamman-Fulcher (VTF) equation [139,140]:

$$\sigma(T) = \sigma_1 \exp \left[ - \frac{E_a}{K_B (T - T_1)} \right] \quad 7$$

where  $\sigma_1$  is the conductivity associated with the number of charge carriers in the system and  $T_1$  is the Vogel temperature. In VTF behavior, the migration of charged carriers depends on amorphous region of the system [139,140].

Moreover, the polymer layer coated nnao-filler surface induces highest resistance region in the conductivity network. This polymer layer plays an important role in conduction mechanism. Because, it acts a potential barrier to efficient charge transport between conducting nano-fillers. In order to explain this charge transport mechanism, Sheng et al. [141] proposed a model which is based on fluctuation-induced tunneling through potential barriers of varying height due to local temperature fluctuations. The model is expressed as:

$$\sigma(T) \propto \exp \left[ - \frac{T_{s1}}{(T + T_{s0})} \right] \quad 8$$

where  $T_{s1}$  is related to the energy required for a charge to overcome the gap between conducting nano-fillers aggregate and  $T_{s0}$  is temperature above which thermal fluctuations are significant. The physical meaning of  $T_{s0}$ , and the effect of voltage fluctuations on the tunnel barrier are made more transparent by the closed form of Equation 8 [142]. It can be viewed that at  $T \ll T_{s0}$ , the equation 8 is represented for simple tunneling. Thus, simple elastic tunneling is just a special case of fluctuation-induced tunneling. But at  $T \gg T_{s0}$ , the equation 8 is represented for hopping.



## 2.3. Thermal properties

This section is concerned with the thermal properties of carbonaceous based conducting polymer nanocomposites. The thermal properties of the composites find numerous application in the aerospace, electronics, and energy storage industries. The thermal properties of the materials depend on the flux of thermal energy or the energy transmitted across unit area per unit time. Generally thermal energy transfer is a random process in which the energy does not simply enter one end of the system and proceed directly in a straight path to the other end, but diffuses through the system, suffering frequent collisions [143]. In order to describe the thermal properties of materials, there are many important thermophysical parameters which are considered in the context of heat transfer. These are heat capacity, thermal diffusivity, thermal effusivity, and thermal conductivity, which are presented here.

### 2.3.1. Heat capacity (C)

The heat capacity (C) of a material is defined as the amount of heat required to change its temperature by one unit of temperature. The SI unit of C is  $\text{J}\cdot\text{m}^{-3}\cdot\text{K}^{-1}$ . The heat capacity is associated with the energy consumption in the heating processes.

### 2.3.2. Thermal diffusivity ( $\alpha$ ) and thermal effusivity (e)

Thermal diffusivity is a crucial parameter for thermal management because it reflects the ability of the subsurface of a material to transfer thermal energy away from the surface being exposed to a heat source. Thermal diffusivity is defined as the speed of heat propagation by conduction during changes of temperature. The SI unit of thermal diffusivity is  $\text{m}^2/\text{s}$ . In general, a higher thermal diffusivity makes the heat propagation faster. Also the thermal diffusivity can be defined as the ratio of the time derivative of temperature to its curvature. That expression is described by using the heat equation:

$$\frac{\delta T}{\delta t} = \alpha \nabla^2 T \quad 9$$

Where,  $\nabla$  is the Laplace operator,  $T(x,y,z,t)$  is the temperature and  $\alpha$  is the thermal diffusivity.  $T(x,y,z,t)$  is the function of three spatial variables  $(x,y,z)$  and the time variable  $t$ . It can be said from the equation that in higher thermal diffusivity material, heat moves rapidly through it because the substance conducts heat quickly relative to its volumetric heat capacity.

Thermal effusivity is another thermophysical parameter for the description of the heat transport properties of a component. Thermal effusivity corresponds to the thermal impedance of a material and measures the rate at which a material can absorb heat or its ability to exchange heat energy with its environment. The SI unit of thermal effusivity is  $W.s^{0.5}m^{-2}.K^{-1}$ .

### 2.3.3. Thermal conductivity (k)

#### 2.3.3.1 Background

Thermal conductivity is defined as a measure of the ability of a material to conduct heat. The SI unit of thermal conductivity is  $W.m^{-1}.K^{-1}$ . In general, the thermal conductivity depends on many factors that affect the heat flow paths such as composition, homogeneity, porosity and shape, size and arrangement of void spaces etc. According to the second law of thermodynamics, heat always flows from a hot zone to a cold zone. Generally, the net heat transfer depends on the temperature gradient. To obtain the high thermal conductivity of a material, the rate of heat transfer across that material should be higher. The reciprocal of the thermal conductivity of a given material is defined as the thermal resistivity of the material. That means, higher the thermal resistivity, lower the thermal conductivity.

The thermal conductivity is evaluated in terms of Fourier's Law for heat conduction. According to Fourier's law, the rate of flow of heat energy ( $q$ ) per unit area through a surface is proportional to the negative temperature gradient ( $-\nabla T$ ) across the surface, which is expressed as:

$$q = -k \nabla T \quad 10$$

where,  $k$  is the thermal conductivity and  $T$  is the temperature. The equation 10 is known as the heat equation which is derived from Fourier's law and conservation of energy. The heat equation can also be expressed in terms of density, specific heat capacity, and thermal conductivity of the system, which is:

$$\frac{\delta T}{\delta t} = \frac{k}{\rho C} \nabla^2 T \quad 11$$

Above two equations (Equation 9 and 11) show that the thermal diffusivity is correlated to the thermal conductivity, heat capacity and density of the materials by using the given equation:

$$k (T) = \alpha (T) \times \rho (T) \times C (T) \quad 12$$

Where,  $\alpha (T)$  is thermal diffusivity,  $\rho (T)$  is the density, and  $C (T)$  is specific heat capacity of the material.

The thermal energy transfer in the system is carried out through phonon and/or electronic carriers (electron and hole). So, the thermal conductivity ( $k$ ) of the materials is strongly correlated with phonon and electronic contribution in the systems. The effective thermal conductivity can be written as  $k = k_{\text{phonon}} + k_e$ , where  $k_{\text{phonon}}$  and  $k_e$  are phonon and electronic contributions to the thermal conductivity, respectively. It is to be mentioned that in pure metals, the electronic contribution is dominant term in the  $k$  value, while in impure metals, amorphous system, and disordered materials the phonon contribution is dominant [143]. In addition, the value of the thermal conductivity can be controlled by scattering processes taking place in the materials. Such phenomena may include geometrical scattering which can be induced by collisions of phonons with crystal boundary, phonon-phonon scattering, electron-electron scattering, and scattering by the distribution of isotopic masses in natural chemical elements, chemical impurities, lattice imperfections, and amorphous structures. These scatterings determine the mean free path of phonons and electrons which are directly connected to the thermal conductivity of the materials. The dimension of the specimen is also an important parameter that governs the thermal conductivity, e. g. when the mean free path of phonons and electrons become comparable to the width of the test samples. For example, the thermal conductivity of a pure crystal at low temperatures is found to abruptly decrease due to the reduced size effect [143].

The thermal conductivity of nanocomposites with their constituents exhibiting different dimensions is quite interesting because of their combined hybrid properties. A combination of thermal conductivities of the filler and matrix decides the effective thermal conductivity of the nanocomposites. A schematic diagram of the thermal conductivity range of the materials is depicted in Figure 23. In this Figure, it is found that the thermal conductivity of the polymers is very low (less than  $1 \text{ W.m}^{-1}.\text{K}^{-1}$ ) while that of the carbonaceous materials are high ( $1000\text{—}6000 \text{ W.m}^{-1}.\text{K}^{-1}$ ) [36].

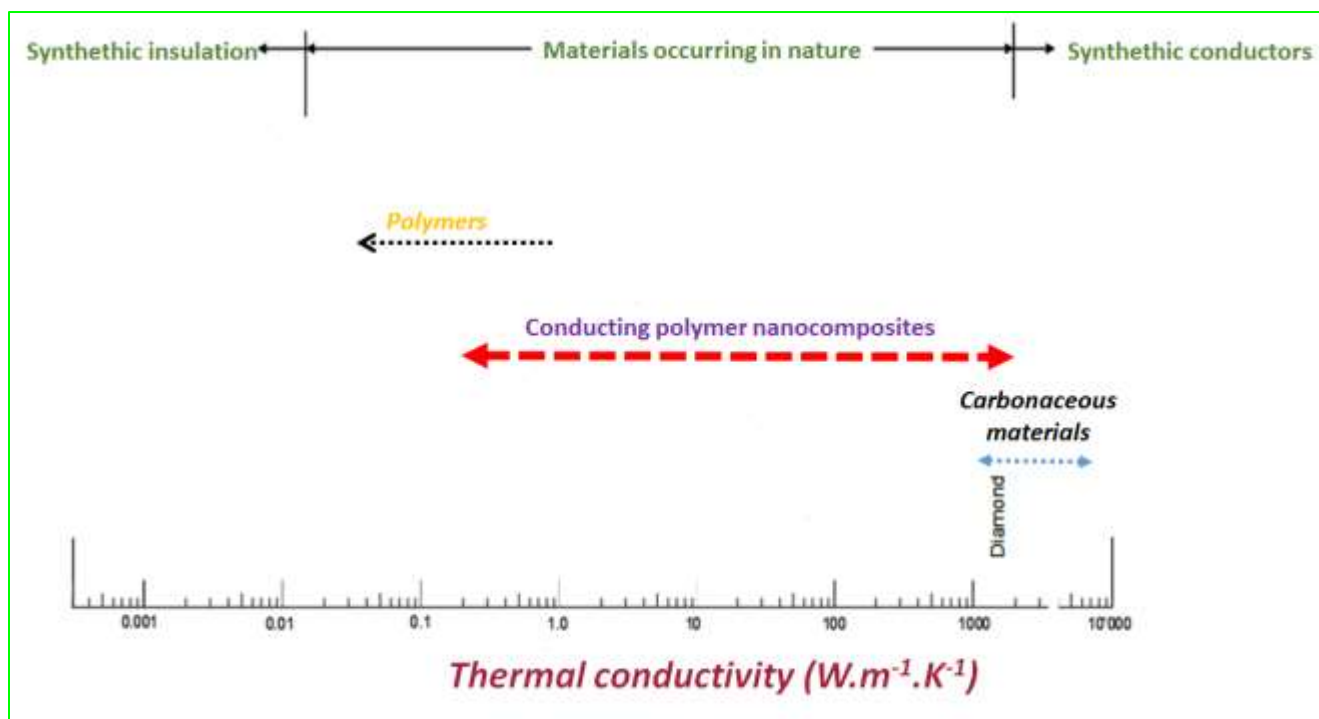


**Figure 23.** Thermal conductivity range of materials.

The value of the thermal conductivity of the carbonaceous based conducting polymers nanocomposites is derived from both filler and matrix. So, the effective thermal conductivity ( $k$ ) of nanocomposites can be expressed as a combination of the thermal conductivity of filler ( $k_{\text{filler}}$ ), and matrix ( $k_{\text{matrix}}$ ). An other critical parameter affects the overall conductivity of nanocomposites as well: void fraction [144,145]. Presumably, these voids arose from different sources such as strong  $\pi$ - $\pi$ /aromatic rings interactions of matrix and inclusions, Van der Waals interactions between the high aspect ratio inclusions [145,146]. Thus, the overall effective thermal conductivity of the nanocomposites can be contributed for the thermal conductivity of filler, matrix, and void ( $k_{\text{void}}$ ).

In addition, thermal conductivity is affected by the nature and the density of the interfaces present in between the constituents of the nanocomposites. These interfaces may involve the filler-matrix, filler-filler, matrix-matrix, filler-air, and matrix-air. Among these, filler-matrix interfaces are more important in the case of carbonaceous based polymer nanocomposites because of a large scale of interfacial spaces [35]. Thus, the thermal resistance, also called

Kapitza contact resistance, is limited by these interfacial effects [147]. In the context of thermal transport in nanocomposites, molecular dynamics (MD) simulation determines that the value of the thermal conductivity depends on the mode (in-plane or cross-plane) of the thermal energy transfer in the interfaces [148,149]. In the interfacial thermal transport mechanism, the thermal energy is dominated by phonons. Consequently, the effective thermal conductivity of the nanocomposites can also depend on the thermal conductivity across the interfaces ( $k_{\text{interface}}$ ).

### 2.3.3.2 Thermal conductivity models

As in the case of electrical conductivity, it is vital to study the evolution of thermal conductivity as a function of filler volume or mass fraction. This evolution can be interpreted by many models. A common way to explain the enhancement and quantification of the thermal conductivity of nanocomposites is through the use of scaling law of percolation model [150] :

$$k = k_0 (\Phi_{\text{filler}} - \Phi_c)^t \quad 13$$

where  $k_0$  is the thermal conductivity prefactor,  $\Phi_c$  is the volume percolation concentration or percolation threshold and  $t$  is the critical exponent. The model explains that a percolating network of the thermal conductivity could be formed with the introduction of thermal conducting fillers into polymer matrix. P. Bonnet *et. al.* [21] explained the enhanced thermal conductivity of the composites by using percolation critical power law as :

$$\Delta k = k_0 [(\Phi_{\text{filler}} - \Phi_c)/(1 - \Phi_c)]^t \quad 14$$

where  $\Delta k = k - k_{\text{matrix}} \times (1 - \Phi_{\text{filler}})$  is the difference in thermal contribution between the thermal conductivity of the composite and that of the polymer matrix. In this model, the increased thermal conductivity is presented as a function of reduced fraction of the filler which is defined as  $(\Phi_{\text{filler}} - \Phi_c)/(1 - \Phi_c)$ .

In determining the thermal properties of composites, the interesting debate is whether the enhancement of the thermal conductivity should be described with percolation concepts or with the use of effective medium approaches. Of interest to point out is that the presence of electrical percolation behavior in a material is not necessarily accompanied with thermal percolation [21]. Several reasons can be evoked to explain this phenomenon. It can be predicted that the highly thermally conducting fillers network are not sufficiently connected to allow direct heat transfer because the thermal resistance between two adjacent fillers is too high [147]. Also it can be assumed that a poor heat transfer occurs between filler and matrix and the heat flows through the matrix [151]. Consequently, to describe the enhancement of the thermal conductivity a vibrational or an effective medium approach is used in this study [152]. Several physical models based on effective medium approximations have been proposed.

One of the simplest models is “parallel model” (upper bound) [150] which is defined as:

$$k = k_{\text{filler}} \cdot \Phi_{\text{filler}} + k_{\text{matrix}} \cdot \Phi_{\text{matrix}} \quad 15$$

where  $\Phi_{\text{filler}}$  and  $\Phi_{\text{matrix}}$  are the volume fraction of the filler and matrix, respectively. Here, each phase contributes to the overall conductivity. Another simplest model is ”series model” (lower bound) [150] which is expressed as:

$$\frac{1}{k} = \frac{\Phi_{\text{filler}}}{k_{\text{filler}}} + \frac{\Phi_{\text{matrix}}}{k_{\text{matrix}}} \quad 16$$

However, most reported experimental results were unsuccessfully interpreted by these two models [150]. In consequence, a number of different models have been developed which take into account the different parameters such as nano-fillers orientation and the geometry of nano-filler and matrix, nano-filler/matrix and/or nano-filler-nano-filler thermal boundary resistance on thermal conductivity. Nan *et.al.* [147] proposed the following simplified model, in which the nano-fillers are considered spherical:

$$k = k_{\text{matrix}} \frac{\Phi_{\text{filler}} \left( \frac{k_{\text{filler}}}{k_{\text{matrix}}} \right)}{3 \left( p + \frac{2R_k k_{\text{matrix}} k_{\text{filler}}}{k_{\text{matrix}}} \right)} \quad 17$$

$$\text{here, } p = \frac{L}{d_f} \quad 18$$

In the equation 17 and 18,  $L$ ,  $d_f$ , and  $R_k$  are the length of the filler, diameter of the filler, and interfacial thermal resistance respectively. This model is used to extrapolate the thermal boundary resistance (TBR) between a nano-filler and an isolated nanoparticle. For nanoplatelets nano-fillers, the effective thermal conductivity as a function of volume fraction can be interpreted by a Maxwell–Garnett type effective medium approximation (MG-EMA) which is [146,153]:

$$k = k_{\text{filler}} \left[ \frac{3k_{\text{matrix}} + 2\Phi_{\text{filler}}(k_{\text{filler}} - k_{\text{matrix}})}{(3 - \Phi_{\text{filler}})k_{\text{filler}} + \Phi_{\text{filler}}k_{\text{matrix}} + \frac{R_k k_{\text{filler}} k_{\text{matrix}} \Phi_{\text{filler}}}{t_h}} \right] \quad 19$$

where  $R_k$  is the interfacial thermal resistance at the filler/matrix interface, and  $t_h$  is the thickness of the filler nano-platelets. This model is valid at low filler volume fractions in composites. Therefore, much intense theoretical and applied researches of thermal properties of the nanocomposites are still being conducted in hope to better understand the synergistic role played by fillers with matrix at nanoscale level. In our investigations, we have used the model of Nan (equation 17) when the fillers are SWCNT and that of MG-EMA when RGO is the filler in order to calculate the interfacial thermal resistance.







## 2.4. Thermoelectric (TE)



### 2.4.1. Background on thermoelectric

The term ‘thermoelectric’ is not new. The study on thermoelectric was started almost 200 years ago. So, thermoelectric has a long history of providing simple, reliable power generation solutions. In the 100 years (from 1820-1920) thermoelectricity was discovered and developed in western Europe by academic scientists, with much of the activity centered in Berlin. The key contributions are listed in the below Table 1.

**Table 1:** The key contributions on thermoelectrics from 1820 to 1920




| Year      | Name  | Contribution  |
|-----------|---|---|
| 1821-1823 | <br>Thomas Johann Seebeck | <p>During the experiment, Thomas Johann Seebeck observed the deflection of a compass needle due to a thermoelectric induced current from heating the junction of two dissimilar metals [154]. More specifically, two different metals make the temperature difference and electric potential difference which can drive an electric current in a closed circuit is developed across the terminals of an open circuit made from a pair of dissimilar metals. This phenomenon is well known as the Seebeck effect.</p> <p>The produced voltage is proportional to the temperature difference between the two junctions. The proportionality constant is defined as the Seebeck coefficient, and is known as the "thermopower" even though it is more related to potential than power.</p> |



|      |  |   |
|------|--|---|
| 1834 |  <p data-bbox="310 684 695 716">Jean Charles Athanase Peltier</p> | <p data-bbox="764 197 1396 499">Jean Charles Athanase Peltier, a French watchmaker and part time physicist explained that at the junction of two different metals, heating or cooling are produced due to electrical current. The mechanism is known as the Peltier effect.</p>   |
| 1838 |  <p data-bbox="402 1276 647 1308">Heinrich F.E. Lenz</p>         | <p data-bbox="764 758 1396 1224">Heinrich F.E. Lenz found that depending on the direction of current flow, heat could be either removed from a junction to freeze water into ice, or by reversing the current, heat can be generated to melt ice. The amount of heat absorbed or created at the junction is proportional to the electrical current. The proportionality constant is defined as the Peltier coefficient.</p> |
| 1851 |  <p data-bbox="423 1839 626 1871">Gustav Magnus</p>             | <p data-bbox="764 1352 1396 1709">Gustav Magnus found that the Seebeck voltage does not depend on the distribution of temperature along the metals between the junctions [155] indicating the thermopower as a thermodynamic state function. Actually, this is the physical basis for a thermocouple used for temperature measurement.</p>  |

|           |   |   |
|-----------|---|---|
| 1855      |  <p style="text-align: center;">William Thomson</p>    | <p>William Thomson (later Lord Kelvin) [156] described their interrelationship between the Seebeck and Peltier effects, which is known as the Kelvin Relations. Thomson noticed that heat is absorbed or produced when current flows in a material with a temperature gradient. This effect is known as the Thomson effect. Here, the heat is proportional to both the electric current and the temperature gradient. The proportionality constant is defined as the Thomson coefficient.</p> |
| 1909-1911 |  <p style="text-align: center;">Edmund Altenkirch</p> | <p>By using the constant property model, Edmund Altenkirch derived the maximum efficiency of a thermoelectric generator (1909) as well as the performance of a cooler (1911) when the design and operating conditions are fully optimized [157,158].</p>  |

After discovering the basic concepts of different thermoelectric effects, research on thermoelectric is carried out to renew the concept of the thermoelectric. From 1920 to 2000, many researchers provided new ideas for better understanding of thermoelectric. Herein are the important contributions on the TE during this period (Table 2).

**Table 2:** The important contributions on thermoelectrics from 1920 to 2000

|                |   |   |
|----------------|---|---|
| <p>1949-56</p> |  <p>Abram Fedorovich Ioffe</p> | <p>In order to develop the modern theory of thermoelectricity, Abram Fedorovich Ioffe used the concept of the “figure of merit” which is expressed as <math>ZT</math> [159,160].</p> <p>He also developed the use of the semiconductors in thermoelectrics and semiconductor physics in order to explain results and optimize performance.</p>  |
| <p>1953</p>    |  <p>Maria Telkes</p>          | <p>Maria Telkes created the first thermoelectric refrigerator by using the principles of semiconductor thermoelectricity.</p>   |
| <p>1954</p>    |  <p>H. Julian Goldsmid</p>   | <p>H. Julian Goldsmid demonstrated 0 C cooling using thermoelements based on <math>\text{Bi}_2\text{Te}_3</math> [161]. First time, he utilized the thermoelectric quality factor, identifying the importance of high mobility and effective mass combination and low lattice thermal conductivity in semiconductors that when properly doped make good thermoelectric materials.</p> |

|           |   |  |
|-----------|---|--|
| 1970      |  <p style="text-align: center;">Glen Slack</p>           | <p>Glen Slack studied small band gap semiconductors made from heavy elements in order to optimize ZT values [162].</p> <p>He suggested the “phonon-glass electron-crystal” concept for thermoelectric materials, so that the phonons should be disrupted like in a glass but the electrons should have high mobility like they do in crystalline semiconductors.</p> |
| 1990-2000 |  <p style="text-align: center;">Mildred Dresselhaus</p> | <p>Mildred Dresselhaus reported that nanotechnology may offer significant advances in the efficiency of thermoelectric materials [163,164].</p>  |

From 2000, around the world many research groups are working to improve ZT value. For example, thermoelectric properties at nanoscale level have been tremendous interest [165,166]. G. J. Snyder et al. reported entirely new classes of complex thermoelectric materials [167]. It is, therefore, not surprising that much intense theoretical and applied research are still being conducted in hope to better performance of the TE materials.

In summary, basic concept of TE suggests that the electrical and thermal currents are coupled. More specifically the particles that carry electric charge in a material also carry heat. There are three effects which are responsible for the studied mechanism. These are; Seebeck,

effect, Peltier effect, and Thomson effect. Below is some schematics and descriptions of Seebeck effect which is related in this work.

## 2.4.2. Seebeck Coefficient

The present study focuses on the Seebeck effect. A discussion on TE effect or TE performance of the materials should start with one of the most fundamental quantities called Seebeck coefficient (S) also known as thermopower or thermoelectric power. S is defined as a ratio between induced thermoelectric voltage or Seebeck voltage ( $\Delta V$ ) and temperature difference ( $\Delta T$ ) across that material. The Seebeck voltage is induced by Seebeck effect which is the conversion of heat directly into electricity. If it is assumed that one side of a material is heated while temperature at the other side is maintained at a low temperature, a voltage difference ( $\Delta V = V_{\text{cold}} - V_{\text{hot}}$ ) is found for a temperature difference ( $\Delta T = T_{\text{hot}} - T_{\text{cold}}$ ) (shown in Figure 24). If  $\Delta T$  is small, the Seebeck coefficient is defined as:

$$S = \frac{V_{\text{cold}} - V_{\text{hot}}}{T_{\text{hot}} - T_{\text{cold}}} = \frac{\Delta V}{\Delta T} \quad 20$$

Where  $V_{\text{cold}}$  and  $T_{\text{cold}}$  are the voltage and temperature at cold side of the material respectively and  $V_{\text{hot}}$  and  $T_{\text{hot}}$  are the voltage and temperature at hot side of the material respectively. S ( $\mu\text{V/K}$ ) is significantly dominated by the contribution of charge carriers, which are available for the electrical conduction in the materials. Under the influence of temperature gradient, the charge carriers start to diffuse from hot end side to cold end side of the material. This process continues until a compensating voltage has built up, which is analyzed by a stable Seebeck coefficient and the induced force (electromotive force) prevents the further migration of charge carriers. If the Seebeck coefficient is responsible for positively charged carriers (holes) the value of S is positive while it is negative for negatively charged carriers (electrons). For examples, p-type semiconductor materials give a positive value of S whereas a n-type semiconductor materials

provide the negative value. The phonon contribution is also most important in the Seebeck effect [168]. Especially, if phonon-electron interaction is predominant in the materials, the phonons will push the electrons to one end of the material which increases the Seebeck coefficient: this phenomenon is called the phonon drag effect.

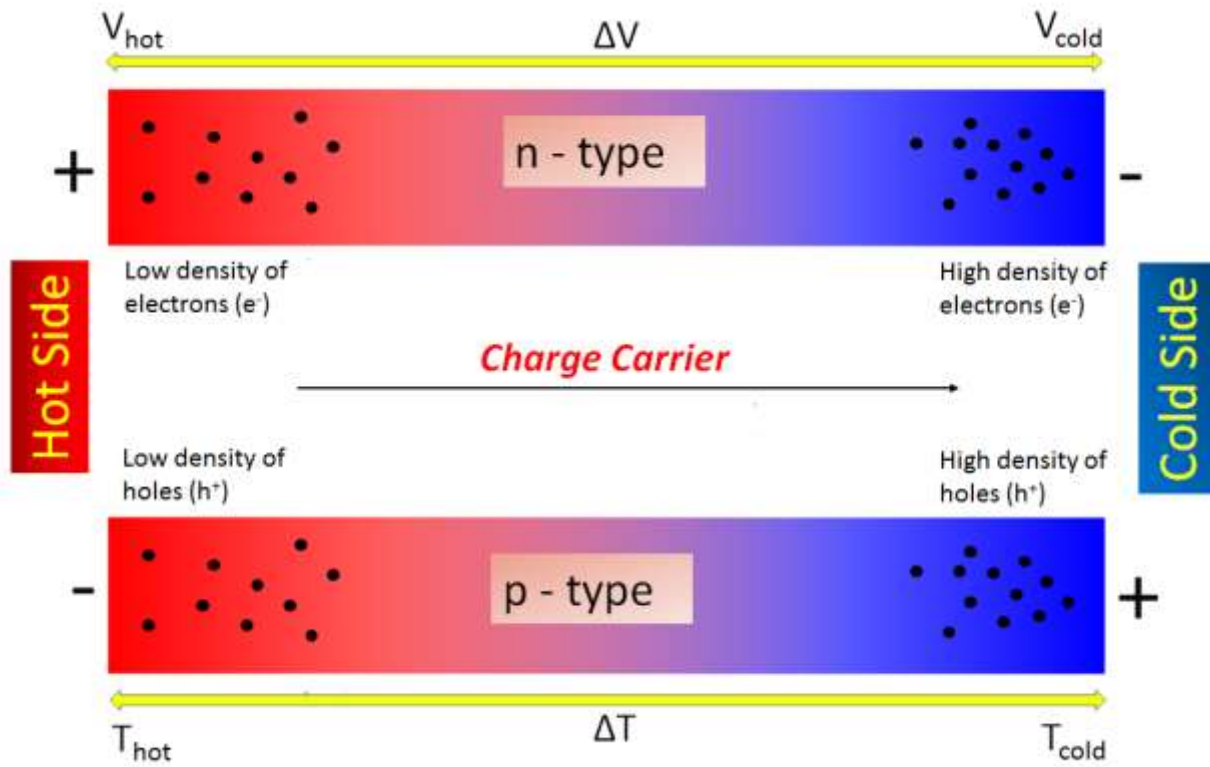


**Figure 24.** Presentation of Seebeck effect: electric potential formation in response to the temperature gradient of n-type and p-type material.

Figure 25 shows the charts for some typical Seebeck values of metals, non metals, metalloids and hybrid materials [169]. It could be confusing that the Seebeck coefficient may be defined as an absolute value or relative to a reference material, such as the case for the Table (Figure 25) where the reference material is platinum. The reason is that it is much easier to measure a relative Seebeck coefficient. To find the ‘real’ absolute values, the absolute value for Pt (i.e.,  $5 \mu\text{V/K}$ ) should be subtracted from each value listed in the Table.



**Seebeck Coefficients for Some Metals and Alloys.**

| Metals     | Seebeck Coefficient |
|------------|---------------------|
|            | $\mu\text{V/K}$     |
| Antimony   | 47                  |
| Nichrome   | 25                  |
| Molybdenum | 10                  |
| Cadmium    | 7.5                 |
| Tungsten   | 7.5                 |
| Gold       | 6.5                 |
| Silver     | 6.5                 |
| Copper     | 6.5                 |
| Rhodium    | 6.0                 |
| Tantalum   | 4.5                 |
| Lead       | 4.0                 |
| Aluminum   | 3.5                 |
| Carbon     | 3.0                 |
| Mercury    | 0.6                 |
| Platinum   | 0                   |
| Sodium     | -2.0                |
| Potassium  | -9.0                |
| Nickel     | -15                 |
| Constantan | -35                 |
| Bismuth    | -72                 |

**Seebeck Coefficients for Some Semiconductors.**

| Semiconductors                                  | Seebeck Coefficient |
|---|---------------------|
|   | $\mu\text{V/K}$     |
| Se  | 900                 |
| Te  | 500                 |
| Si  | 440                 |
| Ge  | 300                 |
| n-type $\text{Bi}_2\text{Te}_3$                 | -230                |
| p-type $\text{Bi}_{2-x}\text{Sb}_x\text{Te}_3$  | 300                 |
| p-type $\text{Sb}_2\text{Te}_3$                 | 185                 |
| PbTe  | -180                |
| $\text{Pb}_{0.3}\text{Ge}_{0.9}\text{Se}_{0.8}$ | 1670                |
| $\text{Pb}_{0.6}\text{Ge}_{0.6}\text{Se}_{0.8}$ | 1410                |
| $\text{Pb}_{0.9}\text{Ge}_{0.3}\text{Se}_{0.8}$ | -1360               |
| $\text{Pb}_{1.3}\text{Ge}_{0.9}\text{Se}_{0.8}$ | -1710               |
| $\text{Pb}_{1.5}\text{Ge}_{0.7}\text{Se}_{0.8}$ | -1990               |
| $\text{SnSb}_4\text{Te}_7$                      | 25                  |
| $\text{SnBi}_4\text{Te}_7$                      | 120                 |
| $\text{SnBi}_3\text{Sb}_1\text{Te}_7$           | 151                 |
| $\text{SnBi}_{2.5}\text{Sb}_{1.5}\text{Te}_7$   | 110                 |
| $\text{SnBi}_2\text{Sb}_2\text{Te}_7$           | 90                  |
| $\text{PbBi}_4\text{Te}_7$                      | -53                 |

**Figure 25.** The charts for some typical Seebeck values of metals, non metals, metalloids and hybrid materials.

The Seebeck coefficient is conceptually simple. But the accurate measurement of Seebeck coefficient can be difficult [170] because it depends on the instrument geometry, thermal contact, and electrical contact. However, semiconductor materials are known to have high Seebeck coefficient values (0-300  $\mu\text{V/K}$ ) whereas metals have low Seebeck coefficient (0-10  $\mu\text{V/K}$ ) [170]. Both metals and semiconductors can exhibit positive and negative value of S. The choice of material combinations is important for having the required S value. The tailoring can be achieved by using composite materials or by composite engineering which is one of the



most valuable processes [171]. This process could be an in-situ (during chemical or electrochemical syntheses) or ex-situ (post syntheses) mixing of fillers and matrix. Although complex phenomena take place during measurements of TE properties (diffusion of charges carriers and reaction at interface), it can be possible to achieve a stable Seebeck coefficient. There are numerous parameters which are strongly associated with the tailoring of a stable Seebeck coefficient. These parameters are components (e.g., fillers and matrix), the continuity of the components (e.g., fillers being continuous or discontinuous), the orientation of the components (e.g., fillers orientation), the relative orientation of the unit of the component (e.g., continuous fillers being unidirectional or crossplane), the volume fraction of the fillers into matrix, and the interface between filler and matrix.

The behavior of the Seebeck coefficient can be interpreted by quantum theory of thermoelectric power [172]. For example, to understand the nature of Seebeck coefficient for homogeneous materials, the evolution of  $S$  can be explained by Mott formula which can be expressed as follows [173,174]:

$$S = \frac{\pi^2 K_B^2 T}{3e} \left[ \frac{\partial \ln \sigma(\epsilon)}{\partial \epsilon} \right]_{\epsilon=\epsilon_F} \quad 21$$

where  $e$ ,  $\sigma(\epsilon)$ , and  $K_B$  are charge of the carrier, electrical conductivity, and Boltzmann constant respectively. The equation gives an explanation that both carrier concentration and carrier mobility affect the Seebeck coefficient. Also, low values of Seebeck coefficient can be explained by a conventional model based on band theory or electron-phonon scattering [175]. It is worthwhile to notice that an important Seebeck coefficient is obtained with an important effective mass and low charge carrier concentration. Also for heterogeneous semiconductor materials,  $S$  can be explained by given formula [176]:

$$S = \frac{K_B}{q} \left[ r + 2 + \ln \frac{2 \mu_H q (2\pi m^* K_B T)^{3/2}}{h^3 \sigma} \right] \quad 22$$

Where,  $q$  = charge,  $K_B$  = Boltzmann constant,  $r$  = scattering parameter,  $\mu_H$  = mobility,  $m^*$  = effective mass,  $h$  = Planck's constant, and  $\sigma$  = electrical conductivity.

The most common application of the Seebeck effect is in the thermocouples. Another application of Seebeck effect is the conversion of waste heat into electricity while the use of TE devices in refrigeration illustrates the Peltier effect.

### 2.4.3. Thermoelectric performance or figure of merit (ZT)

Thermoelectric performance of the thermoelectric device indicates the quality of thermoelectric power generation. A thermoelectric device consists of thermoelectric modules where the thermoelectric module is an array of thermocouples connected electrically in series but thermally in parallel (Shown in Figure 26).

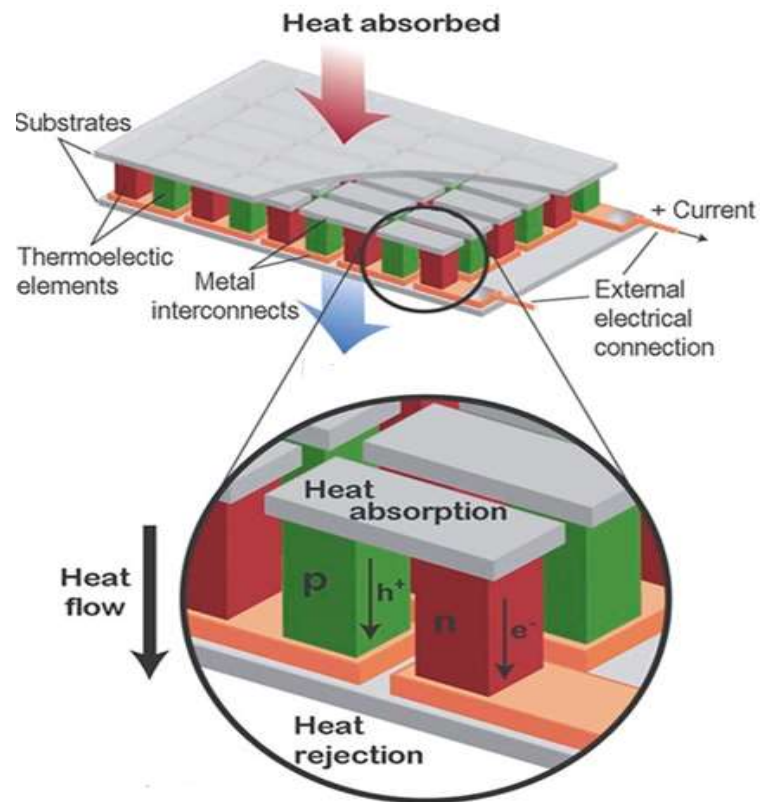


**Figure 26.** Thermoelectric device is made of thermoelectric modules [167].

In order to determine the thermoelectric performance of the devices, thermopower is not only the parameter but also the electrical conductivity and thermal conductivity play significant role in thermoelectric performance. The electrical resistivity and thermal resistivity are coupled in a thermoelectric generator. So, the Seebeck coefficient, electrical conductivity, and thermal conductivity control the overall thermoelectric performance. However, for a practical standpoint, the potential commercial application of a TE material is very much dependent on a dimensionless quantity called “figure of merit” or  $ZT$  whose expression is given as:

$$ZT = (S^2 \sigma T) / k \quad 23$$

where  $S$ ,  $\sigma$ ,  $T$  and  $k$  are the Seebeck coefficient, electrical, temperature in Kelvin and thermal conductivity, respectively. For better performance, the electrical resistivity should be small so energy is not wasted in Joule heating and also the thermal conductivity should be small so heat we pump to the hot end stays there. The maximization of each material's dimensionless Figure of Merit ( $ZT$ ) provides the maximum device efficiency. The best TE materials currently used have  $ZT$  values close to 1 or slightly higher [27]. In theory,  $ZT$  can be increased by raising  $S^2$ ,  $\sigma$  and decreasing  $k$ . In practice, achieving this remains highly difficult because electrical conductivity often goes hand in hand with thermal conductivity, i.e., a rise in electrical conductivity is also accompanied with a rise in thermal conductivity or vice versa. So, the challenge for materials scientists is to come up with TE materials that are good electrical conductors but poor thermal conductors. It should also be mentioned that there are several works currently under way for solving engineering challenges related to creating thermoelectric devices. Finally the main goal should be to find out new materials with  $ZT > 1$  at or below room temperature.

## 2.5. Dielectric properties

Herein, we present a brief description of the dielectric properties of the materials. A dielectric material is defined as a substance which is a poor conductor of electricity over a specified electromagnetic field. For a perfect dielectric material, electrical conductivity is zero. The dielectric properties provide a great deal of information about the suitability of the material for various applications. There are many ways to characterize the dielectric materials in order to investigate the dielectric behavior. These are relative permittivity ( $\epsilon_r$ ), dielectric constant, loss tangent or  $\tan\delta$ , breakdown field. Dielectric permittivity and dielectric loss are important parameters while we discuss leakage conduction mechanism as well as capacitance effect. The value of dielectric permittivity over a specified electromagnetic field provides the information about the capacitance. The capacitance is a measure of how much the energy stored in a capacitor of a given volume at a given voltage. In general, the capacitance is increased by a factor of the dielectric permittivity due to presence of insulating medium. The capacitance is attributed to polarization of the dielectrics where charge distribution is distorted by applied electrical field. There are various molecular mechanisms associated with this polarization, including electronic, ionic, molecular (dipole), and interfacial (space-charge) polarization.

The capacitance ( $C'$ ) for a parallel plate capacitor when a dielectric material completely fills the space between the plates is:

$$C' = \epsilon_r \epsilon_0 A/t \quad 24$$

where  $\epsilon_0$  is the permittivity of free space and is equal to  $8.854 \times 10^{-12}$  F/m, A is the area of electrode, t is the separation between two electrodes and  $\epsilon_r$  is called the dielectric constant of the dielectric material. For an alternating electric field, the dielectric constant of the materials can be expressed as complex permittivity:

$$\varepsilon^*(\omega, T) = \varepsilon'(\omega, T) - i \varepsilon''(\omega, T)$$

where  $\varepsilon'$  is real permittivity and  $\varepsilon''$  is imaginary permittivity. The capacitance is attributed to polarization of the dielectrics where charge distribution is distorted by applied electrical field. There are various molecular mechanisms associated with this polarization, including electronic, ionic, molecular (dipole), and interfacial (space-charge) polarization.

Furthermore, the complex dielectric function in its dependence on angular frequency ( $\omega = 2\pi f$ , where  $f$  is the frequency of the outer electric field) and temperature can originate from the following process [177]:

- (i) Microscopic fluctuations of molecular dipoles (rotational diffusion)
- (ii) The propagation of mobile charge carriers (translational diffusion of electrons, holes or ions)
- (iii) The separation of charges at interfaces which provides rise to an additional polarization.

The latter process can take place at inner dielectric boundary layers and/or at the external electrode/sample interface, presented as electrode polarization on a mesoscopic scale. Each of the above mentioned processes shows specific features in frequency and temperature dependence of the real and imaginary part of the complex dielectric function.

A schematic representation of the frequency dependence of complex permittivity is shown in Figure 27. It can be seen in Figure 27, relaxation process is characterized by a peak in imaginary part ( $\varepsilon''$ ) and a step-like decrease of the real part  $\varepsilon'$  of complex dielectric function with increasing frequency. And an increase of the imaginary part of complex dielectric function with decrease in frequency is obtained for conduction phenomena. For pure ohmic conduction the real part of complex dielectric function is independent of frequency while for non-ohmic conduction or polarization effects (at inner boundaries or external electrodes) the real part increases with decrease in frequency. Thus, the analysis of complex dielectric spectra emphasizes different aspects of charge transport and polarization in the materials. Figure 27(a) shows that conductivity contribution is observed at low frequency peak in imaginary part of complex dielectric function with slope = -1.

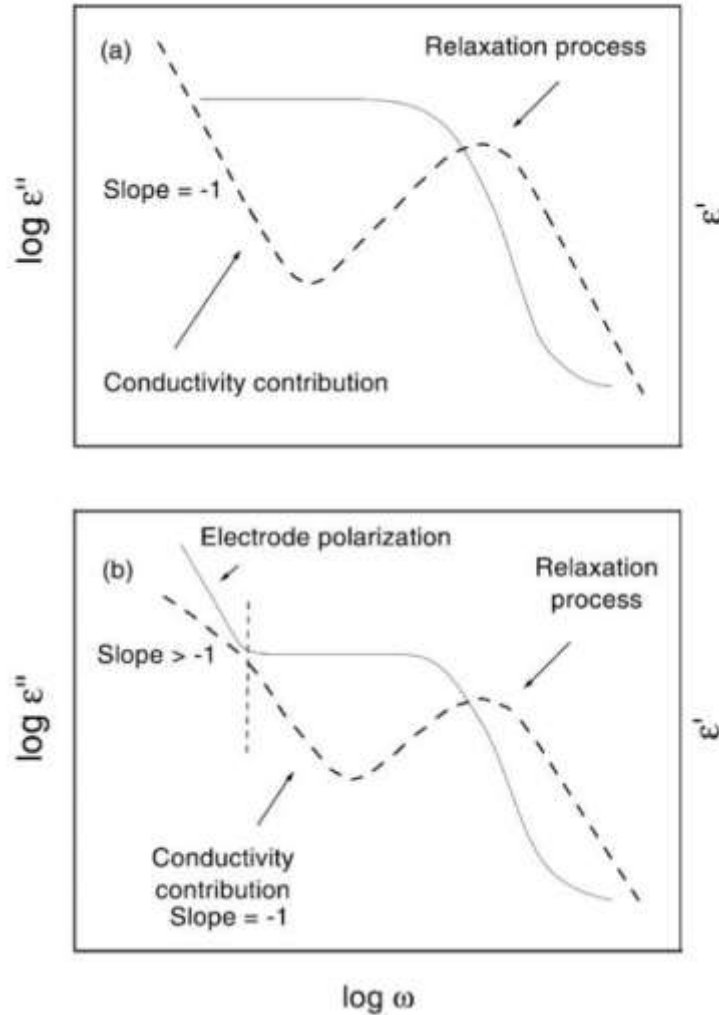


**Figure 27.** Scheme of the real  $\epsilon'$  (solid line) and the imaginary  $\epsilon''$  (dashed line) part of the complex dielectric function for a relaxation process and an (a) ohmic or (b) non-ohmic conductivity. In the latter case electrode polarization is observed [177].

In this thesis, the objective is to investigate the conducting properties (through plane measurements) and/or interfacial relaxation in the materials by analyzing imaginary part of complex dielectric permittivity spectra over a wide range frequency (1Hz-1MHz).



## CHAPTER 3 EXPERIMENTAL TECHNIQUES

This chapter is intended to provide a brief description on the syntheses of nanocomposites and the techniques used for their characterization.

### 3.1. Material preparation

In order to synthesis the polymer/carbonaceous nanocomposites, carbonaceous nano-fillers such as single wall carbon nanotubes (1-D), multi wall carbon nanotubes (1-D), and reduced graphene oxide (2D) are dispersed into polymer matrix (polyaniline). The specifications of studied nano-fillers are shown in Table 3 (for single wall carbon nanotubes, multi wall carbon nanotubes) and 4 (for reduced graphene oxide). It is important to point out that all the three nano-fillers hold same electrical conductivity values ( $10^4$  S/m).

**Table 3:** Specifications of 1-D nano-fillers

| Samples | Purity (wt-%) | Outer diameter (nm) | Length ( $\mu\text{m}$ ) | Electrical conductivity (S/m) |
|---------|---------------|---------------------|--------------------------|-------------------------------|
| SWCNT   | 90            | 1-2                 | 30                       | $10^4$                        |
| MWCNT   | 95            | 10-20               | 30                       | $10^4$                        |

**Table 4:** Specifications of 2-D nano-fillers

| Samples | Purity (wt-%) | Thickness (nm) | Size ( $\mu\text{m}$ ) | Electrical conductivity (S/m) |
|---------|---------------|----------------|------------------------|-------------------------------|
| RGO     | 99            | 0.55-3.74      | 0.5-3                  | $10^4$                        |

The synthesis of all samples used in this work was conducted at the University of Science and Arts of Oklahoma (USA) by Dr. Roch Chan Yu King.



### 3.1.1. Synthesis of polyaniline/SWCNT or polyaniline /MWCNT nanocomposites

Single-walled carbon nanotube (containing 3.96% OH) and MWCNT (containing 3.06% OH) are purchased from Times Nano (China) and the remaining chemicals are purchased from Aldrich Chemical Co. PANI/SWCNT or PANI/MWNT nanocomposites are synthesized through an in situ chemical polymerization method combining aniline monomers, SWCNT or MWCNT, ammonium peroxydisulfate as oxidizing agent and 1.0 M (aq.) HCl as dopant. Various weight fraction of SWCNT, and MWCNT (ranging from 0.010 wt-% to 17.0 wt-%) nanocomposites have been prepared. For the synthesis of 1 wt-% MWCNT/PANI composite a typical procedure is as follows:

Into a test tube were placed 3.50 mg MWCNT, 0.347g aniline and 18.0 ml of 1.0 M HCl (aq.). This mixture was sonicated for 1 hour for better dispersion and then transferred into a beaker to which was added a solution of 0.913g ammonium peroxydisulfate in 7.0 ml of 1.0 M HCl (aq.). The resulting mixture was magnetically stirred for 24 h. It was then suction filtered, sequentially washed with de-ionized water, acetone and hexanes until a colorless filtrate was obtained. The product was high-vacuum dried (50.0 °C; 12 h) and then stored in a desiccator.

### 3.1.2. Synthesis of polyaniline/reduced graphene oxide (PANI/RGO) nanocomposites

Reduced graphene oxide (RGO) (purity > 99%) is purchased from Times Nano (China) and the remaining chemicals are purchased from Aldrich Chemical Co. PANI/RGO nanocomposites are synthesized through an in situ chemical polymerization method combining aniline monomers, RGO and ammonium peroxydisulfate as the oxidizing agent. Various weight fraction of RGO (ranging from 0.005 wt-% to 20.9 wt-%) nanocomposites have been prepared. For the synthesis of an RGO (12.6 wt-%)/PANI composite a typical procedure is as follows: RGO (33.0 mg) and 10.0 mL 1.00 M (aq) camphorsulfonic acid (HCSA) (dopant) were placed into a glass tube. This mixture was sonicated for one hour in order to improve the dispersion of RGO nanoplatelets. It was then mixed with freshly distilled aniline (0.300 mL; 3.30 mmol). The

resulting suspension is further sonicated for one hour. After that, it was transferred into a beaker and a solution of ammonium peroxydisulfate (0.808g ; 3.54 mmol) in 15 mL of 1.00 M aq. HCSA was added. The black suspension was stirred overnight at room temperature, it was suction filtered, and then subsequently washed with de-ionized water and small amounts of acetone until a colourless filtrate was obtained. The product was high-vacuum dried (50.0 °C; 12 h) and then stored in a desiccator.

## 3.2. Samples preparation and characterization techniques

Pellets of the nanocomposites were prepared from the as-synthesized product which was pulverized in a mortar with pestle. The resulting powder was cold pressed (450 MPa) which provided pellets of test samples having a diameter of 13 mm and a thickness of 220-340  $\mu\text{m}$ .

Different characterization techniques were used to get detailed information regarding structural, morphological, electrical, thermal and dielectric aspects. Morphologies and structural properties were investigated via Field Effect Scanning Electron Microscopy (FE-SEM), Transmission Electron Microscopy (TEM), Raman Spectroscopy and X-ray diffraction (XRD). Electrical conductivity, Seebeck coefficient, thermal parameters and dielectric measurements were performed by the conventional 4 probe-method, a homemade instrument, photothermal radiometry, laser flash method, DSC and dielectric Spectroscopy, respectively. Multiple repeats were performed for each sample in all measurements to analyze the reproducibility. All of the above techniques are briefly described in the next section.

### 3.2.1. Scanning electron microscopy (SEM)

We used the Hitachi S4700 FE-SE (Figure 28) at UMET (*Unité Matériaux et Transformations* - UMR CNRS 8207, University Lille1-Sciences and Technologies) operating at 6 KV and 10–15 mA to obtain detailed structural features and morphologies of samples. The instrument emits beams of electrons aimed at a sample deposited on a conducting black tape. This is a method of choice for high resolution imaging. To prepare the sample for SEM

investigation, a high purity double sided conductive adhesive carbon tab has been used. A very small amount of powder samples was placed on that tabs for SEM mounting.



**Figure 28.** Picture of Hitachi S4700 FE-SEM in UMET.

### 3.2.2. Transmission electron microscopy (TEM)

Nowadays, there is an increasing demand to observe materials at the nanoscale level. For this, a high magnification (in nanoscale range) is necessary in order to produce a high quality imaging. Transmission electron microscopy (TEM) is one of the most powerful techniques used for this purpose. It provides the constitutional characteristics of these nanocomposites such as nanostructures, grain shape and size, crystallinity and chemical variations/distribution at nanometer scale. TEM used in the present study was a FEI Technai G2 20 instrument which is

housed in UMET of the University Lille1-Sciences and Technologies. A photo of the instrument is shown in Figure 29. Like SEM instruments also it emits beams of electrons and operates at 20 kV to produce high quality images of the materials. For preparing the TEM samples, a very small amount of powder was loaded in the TEM grid.



**Figure 29.** Picture of FEI Technai G2 20 instrument used for TEM measurement in UMET.

### 3.2.3. Raman spectroscopy

Another commonly used method for a detailed investigation of structural properties of the materials is Raman spectroscopy. This spectroscopic technique can be used in the fields of condensed matter physics and chemistry to study vibrational, rotational, and other low-frequency modes in a system. It is based on inelastic scattering which means that the frequency of photons in monochromatic light changes upon interaction with the sample, or Raman scattering of monochromatic light, usually from a laser source in the visible, near infrared, or near ultraviolet range.

In this work, Raman spectroscopy analyses were performed with a Horiba Yvon Labram HR system at LASIR laboratory at University Lille1-Sciences and Technologies (Figure 30). The system is a “multi excitations” system. It is coupled with three different lasers sources: a HeNe laser (623.8 nm) and two solid state lasers (one at 532 nm and another one at 473 nm) that can be easily handled. So, the instrument allows the study of samples at the same point with various exciting lines. The basic set up of the Raman spectrometer is presented in Figure 30. In the present study, Raman spectroscopy measurement was performed at 632.8 nm laser excitation determined by calibration using the output of a HeNe laser. This spectrometer is equipped with an open confocal microscope allowing big size objects to be placed under the objective, an 800 mm focal length spectrometer which can reach a spectral dispersion of the order of  $0.35 \text{ cm}^{-1}/\text{pixel}$ , a  $1024 \times 256$  pixels CCD detector cooled by liquid nitrogen, an XY motorized table that makes it possible to obtain Raman maps along the two axes ( $0.1 \text{ }\mu\text{m}$  resolution in X and Y), and an XYZ piezoelectric table that makes it possible to record Raman maps with nanometric displacements. This set-up increases significantly the quality of the Raman imaging in terms of positioning and reproducibility of the measurements. The displacements of this stage are  $100 \times 100 \times 100 \text{ }\mu\text{m}$  with a step that can reach the nanometer in the three directions. The instrument was performed with  $P = 1 \text{ mW}$  at room temperature. A small amount of powder was added on the scotch tape which was stuck on glass substrate for this experiment. The Raman Spectra is analyzed with the FOCUS software [178].



**Figure 30.** Image of the set up of a Horiba Yvon Labram HR Raman spectroscopy.

### 3.2.4. X-Ray diffraction (XRD)

X-ray diffraction (XRD) is an important, non-destructive technique that confirms detailed information about the structure of a material.

In this study, we use the powder diffraction method, (Debye-Scherrer). X-Ray diffractograms were recorded on a curved multidetector INEL-CPS 120 set up (Figure 31). The pulverulent samples were introduced into Lindeman glass capillary tubes (diameter 0.70 mm) and irradiated with a collimated monochromic beam ( $\lambda_{\text{CuK}\alpha 1} = 0.154056 \text{ nm}$ ). Samples were rotated around the vertical axis of the goniometer head to ensure randomization of preferential orientations.

When considering X-ray diffractograms of polymers, it is important to realize they are very far from diffractograms of ideal crystals. Polymers structures generally have a significant amorphous volume fraction. The resulting diffraction pattern comprises both diffraction peaks from the crystalline part and broad features consistent with the diffuse scattering from the amorphous part.





**Figure 31.** Photograph of the X-ray powder diffractometer used in this study.

As a result of low average degree of order in polymers, the observed diffraction peaks are generally few and broad. The positions and intensities of the peaks are a result of a crystal structure as related by Bragg's law:

$$2d \cdot \sin\theta = n\lambda \quad 26$$

where  $n$  is the order of reflection,  $\lambda$  is the wavelength of incident X-rays,  $2\theta$  is the diffraction angle.

The width of Bragg peaks contains information about the coherence length (crystallites dimensions) in the sample. The Debye-Scherrer formula gives estimate of the crystallite dimensions  $D$ :

$$D = [0.9 \lambda] / [\delta \cos \theta] \quad 27$$

where  $\delta$  is a full width at half maximum (FWHM).

### 3.2.5. Four-probe technique

Resistivity is a fundamental and critical parameter of every conductor as well as semiconductor materials. A lot of techniques are being used to investigate the electrical properties of semiconducting materials. Out of these, 4-probe method is the most common way to measure the resistivity of the systems. Because this technique is able to eliminate measurement errors due to the probe resistance, the spreading resistance under each probe, and the contact resistance between each metal probe and the specimen sample. The 4-probe set up consists of four equally spaced tips with finite radius (Figure 32).

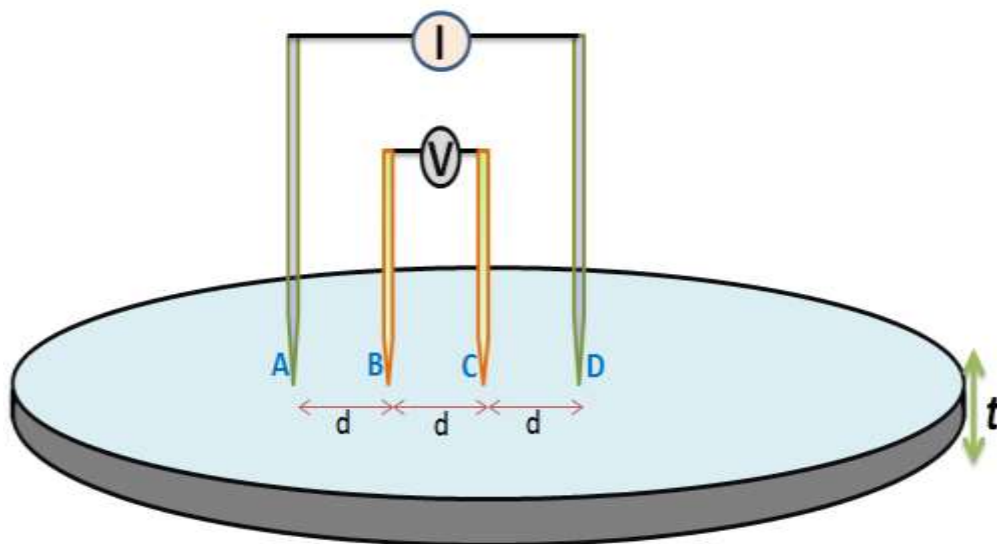


**Figure 32.** Schematic display of 4- probe technique

In the method, two probes are connected to a high impedance current source while two others are used to measure the voltage. The electrical current is carried through the two outer probes (A and B) providing an electrical field in the sample. And the other two inner probes measure the potential difference between B and C.



However, the electrical conductivity measurements are approached by measuring the resistive properties of a sample. The resistance of a resistor can be expressed in terms of the voltage drop (V) across the resistor and current through the resistor by:

$$R = \frac{V}{I} \quad 28$$

The resistance of the sample remains same for all voltages over a given range. Over the range, materials obey Ohm's law. The unit of resistor is volt/ampere or Ohm.

For further consideration of electrical properties of the material, sheet resistance ( $\rho_s$ ) is utilized to calculate the electrical conductivity ( $\sigma$ ) in S/m. Conductivity is the inverse of resistivity ( $\rho$ ). Since the electrical conductivity is the reverse of resistivity, the conductivity can be defined as:

$$\sigma = \frac{1}{\rho} = \frac{1}{\rho_s \times t} \quad 29$$

where  $\rho_s$  is sheet resistivity and t is the thickness (t) of samples. The sheet resistivity is obtained for an infinite sheet by using below equation [179]:

$$\rho_s = \ln 2 \times \frac{V}{I \times \pi} \quad 30$$

But in order to obtain the sheet resistivity on a finite sample, the method of images can be applied [180]. However, to optimize the electrical conductivity of the conducting pellets, a collier four point probe shown in Figure 32 is used to measure the sheet resistivity. This four-point probe method can be used to determine the sheet resistivity of specimen having a wide variety of shapes, including having irregular boundaries and also the sheet resistivity of smaller

region in a matrix with different electrical properties. This resistivity can be calculated by [179]:  
:

$$\rho_s = C \times \frac{V}{I} \quad 31$$

where C is a correction factor which depends on various shapes of the sample. F. M. Smith [179] reported the calculation of C. The values of C for the measurement of sheet resistivities with four point probe are listed in Table 5 [179].

**Table 5:** Correction factor C for the calculation of the sheet resistivity measured by a collinear four point probe apparatus.

| <b>d/t</b> | <b>C for circle</b> | <b>C for square</b> |
|------------|---------------------|---------------------|
| 1          |                     |                     |
| 1.5        |                     |                     |
| 2          |                     |                     |
| 3          | 2.2662              | 2.4575              |
| 4          | 2.9289              | 3.1137              |
| 5          | 3.3625              | 3.5098              |
| 10         | 4.4364              | 4.2209              |
| 20         | 4.4364              | 4.4516              |
| infinite   | 4.4524              | 4.5324              |

In the Table 5, d is the distance between two probes and t is the thickness of samples. In this way, the conductivity can be obtained if data of  $\rho_s$  and the thickness (t) of samples are available.

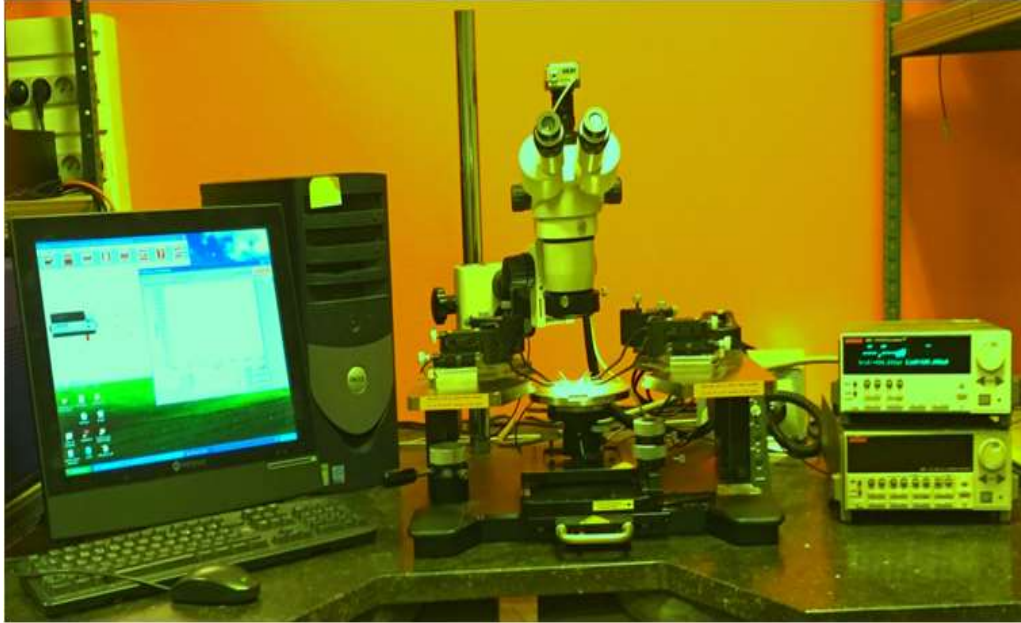


**Figure 33.** Equipment of 4-point-probe technique.

In the present studies, the sheet resistance is measured by a conventional collinear four-probe method using a Cascade Microtech EP6 probe station equipped with a Keithley 2635 source meter (Figure 33). The typical probe spacing was 1 mm and the geometry of the pellet samples was a circle. For each sample, measurements were made with the probes placed on several positions and a final value of sheet resistivity is obtained by taking the mean average from the measurements on both sides of the samples. However, good electrical contact is very important factor for all electrical conductivity measurements since the calculation assumes negligible resistance between the probe and sample. A sharp point and high comprehensive forces are used to ensure the negligible resistance between probe and polymer nanocomposites. Because the samples are finite size and made of mixed materials, the thickness correction factor is included to measure the electrical conductivity [179]. The total error of the conductivity can be for measurements error, error of the thickness, and error of the correction factor. However, the conductivity can be determined using sheet resistivity and thickness data.

### 3.2.6. Seebeck measurement technique

Seebeck coefficient (S) is an essential parameter for evaluating the nature and density of charge carriers and the potential performance of thermoelectric materials. There are two methods to measure the Seebeck coefficient of a material: a differential or an integrated method [181]. In the differential method, a small temperature gradient is created across the sample and Seebeck coefficient is calculated by following equation:

$$S(T) = \Delta V / \Delta T \quad 32$$

where  $\Delta V$  is the voltage difference between the hot and cold sides of a sample and  $\Delta T$  is the change in temperature between the sides. The  $\Delta V$  can be positive or negative, depending on whether the mobile charges are holes or electrons. So, the charge carriers dictate the sign of the Seebeck coefficient. In the present work, a setup had been developed on the basis of differential method (Figure 34). In this set up, prepared pallet was placed in between two aluminum (Al) discs with diameter 13mm. During calibration of temperatures of hot and cold sides, the Al was used as a reference material. This sample holder was separated from heating elements through electrical insulation. One side of the sample was heated while the other was used as a cold side. When one side of the sample was heated up, thermocouples of Standard ST-9612 Thermometer connected with the sample holders registered the value of temperature difference between upper surface and lower surface of the sample. The difference in temperature induces a detectable voltage drop, which was measured by a Keithley 2182 nanovoltmeter connected through two electrodes of Al sample holders. This set up for the measurement of the Seebeck coefficient is one of the simplest and most widely used. The measurements of the Seebeck coefficient were performed at ambient temperature. Knowing the values of  $\Delta T$  and  $\Delta V$ , the Seebeck coefficient can be determined from the slope of the plot of Seebeck voltage versus temperature difference. Finally, in order to calculate the absolute Seebeck coefficient of the samples, the Seebeck coefficient value of Al was put in equation 20.

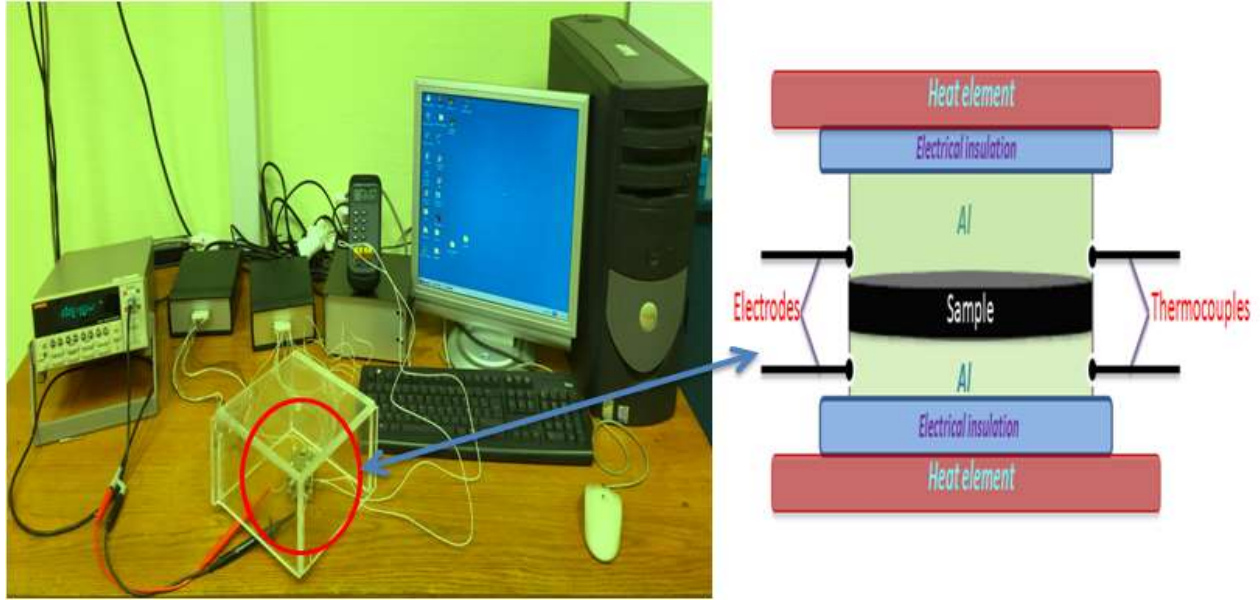


**Figure 34.** Set up for measurement of the Seebeck coefficient.

### 3.2.7. Laser flash method

For determining the thermal conductivity and thermal diffusivity, laser flash method can be used. This method is based on the measure of the thermal transient of the rear surface of the sample when a pulsed laser illuminates the front. It is possible to avoid interferences between the thermal sensor and the heat source in this method. Especially, thermal diffusivity ( $\alpha$ ) of the pellets was measured via this method. The measurements presented in this thesis were measured using a NETZSCH LFA (Laser Flash Analysis) 467 HyperFlash apparatus which is displayed in Figure 35.

In the laser flash method, a laser pulse of 1ms width or less is used to momentarily heat the front side of a 13 mm diameter discoid sample. As a consequence, the temperature at the back of the sample is changed. This back side temperature change is measured. According to the theoretical solution proposed for insulation conditions, when the sample backside temperature increases, the temperature rise becomes a constant value ( $\Delta T$ ) after uniform temperature

distribution is achieved. Sample back side temperature change ( $\Delta T/2$ ) is measured as a function of elapsed time ( $t_{1/2}$ ). The coefficient of thermal diffusivity  $\alpha$  is calculated from:

$$t_{1/2} = (0.1388 L_s^2) / \alpha \quad 33$$

where,  $L_s$  is the thickness of sample.

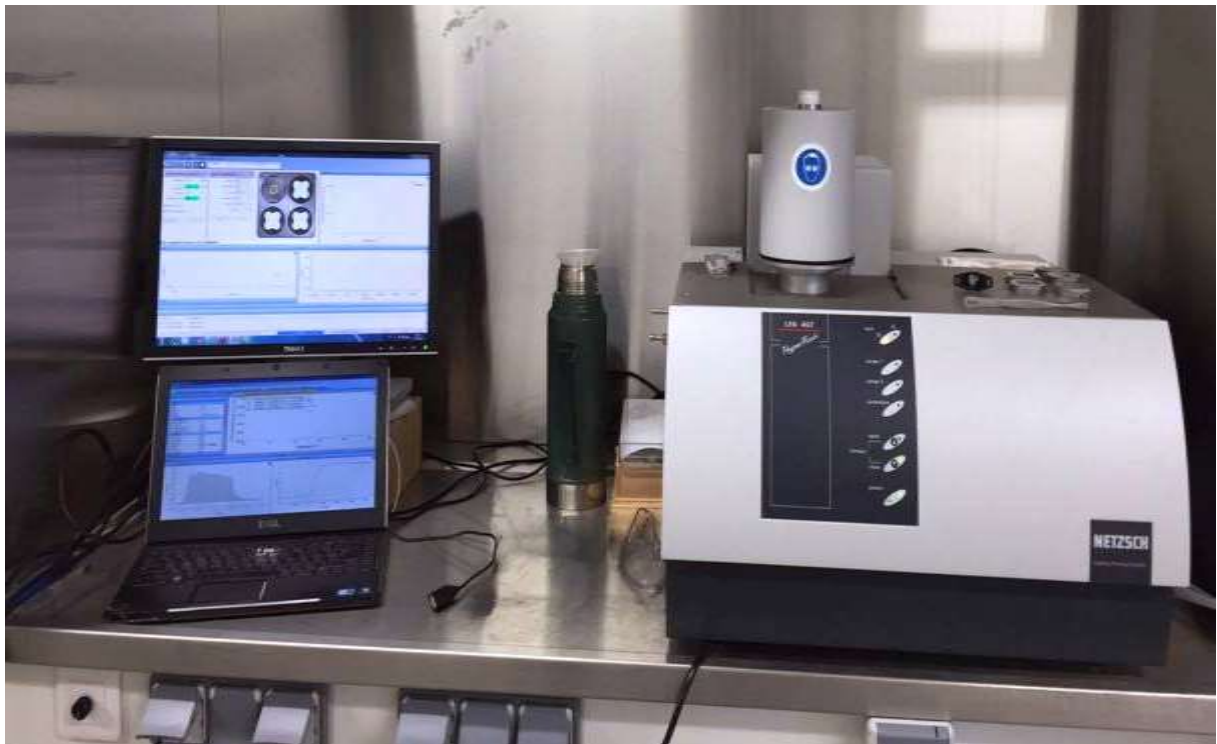


**Figure 35.** Equipment of laser flash analysis (NETZSCH LFA 467).

### 3.2.8. Differential scanning calorimetry (DSC)

It may be worth mentioning that nowadays, some commercial flash diffusivity systems can estimate the heat capacity ( $C$ ) of materials relative to a standard, but the measurement is often inaccurate and can lead to underestimates of thermal conductivity [144]. In order to obtain the better accuracy of  $C$ , differential scanning calorimetry (DSC) is more frequently used. Differential scanning calorimetry (DSC) is a technique which monitors heat effect as a function of temperature. DSC is used to obtain the enthalpy, glass transition temperature, heat capacity ( $C$ ), and change in heat capacity. The DSC set-up consists of a measurement chamber and a computer with required software. In the measurement chamber, there are two pans containing sample being investigated and a reference respectively. In that process, the difference in heat flow to the sample and the reference at the same temperature is monitored via the computer as a function of temperature. The heating and cooling rate was around  $10^{\circ}\text{C}/\text{min}$ .

The heat capacity of powder samples was measured by this technique. The measurements were performed on a DSC Q200 by TA instrument which is presented in Figure 36.



**Figure 36.** Equipment of DSC Q200.



### 3.2.9. Photothermal radiometry

The thermal properties of the composites were studied using the photothermal radiometry (PTR) setup at room temperature (Figure 37). A wavelength  $\lambda=532$  nm operated solid state laser (COMPASS, COHERENT) was used as radiation light source. The laser beam was modulated by an acousto-optic modulator (AOM-40, IntraACTION). The spectral bandwidth of the infrared detector (HgCdTe,  $1 \times 1$  mm) is  $2-1 \mu\text{m}$ . To process the PTR signal, a digital lock-in amplifier (EG&G 7260) was employed. Experimental parameters and data acquisition were processed by a computer using Labware software. This experiment was performed at Unité de Dynamique et Structure des Matériaux Moléculaires EA 4476 (UDSMM), Université du Littoral à Calais et à Dunkerque. A theoretical description of the resulting PTR signal has been described by Tom et al [183].

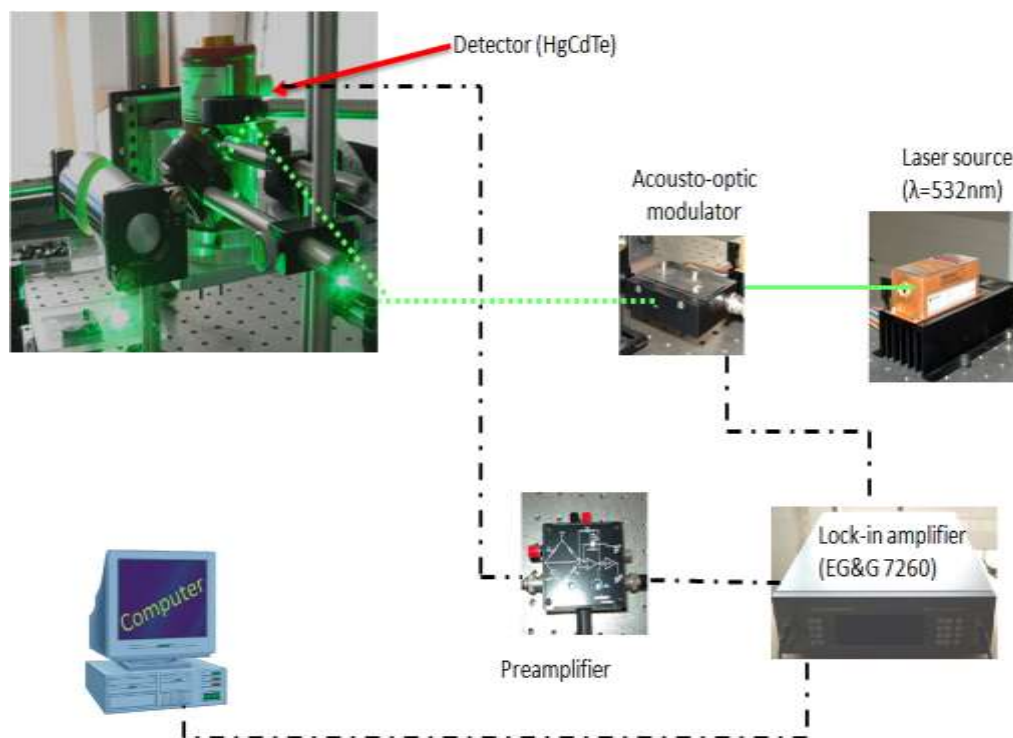


**Figure 37.** Experimental set up of photothermal radiometry.



PTR signals can be obtained by solving simultaneously the heat diffusion and the radiation transport equation. The distribution of the deposited energy within the sample caused by the internal scattering at inner interfaces and absorption strongly controls the PTR signal. One dimensional photothermal model of a three layered system (front medium (a), sample (s) and back medium or substrate (b)) has been considered here (Figure 38).

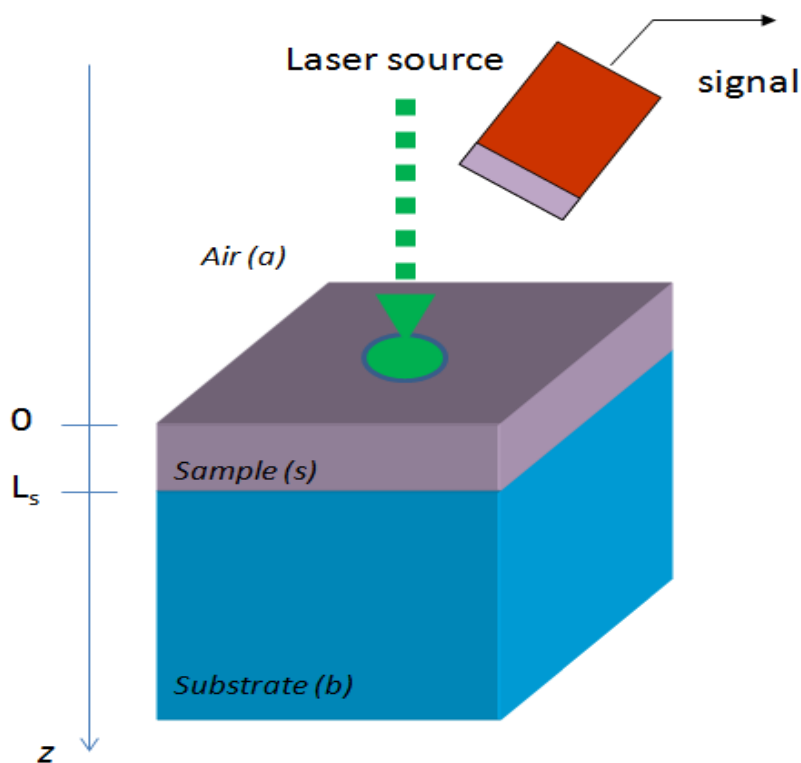


**Figure 38.** Schematic diagram of one dimensional photothermal model of a three layered system (front air medium (a), sample (s) and back medium or substrate (b)).

When a laser beam is periodically illuminated on the sample, absorptivity in the spectral range of detection (IR) generates the PTR signal. In order to minimize the instrumental error, a normalization procedure using the ratio of PTR signals obtained from with and without substrate

has been taken. The expression of the normalized signal for an optically opaque sample at heating beam wavelength, is given by [184] :

$$S_N = \frac{1 + (R_{sb} - 1) \exp(-2\sigma_s L_s)}{1 - (R_{sb} - 1) \exp(-2\sigma_s L_s)} \quad 34$$

where  $L_s$  is the sample thickness and  $\sigma_s$  is complex thermal diffusion coefficient of the sample which is defined as-

$$\sigma_s = (1 + j) (\pi f / \alpha_s)^{1/2} \quad 35$$

where  $j = \sqrt{-1}$ ,  $f$  is chopping frequency and  $\alpha_s$  is the thermal diffusivity of the sample.  $R_{sb}$  represents the reflection coefficient of the thermal waves at the s-b interface [184]. A detail investigation of PTR measurements is reported in the literatures [184,185].

However, from the amplitude and phase of the normalized signal at a given frequency, we get the thermal diffusivity and the thermal effusivity of the samples. These thermal diffusivity and thermal effusivity have been calculated by using a fitting procedure which is reported in the previous literatures [184,185]. However, thermal diffusivity ( $\alpha$ ) is related to the other thermal parameters, the mass specific heat  $c$ , the thermal conductivity ( $k$ ) and thermal effusivity ( $e$ ) by [184]:

$$\alpha = k / \rho c \quad 36$$

$$e = \sqrt{\rho c k} \quad 37$$

where  $\rho$  is the density of the materials. By using the above equations, the thermal conductivity and volumetric heat capacity can be calculated.

### 3.2.10. Dielectric spectroscopy

Dielectric spectroscopy is a powerful tool for the characterization of semiconducting materials, especially the measurement of complex dielectric properties of materials as a function of frequency is important in order to study the electrical and dielectrical properties. Recent development of technology makes the system user-friendly because of new software which provides the required data for further investigation.



**Figure 39.** Picture of equipment for dielectric measurement.

In this study, the dielectric measurement of the sample was carried out on a ModuLab-MTS system (Solartron Analytical-Amtek) (Figure 39). The instruments for the measurement were fully controlled by a computer using ModLab software. In this set up, the sample was placed between aluminum electrodes which are connected with the Solartron Analytical

impedance analyzer (Figure 40). The amplitude of the oscillating voltage was set to 100 mV. The complex permittivity of the samples was measured in the frequency rang 1mHz-1MHz. Also the measurements were performed for various temperatures ( $20^{\circ} - 143^{\circ}\text{C}$ ). In order to obtain through plane electrical conductivity, the complex permittivity data are fitted with Grafity software [186]. In order to insure the effect of electrodes and interfaces (electrode/wafer), different metals were used. The use of different metals for electrodes did not affect the measurements. So, what we trace is not practically affected by sample-electrode effects (which are also labeled as ‘space charge polarization’).

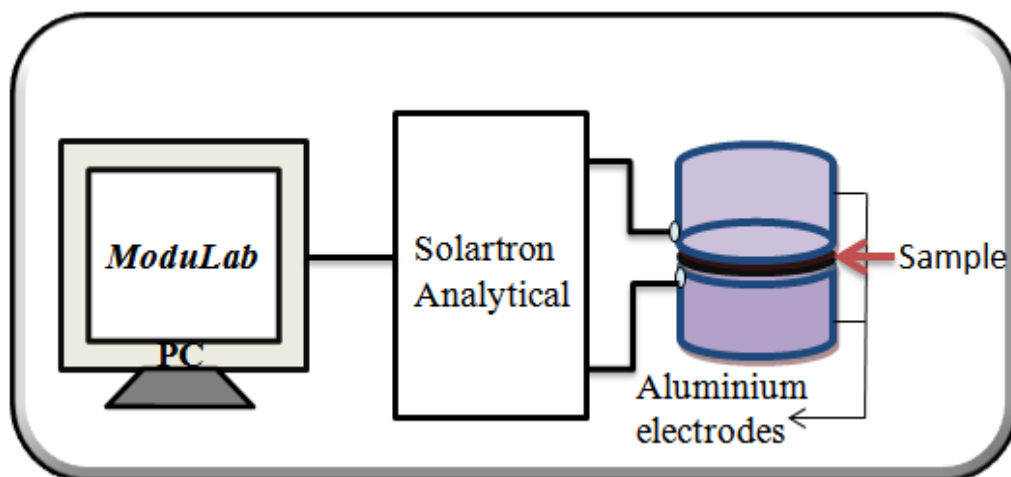


**Figure 40.** Layout of set up for dielectric measurements



## CHAPTER 4 RESULTS AND DISCUSSIONS

In this chapter, we present results and discussions for different carbonaceous based polymer nanostructured composites which have been characterized by different techniques. These techniques are explained in previous chapter.

### 4.1. Single wall carbon nanotubes based polymer nanocomposites

In this section, structural, morphological, electrical, thermal, and thermoelectric properties of synthesized polyaniline (PANI)/single wall carbon nanotubes (SWCNT) nanocomposites have been investigated at room temperature as a function of SWCNT (filler) loading.

#### 4.1.1. Density ( $\rho$ )

To calculate the density ( $\rho$ ) of the pellets of PANI and PANI/SWCNT nanocomposites, the mass ( $m$ ) was measured with electronic balance ( $\pm 0.1$  mg) and the volume of a disc of base radius  $r$  and thickness  $h$  was calculated through the given equation:

$$v = \pi r^2 h \quad 38$$

The density of the prepared pellets was calculated through below relation:

$$\rho = m/v \quad (\text{g/cm}^3) \quad 39$$

The measured density of the nanocomposites as a function of SWCNT weight percentage (wt-% SWCNT) is depicted in Figure 41.

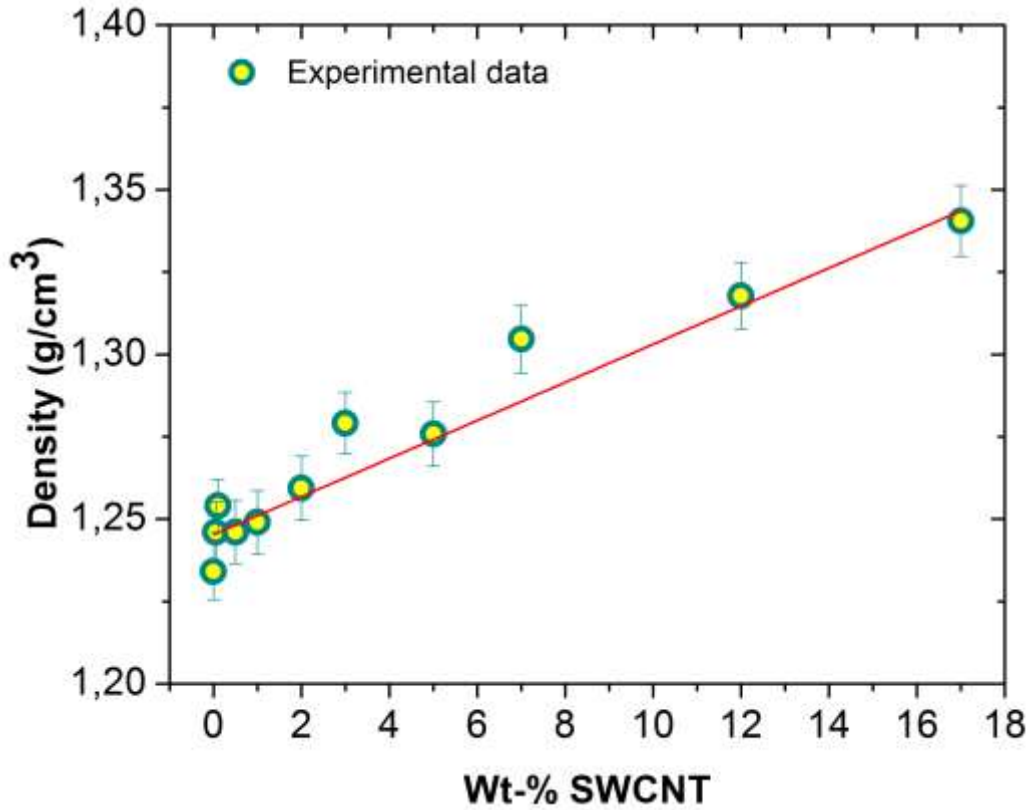


**Figure 41.** Density ( $\rho$ ) of pellets of PANI/SWCNT nanocomposites as a function of wt-% SWCNT. The red solid line is the linear fit.

The experimental result gives an estimation of the density of PANI ( $= 1.24 \text{ g/cm}^3$ ) and SWCNT ( $=1.82 \text{ g/cm}^3$ ) as used in the composites.

Then, volume percentage of filler, the pertinent parameter for further study, denoted as  $\Phi$  (%) or vol-% has been correlated to the density of pellets via equation 40 [187]:

$$\text{Vol} - \% = \frac{\text{wt} - \% \times \rho_{\text{matrix}}}{\text{wt} - \% \times \rho_{\text{matrix}} + (100 - \text{wt} - \%) \rho_{\text{filler}}} \times 100 \quad 40$$

## 4.1.2. Morphological and structural characterizations

### 4.1.2.1 SEM investigation

The morphological study of SWCNT, PANI, and PANI/SWCNT nanocomposites has been conducted by using FE-SEM analysis. The SEM image of commercially available SWCNT with diameter 1-2 nm and length 30  $\mu\text{m}$  is presented in Figure 42(a). The figure shows that there is almost apparent aggregation in the sample. The initial density of primary particles greatly influences the final structure of the agglomerate [188]. Figure 42(b) depicts the morphology of chemically synthesized pure PANI. It exhibits interconnected nanofibers with an average diameter of  $79\pm 15$  nm. The SEM images of PANI/SWCNT nanocomposites filled with different concentrations of SWCNT are shown in Figure 42(c)-(i). At lower concentration of SWCNT, PANI dominates the morphology (see Figure 42(c) and Figure 42(d), with 0.034 vol-%, and 0.68 vol-% SWCNT loading respectively) with the corresponding nanofiber with diameters of  $80\pm 15$  nm, and  $70\pm 15$  nm respectively. The presence of SWCNT and PANI can be clearly observed in Figure 42(e)-(i). Figure 42(e) displays a mixed morphology containing SWCNT bundles with diameter ranging from 6 to 25 nm and rich domains of PANI nanofibers with diameter of  $60\pm 10$  nm. Figure 42(f)-(i) reveal a nice encapsulation of SWCNT by PANI forming core-shell structures in which, SWCNT (3-15 tubes can be defined as SWCNT bundle) as core and PANI as shell.

The results indicate that nanocomposites are successfully synthesized and favourable interactions are present between SWCNT and PANI. It is also observed that with increasing SWCNT loading the diameter of core-shell composites is reduced from  $180\pm 30$  nm (for 2.06 vol-% PANI/SWCNT) to  $80\pm 20$  nm (for 12.25 vol-% PANI/SWCNT) i.e., the diameter of PANI nanofibers is reduced with inclusion of fillers into matrix.



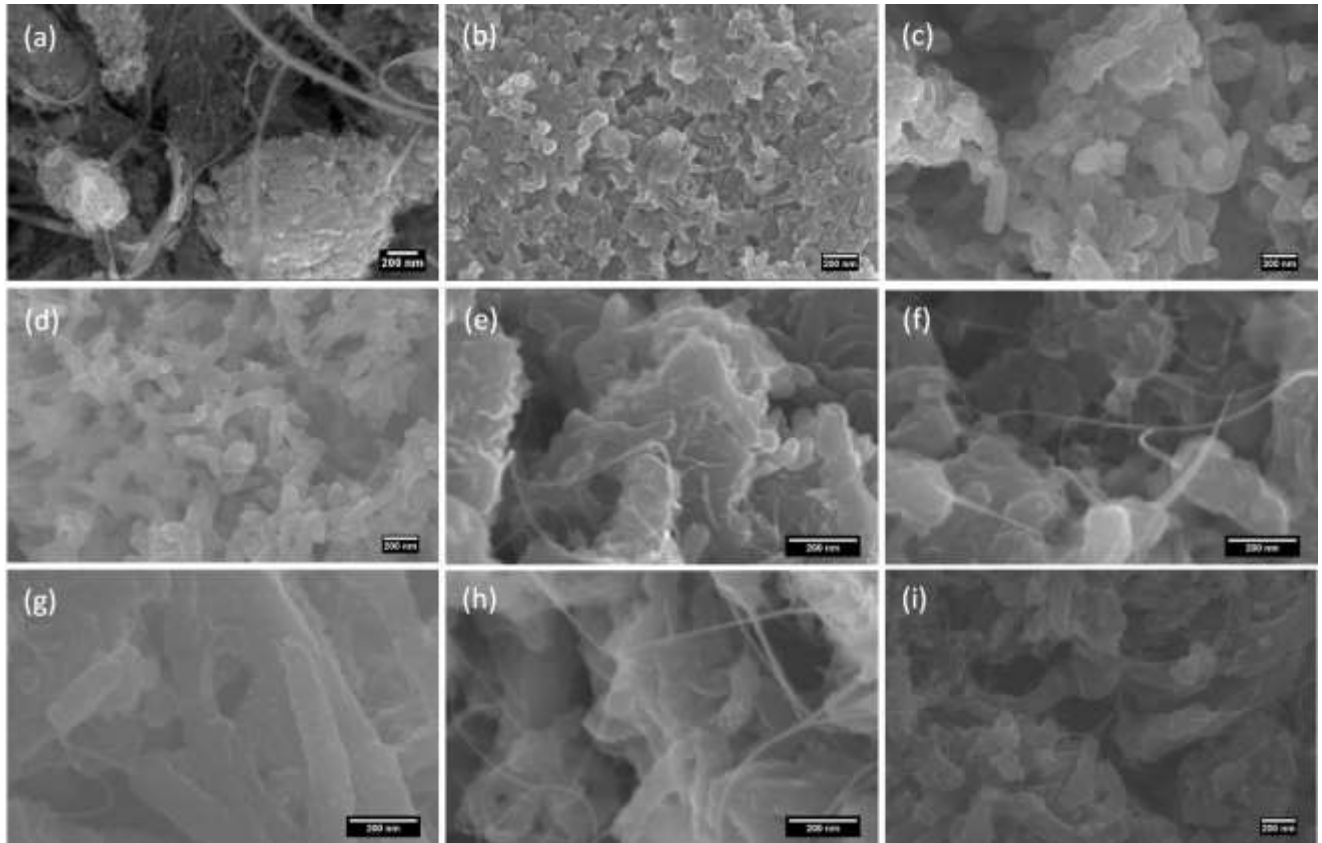


**Figure 42.** Images observed by FE-SEM for (a) pure SWCNT, (b) pure PANI, and PANI/SWCNT nanocomposites with (c) 0.034 vol-%, (d) 0.68 vol-%, (e) 2.06 vol-%, (f) 3.46 vol-%, (g) 4.88 vol-%, (h) 8.50 vol-%, and (i) 12.25 vol-% SWCNT loading respectively with scale bar of 200 nm.

#### 4.1.2.2 TEM investigation

The TEM images of PANI/SWCNT nanocomposite containing 12.25 vol-% SWCNT are presented in Figure 43(a)-(d) with scale bars of 1000 nm, 500nm, 50 nm, and 20 nm, respectively.

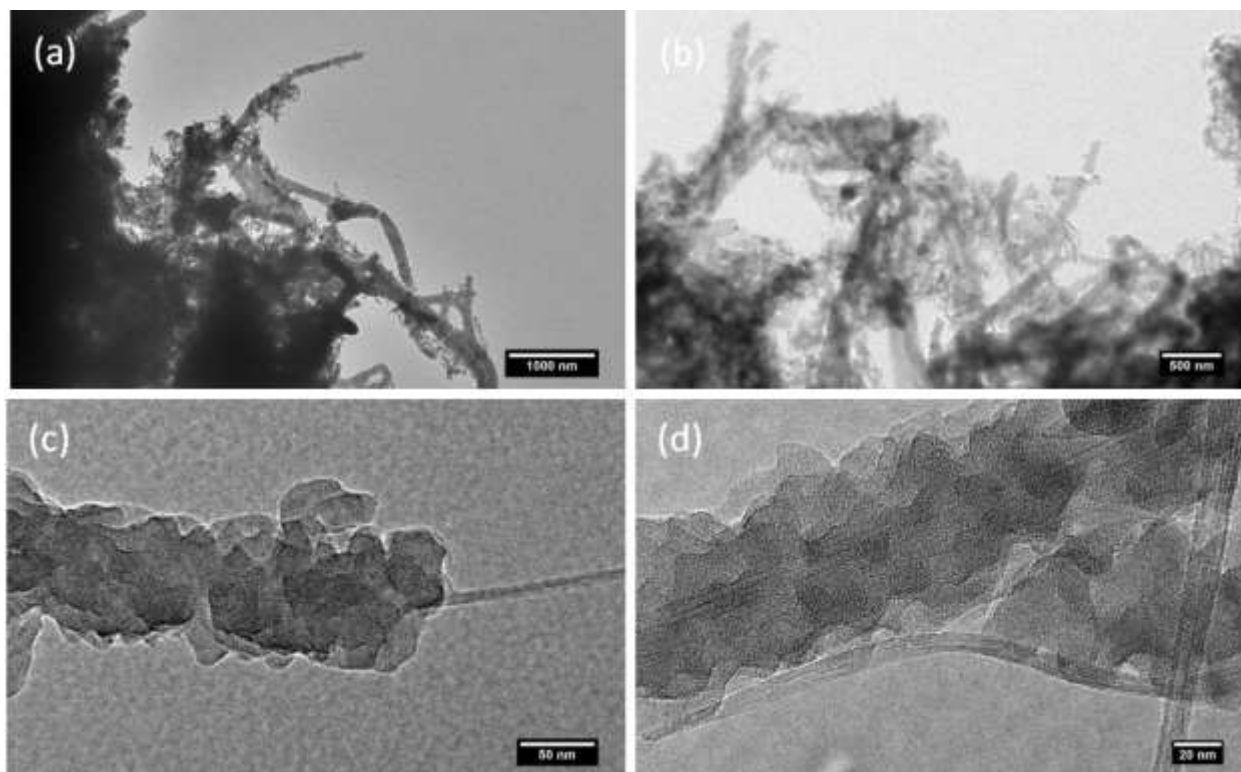


**Figure 43.** High resolution TEM images of 12.25 vol-% with scale bars (a) 1000 nm, (b) 500 nm, (c) 50 nm, and (d) 20 nm.

These TEM images reveal more detailed features of PANI/SWCNT and/or SWCNT bundles. In general, the TEM characterizations of the composites show a wrapping of SWCNT by PANI resulting core-shell nanocomposites which further confirm SEM investigations. It is believed that in the wrapping process, the molecular chain of PANI first stretch and move toward the SWCNT, then wrap the surface of SWCNT until equilibrium is achieved [189]. Figure 43(c) and (d) show high resolution TEM images which clearly indicate SWCNT bundles coated with PANI layers whose structures are similar to those reported in the literatures [4,190]. The diameter of formed core-shell nanostructures is  $75 \pm 15$  nm which is almost similar to that derived from SEM. That is, PANI nanofibers with diameter ca. 25-35 nm are deposited around SWCNT bundles with diameter of 6-25 nm. Such a core-shell nanostructured composites feature is favoured by good aromatic basal ring  $\pi$ - $\pi$  interactions between PANI and SWCNT [7,190,191]. In this process, it can be envisioned that the aromatic rings of PANI gradually orient such that their planes are parallel to those of SWCNT, thereby favouring good intermolecular interactions.

The energy of the strong interactions is supported by early force-field based molecular mechanics (MM) calculations which provide the binding energies between carbon nanotubes and a range of polymer matrices [192]. Additional studies show that this intermolecular interaction is strongly controlled by the SWCNT morphology and the specific monomer structure [193].

### 4.1.3. Electrical properties

Figure 44 exhibits the experimental data of the electrical conductivity ( $\sigma$ ) of PANI/SWCNT nanocomposites as a function of vol-% ( $\Phi$  (%)) SWCNT from which it can be seen that the electrical conductivity increases with increase in SWCNT loading.

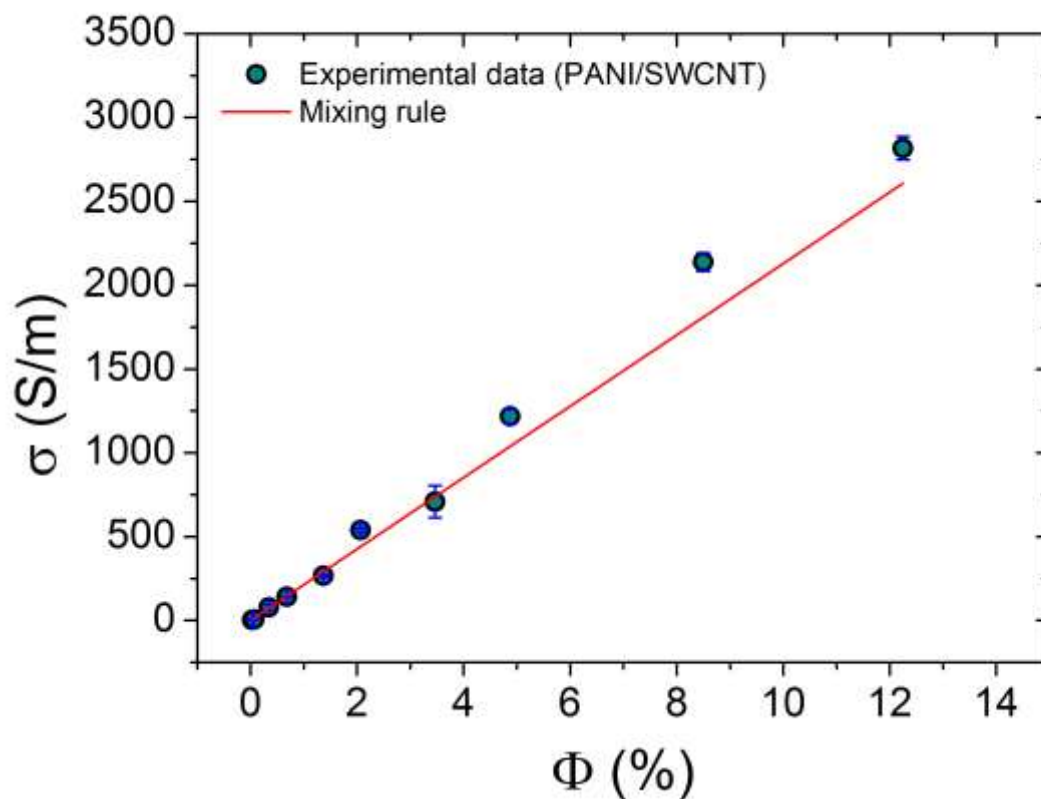


**Figure 44.** Electrical conductivity ( $\sigma$ ) of PANI/SWCNT nanocomposites as a function of vol-% SWCNT. Symbols are experimental data whereas red solid line is the best fit of equation 2.

It can be assumed that at low vol-% SWCNT, the electrical conductivity of the composite shows poor value (in the order of 10 S/m). However, with increased loading of the filler, a conductivity network is perfectly established resulting in an increase of conductivity up to  $2817 \pm 69$  S/m for the composite with 12.25 vol-% SWCNT. Knowing that the experimental value of the electrical conductivity of pure PANI is  $0.05 \pm 0.01$  S/m, the result shows that inclusion of SWCNT into the matrix enhances the overall electrical conductivity of the composites by at least five orders of magnitude.

Moreover, the electrical conductivity of PANI/SWCNT composites is changed as a function of SWCNT filler concentration. So, the electrical conductivity of the composites is analyzed by its dependence on volume fraction. In order to further rationalize this behavior of the electrical properties of the composites, the behavior of electrical conductivity as a function of filler volume fraction is interpreted by using mixing rule which is the simplest models as well as the first step. Here, the mixing rule (upper bond) which is presented in the equation 2 is used to fit the experimental data of the electrical conductivity of the composites. The fitting curve is depicted in the Figure 44. The fit provides the values of the electrical conductivity of filler ( $\sigma_{\text{filler}} \sim 21288$  S/m) and the electrical conductivity of matrix ( $\sigma_{\text{matrix}} \sim 0.05$  S/m). The result shows that the electrical conductivity value ( $\sigma_{\text{filler}} = 21288$  S/m) of SWCNT as used in nanocomposites, which is almost 2 times greater than SWCNT purchased from company. The result indicates that the fits are quite well at low SWCNT volume fraction but there are some differences at high SWCNT volume fraction. Also it can be observed that there is a big difference between the conductivity value ( $\sigma \sim 0.05$  S/m) of pure PANI (and the conductivity value ( $\sigma \sim 3.67$  S/m) of PANI/SWCNT composite with 0.034 vol-% SWCNT loading. The finding indicates a modification of conducting state of the PANI as well as SWCNT in the composites.

An alternative explanation for the observation is that the conductivity is driven by the percolation model which means that the transport properties are only controlled by the connectivity of the filler (SWCNT) network. In order to investigate the electrical transport properties of the composites, the experimental evolution of the conductivity is fitted with the percolation critical power law which is presented in equation (below):

$$\ln \sigma = \ln \sigma_0 + t \ln(\Phi_{\text{filler}} - \Phi_c) \quad 41$$

where  $\sigma$  (S/m) is the electrical conductivity of the composites,  $\Phi_{\text{filler}}$  is the volume fraction of fillers,  $\Phi_c$  is the volume percolation concentration or percolation threshold, and  $t$  is a critical exponent. As shown in Figure 45, a good agreement is obtained between experimental data points and the fit (solid line).

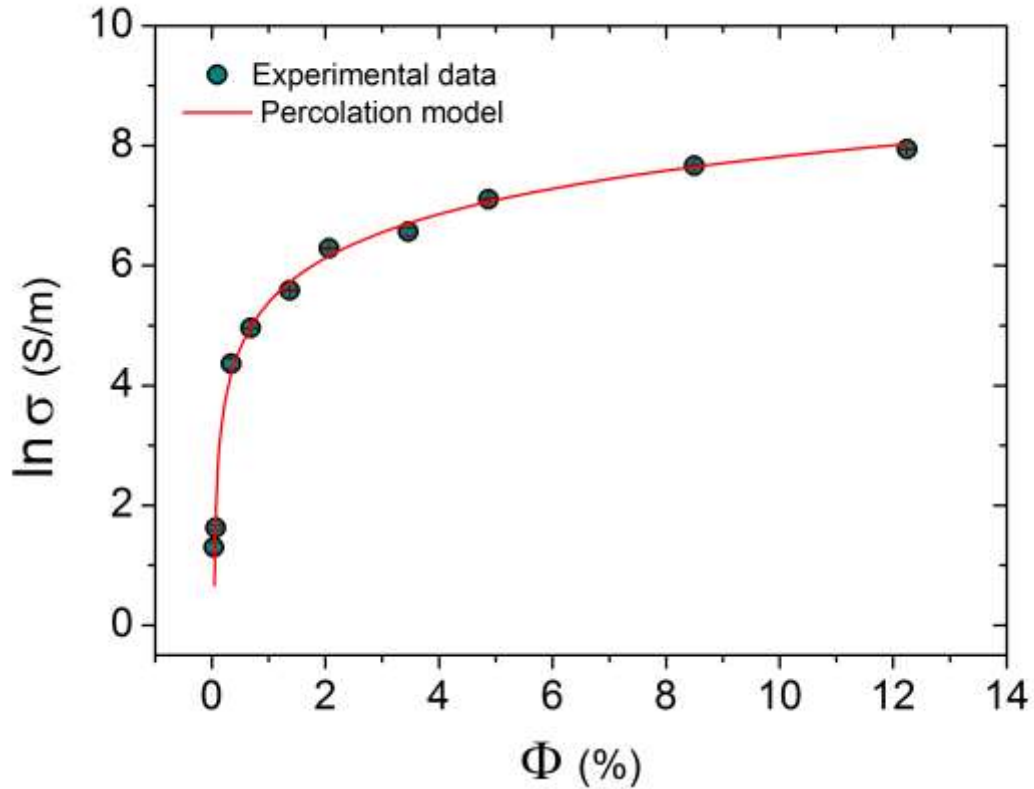


**Figure 45.** Electrical conductivity ( $\sigma$ ) of PANI/SWCNT nanocomposites as a function of vol-% SWCNT. Symbols are experimental data whereas red solid line is the fit of equation 41.

The fitting provides the values of  $\Phi_c=0.004$  vol-%,  $t=1.04$ , and  $\sigma_0=27.44$  S/m. The result reveals percolation behavior in which the presence of SWCNT into PANI results in a dramatic increase in their electrical conductivity. Also it shows that the percolation is occurring at quite low concentration (0.004 vol-%). To the best of our knowledge, this value is much lower than those reported previously. For example, for similar PANI/SWCNT composites, the percolation threshold was reported to be 0.3 vol-% [194]. We believed that the lower percolation threshold of PANI/SWCNT composites observed in this study stems from a better distribution of SWCNT which can make use of the low SWCNT filler content to form effective conductive network.

The log-log plot of  $\sigma$  versus reduced volume fraction ( $\Phi - \Phi_c$ ) of SWCNT plotted in Figure 46 has an expected linear dependence whose the slope represents also the critical exponent.

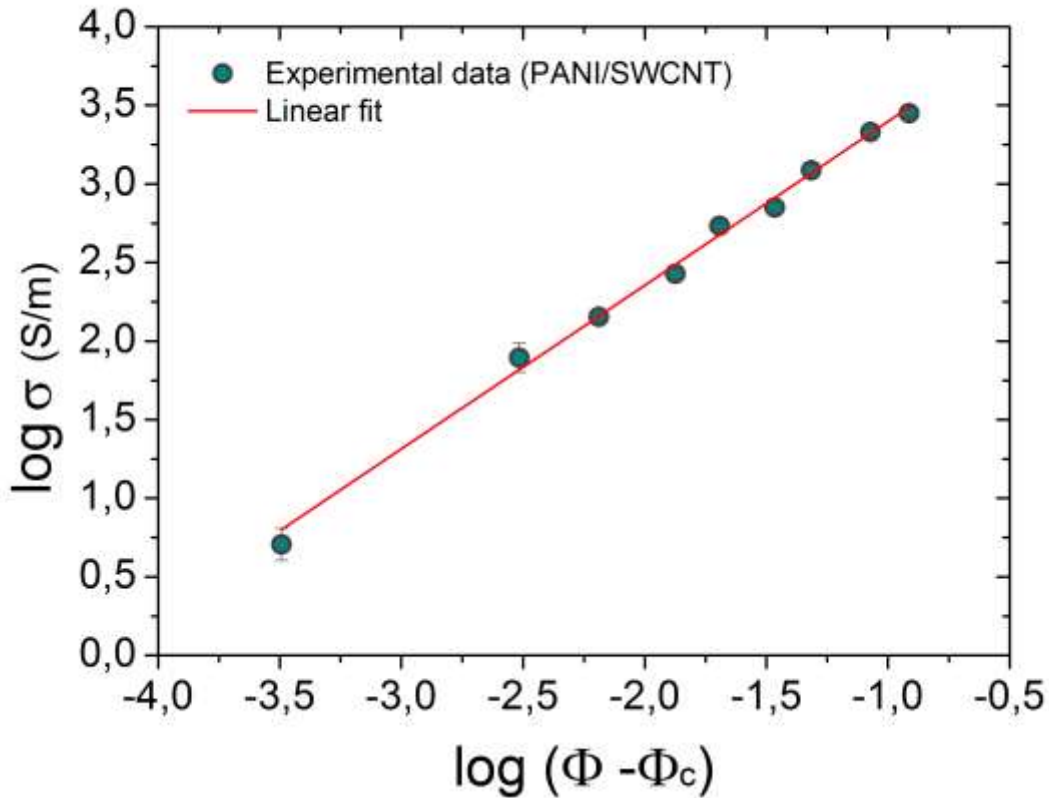


**Figure 46.** log-log plot of  $\sigma$  versus reduced volume fraction of SWCNT.

The obtained value is  $t \sim 1.04$ . The value of  $t$  is close those reported in the literature [20,195,196]. In general the critical exponent ( $t$ ) for 1-D carbon nanotubes filled composites is higher than the obtained  $t$  value [194,195]. The low value of  $t$  suggests that an aggregation of the carbon nanotubes is still presented in the composites after sample preparation which is evidenced by SEM and TEM images (Figure 42 and 43). So, the low exponent  $t$  does not reflect a reduction in system dimensionality in the present case but rather the aggregation process of the SWCNT during sample preparation. The agglomeration of filler plays an important role to form effective conductive network. Also, the formation of these conducting networks is not a true statistical percolation process based on the random distribution of individual high aspect ratio fillers, but rather is attributed to the mutual attraction of the nanotubes in the composites. Thus, the

morphology of PANI/SWCNT can be related to the low  $t$  value. The conclusions are: the threshold is very low and the critical exponent  $t$  is close to 1 which is not really in adequation with conventional percolation behavior.

The above studies suggest that the conductivity is related to the fact that PANI is not same conducting state after processing. It means that the PANI is changed from insulating to semi-conducting. This modification can be explained by charge transfer process. Furthermore, It is shown that the strong interfacial interaction of SWCNT with the PANI through  $\pi$ - $\pi$  interaction significantly contributes to produce core-shell SWCNT-PANI nanocomposites [7,96–98] which is evidenced in the SEM and TEM images (Figure 42 and 43). The synthesis of PANI/SWCNT by an in-situ process leads to effective site-selective interactions between the quinoid ring of the PANI and the SWCNT facilitating charge-transfer processes between the two components. In particular, a strong coupling between SWCNT and PANI through  $\pi$ - $\pi$ -interaction enhances the electrical conductivity. In such case, it can be expected that the mixing rule relation is better to explain the electrical conductivity behavior of the composites.

#### 4.1.4. Thermal properties

The thermal properties of PANI/SWCNT composites are studied here. Specifically, data on thermal diffusivity ( $\alpha$ ) carried out using the “laser flash” (NETZSCH LFA 467) method and heat capacity ( $C$ ) obtained via DSC are presented. Moreover, thermal conductivity of the samples has been investigated in order to understand the thermal properties and conduction mechanism of the PANI/SWCNT composites.

##### 4.1.4.1 Thermal diffusivity ( $\alpha$ )

The measured thermal diffusivity of PANI/SWCNT nanocomposites as function of vol-% SWCNT is depicted in Figure 47.

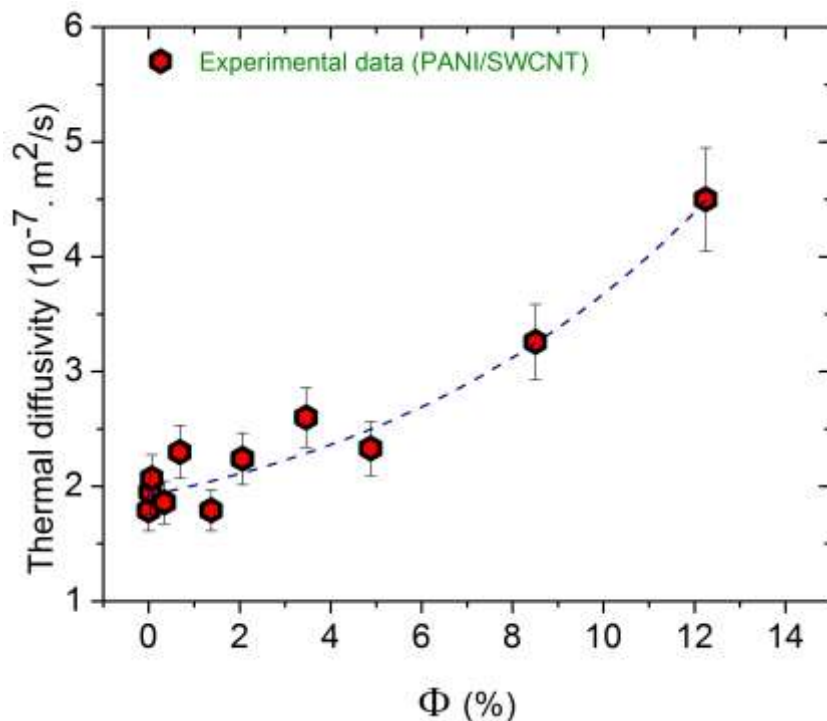


**Figure 47.** Thermal diffusivity ( $\alpha$ ) of PANI/SWCNT nanocomposites as a function of SWCNT content. Dashed line is guides to the eyes.

The obtained thermal diffusivity ( $\alpha$ ) value of pure PANI is  $1.79 \times 10^{-7} \text{ m}^2/\text{s}$ . It is found that, the thermal diffusivity ( $\alpha$ ) of the nanocomposites barely changes at lower SWCNT nano-fillers loading ( $<2 \text{ vol-\%}$ ) but rises sharply beyond that percentage. It can be inferred that at higher content of SWCNT nano-fillers in the nanocomposites, more thermal conducting pathways are induced which increase in the thermal diffusivity of the composites.

#### 4.1.4.2 Volumetric heat capacity ( $\rho C$ )

With the use of laser flash method, measurements of the heat capacity ( $C$ ) are made possible and this parameter can then be correlated to thermal conductivity. In order to obtain the value of  $C$ , modulated differential scanning calorimetry (DSC) has been employed. The volumetric heat capacity ( $\rho C$ ) is calculated using the value of density ( $\rho$ ) which is studied in the section



4.1.1, and heat capacity (C). Figure 48 presents the evaluation of volumetric heat capacity ( $\rho C$ ) of the PANI/SWCNT nanocomposites. The volumetric heat capacity of pure PANI is found to be  $1.04 \pm 0.07 \text{ MJm}^{-3}\text{K}^{-1}$  while the values for the composites vary from  $1.35 \pm 0.07 \text{ MJm}^{-3}\text{K}^{-1}$  (4.88 vol-%) to  $1.89 \pm 0.07 \text{ MJm}^{-3}\text{K}^{-1}$  (2.06 vol-%). The result suggests that the volumetric heat capacity of the PANI/SWCNT composites increases with adding of SWCNT in comparison with pure PANI. It also is observed that the volumetric heat capacity is almost  $1.5 \text{ MJm}^{-3}\text{K}^{-1}$  with very low SWCNT loading. The gap between this value ( $1.5 \text{ MJm}^{-3}\text{K}^{-1}$ ) and pure PANI value ( $1.04 \pm 0.07 \text{ MJm}^{-3}\text{K}^{-1}$ ) indicates that heat transport mechanism is modified in PANI as used in the nanocomposites like electrical properties.

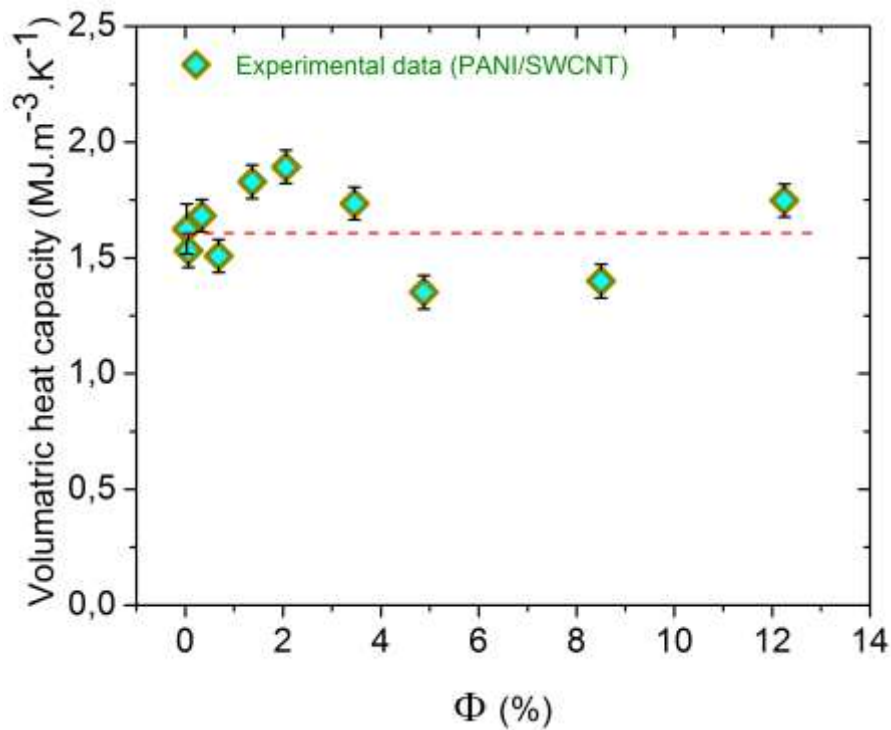


**Figure 48.** Volumetric heat capacity ( $\rho C$ ) of PANI/SWCNT nanocomposites as a function of SWCNT content. Dashed line is guides to the eyes.

#### 4.1.4.3 Thermal conductivity (k)

To gain further insight into the thermal properties of the composites, thermal conductivity (k) of the PANI/SWCNT composites is studied in this section. This parameter is calculated as:

$$k = \rho C \times \alpha \quad 42$$

where  $\alpha$  is the thermal diffusivity. In the thermal conductivity calculation the errors coming from instruments and thickness are taken into account. The filler concentration dependency of thermal conductivity of the PANI/SWCNT is shown in Figure 49.

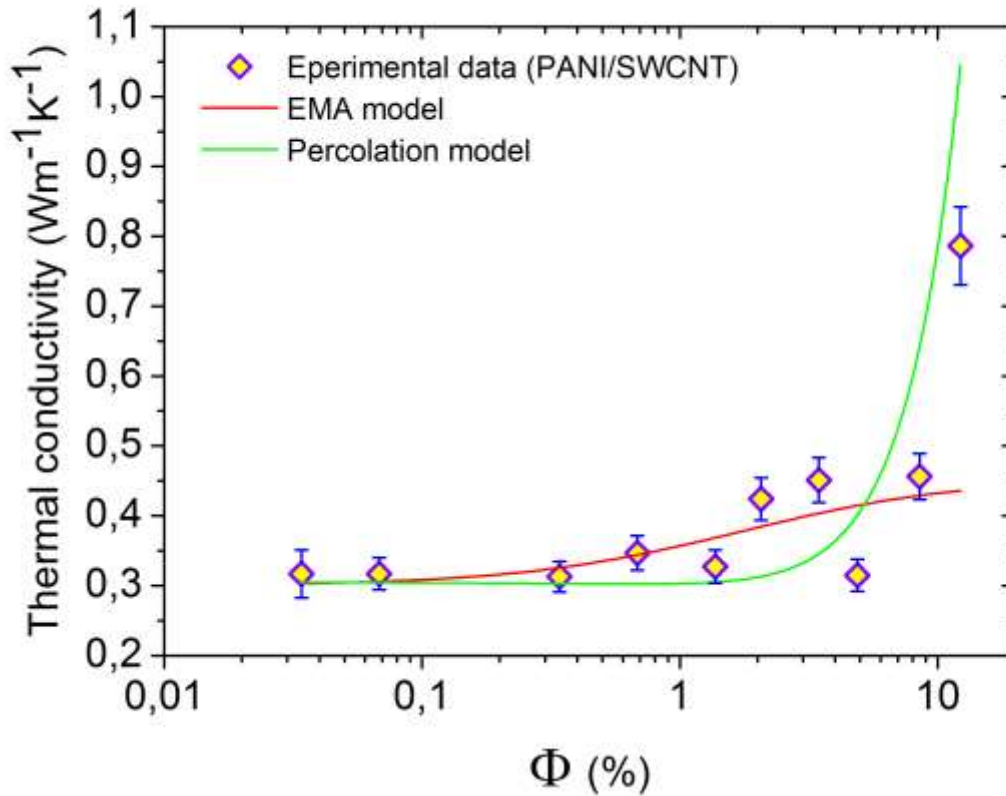


**Figure 49.** Thermal conductivity (k) of PANI/SWCNT nanocomposites as a function of SWCNT content.

The Figure 49 reveals an increase in thermal conductivity of PANI/SWCNT composites up to  $0.79 \pm 0.06 \text{ W.m}^{-1}.\text{K}^{-1}$  for 12.25 vol-% SWCNT content whereas the value of thermal conductivity of pure PANI  $k_{\text{PANI}}$  is  $0.19 \pm 0.01 \text{ W.m}^{-1}.\text{K}^{-1}$ . Again, great dispersion (around  $0.1 \text{ W.m}^{-1}.\text{K}^{-1}$ ) is observed in the experimental values of pure PANI and smallest loading (0.034 vol-%) PANI/SWCNT composite ( $0.32 \text{ W.m}^{-1}.\text{K}^{-1}$ ). This dispersion can be attributed to the volumetric heat capacity of the composites. Thus, thermal conductivity enhancement ( $\text{TCE}\% = ((k - k_{\text{PANI}}) \times 100 / k_{\text{PANI}})$ ) is obtained up to  $\sim 323\%$  which is lower than that of epoxy/SWCNT obtained with similar technique (Laser flash) [197]. It is worth mentioning that the relatively low thermal conductivity value of our composites is advantageous and it could be exploited to improve the overall characteristics of thermoelectric materials.

Like electrical conductivity, to investigate a percolation behavior of thermal conductivity, the simulated green curve is presented (Figure 49) by using percolation power law presented in equation 14. Based on the literature, we expect that a) if thermal percolation is present in our composites, then the percolation threshold ( $\Phi_c$ ) of electrical conductivity is the same as that of the thermal conductivity [21] b) the signature of a 3D thermal transport process is also taking place for which critical exponent is close to 2 [21] and c) the thermal conductivity prefactor ( $k_0$ ) is in the range of  $25\text{-}55 \pm 10 \text{ W/mK}$  depending on the value of the critical exponent [21]. However, the presented curve for percolation model is the result of  $\Phi_c = 0.004 \text{ vol-\%}$ ,  $\beta=2$  with  $k_0=55 \pm 10 \text{ W/mK}$ . The fact that the green curve does not match with the thermal conductivity values (Figure 49), indicates that no thermal percolation behavior has been detected within the range of SWCNT volume fraction. The lack of thermal percolation is found to be consistent with those reported in literatures [150,198,199]. The result further highlights the difference in thermal vs. electrical conduction mechanisms i.e, the predominant path for thermal transport is via phonon propagation and that of electrical transport is via charge carrier transport. It can be observed that the thermal conductivity ratio  $k/k_{\text{PANI}}$  is much smaller than the electrical conductivity ratio  $\sigma/\sigma_{\text{PANI}}$ . For the relatively low thermal conductivity of the PANI/SWCNT composites, it can be inferred that a larger fraction of phonons are likely to travel through the matrix [200] and their propagation is somewhat impeded by the interfacial thermal resistance between nano-fillers and matrix and the contact resistance for the heat flow between two nano-fillers [147].

Moreover, inclusion of highly thermally conductive SWCNT into relatively poor thermal conducting PANI can show two reversed effects in thermal conductivity of the nanocomposites depending on filler concentration [199]. That is, at low SWCNT content (below~1.5 vol-%), the presence of induced surface and interfacial layer lead to the reduction of the heat flow transport because of large amount of phonon scattered by these new features. And the thermal conductivity at higher SWCNT loading gradually increases because of a new phase with higher thermal conductivity is established.

To shed more light on interfacial effect in the thermal conductivity of PANI/SWCNT, the thermal conductivity of the composites has been interpreted by the effective mass approximation (EMA) theory (equation 17) which was developed by Nan *et.al.* for the effective thermal conductivity of CNT composites [153]. This model is valid for the nanotubes based composites filled with small loading. For examples, Nan *et. al.* used this model for carbon nanotubes composites containing up to 6 vol-% filler [150]. Our data (Figure 49) is fitted with same model up to 10 vol-% SWCNT content. The resulted value of thermal resistance between SWCNT and PANI is  $2.34 \times 10^{-8} \text{ m}^2 \text{KW}^{-1}$  which is similar order of magnitude with those reported in literatures [147,199].

#### 4.1.5. Seebeck coefficient (S) and power factor (PF)

Seebeck coefficient (S) is calculated by measuring the thermoelectric (TE) voltages ( $\Delta V$ ) as a function of temperature gradient ( $\Delta T$ ) by using equation 20. The Seebeck coefficient of PANI/SWCNT nanohybrids is plotted as a function of SWCNT volume fraction in Figure 50. The measured Seebeck coefficient of pure PANI is  $9.77 \pm 0.17 \text{ } \mu\text{V/K}$ . Moreover, the figure reveals that with the incorporation of SWCNT into matrix, the Seebeck coefficient of PANI/SWCNT composites is enhanced. The composite with 12.25 vol-% SWCNT has Seebeck value of  $28.70 \pm 0.10 \text{ } \mu\text{V/K}$ , which is almost 3 fold larger than that of pure PANI. Here also in Seebeck coefficient values, there is gap between pure PANI and PANI/SWCNT composites with low SWCNT volume fraction. The result indicates that PANI is changed in the composites during sample preparation. More specifically, charge carriers transport is modified in the composites forms resulting in the gap of Seebeck coefficient values.

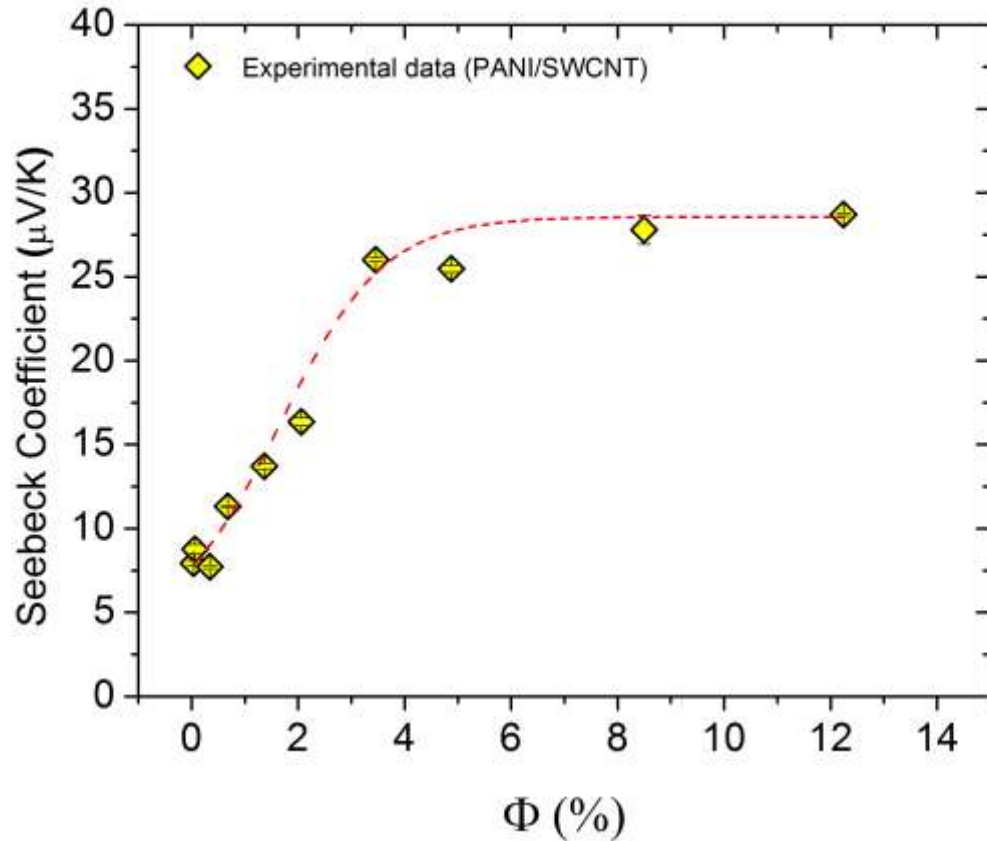


**Figure 50.** Experimental evolution of Seebeck coefficient ( $S$ ) as function of vol-% SWCNT. Dashed line is guides to the eyes.

In addition, all Seebeck coefficients are positive, indicating p-type semiconductors i.e., holes are the dominant carriers to electrical conductivity. The interesting observation is that the Seebeck coefficient and electrical conductivity of the nanocomposites simultaneously increase which is shown in Figure 51. In general, these two parameters cannot enhance simultaneously due to the gap between narrow transport level ( $\epsilon_T$ ) and Fermi level ( $\epsilon_F$ ) of the material [201]. The result suggests that the conduction mechanism in PANI/SWCNT composites up to 12.25 vol-% SWCNT loading cannot be interpreted by a conventional model based on the band theory or the electron-phonon scattering [175].

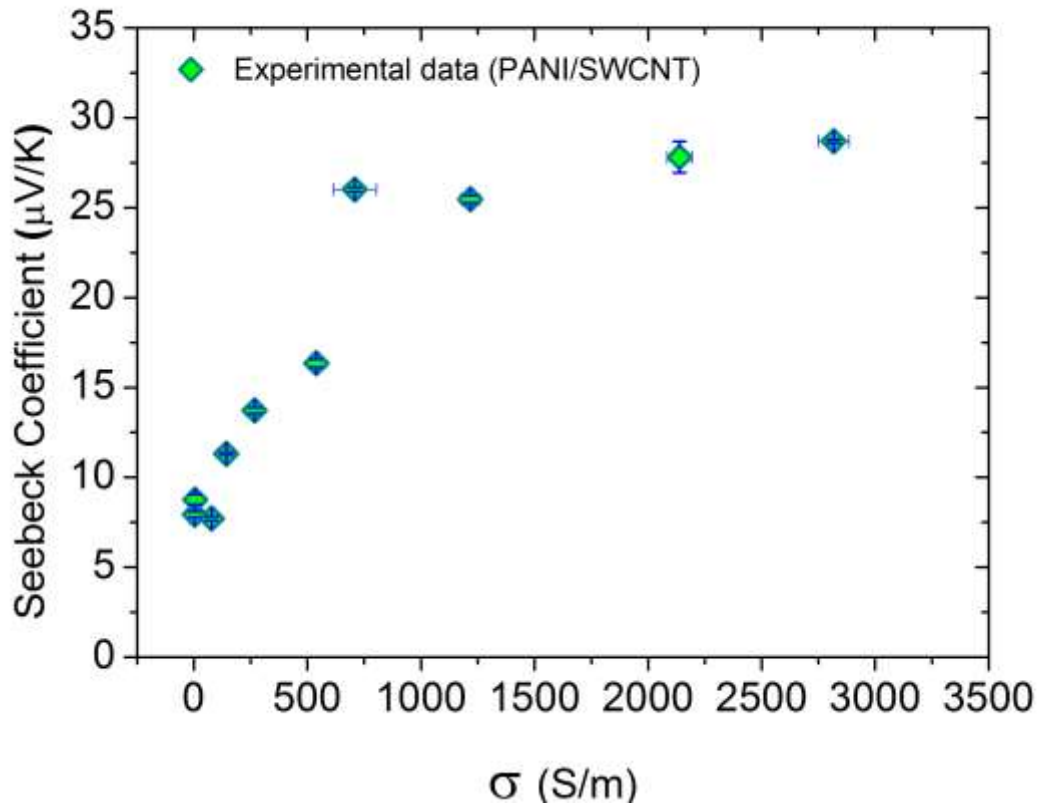


**Figure 51.** Experimental evaluation of Seebeck coefficient (S) of PANI/SWCNT composites as function of electrical conductivity.

In order to understand the nature of the Seebeck coefficient, the equation 22 is used which can be expressed as follows [176]. The equation gives an explanation that Seebeck coefficient will depend on both effective electrical conductivity and carrier mobility. It is worth mentioning that if the SWCNT loading increases, the number of charge carriers ( $n$ ) should also increase. Therefore, the effective electrical conductivity ( $\sigma = n \mu q$ ) increases. As shown in equation 22, both quantities (electrical conductivity and Seebeck coefficient) are inversely proportional. So, the experimental data cannot be explained by the enhancement of effective electrical conductivity. The result indicates that Seebeck coefficient of the composites is dominated by the mobility of charge carrier (originating from  $\pi$ - $\pi$  interactions between PANI and SWCNT) because of a proportional relation between these two parameters (see equation 22). The

fact that in this study  $S$  increases with the filler loading is a good indication that number of charge carriers do not play a significant role in the enhancing  $S$ .

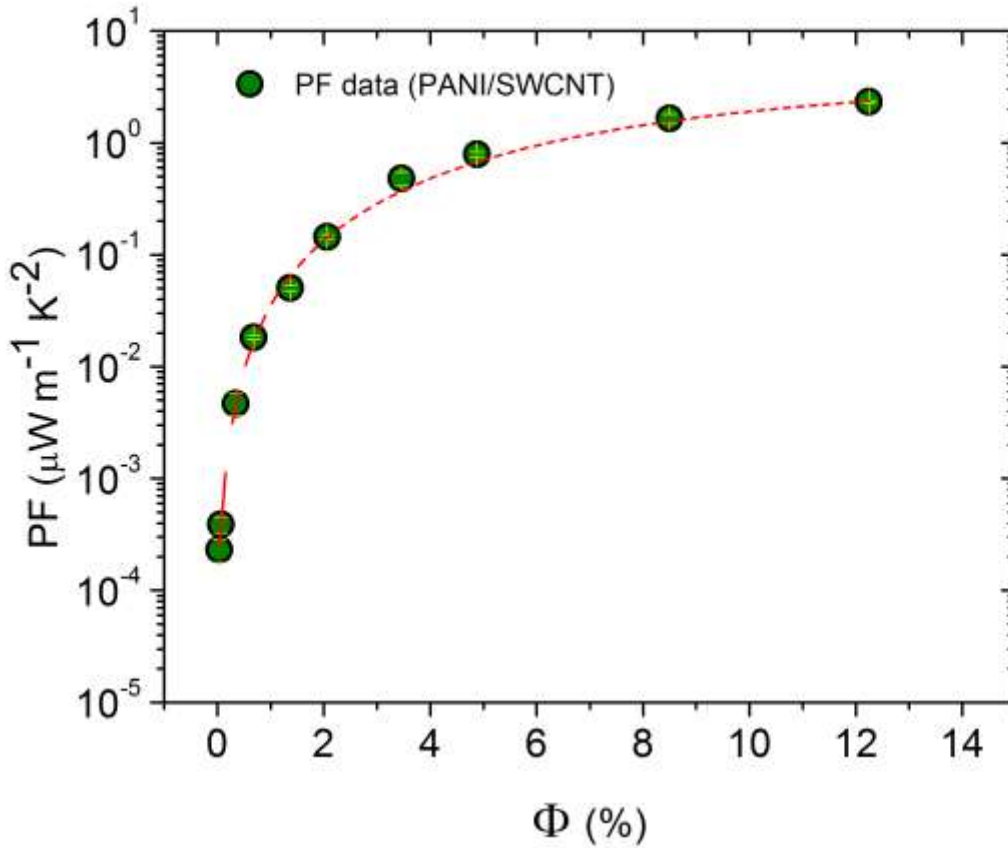


**Figure 52.** Power factor (PF) vs vol-% SWCNT. Dashed line is guides to the eyes.

One of the useful quantities needed to evaluate the performance of a thermoelectric material is called “power factor” (PF) which combines both electrical conductivity and Seebeck coefficient as:

$$PF = S^2 \sigma \quad 43$$

The power factor becomes important when the thermal conductivity of the samples is almost unchanged. More specifically, in the case of similar or low thermal conductivities, a simplified evaluation criterion, power factor, is often adopted. So, the signature of figure of merit can be interpreted by using power factor. The simultaneous rise of both  $S$  (Figure 50) and  $\sigma$  (Figure 44) with increasing amount of filler highlights their critical role in raising the PF as displayed in Figure 52. The highest PF obtained is ca.  $2.32 \pm 0.07 \mu\text{Wm}^{-1}\text{K}^{-2}$  for PANI/SWCNT composite containing 12.25 vol-% SWCNT. This PF value is actually significantly enhanced since it is  $4.8 \times 10^6$  times higher than that of the PANI whose PF is only  $4.77 \times 10^{-6} \mu\text{Wm}^{-1}\text{K}^{-2}$ .

#### 4.1.6. Thermoelectric properties

The performance of thermoelectric materials is traditionally determined by the dimensionless figure of merit  $ZT$  which has been presented in equation 23. The figure of merit  $ZT$  ( $T = 300\text{K}$ ) of PANI/SWCNT composites as a function of SWCNT content is presented in Figure 53 from which it can be seen that  $ZT$  increases with increasing SWCNT concentration.

The results from the above study indicate that both electrical conductivity, Seebeck coefficient (and PF) of PANI/SWCNT composites are higher than those of PANI and the thermal conductivity of the composites is also increased but is more mitigated (Figure 49) even with higher SWCNT concentration. These trends when tied to equation 23 contribute in raising  $ZT$  which reaches a maximum value of 0.0011 for a sample with 8.50 vol-% SWCNT content. This  $ZT$  value is about five orders of magnitude higher than that of the pristine PANI ( $7.71 \times 10^{-9}$ ). Therefore, the results show that the performance of a thermoelectric device is very much dependent on finding ways to simultaneously raise both the electrical conductivity and Seebeck coefficient.



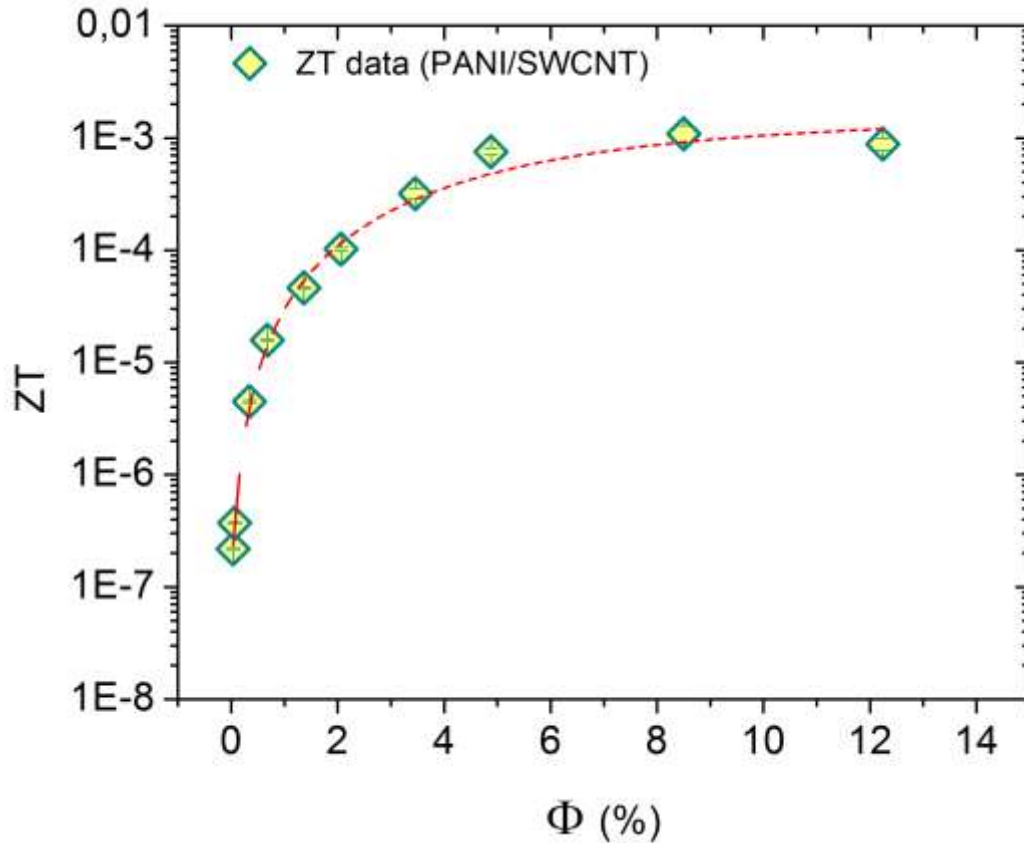


**Figure 53.** Thermoelectric performance (ZT) of PANI/SWCNT nanocomposite. Dashed line is guides to the eyes.

In summary, this study clearly supports the synergistic role played by SWCNT as filler in enhancing the electrical conductivity/Seebeck coefficient of the composites and the use of PANI as a poorer electrical and thermal matrix to enhance the overall ZT. Thus, SWCNT/PANI composites are good candidates for organic thermoelectric materials.

## 4.2. Multi wall carbon nanotubes based polymer nanocomposites

In previous section, we showed investigations of structural, morphological, electrical, thermal, and thermoelectric properties of chemically synthesized PANI/SWCNT nanocomposites. Here, we demonstrate the similar properties for chemically synthesized polyaniline (PANI)/multi wall carbon nanotubes (MWCNT) nanocomposites.

### 4.2.1. Density ( $\rho$ )

By using equation **38** and **39**, the density ( $\rho$ ) of PANI/MWCNT nanocomposites was obtained for further study. However, Figure **54** represents the density data of the composites as a function of weight percentage (wt-% MWCNT). The experimental result provides an estimation of the density of PANI and MWCNT as presented in the nanocomposites. The density value of PANI ( $= 1.24 \text{ g/cm}^3$ ) and MWCNT ( $=1.86 \text{ g/cm}^3$ ) are found. By taking the value of the density of PANI and MWCNT the volume fraction ( $\Phi$ ) of PANI/MWCNT nanocomposites has been calculated with equation **40**.

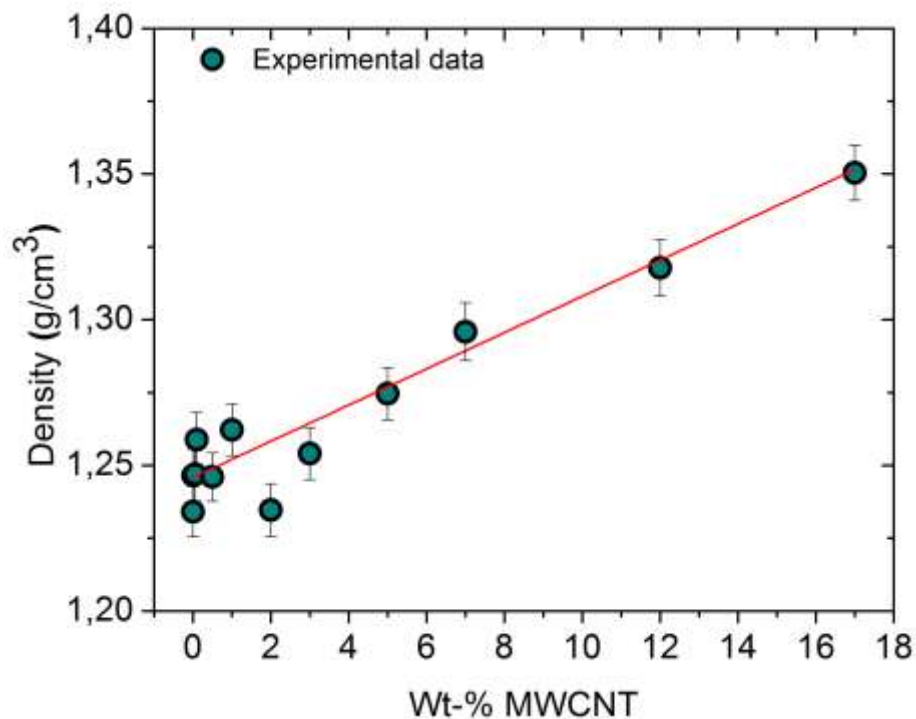


**Figure 54.** Density ( $\rho$ ) of pellets of PANI/MWCNT nanocomposites as a function of wt-% MWCNT. The red solid line is the linear fit.

## 4.2.2. Morphological and structural characterizations

### 4.2.2.1 SEM investigation

FE-SEM images of MWCNT and PANI/MWCNT composites are used to study the morphology of the composites (Figure 55). Figure 55(a) shows the morphology of pure MWCNT with outer diameter 10-20 nm and length 30  $\mu\text{m}$  provided by manufactured company. Figure 55(b)-(e) represents the FE-SEM images recorded for 0.0067 vol-%, 0.03 vol-%, 0.33 vol-%, and 0.67 vol-% MWCNT loading PANI/MWCNT nanocomposites and the diameter of the composites are approximately  $80 \pm 15 \text{ nm}$ ,  $75 \pm 10$ ,  $70 \pm 10$ , and  $65 \pm 15 \text{ nm}$ . As can be seen from Figure 55(b)-(e), the polyaniline favors the overall morphology of the composites. The presence of rough coating layer of PANI around the surface of MWCNT can be found in Figure 55(f) which depicts the morphology of PANI/MWCNT composite containing 3.39 vol-% MWCNT. It

can be observed that core-shell structures with diameter approximately  $180\pm 30$  are formed where filler (MWCNT) serves as the core and matrix (PANI) represents the shell with diameter  $65\pm 15$ nm. Like PANI/SWCNT nanocomposites, the aniline monomer is uniformly polymerized around the surface of MWCNT and forms the core-shell structures [202]. Figure 55(g) is confirming a mixed morphology of core-shell structures with diameter  $125\pm 20$ nm and PANI with  $45\pm 10$ nm for 4.78 vol-% MWCNT loading PANI/MWCNT composite. The FE-SEM images of 8.33 vol-% and 12.01 vol-% MWCNT loading PANI/MWCNT composites are displayed in Figure 55(h) and (i) respectively. The SEM characterization of these composites reveals a uniform wrapping of MWCNT by PANI forming core-shell nanostructured composites. The outer diameter of the core-shell in Figure 55(h) is  $90\pm 10$ nm while core-shell structures with outer diameter  $75\pm 10$ nm can be seen in Figure 55(i).

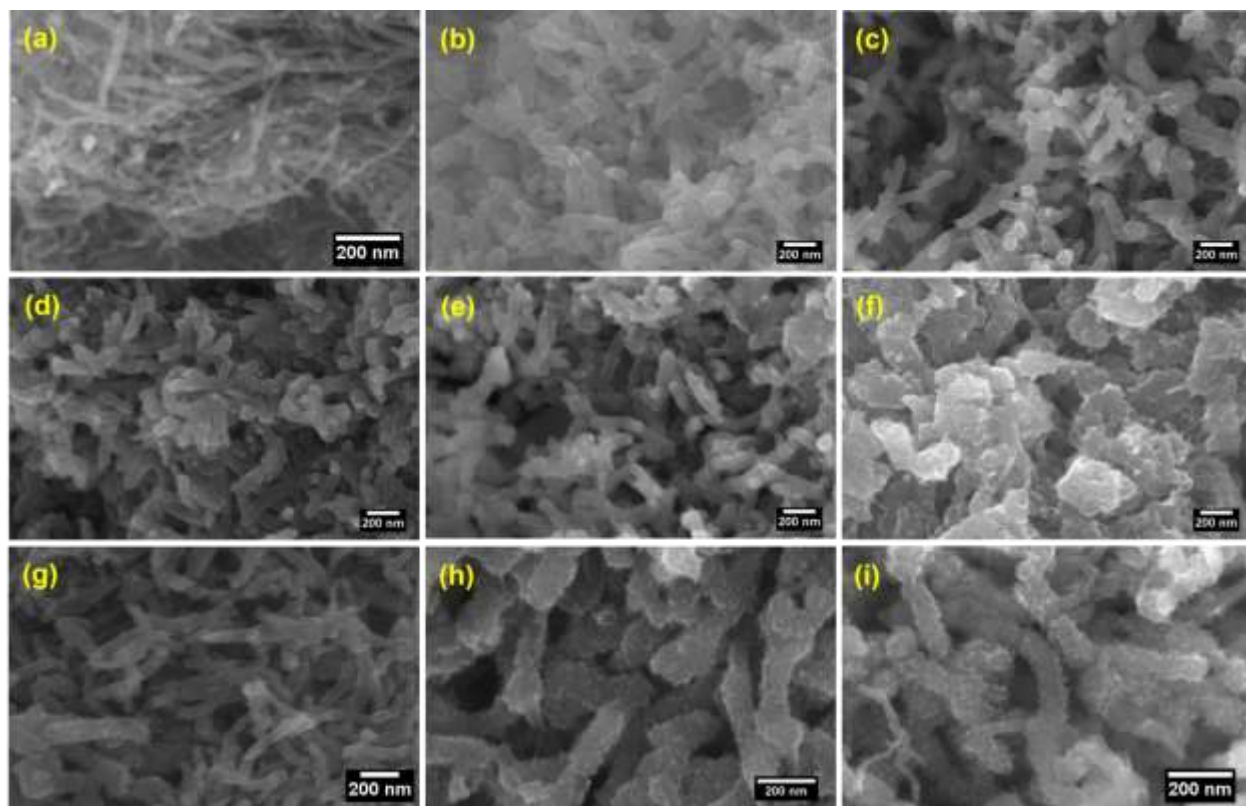


**Figure 55(a)-(i).** Images observed by FE-SEM for different concentrations of MWCNT loading (0 – 12.01 Vol-%) in PANI/MWCNT nanocomposites (scale bar 200nm).

The FE-SEM studies of the composites insure that the shell diameter depend on PANI content in the composites. Herein, when the PANI content in the composites is decreased, the coating thickness of the PANI on the MWCNT surface decreases. The result is found to be in good agreement with those reported in literature confirming the successfully prepared core-shell nanocomposites [105,203]. It was also reported that at very high filler content (>60 vol-%), the wrapping gets terminated and the matrix is deposited independently around the surface of the composite [204]. Such the formation mechanism of core-shell nanostructured composites is believed to involve a good interaction between PANI and MWCNT [7,105,202]. The interaction is caused by the presence of  $\pi$ - $\pi$  interactions between pristine MWCNT and aniline monomer [202]. Thus, the provided core-shell structures of the PANI/MWCNT composites can provide large interfacial space which can be an important parameter in properties of the composites.

#### 4.2.2.2 TEM investigation

In order to observe the fine morphology details of the PANI/MWCNT composites, TEM images were obtained. The TEM images of the composites are presented in Figure 56. For the PANI/MWCNT composite with 4.78 vol-% of MWCNT, the TEM images with scale bars of 500nm and 200nm are shown in Figure 56(a) and (b) respectively. The result also confirms that surfaces of MWCNT are covered by PANI and the outer diameter of the resultant core-shell structure is  $115\pm 15$  nm which is similar to SEM observation. Moreover, Figure 56(c) and (d) displays the morphology of the PANI/MWCNT composite containing 12.01 vol-% MWCNT with scale bars of 200nm and 100nm respectively. The outer diameter of the core-shell nanostructures in the composite is  $75\pm 10$  nm which is also match up with SEM examination. The result reveals a uniform coating of PANI with diameter ca. 25-35nm around the surface of MWCNT. However, it can be seen from the morphologies of the composites that the resulting composites all mainly have one-dimensional (1-D) core-shell structures and the result is in accord with previous reported studies [7,105,205]. It also can be observed that by changing ratio of MWCNT to PANI, the diameter as well as thickness of the PANI layer (shell) or diameter of the PANI can easily be controlled. For example, increasing the MWCNT content from 4.778 vol-

% to 12.01 vol-%, the diameter of PANI is decreased from  $ca.45\pm 10\text{nm}$  to  $ca.30\pm 5\text{nm}$  which was also evidenced by SEM investigation.

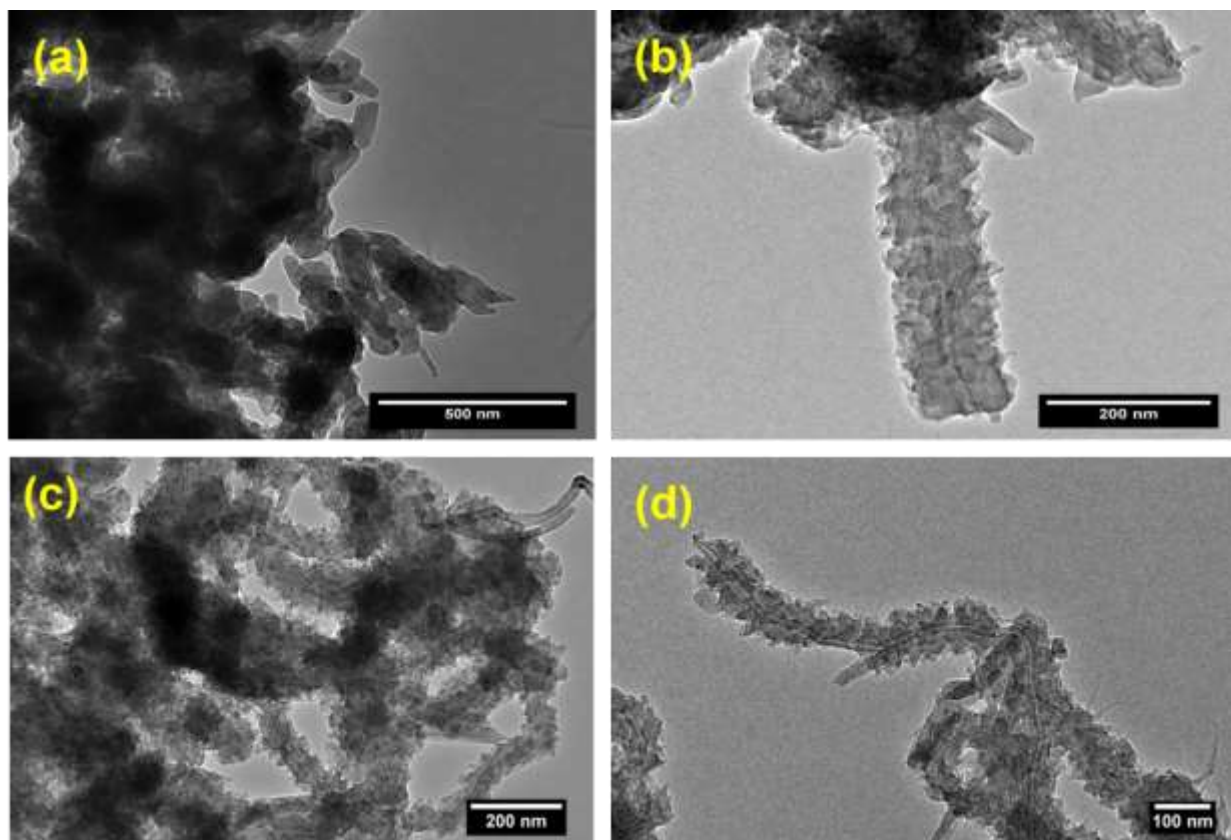


**Figure 56.** High resolution TEM images of PANI/MWCNT composite (4.78 vol-% MWCNT) with scale bars (a) 500 nm, (b) 200 nm, and PANI/MWCNT composite (12.01 vol-% MWCNT) with scale bars (c) 200 nm, and (d) 100 nm.

### 4.2.3. Electrical properties

Figure 57 displays the electrical conductivity of the as-prepared PANI/MWCNT composites as a function of MWCNT content. The composites exhibit a significant increase in electrical conductivity by the incorporation of MWCNT. The enhancement in the electrical conductivity is associated with increase in conductive pathways in the composites due to inclusion of conductive MWCNT. Therefore, the incorporation of electrical conducting filler (MWCNT) into polymer matrix (PANI) endows the composite with high electrical conductivity. When the value of electrical conductivity of PANI/MWCNT containing 0.00678 vol-% MWCNT is almost 1.69 S/m, the electrical conductivity reaches maximum value of  $471.4 \pm 20.8$  S/m for PANI/MWCNT composite filled with 12.01 vol-% MWCNT. Thus, it can be found that there is an enhancement in the electrical conductivity of about four orders of magnitude when increasing the loading fraction from 0.00678 vol-% to 12.01 vol-%. It can be clearly observed that the electrical conductivity of PANI/MWCNT composites is enhanced as function of MWCNT volume fraction. So, the electrical conductivity of the composites is analyzed by its dependence on volume fraction of MWCNT.

In order to investigate the electrical conductivity dependence with the volume fraction in PANI/MWCNT composites, mixing rule (upper bond, equation 2) is used to fit the experimental data of the electrical conductivity. The fitting curve is presented in the Figure 57. The electrical conductivity of filler ( $\sigma_{\text{filler}} \sim 3235$  S/m) and the electrical conductivity of matrix ( $\sigma_{\text{matrix}} \sim 0.05$  S/m) are obtained from the fit. The result evidences the electrical conductivity value ( $\sigma_{\text{filler}} = 3235$  S/m) of MWCNT as used in nanocomposites is lesser than MWCNT purchased from company. So there is clear gap in electrical conductivities of pure PANI ( $\sigma \sim 0.05$  S/m) and low MWCNT loading (0.0067 vol-%) PANI/MWCNT composite ( $\sigma \sim 1.69$  S/m) and pure MWCNT and MWCNT as used in the composites. Also, the Figure 57 depicts that the fits are quite well at low MWCNT volume fraction but there are some differences at high MWCNT volume fraction. This dispersion may arise from a modification of the PANI in the composites and charge transfer process in the composites resulting in new conducting network.



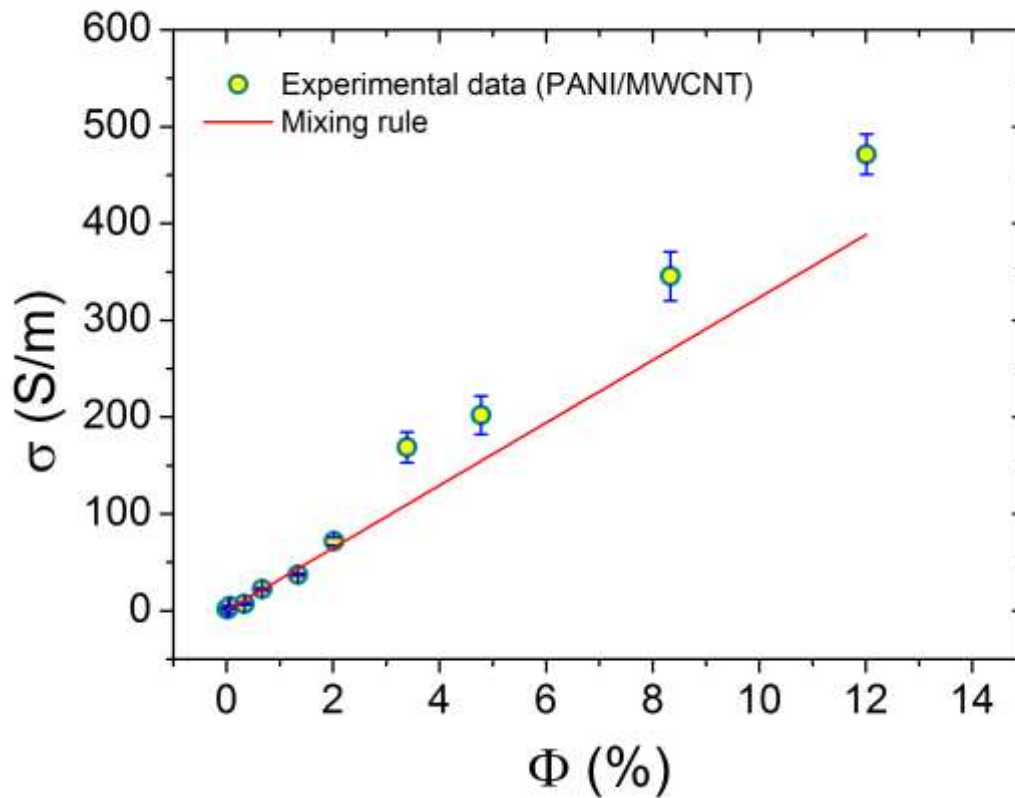


**Figure 57:** Electrical conductivity ( $\sigma$ ) of PANI/MWCNT nanocomposites as a function of vol-% SWCNT. Symbols are experimental data whereas red solid line is the best fit of equation 2.

Alternatively, this increase in conductivity of PANI/MWCNT composites can be interpreted by using percolation model which suggests that an infinite percolated network of electrical conductivity starts forming at low loading of MWCNT. To verify the percolation behavior, the experimental evaluation of the conductivity ( $\sigma$ ) is further analyzed with percolation critical power law which has been presented in equation 41 (Figure 58).



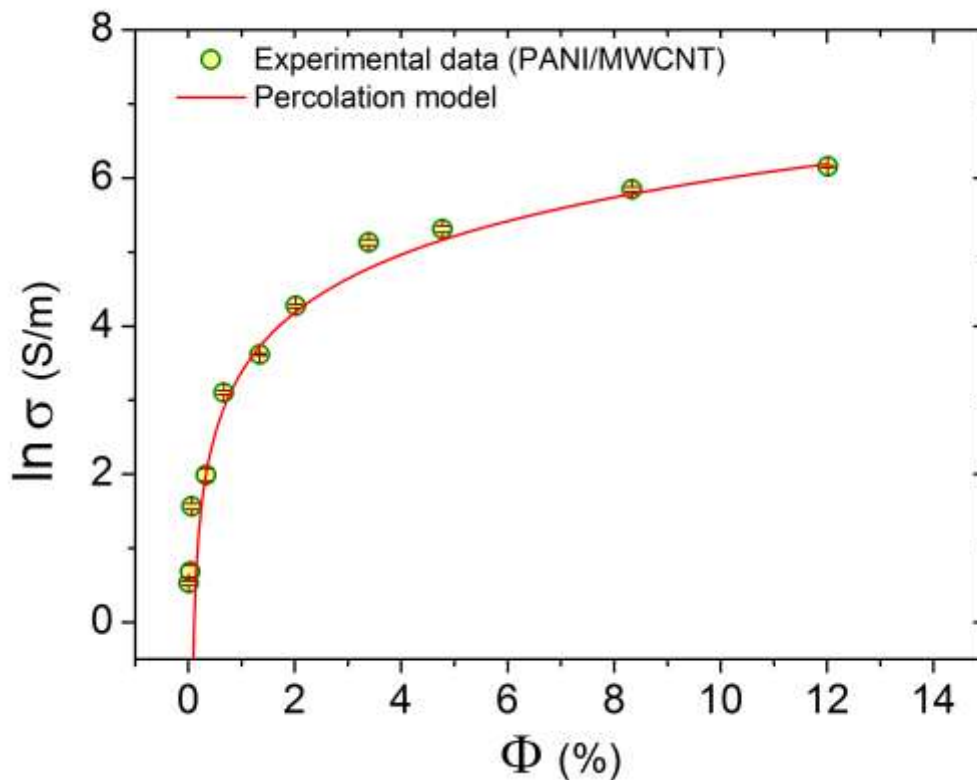


**Figure 58.** Electrical conductivity ( $\sigma$ ) of PANI/MWCNT nanocomposites as a function of vol-% MWCNT. Symbols are experimental data whereas red solid line is the fit of equation 41.

As shown in Figure 58, a good agreement is obtained between experimental data points and the fit (solid line). This analysis reveals that the electrical conductivity of PANI/MWCNT composites follows a percolation behavior. The result provides percolation threshold of  $\Phi_c=0.07$  vol-% (0.5 wt-%) and a critical exponent  $t$  of 1.11 for the PANI/MWCNT composites. The percolation threshold value is lower than those reported previously for PANI/MWCNT nanocomposites [103,104]. For example, E.N. Konyushenko *et. al.* [103] found a percolation threshold of 4 wt-% for PANI/MWCNT nanocomposites prepared by in situ polymerization. Our percolation threshold value is lower than expected for tube structured fillers (almost 16 vol-%) which reflects the nanotubular character of CNT in the composites. Also, Y. Long *et. al.* [104] estimated the percolation threshold in between 15 wt-% and 20 wt-% MWCNT with polypyrrole. The different values of percolation threshold in electrical conducting network can depend on the

different degrees of dispersion of the filler in the polymer matrix [103]. However, this result suggests that the distribution of MWCNT in the composites can significantly increase their utilization ratio in forming conducting network at low concentration of MWCNT.

Also, an expected linear relationship between  $\log(\sigma)$  vs  $\log(\Phi - \Phi_c)$  is obtained (Figure 59) and best linear fit provides the value of  $t = 1.11$ . The value of  $t$  is close to a the value of  $t=1.2$  reported by J.K.W. Sandler *et al.* [19] for epoxy composites based on aligned CVD-grown multi-wall carbon nanotubes [19]. And B. E. Kilbride *et al.* [206] reported the value of  $t = 1.36$  for dispersed multi-wall carbon nanotube-PVA and PmPV composites. Also many literatures shows a higher  $t$  value for MWCNT filled composites [195]. It concludes that the critical exponent ( $t$ ) for 1-D carbon nanotubes filled composites is higher than the present  $t$  value.

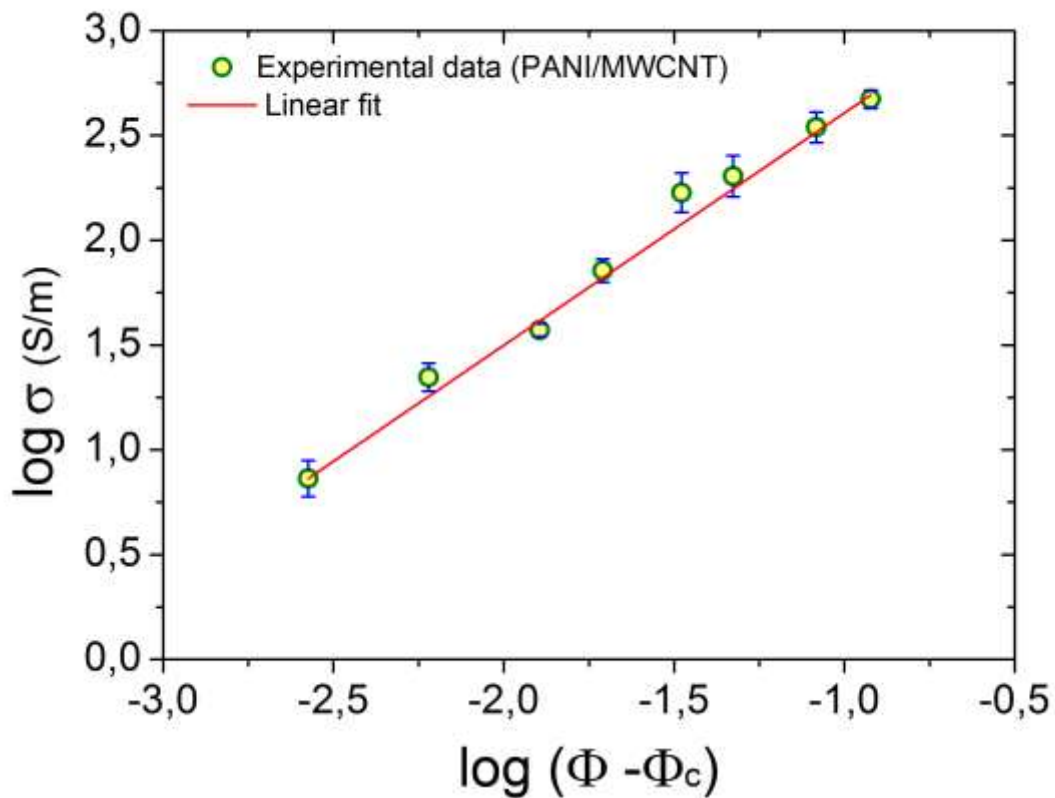


**Figure 59.** log-log plot of  $\sigma$  versus reduced volume fraction of MWCNT.

The low value of  $t$  can be attributed to the aggregation process of the fillers in samples. The agglomeration of MWCNT in the PANI/MWCNT composites is evidenced by SEM and TEM images (Figure 55 and 56). To induce effective conductive network this agglomeration process plays a key role. Also, the above analysis reveals that the formation of these conducting networks is not a true statistical percolation process based on the random distribution of individual high aspect ratio fillers. So, in this case, like the behavior of electrical conductivity of PANI/SWCNT composites the low exponent  $t$  does not reflect a reduction in system dimensionality. Also the low  $t$  value can be associated with the mutual attraction of the fillers in the composites. The conclusion is that the signature of electrical conductivity of PANI/MWCNT composites is strongly correlated with their morphology.

Furthermore, the analysis of the signature of electrical conductivity of PANI/MWCNT reveals that conducting state of PANI is changed in the composites where the PANI becomes more conducting than pure PANI. This modification can be interpreted by charge transfer process. M. Cochet et al. [108] reported the charge transfer process between the quinoid ring of the PANI and the MWCNT. Generally, there is the strong interfacial interaction of MWCNT with the PANI through  $\pi$ - $\pi$  interaction in PANI/MWCNT composites resulting in core-shell structures which is evidenced in the SEM and TEM images (Figure 55 and 56). In consequence, the strong  $\pi$ - $\pi$ -interaction between MWCNT and PANI increases the electrical conductivity of the composites. Like PANI/SWCNT, in such condition it can be expected that the mixing rule relation is better to explain the electrical conductivity behavior of the composites.

#### 4.2.4. Thermal properties

In this section, the thermal properties of PANI/MWCNT composites are investigated as a function of volume fraction of filler (MWCNT). Thermal diffusivity ( $\alpha$ ) and volumetric heat capacity ( $\rho C$ ) of the PANI/MWCNT composites were carried out in order to determine the thermal conductivity.

##### 4.2.4.1 Thermal diffusivity ( $\alpha$ )

The dependence of thermal diffusivity on filler (MWCNT) concentration for PANI/MWCNT nanocomposites is presented in Figure 60.

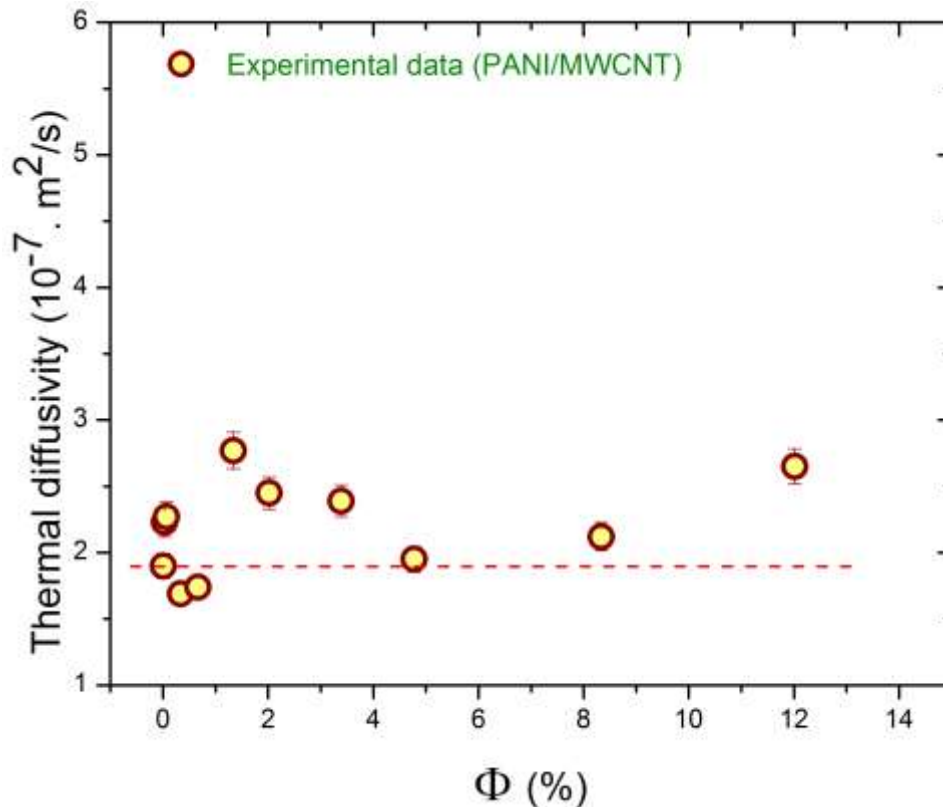


**Figure 60.** Thermal diffusivity ( $\alpha$ ) of PANI/MWCNT nanocomposites as a function of MWCNT content (vol-%). Dashed line is guides to the eyes.

As shown in Figure 60, thermal diffusivity of the composites is found between  $\sim 1.97 \times 10^{-7} \text{ m}^2\text{s}^{-1}$  and  $\sim 2.77 \times 10^{-7} \text{ m}^2\text{s}^{-1}$ . The result insures that the values of thermal diffusivity of the composites are larger than that of pure PANI ( $\sim 1.79 \times 10^{-7} \text{ m}^2\text{s}^{-1}$ ). This enhancement of thermal diffusivity is due to introduced thermal conducting path. More specifically, MWCNT has larger thermal conductivity than pure PANI. Thus, inclusion of MWCNT into matrix increases new thermal conducting paths in the composites which enhance the thermal diffusivity of the samples.

#### 4.2.4.2 Volumetric heat capacity ( $\rho C$ )

The evaluated volumetric heat capacity of the PANI/MWCNT composites as a function of MWCNT concentration is shown in Figure 61. The figure implies that the volumetric heat capacity is increased with increased MWCNT volume loading in comparison with pure PANI ( $1.04 \pm 0.07 \text{ MJm}^{-3}\text{K}^{-1}$ ). The present data also reveals that like electrical properties the value of pure PANI and the value ( $1.54 \text{ MJm}^{-3}\text{K}^{-1}$ ) of PANI/MWCNT for 0.0067 vol-% provide a great dispersion in the values of the volumetric heat capacity. This gap can arise from modified heat transport mechanism in PANI as used in the nanocomposites. Also as shown in Figure 61, it is notable that the volumetric heat suddenly drops to a value ( $\sim 0.95 \text{ MJm}^{-3}\text{K}^{-1}$ ) which is less than the value of PANI. As we have only one value which can be related to experimental errors, it is neglected for further interpretation. However, the maximum value of the volumetric heat capacity reaches up to  $1.85 \pm 0.10 \text{ MJm}^{-3}\text{K}^{-1}$  for PANI/MWCNT composites containing 8.33 vol-% MWCNT. This value is almost two times larger than that of pure PANI.

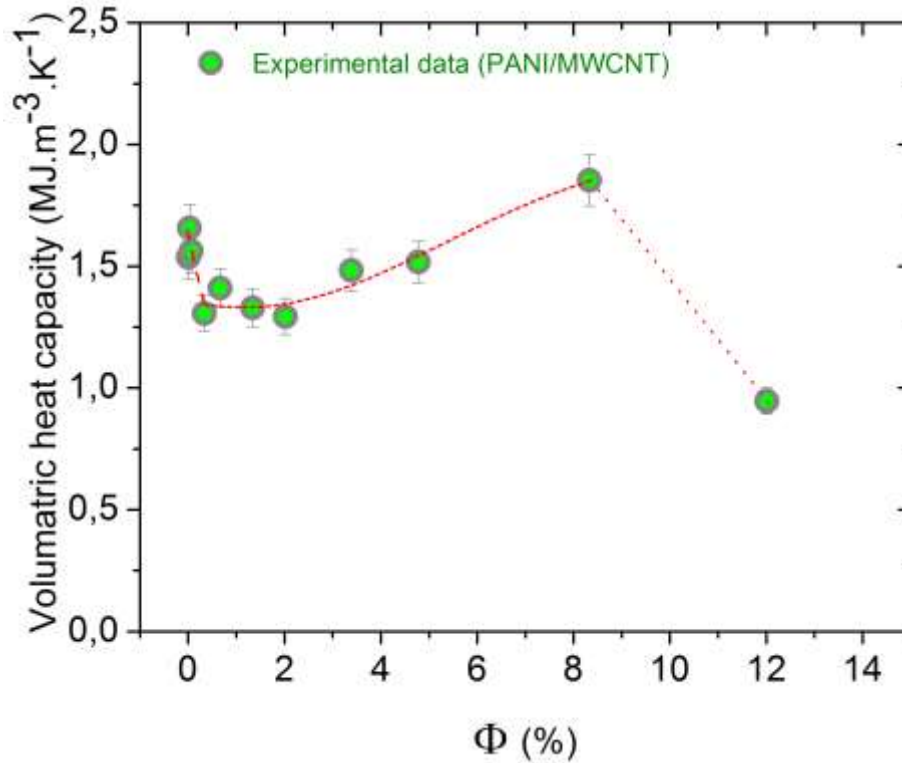


**Figure 61.** Volumetric heat capacity ( $\rho C$ ) of PANI/MWCNT nanocomposites as a function of MWCNT content (vol-%). Dashed lines are guides to the eyes.

#### 4.2.4.3 Thermal conductivity ( $k$ )

The thermal conductivity of the PANI/MWCNT composites is calculated by using equation 42 and presented in Figure 62. However, values of thermal conductivities are noted to be in between 0.22 W/m.K (0.33 vol-% MWCNT PANI/MWCNT composite) and 0.39 W/m.K (8.33 vol-% MWCNT PANI/MWCNT composite). It also is observed that the thermal conductivity is almost 0.29 W/m.K for very low MWCNT loading (0.0067 vol-%). So there is 0.1 W/m.K enhancement from the value (0.19 W/m.K) of thermal conductivity for pure PANI. This separation can arise from volumetric heat capacity contribution.

However, the maximum thermal conductivity enhancement ( $TCE\% = ((k - k_{PANI}) \times 100 / k_{PANI})$ ) 110% is obtained at 8.33 vol-% MWCNT loading whereas the thermal conductivity of pure PANI  $k_{PANI}$  is 0.19 W/m.K. Such low values of thermal conductivities

suggest that matrix (polymer) strongly influences the thermal conductivity of the composites. The result reveals that the thermal conductivity is almost insensitive to inclusion of fillers. The low thermal conductivity values can meet the requirements for thermoelectric applications. Further analysis shows that like PANI/SWCNT composites, there is no percolation behavior in thermal conductivity. In summary, although the thermal conductivity values of PANI/MWCNT composites are very low, the values can be considered for good thermoelectric as well as good heat storage performance.

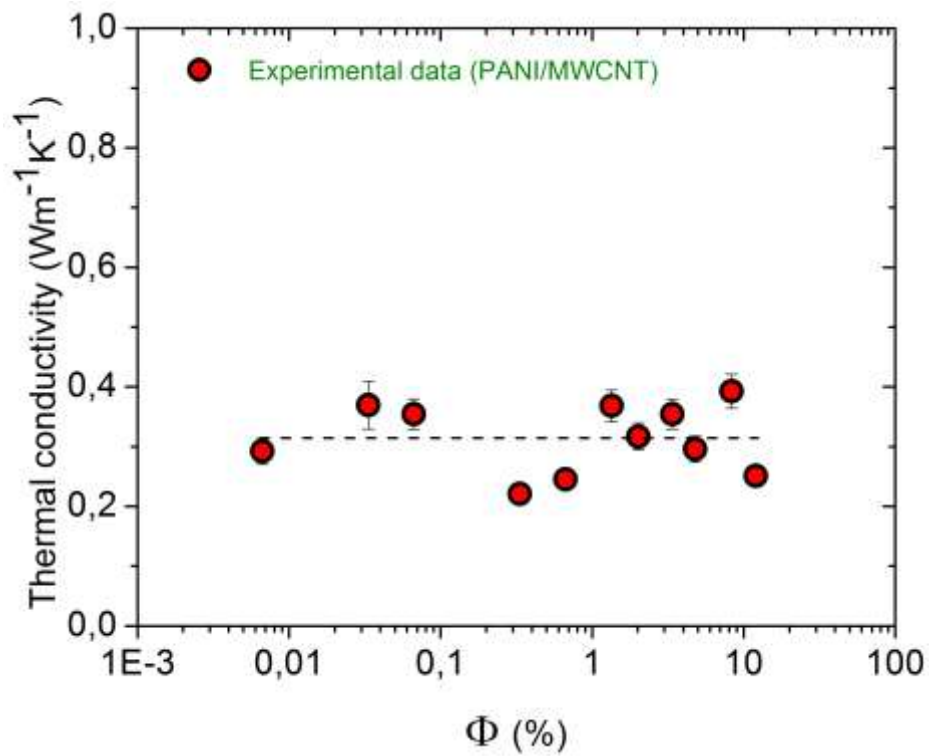


**Figure 62.** Thermal conductivity ( $k$ ) of PANI/MWCNT nanocomposites as a function of MWCNT content (vol-%). Dashed line is guides to the eyes.

#### 4.2.5. Seebeck coefficient (S) and power factor (PF)

Figure 62 shows the experimental data of the Seebeck coefficient of PANI/MWCNT composites as a function of MWCNT volume fraction. As shown in Figure 63, the positive Seebeck coefficient of the composites indicates that the composites are p-type semiconductor in which holes are the dominant contributors to electrical conductivity. The Seebeck coefficient value for pure PANI and the Seebeck coefficient value ( $7.54\mu\text{V/K}$ ) for very low filler loading PANI/MWCNT composite (0.0067 vol-%) show a dispersion. This signature can be occurred due to modified conducting state of PANI in the composites forms which is interpreted in electrical properties of PANI/MWCNT.

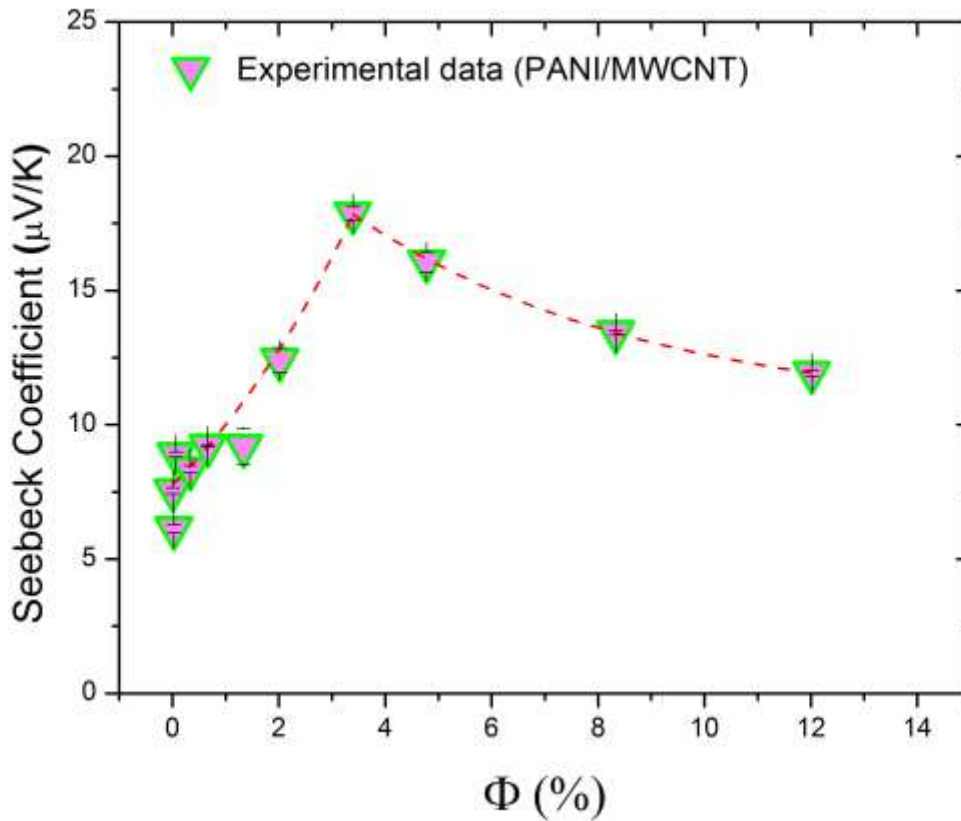


**Figure 63.** Experimental evaluation of Seebeck coefficient (S) of PANI/MWCNT composites as function of MWCNT concentration (vol-%). Dashed lines are guides to the eyes.



The Figure **63** displays an interesting observation of Seebeck coefficient of the composites. The result reveals two different behaviors of Seebeck coefficient as a function of MWCNT loading (vol-%). On hand, up to 3.39 vol-% MWCNT loading, the Seebeck coefficient shows great increase with addition of filler into matrix. The obtained maximum Seebeck coefficient is to be  $\sim 17.86 \mu\text{V/K}$  for PANI/MWCNT composite filled with 3.39 vol-% MWCNT. The value is almost 2 times larger than pure PANI ( $9.77 \pm 0.17 \mu\text{V/K}$ ). On the other hand, the opposite trend is observed in the Seebeck coefficient at high concentration of MWCNT ( $>3.39$  vol-%).

The former behavior in which the Seebeck coefficient and electrical conductivity of the composites are simultaneously increased which is shown in Figure **64**, can be interpreted in same way like Seebeck coefficient signature of PANI/SWCNT composites. It can be seen in equation **22** that the Seebeck coefficient is directly proportional to charge carrier mobility originating from strong  $\pi$ - $\pi$  interaction between PANI and MWCNT. Herein, inclusion of MWCNT into PANI increases the carrier mobility in the composites at low concentration of MWCNT. So, the Seebeck is dominated by carrier mobility which gives an enhancement of Seebeck coefficient of the PANI/MWCNT composites. The latter one can be explained by a conventional model based on the band theory or the electron-phonon scattering [175]. Also equation **22** shows that the Seebeck coefficient is inversely proportional to effective electrical conductivity. It can be assumed that the charge carrier concentration is increased with increase MWCNT loading into matrix and the electron-phonon scattering reduce the carrier mobility in the composites. Thus, the Seebeck coefficient is decreased as a function of MWCNT loading at higher concentration. As a consequence, it can be said that in PANI/MWCNT composites, both carrier concentration and carrier mobility play important roles in Seebeck coefficient of the composites.

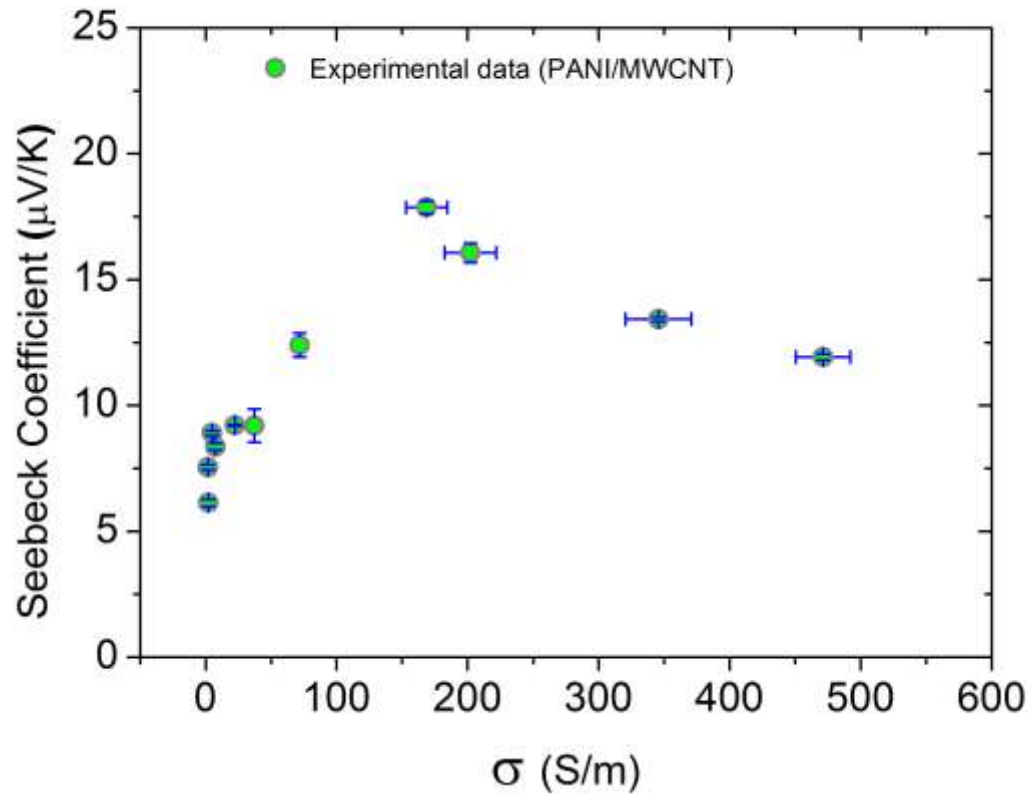


**Figure 64.** Experimental evaluation of Seebeck coefficient (S) of PANI/MWCNT composites as function of electrical conductivity.

By using equation 43, the power factor (PF) of PANI/MWCNT nanocomposites is calculated and depicted in Figure 65. Although the Seebeck coefficient of the composites shows two different trends, the PF of the composites is enhanced as a function of MWCNT loading due to the significant increment in electrical conductivity of the composites. It can be observed that the PF of the composites is increased rapidly at low loading of MWCNT (<3.39 vol-%) because of enhancement in both  $S^2$  and  $\sigma$  of the composites. But at high loading of MWCNT (>3.39 vol-%), the PF is almost constant. The result can be explained by the two different signatures in electrical conductivity and Seebeck coefficient. As shown in Figure 57 and Figure 65, the electrical conductivity is increased at high loading MWCNT while Seebeck coefficient is decreased. So, the calculated value of  $S^2 \sigma$  evidences that the PF is almost constant at high concentration of MWCNT in the composites. The maximum power factor ( $0.067 \pm 0.004 \mu\text{Wm}^{-1}\text{K}^{-2}$ ) is observed in

PANI/MWCNT composite containing 12.01 vol-% MWCNT. This value is four orders of magnitude larger than that of pure PANI ( $\sim 4.77 \times 10^{-6} \mu\text{Wm}^{-1}\text{K}^{-2}$ ).

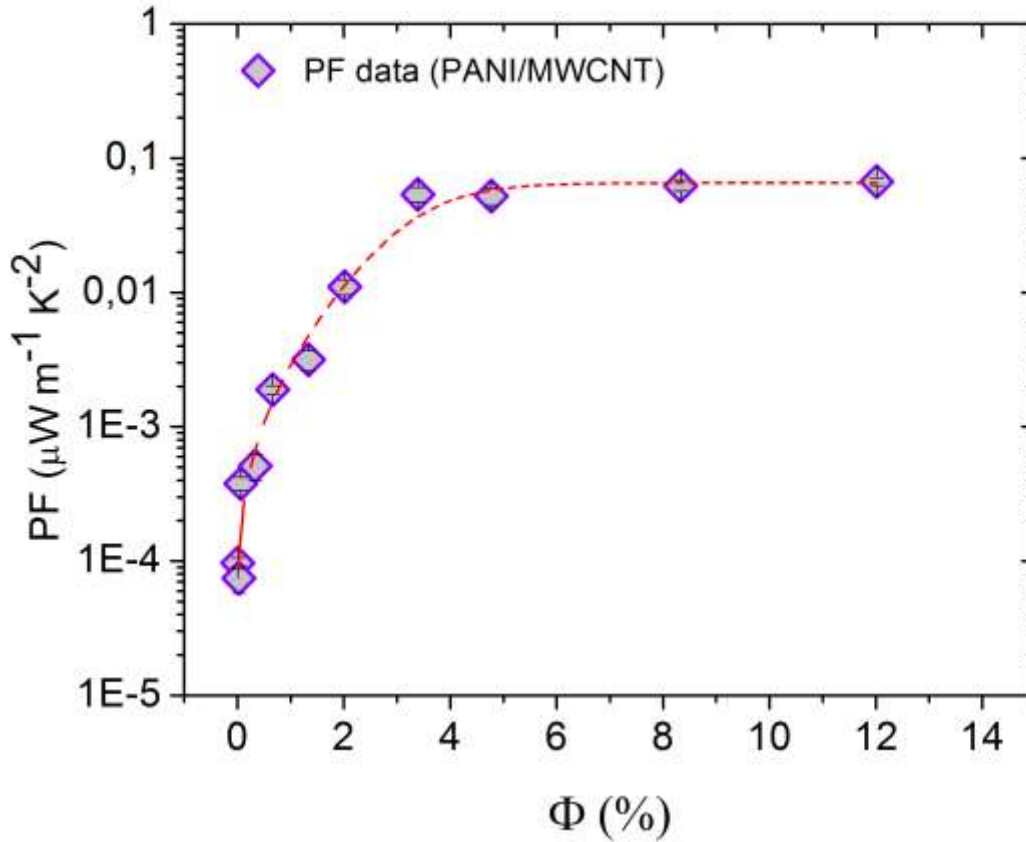


**Figure 65.** Experimental evaluation of Power factor (PF) as a function of vol-% MWCNT. Dashed lines are guides to the eyes.

#### 4.2.6. Thermoelectric properties

The figure of merit  $ZT$  of PANI/MWCNT composites is calculated at  $T=300\text{K}$  via equation 23. The  $ZT$  values of the composites are presented in Figure 66. The Figure shows that with the inclusion of fillers into matrix, the  $ZT$  is increased. The result reveals that the signature of  $ZT$  for PANI/MWCNT is very similar to the power factor characteristic of the composites.

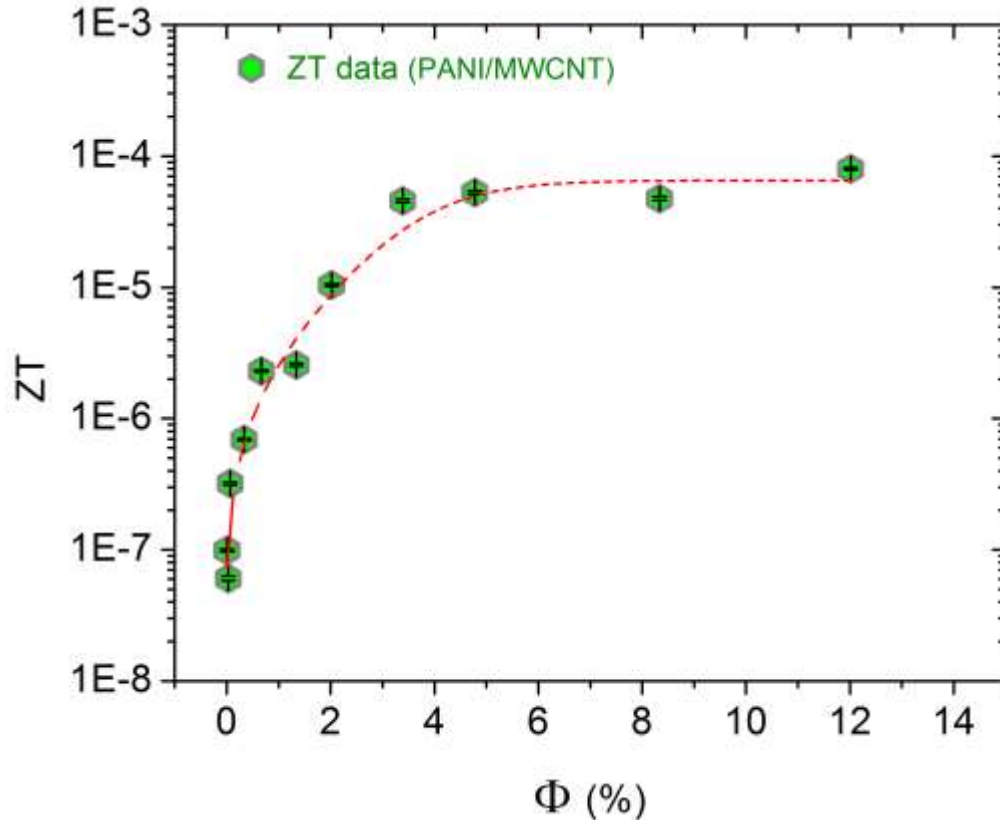


**Figure 66.** Thermoelectric performance (ZT) of PANI/MWCNT nanocomposite. Dashed line is guides to the eyes.

At lower volume fraction of MWCNT (<3.39 vol-%), the ZT increases sharply where the enhancement is quite slow above that concentration. The ZT value of 0.0067 vol-% PANI/MWCNT is found to be  $9.91 \times 10^{-9}$  and reaches up to  $4.56 \times 10^{-5}$  for 3.39 vol-% PANI/MWCNT. Thus, in the range between 0.0067 vol-% and 3.39 vol-% MWCNT loading, the ZT shows the improvement of four order of magnitude. Furthermore, above 3.39 vol-% MWCNT, the ZT value is increased less than one order of magnitude. The maximum ZT value  $8.02 \times 10^{-5}$  is obtained at 12.01 vol-% MWCNT loading. This result suggests that the low thermal conductivity (< 0.5 W/m.K) of composites does not strongly contribute in the figure of merit. Generally, the enhancement of thermoelectric performance can be attributed to the large improvement of the electrical conductivity of the composites. However, the maximum thermoelectric performance is four orders of magnitude larger than that of pure PANI ( $7.71 \times 10^{-9}$ ).



### 4.3. Reduced graphene oxide based polymer nanocomposites

We discuss here the properties of 2-D nano-fillers based polymer nanostructured composites. Reduced graphene oxide (RGO) has been used as nano-fillers whereas polyaniline (PANI) has been used as matrix. The chemically synthesized PANI/RGO composites ranging from 0.005 wt-% to 20.9 wt-% RGO content are investigated. Structural, morphological, electrical, thermal, and thermoelectric properties of the composites as a function of volume fraction of RGO are discussed. In addition, the through plane electrical conductivity of PANI/RGO nanohybrids investigated by broadband dielectric spectroscopy are highlighted.

#### 4.3.1. Density

The density of the prepared pellets of the PANI/RGO nanocomposites was determined by taking the ratio of measured mass to volume. The plot between density of the pellets and RGO weight percentage (wt-%) is presented in Figure **67**. The experimental result gives an estimation of density of the PANI ( $=1.24 \text{ g/cm}^3$ ) and RGO ( $= 2.24 \text{ g/cm}^3$ ). For further study of the composites, volume percentage (vol-%) is determined by using the equation **40**.

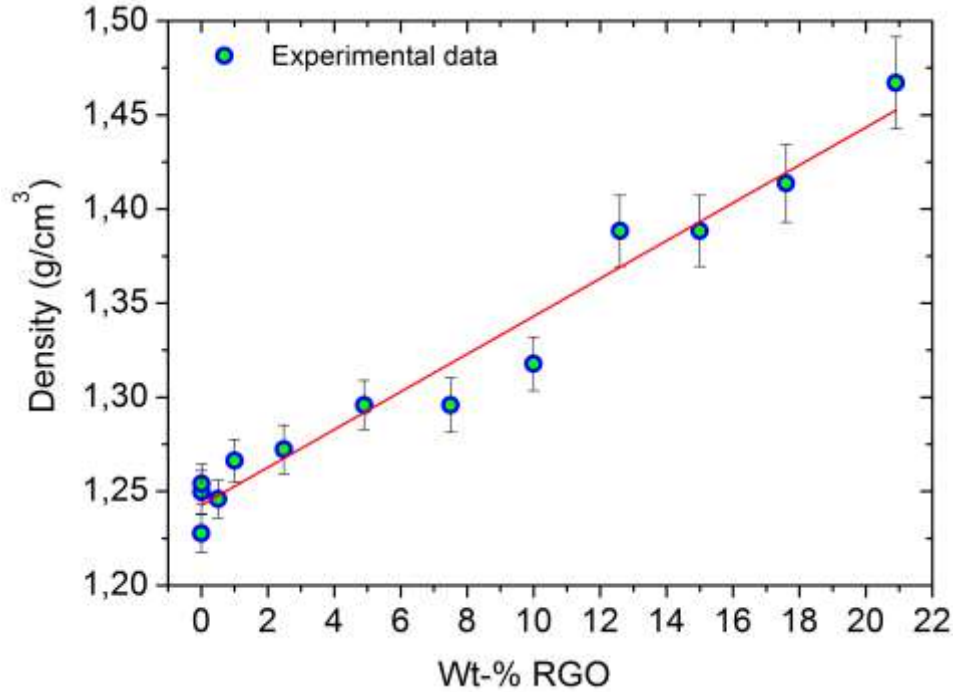


**Figure 67.** Density ( $\rho$ ) of pellets of PANI/RGO nanocomposites as a function of RGO fraction. The red solid line is the linear fit.

## 4.3.2. Morphological and structural characterizations

### 4.3.2.1 SEM Investigation

The morphological investigations of pristine RGO, and PANI/RGO composites were performed by FE-SEM. Figure 68(a) – (i) depict the SEM images for PANI/RGO composites. Micrograph 68(a) shows the typical nanosheet morphology of the as-received reduced graphene oxide. In Figure 68(b)-(e) the morphology of PANI/RGO composites is confirming the presence of RGO- and PANI-rich domains. Figure 68(e) shows a combination of platelets with sizes ranging from 0.5 to 2  $\mu\text{m}$  and nanofibers with diameter of ca.  $84 \pm 20$  nm.

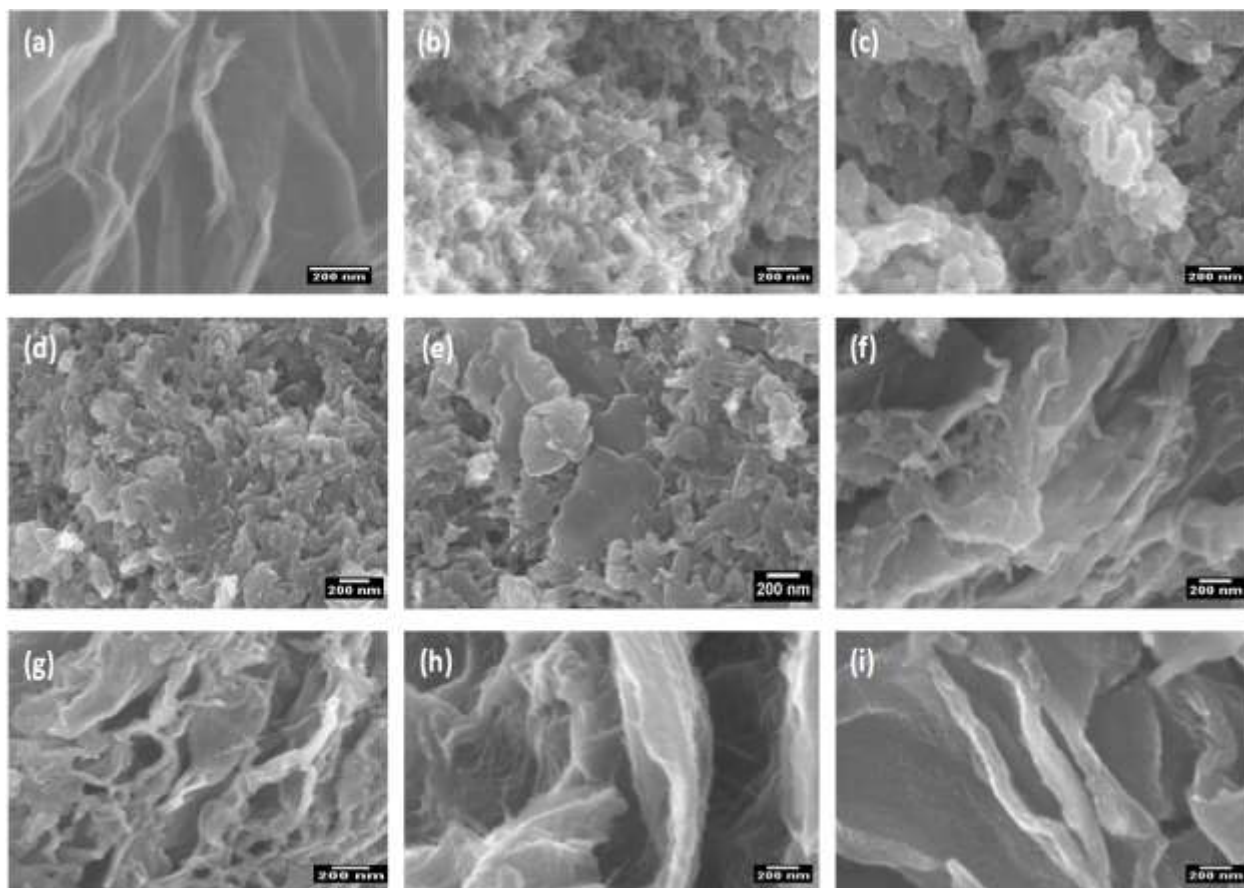


**Figure 68.** Images observed by FE-SEM for (a) RGO, (b) 0.028 vol-%, (c) 0.28 vol-%, (d) 0.56 vol-%, (e) 2.77 vol-%, (f) 7.39 vol-%, (g) 8.90 vol-%, (h) 10.57 vol-%, and (i) 12.76 vol-%, respectively.

It can be seen that with increasing RGO contents the composites exhibit predominantly a platelet-like morphology (Figure 68(f)-(i)). The presented micrographs show that the RGO sheets have an average size of 0.5-3 $\mu$ m which is in agreement with the manufacturer's specifications. This confirms that RGO structural integrity is essentially unaffected by the experimental protocol. These sheets act as 2-D templates for aniline monomer adsorptions at the initial stage of polymerization. This physisorption of monomers and ensuing nucleation of oligomers are most likely favoured by  $\pi$ - $\pi$  interactions between the basal planes of RGO and anilines, thereby promoting the polymerization of anilines along both sides of the 2-D plane of RGO. For example, the thickness of the resulting platelets is from about 35 to 50 nm (Figure 68(i))



indicating that each side of the RGO sheet (0.5-3 nm thick according to the manufacturer) is covered by a PANI layer with a thickness of ca. 15-20 nm.

#### 4.3.2.2 TEM investigation

For the further insight of the morphology, the composites were investigated by TEM. Figure 69 shows the high resolution TEM images of the nanohybrids. The TEM image of the 5.79 vol-% is presented in Figure 69(a) where Figure 69(b)-(c) are TEM images of 12.76 vol-% PANI/RGO composite with different scale bars.

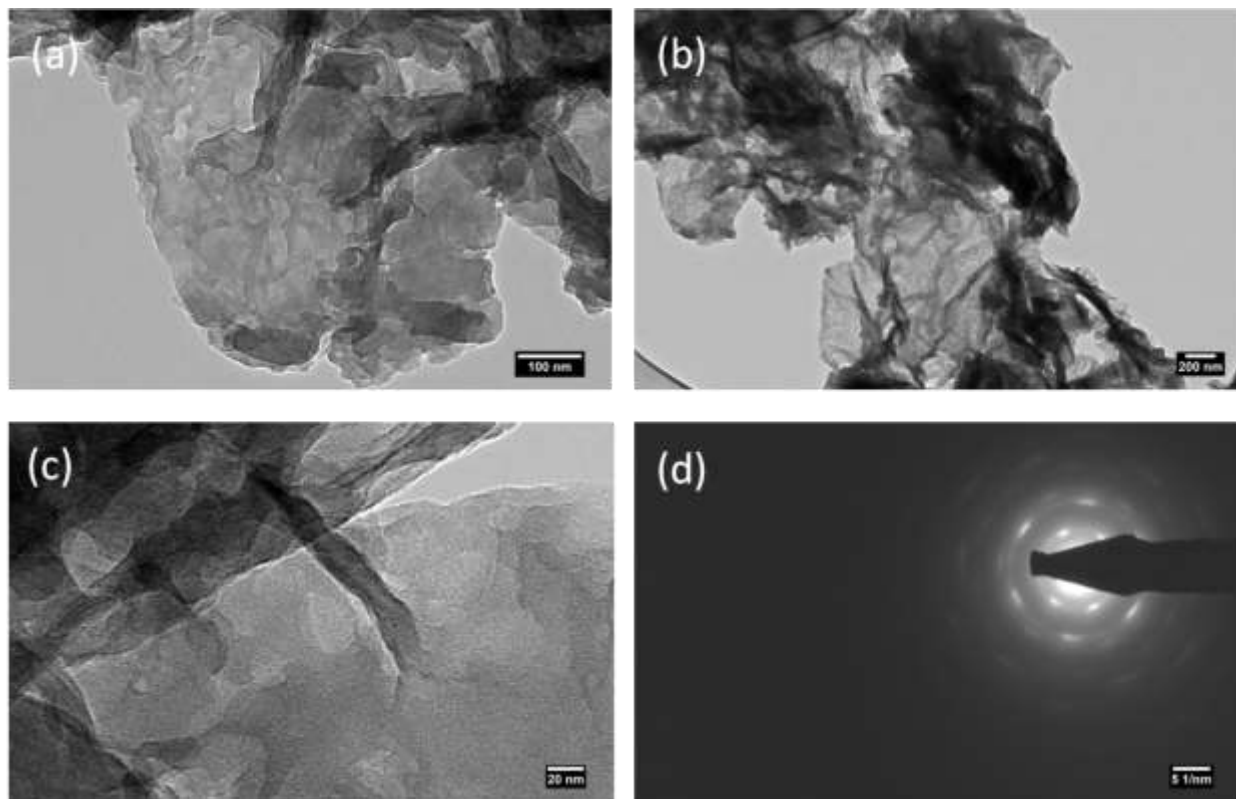


**Figure 69.** High resolution TEM images of (a) 5.78 vol-% (b) 12.76 vol-% with scale bars 200 nm, (c) 12.76 vol-% with scale bars 50 nm, and (d) electron diffraction (scale bar 5 nm<sup>-1</sup>).

The TEM investigation reveals that the graphene sheets are covered with a PANI layer resulting in a lamellar morphology which is consistent with SEM investigations. In Figure 69(d) the electron diffraction data show six fold symmetric diffraction points confirming the hexagonal crystalline structure of the graphitic planes of RGO. However, it should be pointed out that the orientational disorder of composites is evident from the lattice fringe patterns as seen in the diffraction pattern. This feature can be associated with a combination of the structural signatures of semi-crystalline PANI and multilayered graphene. To further address this point, detailed X-ray diffraction and Raman spectroscopy investigations are presented below.

#### 4.3.2.3 Raman spectra analysis

To investigate the interactions between PANI and RGO, Raman spectroscopy was performed. The Raman spectra of RGO, PANI, and PANI/RGO composites are presented in Figure 70. The vibrational modes were obtained from fitting the experimental data (Figure 70). The spectrum of pure PANI shows the typical bands of the doped polymer including C-H bending of the quinoid and benzenoid ring at 1145 and 1169  $\text{cm}^{-1}$ , respectively; symmetric C-N stretching at 1222  $\text{cm}^{-1}$ ; C-N<sup>+</sup> stretching at 1340  $\text{cm}^{-1}$ ; C=N stretching of the quinoid ring at 1460  $\text{cm}^{-1}$  and 1500  $\text{cm}^{-1}$ ; and C=C stretching of the quinoid rings at 1591  $\text{cm}^{-1}$ . The characteristic peaks of the materials are in good agreement with previous reports confirming that the synthesized product contains polyaniline [7,207]. The spectrum of RGO exhibits the two typical bands at 1347 and 1597  $\text{cm}^{-1}$ , which are assigned to the D band (disorder-induced band) and the G band (in-plane stretching mode), respectively [208].

All spectra of the RGO-reinforced PANI nanocomposites exhibit the characteristic bands of each constituent. It is interesting to note that the intensity of the vibration at 1460  $\text{cm}^{-1}$  (C=N quinoid stretching) increases with increasing RGO content demonstrating that incorporation of RGO in the composite promotes the quinoid form of PANI, i.e., a conjugated planar geometry is favored. This is further supported by taking the ratio of the intensity of C-H bending vibration in quinoid unit (1145  $\text{cm}^{-1}$ ) over that of the corresponding benzenoid (1169  $\text{cm}^{-1}$ ) [7,207].

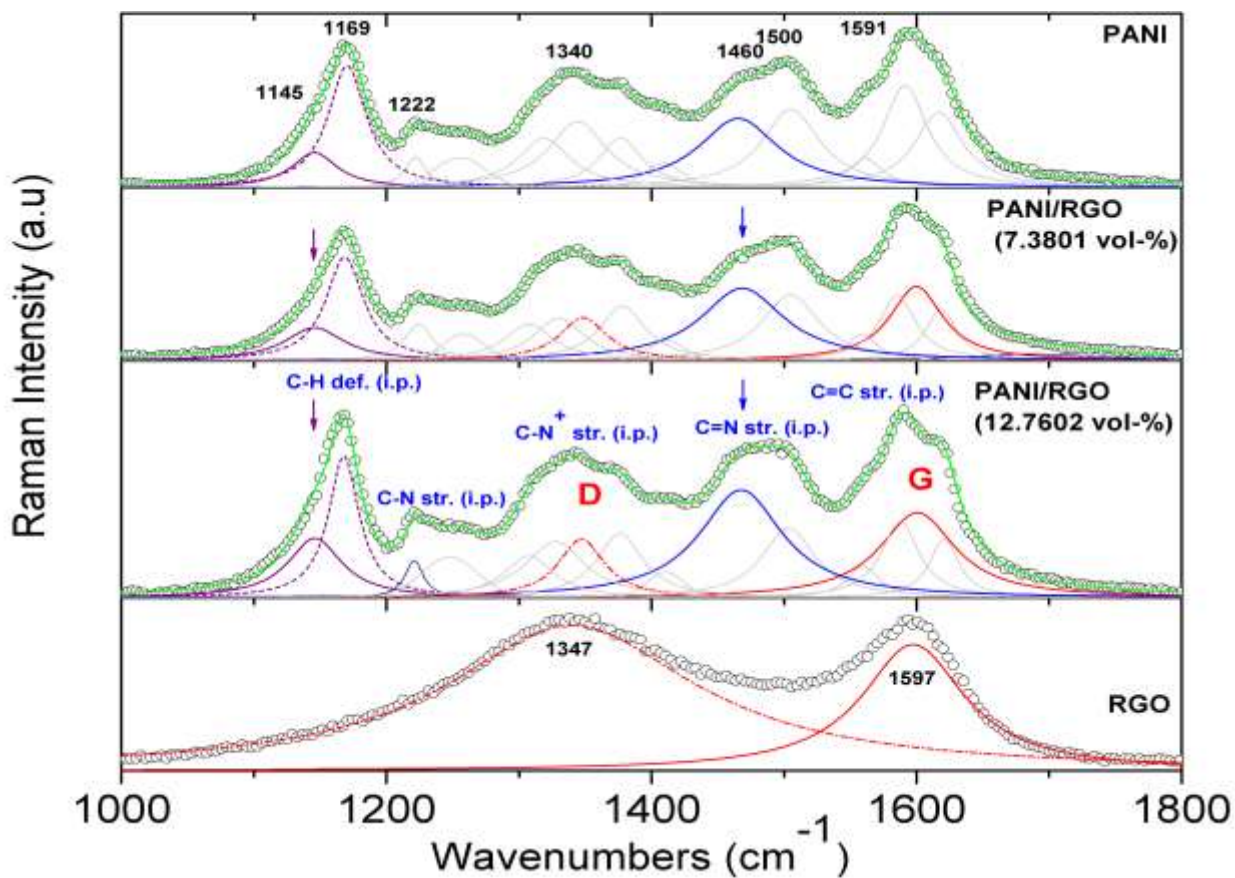


**Figure 70.** Raman spectrum of RGO, PANI and PANI/RGO nanocomposites. Symbols are experimental data whereas solid and dashed lines are retrieved from fitting.

That is with respect to pure PANI, the quinoid/benzenoid integral ratio (1145/1169) increases from ca. 0.24 (pure PANI) to 0.50 (7.3901 vol-% RGO) and in turn reaches 0.72 (12.7602 vol-% RGO) which clearly evidences an important increase of the quinoid fraction in all hybrids. The quinoid rings in the nanocomposites are obviously stabilized through their  $\pi$ - $\pi$  interactions with the basal planes of RGO. Thus, the RGO templates induce a greater polymer chain ordering in the hybrids which improves physical interactions and charge transfer processes between RGO and PANI. This finding corroborates with similar results in which graphene can engage in charge transfer interactions with intrinsically conducting polymers [209] or neutral molecules [210,211].

### 4.3.2.4 XRD analysis

In order to insight the structural properties of RGO, PANI, and PANI/RGO nanocomposites X-ray diffraction was carried out. Figure 71 presents the X-ray diffraction studies of PANI/RGO composites and their individual constituents.

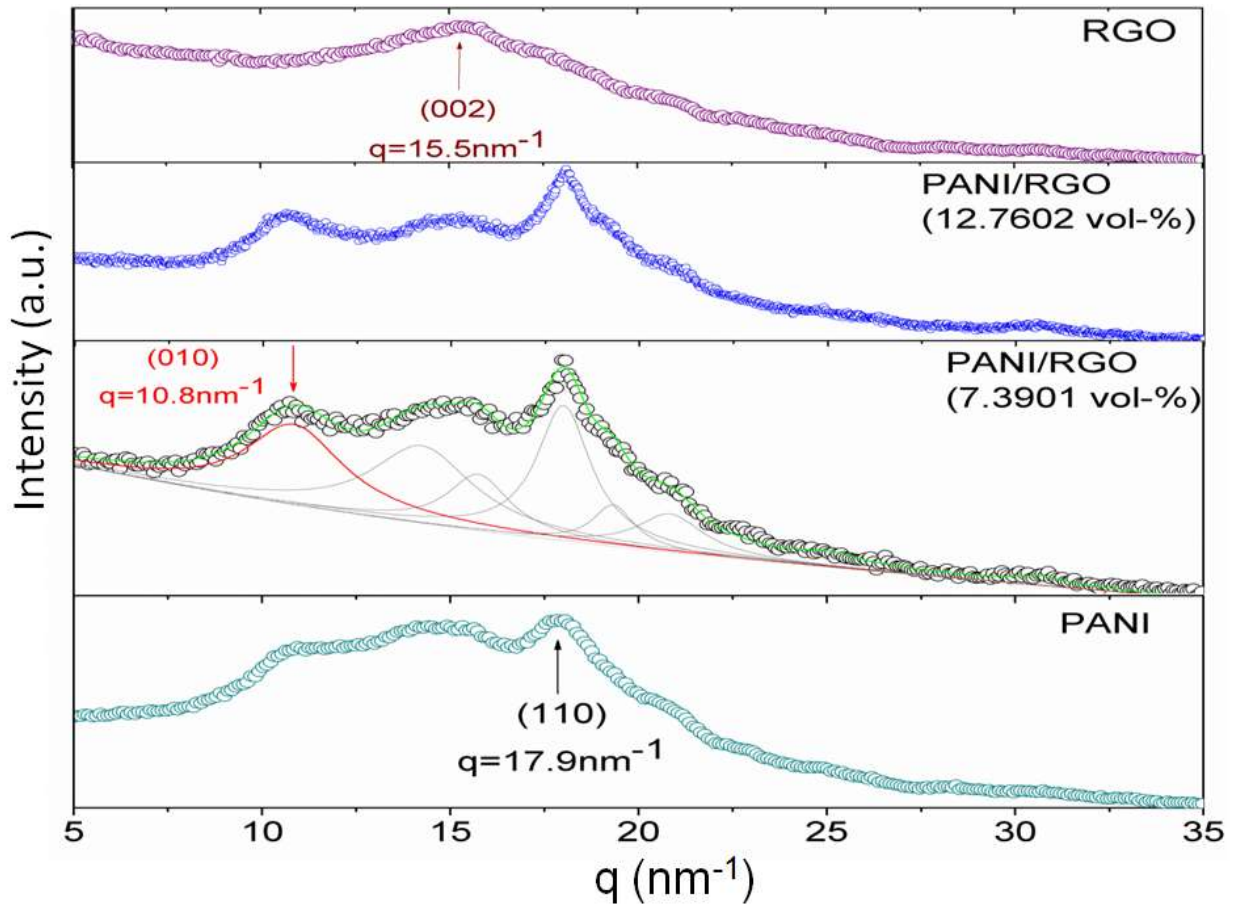


**Figure 71.** XRD of RGO, PANI and PANI/RGO nanocomposites. Symbols are experimental data whereas solid and dashed lines are retrieved from fitting.

As shown in the Figure 71, pristine RGO exhibits a broad peak centred at  $q=15.5\pm 0.5 \text{ nm}^{-1}$ , corresponding to a distance of  $d=2\pi/q = 0.405\pm 0.008 \text{ nm}$ . This value is typical of disordered carbon materials with spacing (0.39 nm) [212]. In general, pure PANI exhibits both amorphous and crystalline structures. Here, a broad peak is observed from  $q=10 \text{ nm}^{-1}$  to  $q=25 \text{ nm}^{-1}$

indicating mainly an amorphous PANI morphology along with a sharper peak at  $17.9 \text{ nm}^{-1}$  which is associated with the (110) reflection of crystallographic planes of the orthorhombic structure reported for semi-crystalline PANI [211,213,214]. Figure 71 shows that with increasing RGO fraction, the diffraction peaks related to PANI domains at  $q=10.8 \text{ nm}^{-1}$  ((010) reflection) and  $q=17.9 \text{ nm}^{-1}$  ((110) reflection) become more intense in the PANI/RGO diffractograms.

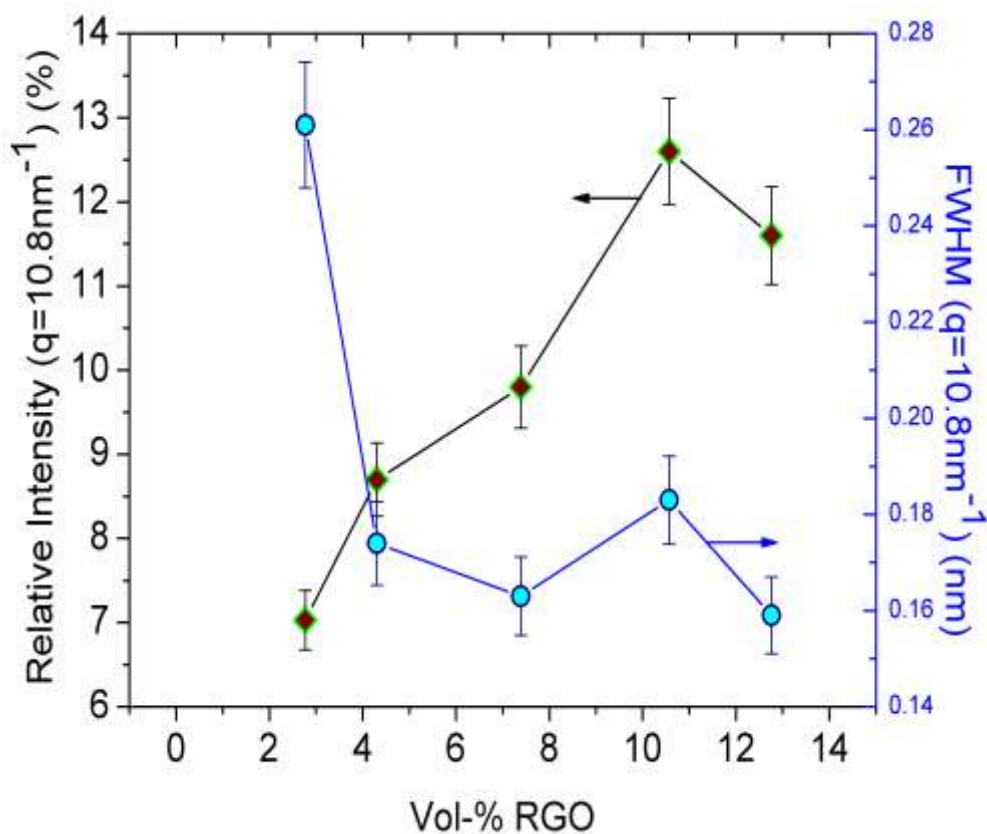


**Figure 72.** FWHM and relative intensity of PANI/RGO nanocomposites. Symbols are experimental data.

In order to quantitatively assess this result, the diffractograms were fitted with Lorentzian curves. Specifically, the peak at  $q=10.8 \text{ nm}^{-1}$ , which does not overlap with one of RGO, was used to track the evolution of the crystallinity of PANI in the nanocomposites. Its relative intensity and width at half maximum (FWHM) are plotted versus volume fraction of RGO in Figure 72 from which it can be seen that the relative intensity increases with RGO content while the FWHM decreases. Thus, the incorporation of RGO in the composites enhances the crystallinity

of PANI leading to more organized domains and longer correlation lengths ( $2.3\text{nm} < L < 3.5\text{nm}$ ) as calculated from the Scherrer formula (equation 27) [213,215]. These results demonstrate that RGO acts as templates for PANI growth and improve the PANI crystallinity, in particular in the (010) direction, i.e., parallel to the benzene rings of PANI chains. Thus, the improved PANI crystallinity in the composites reflects a polymer chain growth mechanism taking place predominantly along the (010). This added feature re-enforces the afore-mentioned strong quinoid (PANI)-basal plane (RGO)  $\pi$ - $\pi$  interactions as evidenced by Raman work.

### 4.3.3. Electrical properties

For PANI/RGO nanocomposites, the electrical properties are studied by using two different methods. In plane electrical conductivity was determined by using four-probe method and through plane electrical conductivity was performed by Broadband dielectric spectroscopy (BDR).

#### 4.3.3.1 Electrical properties characterized by in plane measurement

The evolution of the electrical conductivity ( $\sigma$ ) of PANI/RGO nanohybrids as a function of RGO volume fraction is presented in Figure 73. The figure shows that the electrical conductivity of the composites increases with adding of RGO nano-fillers. The maximum value  $192 \pm 20$  S/m of the electrical conductivity is obtained for PANI/RGO composite filled with 12.76 vol-% RGO while the value of the pure PANI is  $0.05 \pm 0.01$  S/m. Thus, it can be observed that there is an enhancement in the electrical conductivity of about four orders of magnitude.

To analyze the experimental data, the mixing rule (equation 2) is used to fit which is presented in Figure 73. The value of electrical conductivity of RGO ( $\sigma_{\text{matrix}} \sim 1463$  S/m) is obtained from the fit. The result shows that the electrical conductivity value of RGO as used in nanocomposites, which is much lower than RGO purchased from company. The finding indicates the modified conductive behavior of PANI and RGO. Also the computed low value of



RGO suggests that may be an infinite percolated network, formed with RGO loading, of electrical conductivity is responsible for large enhancement (four orders of magnitude).

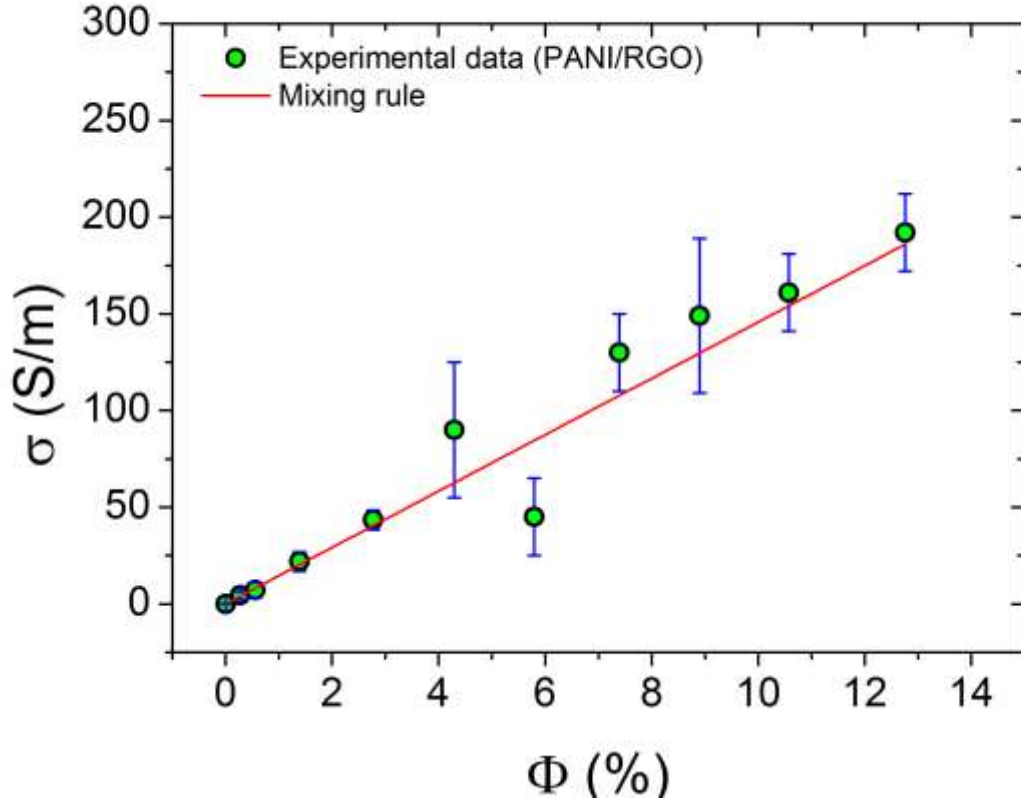


**Figure 73:** Electrical conductivity ( $\sigma$ ) of PANI/RGO nanocomposites as a function of vol-% RGO. Symbols are experimental data whereas red solid line is the best fit of equation 2.

Further, the electrical conductivity of the composites is interpreted through a percolation critical power law (equation 4). As shown in Figure 74, a good agreement is obtained between experimental data points and the fit (solid line). The fitting provides  $\Phi_c=0.099$  vol-%,  $t=0.98$ , and  $\sigma_0=15.3$  S/m.

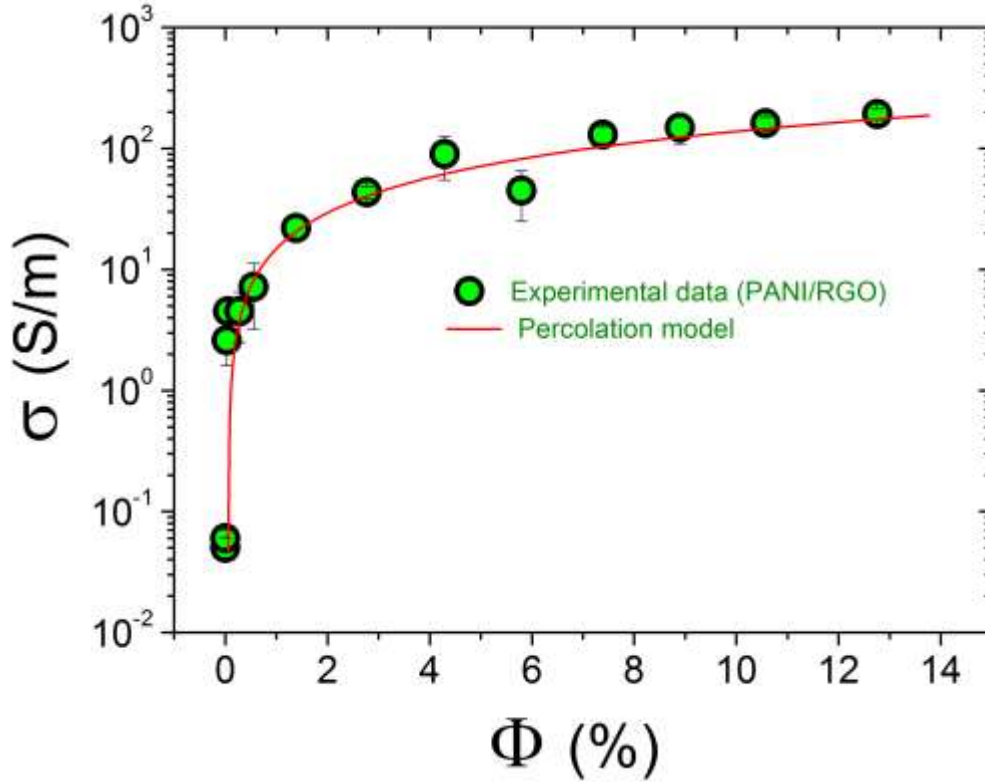


**Figure 74.** Electrical conductivity ( $\sigma$ ) of PANI/RGO nanocomposites as a function of vol-% RGO. Symbols are experimental data whereas red solid line is the fit of equation 4.

According to the model proposed by Li and Kim [216], the percolation threshold ( $\Phi_c$ ) for a composite made of graphitic disk platelets dispersed in a polymer matrix can be estimated from:

$$\Phi_c = 27\pi D^2 t_h / 4(D + D_{IP})^3 \quad 44$$

where  $D$  is the diameter of the platelets,  $t_h$  their thickness and  $D_{IP}$  the distance between filler platelets. In this study the estimated  $D_{IP}$  from SEM measurements is  $\sim 2 \times 15 \text{ nm}$  (PANI thickness between two RGO sheets). Knowing that  $D$  is in the micrometer range, it can be reasonably assumed that  $D_{IP} \ll D$ . Using the manufacturer's RGO specifications,  $D/d \sim 1000$  and equation 44, the volume percolation threshold is found to be within  $2.32 \text{ vol-\%} < \Phi_c < 2.63 \text{ vol-\%}$ . In this work, the percolation in PANI/RGO composites occurs when the RGO fraction is very close to 0.1 vol-% (Figure 74) which is at least twenty times lower than any value from the above  $\Phi_c$  range. Such



a low percolation threshold is not only related to the extremely high aspect ratio of the graphene sheets ( $D/t_h \sim 1000$ ) but is also dependent on the shape of the platelet geometry, i.e. disk (oblate) versus ellipsoid (prolate). Indeed, randomly oriented oblate ellipsoids with an aspect ratio of 1,000 are predicted to have a geometric percolation threshold of 0.1 vol-% which is consistent with our results [217].

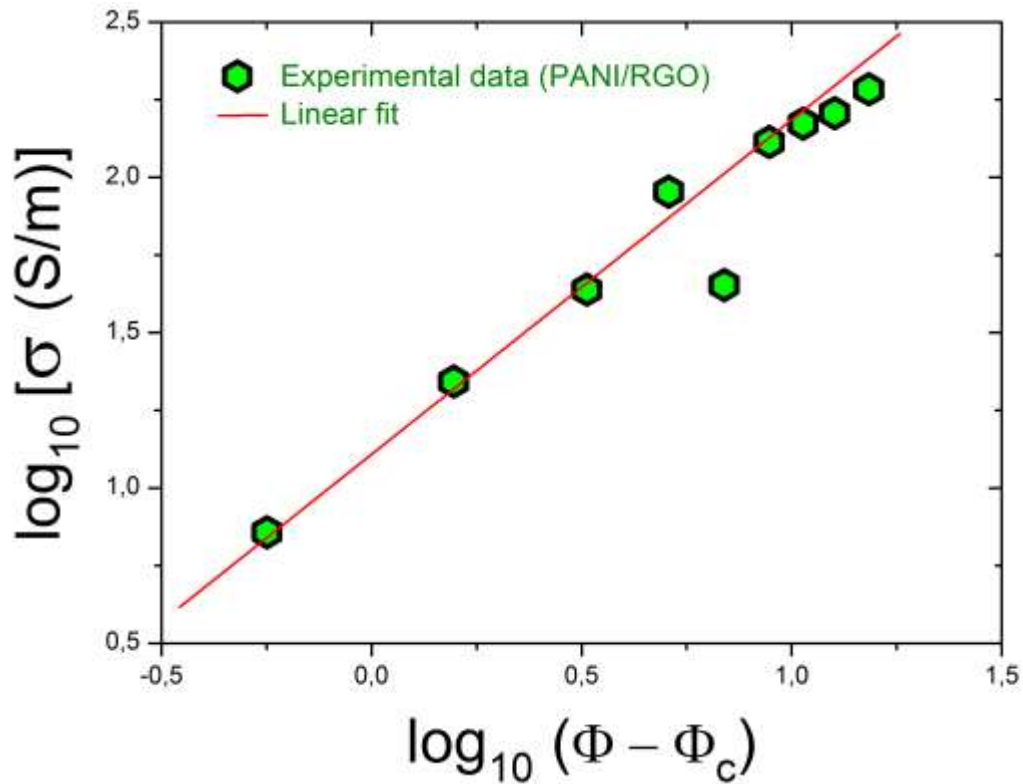


**Figure 75.** log-log plot of  $\sigma$  versus reduced volume fraction of RGO.

Figure 75 shows the log-log plot of  $\sigma$  versus reduced volume fraction ( $\Phi - \Phi_c$ ) of RGO. The result reveals an expected linear relationship between  $\log(\sigma)$  and  $\log(\Phi - \Phi_c)$  providing a slope of 1.07 which is close to the value of  $t$  retrieved from fitting the experimental data to equation 4. Unlike 3D percolation whose  $t > 1.6$ , here, the lower  $t$  value supports a two-dimensional, i.e. in plane, conduction process for the PANI/RGO composites which is obviously favored by the platelet-like morphology observed by SEM and TEM (Figure 68 and 69).

### 4.3.3.2 Electrical properties characterized by through plane measurement

#### 4.3.3.2.1. Introduction

In the present study, the objective of this study is to investigate the conducting properties and/or interfacial contribution in the PANI/RGO nanocomposites characterized by through plane measurements. For this purpose, Broadband Dielectric Spectroscopy (BDS) was employed to investigate the electric and dielectric properties of polyaniline/reduced graphene oxide (PANI/RGO) nanocomposites with various RGO fractions. In particular electric charge transport is explored from frequency dependent AC conductivity measurements providing interesting insights into the relaxation mechanisms which take place in the nanohybrids at various spatio-temporal scales.

In order to achieve the above objectives, imaginary part of dielectric permittivity was recorded by using BDS. Generally, imaginary part is more informative (it captures both DC conductivity and dielectric relaxation due to charge trapping and, subsequently, correlation between these two mechanisms) and is more precisely determined. Real part only traces capacitance due to charge trapping and, as it is proportional to capacitance, suffers from stronger experimental errors.

However, the recorded imaginary parts of dielectric permittivity data are analyzed within the framework of the Kohlrausch-Williams-Watts (KWW) model which is a model commonly used in polymer systems. In present section, through electrical conductivity, dielectric relaxation and interfacial charge trapping phenomena are highlighted. Also the relationship between the morphology and the charge localization within the composites is also studied and discussed according to existing models.

#### 4.3.3.2.2. Investigation of dielectric spectrum

The real part of the complex electrical conductivity  $\sigma^* = \sigma' + j\sigma''$  is related to the imaginary part of the complex permittivity  $\varepsilon^* = \varepsilon' + j\varepsilon''$  through the below relation [218,219]:

$$\sigma' = 2\pi f \varepsilon_0 \varepsilon'' \text{ or } \varepsilon'' = \sigma' / 2\pi f \varepsilon_0 \propto G(f) / f \quad 45$$

where  $f$  denotes the frequency of the harmonic voltage applied to the sample,  $\varepsilon_0$  is the permittivity of free space, and  $G(f)$  is the measured conductance of the sample. A double logarithmic plot of  $\varepsilon''$  vs  $f$ , recorded at room temperature for different RGO volume fraction of RGO/PANI nanocomposites are presented in Figure 76 while the frequency dependence of  $\varepsilon''$  experimental data for pure PANI is displayed in Figure 77.

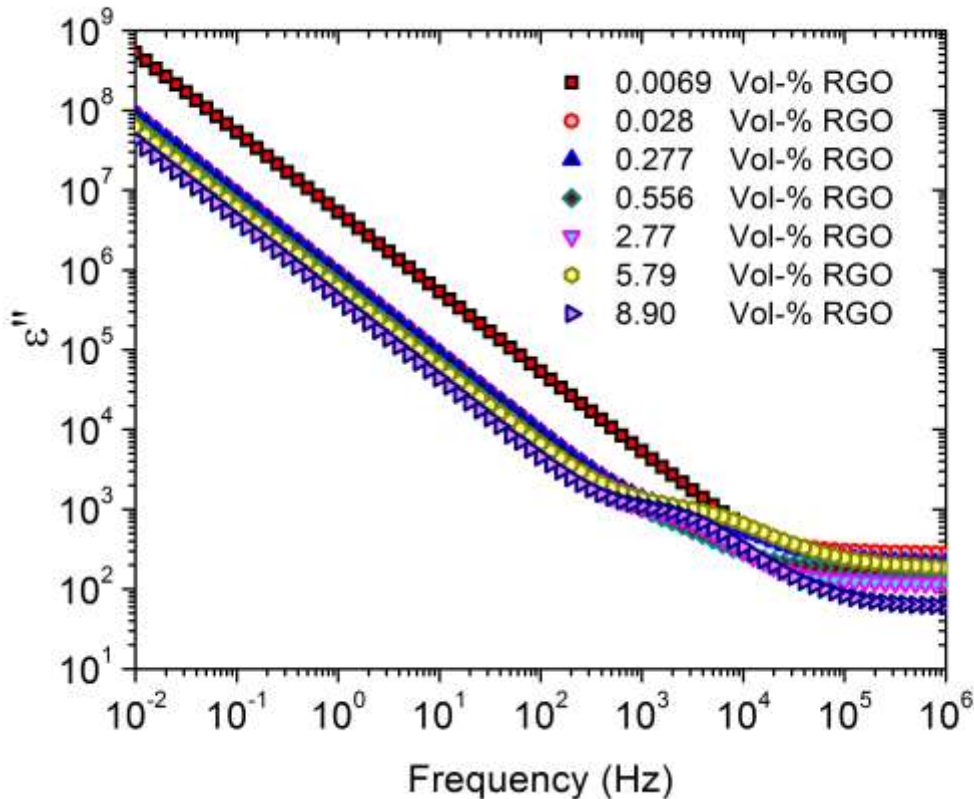


**Figure 76.** Imaginary part of complex permittivity (relative) vs frequency (Hz) of RGO/PANI nanocomposites.

As shown in Figure 76, a relaxation process is detected in the range  $10^3$ - $10^5$  Hz for nanocomposites, but not for pure PANI, indicating that this process must be associated with the presence of RGO in the materials. In the MHz region, an additional relaxation mechanism is partially observed in the vicinity of the detection limit of our impedance analyzer and is beyond the scope of the present work. In order to completely characterize the dielectric spectra, a quantitative analysis of experimental data was carried out using a function:

$$\varepsilon''(f) = \varepsilon_1''(f) + \varepsilon_2''(f) \quad 46$$

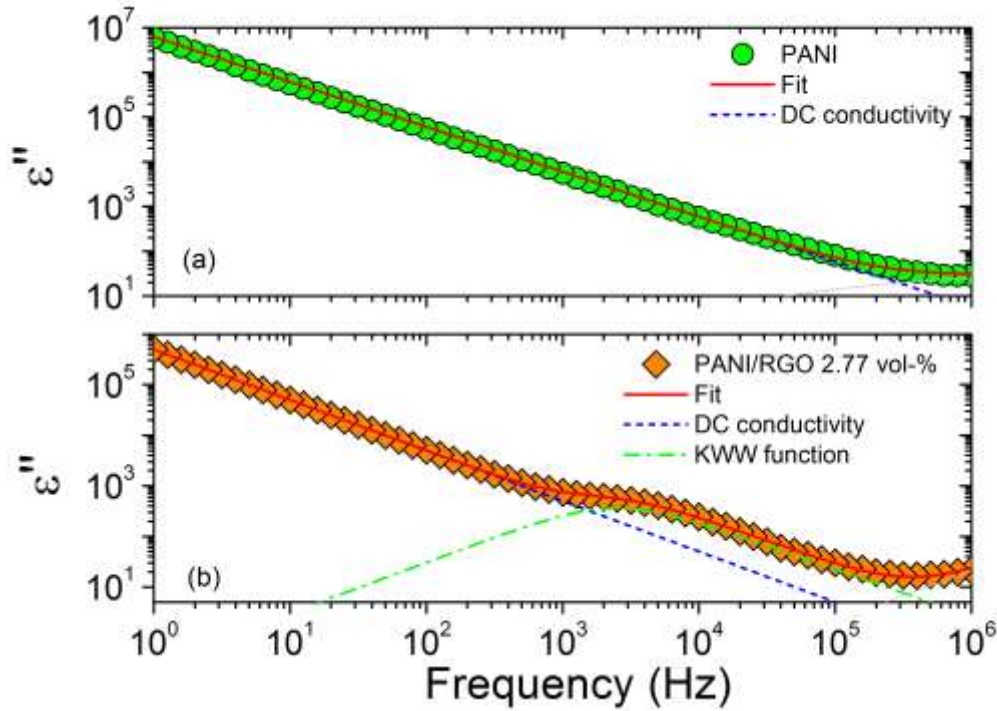
The equation 46 is composed of a low-frequency region, whereas the ac conductivity is frequency independent and equal to the DC-conductivity ( $\sigma$ ) is defined as :

$$\varepsilon_1''(f) = \sigma/\varepsilon_0(2\pi f)^n \quad 47$$

and a high-frequency dispersive region, whereas dielectric loss appears interpreted by the Fourier transform of the Kohlrausch-Williams-Watts (KWW) stretched exponential functions which is [220] :

$$\varepsilon_2''(t) = \Delta\varepsilon_{KWW} e^{-\left(\frac{t}{\tau_{kww}}\right)^\beta} \quad 48$$

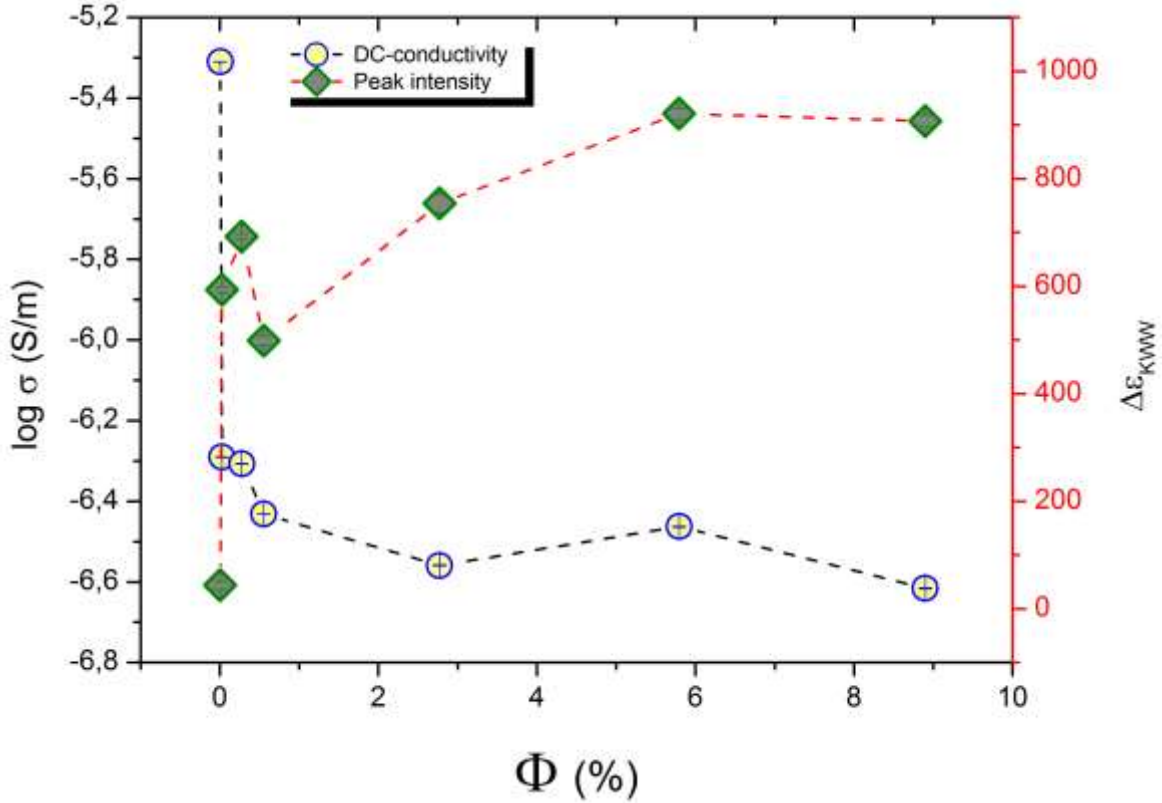
where  $\Delta\varepsilon_{KWW}$  is the relaxation strength,  $\tau_{kww}$  is the KWW-relaxation time, and  $\beta$  is the stretching exponent ( $0 < \beta \leq 1$ ).



**Figure 77.**  $\epsilon''$  vs frequency (Hz) for (a) pure PANI and (b) PANI/RGO nanocomposite (2.77 vol-% RGO).

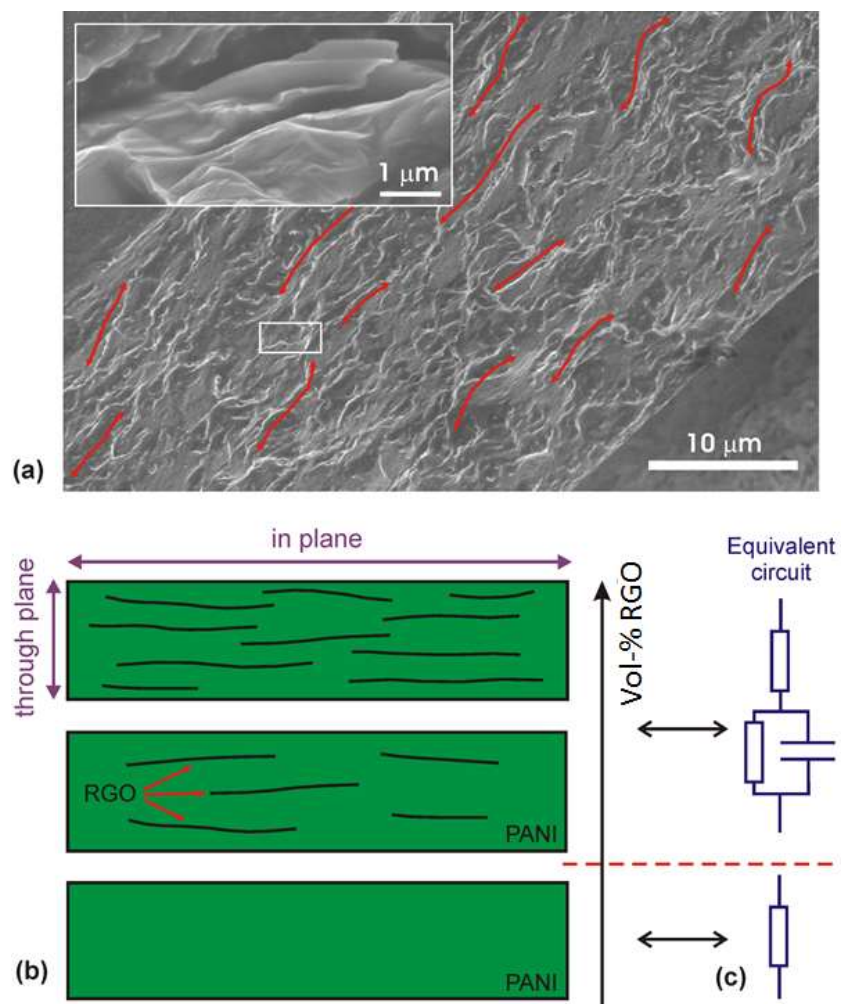
Figure 77 shows the frequency dependence of  $\epsilon''$  experimental data (symbols) and fitting curves (solid and dashed lines) for PANI/RGO nanocomposite (2.77 vol-% RGO). For pure PANI, all data points lie on a straight line with a slope of -1 which is attributed to the DC conductivity term. This statement is also valid for nanocomposites up to  $f = 5 \times 10^2$  Hz above which an additional dielectric relaxation peak is observed. This peak can be fitted with a KWW function (Figure 77 green dashed line) demonstrating that a very good matching is obtained between the experimental data and the fitting curves retrieved from equation 48.

Figure 78 shows the DC-conductivity ( $\sigma$ ), evaluated from the low frequency ac-data, and the intensity of the KWW relaxation peak ( $\Delta\epsilon$ ) as a function of RGO loading of RGO/PANI nanocomposites.



**Figure 78.**  $\log \sigma$  vs vol-% RGO and  $\Delta\epsilon$  vs vol-% RGO

The analysis showed that the DC conductivity is reduced, with inclusion of RGO. This behavior is unexpected because a notable enhancement of percolation process is usually observed for in plane measurement PANI/RGO (see Figure 73). It can be seen that highest value of electrical conductivity measured plane is  $10^{-3}$  S/m when the value for in plane measurement is in  $10^{+2}$  S/m order. It should be notated that the nature of the experiments are different here. These significant differences in the electrical conductivities may arise due to nature of experiments. Also a possible explanation of this finding could come from the sample pelletization process which might favor a parallel arrangement of PANI/RGO platelets as shown in Figure 79(a) by SEM and cartooned in Figure 79(b).



**Figure 79.** (a) Cross sectional SEM view of PANI/RGO pressed pellet (0.56 vol-% RGO). Red arrows illustrate the main orientation of layered platelets; the inset displays the enlarged area of the white rectangle showing PANI-wrapped RGO platelets. (b) Schematic view of pellet cross sections starting from pure PANI (bottom) to higher RGO loadings (top) and (c) proposed schematic equivalent circuits according to dielectric behaviors.

Recalling that PANI/RGO composites were synthesized by in-situ chemical synthesis, RGO acts as a seed for PANI growth, i.e., the surfaces of RGO platelets are fully covered with a layer of PANI forming a core(RGO)/ shell(PANI) structure. Due to their planar 2-D shape, PANI/ RGO platelets are most likely stacked in a parallel manner during compression leading to a layered-like morphology where physical contacts/connections between platelets occurred through their PANI shells. This geometrical arrangement of PANI/RGO platelets is supported by

the previous reports where graphene platelets preferentially lie parallel to each other inducing anisotropic transport properties [221,222]. In such a morphology, PANI/RGO platelets can be electrically assimilated to leaky capacitors assembled in a series of parallel Resistance- Capacitor (RC) components as proposed in Figure 79(c). This system models a Debye-like relaxation process, which can be used to describe the dielectric loss observed. Also two different behaviors (signature of in plane electrical conductivity and through plane electrical conductivity) can be interpreted by using two different circuits. The through plane electrical conductivity behavior can be explained by leaky capacitors assembled in a series of parallel Resistance-Capacitor (RC) (Figure 79(c)) whereas the in plane electrical conductivity behavior can be interpreted by using open circuit concept. In in plane electrical conductivity measurement, leakage resistance plays an important role in the overall enhancement of electrical conductivity but capacitance effect is insensitive.

As shown in Figure 78, the intensity of the peak is higher with increasing composition. It seems that the increase of the RGO phase provides more interfaces, which act as trapping centres for the charge carriers. Consequently, the concentration of carrier that can transfer along the volume of the specimen is decreased in excess of those pinned at interfaces. The DC-conductivity is  $\sigma=n\mu q$ , where  $n$  is the concentration of charges that participate to the DC-transport mechanism,  $\mu$  is their mobility and  $q$  denotes the charge. On increasing the RGO content, interfaces hinder the charge motion along the volume of the specimen; the percolation network structurally changes, fewer pathways are available for carriers to move macroscopically, while clusters bounded by interfaces permit short range electric charge flow. The latter carrier localization reduces  $n$  (yielding lower  $\sigma$  values) and has a resonance frequency identical to the maximum frequency of the observed dielectric loss peak. Within this frame and assuming that the modification of the topology of the percolation network does not affect the dynamics of free charge carriers (i.e.,  $\mu$  is practically unaffected), we assert that the increase of the dielectric loss intensity  $\Delta\epsilon$  is induced by capacitance effects due to charge trapping in excess of  $n$ .



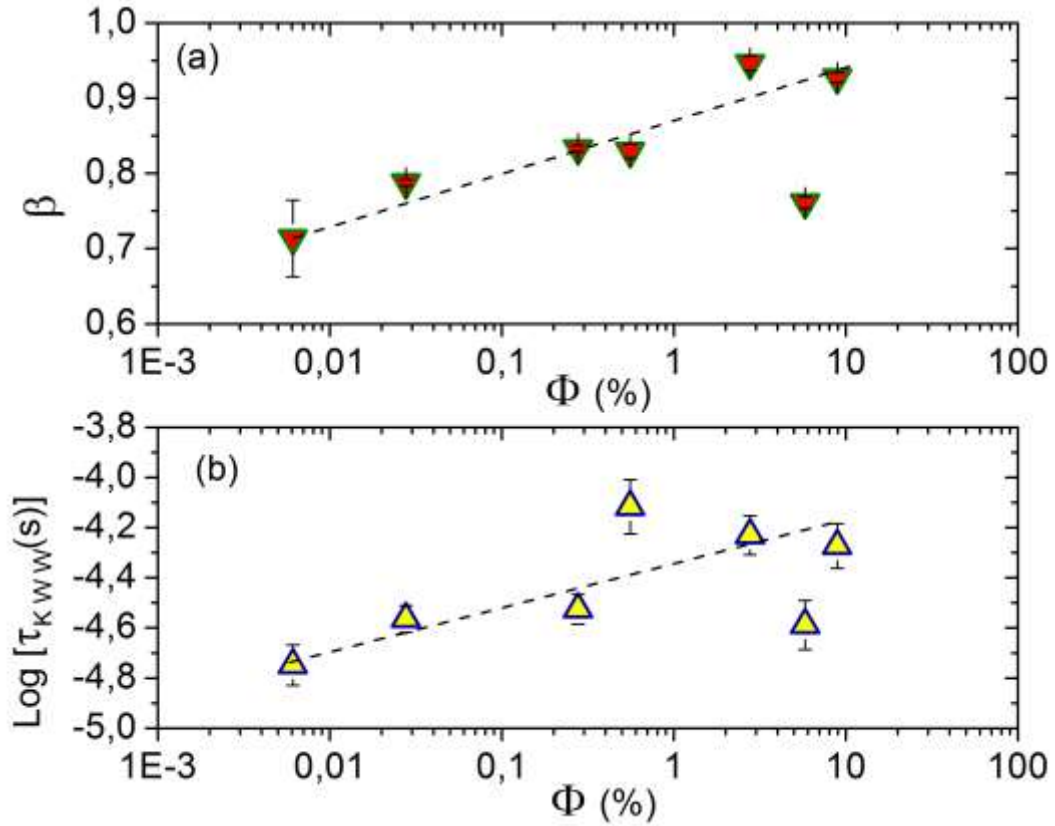


**Figure 80.** (a)  $\beta$  vs vol-% RGO (b)  $\log\tau_{\text{KWW}}$  vs vol-%t RGO.

The characteristic relaxation time  $\tau_{\text{KWW}}$  is increased with composition as increase RGO (Figure 80(b)), while the stretching component ( $\beta$ ) of the KWW model increases (Figure 80(a)), approaching the value 1, which is typical for Debye-like relaxation.

To gain more information we calculated the mean dielectric relaxation time by combining  $\tau_{\text{KWW}}$  and  $\beta$ , through the given relation:

$$\langle\tau\rangle = \tau_{\text{KWW}}\beta^{-1}\Gamma(1/\beta) \quad 49$$

where  $\langle\tau\rangle$  is the mean dielectric relaxation time and  $\Gamma$  is the Gamma function. The equation 49 provides the mean value of  $\langle\tau\rangle = 6.3 \times 10^{-5}$ s.

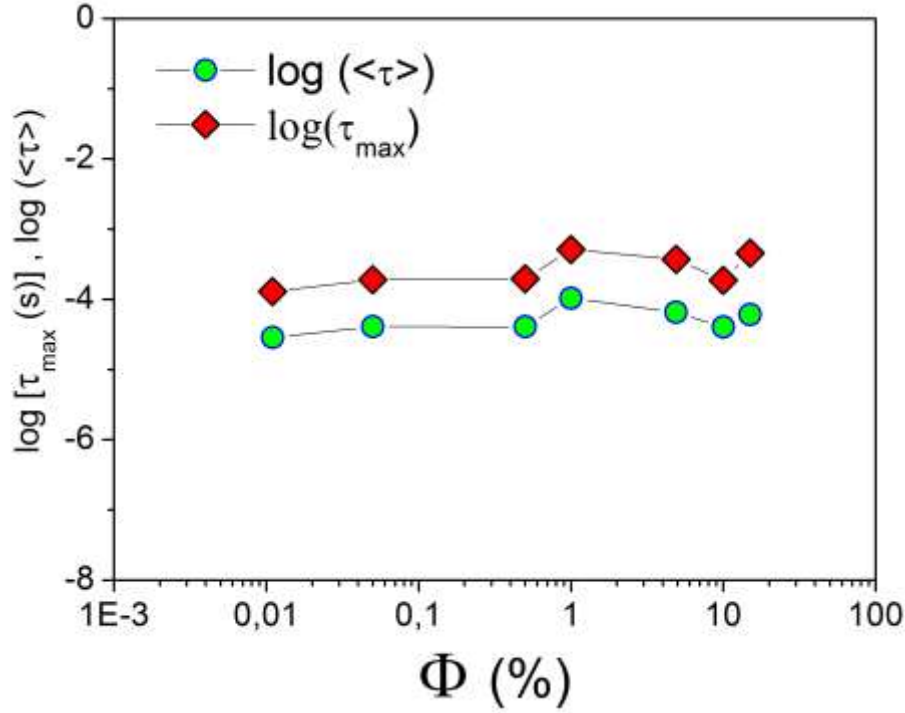


**Figure 81.** The relaxation time  $\tau_{\max} \equiv 1/f_{\max}$  and the mean dielectric relaxation time  $\langle \tau \rangle$  estimated from the  $\tau_{\text{KWW}}$  and  $\beta$  parameters obtained from the KWW fitting.

In Figure 81, we see that both the mean relaxation time  $\langle \tau \rangle$  and the dominant relaxation time  $\tau_{\max} = 1/f_{\max} \approx 2.5 \times 10^{-4} \text{ s}$ , (where  $f_{\max}$  is the frequency where the dielectric loss has its maximum) are roughly insensitive to the increase of RGO. In other words, the relaxation time-scale is practically constant, subsequently, the characteristic scale (which is, to a first approximation, proportional to reciprocal relaxation time), is invariant to increased RGO content. This is compatible with the previous SEM results that the dimensions of the platelets of RGO oblate covered with PANI do not change dramatically with increasing RGO.

Moreover, the invariance of the dielectric relaxation time observed in our RGO/PANI nano-composites is compatible with the predictions of dielectric theories for mixtures. For example, the Sillars model [223] for low concentration of conducting oblate spheroid inclusions (which resemble the platelet-like shape of the RGO inclusions in RGO/PANI nano-composites), predicts a relaxation time :

$$\tau = \varepsilon_0 \frac{\varepsilon^*_{filler}}{\sigma_{filler}} \quad 50$$

where  $\varepsilon^*_{filler}$  and  $\sigma_{filler}$  refer to the dielectric complex permittivity and DC-conductivity of the conducting inclusions (RGO), respectively. The equation 50 shows that the relaxation time is insensitive to concentration effects. Thus, the above result is supported by the Sillars model

On the contrary, the intensity of the polarization or peak intensity ( $\Delta\varepsilon$ ) can be described by the interfacial polarization model proposed by Sillars [223]:

$$\Delta\varepsilon = \Phi \frac{\varepsilon^{*2}_{matrix}}{\varepsilon^{*2}_{filler}} \quad 51$$

The above equation implies that  $\Delta\varepsilon$  is affected by the volume fraction of RGO, even at low concentration values, which complies with the observed concentration dependence of  $\Delta\varepsilon$  in RGO/PANI.

The experimental results in RGO/PANI nanocomposites do not only comply with the Sillars interfacial polarization model but, additionally, indicate that the observed relaxation does not originate merely from some relaxation of the PANI matrix. The observed peak can hardly be attributed merely to relaxation within the PANI phase. In principle, in disorder semi-conductor systems, a relaxation mechanism is correlated with the DC-conductivity through the Barton-Nakajima-Namikawa (BNN) model [224] that interconnect the position  $f_{max}$  of the relaxation mechanism, the relaxation strength  $\Delta\varepsilon$ , and  $\sigma_{dc}$  through the relation:

$$2\pi f_{max} \varepsilon_0 p \Delta\varepsilon = \sigma_{dc} \quad 52$$

where  $p$  is a constant of the order of unity. However, in our RGO/PANI nano-composites  $f_{\max}$  was found to be roughly constant (Figure 80) and  $\Delta\epsilon$  is directly proportional to  $\sigma$  on increasing the RGO content. Hence, the BNN relation is not fulfilled and, subsequently, the observed relaxation peak can hardly be attributed to relaxation within the PANI phase. The latter conclusion is alternatively supported by the fact that the fitting parameters  $\tau_{\text{KWW}}$  and  $\beta$  should be concentration independent, if the observed relaxation originated from the PANI phase itself, but this evidently does not happen (Figure 80 (a) and (b)).

#### 4.3.3.2.3. Conclusion

The decrease of the DC-conductivity with increasing RGO content in RGO/PANI nano-composites is linked to the increase of the intensity of a dielectric relaxation mechanism. On increasing RGO, the nano-composite becomes rich interfaces and, as a result, more charges are trapped; in this way the concentration of charges that are favored to percolate is decreased in excess of the pinned charge concentration, enhancing capacitance effects. While this happens, the analysis of the dielectric relaxation peak within the KWW model, revealed a mean dielectric relaxation time, which is roughly constant, evidencing that the scale where relaxation progresses is roughly constant. The latter is in accordance with previous SEM studies, whereas the RGO sheets keep an average size of 0.5-3  $\mu\text{m}$  on increasing RGO component. Capacitance effects depend on the quantity of RGO sheets but the relaxation time does not, as being proportional to the mean size of these sheets. Our finding that the mean dielectric relaxation time is practically constant for the composition range of RGO studies, while the strength of the dielectric relaxation mechanism is concentration-dependent is in accordance with the predictions of the Sillars model for oblate conducting discs into an insulating matrix, for low concentration values.

### 4.3.3.3 Temperature dependence of electrical properties characterized by through plane measurement

#### 4.3.3.3.1. Introduction

As an extension of the above study in this area, we wish to report, herein, the effect of temperature on electrical properties performed by through plane measurements. In order to investigate these properties, temperature dependent imaginary part of dielectric permittivity was recorded by using BDS. Like before, the recorded imaginary parts of dielectric permittivity data are characterized within the framework of the Kohlrausch-Williams-Watts (KWW) model. The effect of temperature on the charge relaxation mechanisms taking place at the polarized RGO/PANI interfaces is discussed.

#### 4.3.3.3.2. Investigation of temperature dependence of dielectric spectrum

Isotherms of imaginary part ( $\epsilon''$ ) of the complex dielectric permittivity ( $\epsilon^*$ ) of PANI/RGO nano-composites containing different RGO concentration were recorded in the frequency domain ranging from 306 K to 396 K in a double logarithmic representation (Figure 82).

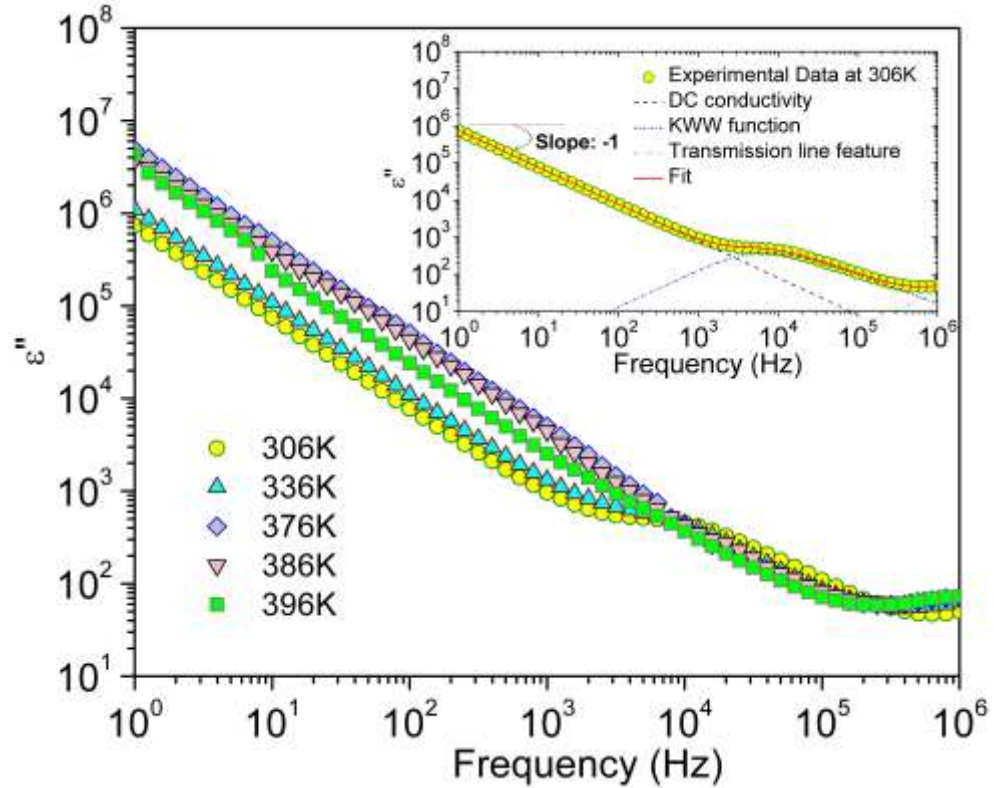


**Figure 82.** Isotherms of imaginary part  $\epsilon''$  of the complex dielectric permittivity ( $\epsilon^*$ ) vs  $f$  for 5.79 vol-% PANI/RGO nano-composite. Inset: fitting of a conductivity line.

Like the room temperature study, the data points are fitted by using equation 47 and 48. We use, to a first approximation, the Arrhenius law to qualitatively describe modifications with  $1/T$ . An Arrhenius relation, i.e.,  $f_{\max} \propto \exp(-E/K_B T)$ , where  $K_B$  and  $E$  are the Boltzmann's constant and the activation energy respectively, fits the  $\log f_{\max}(1/T)$  data points presented in Figure 83. The slopes evaluated are:  $\sim 2.041 \times 10^3 \text{K}$ ,  $2.005 \times 10^3 \text{K}$  and  $2.087 \times 10^3 \text{K}$  for 0.0277, 2.77 and 5.97 vol-% PANI/RGO, respectively. They share a common value, confirming that a common microscopic mechanism underlies the relaxation process, such as electric charge relaxation within RGO nanoparticles. The result reveals that the characteristic frequency is shifted towards lower frequency with increase in temperature. This behavior is discussed below.

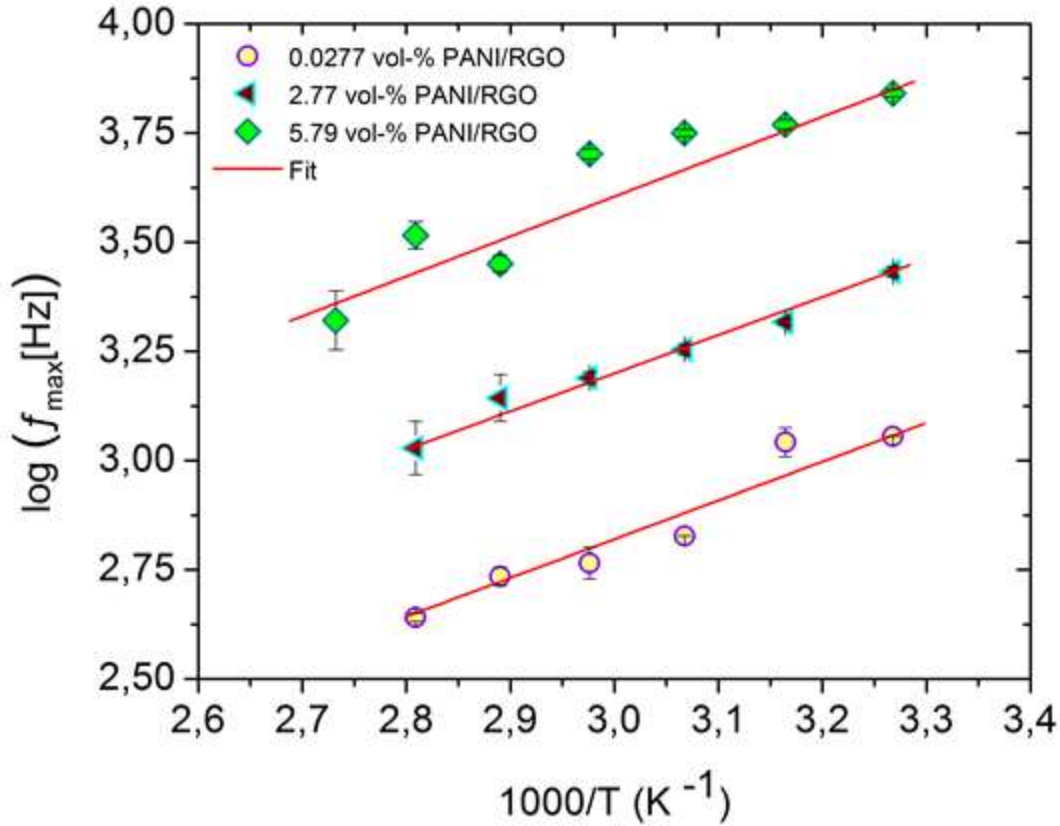


**Figure 83.** The logarithm of the peak maximum  $f_{\max}$  against  $1/kT$ . (straight lines are best fits to the data points).

Effective dielectric theories of interfacial polarization in bi-phase heterogeneous structures consisting of conducting inclusions inside an insulating matrix are based on the assumption that the interface is impermeable to electric charge carriers, i.e., the outward transmission coefficient through the interface is null as different phases do not interact with each other. However, interactions can play a significant role in interfacial polarization phenomena [225–228]. The Sillars model for low concentrations of conducting oblate spheroid inclusions (such as the RGO ‘flakes’) predicts a relaxation time  $\tau$  for interfacial polarization through equation 50. Since  $\tau = 1/f_{\max}$ , equation 50 implies that both  $\sigma_{filler}$  and  $f_{\max}$  have identical temperature dependencies. For graphene sheets, above roughly 150 K, at the Dirac point, where the Fermi surface is at the intersection of the dispersion relation of two bands in an energy-wave vector diagram, the charge carriers form ‘puddles’ of electrons and holes, probably associated with charged impurities [229,230]. As a result, at high temperatures, the dc

resistance rises (with activation energy equal to 50 meV) in a thermally activated process [229,230]. Alternatively, a saturation, rather than activated increase, of the dc conductivity vs temperature has also been observed [231]. In any case, the conductivity  $\sigma_{filler}$  of the RGO phase above room temperature is, more or less (depending on the type of defects formed), a decreasing function of temperature and, according to equation 50 - under the restriction that the host phase is a perfect insulator -  $f_{max}$  should also increase with rising temperature. However, the opposite behavior is observed, i.e.,  $f_{max}$  is lowered on increasing temperature [Figure 82].

The experimental results can alternatively be interpreted as follows: PANI is a semiconductor, rather than an insulator and in an equivalent circuit representation, the polarized RGO flakes act as capacitors being short-circuited by a leakage resistance through the semi-conducting PANI environment. Heating supplies thermal energy to the electric charge carriers, relaxing within the RGO, and assists their outward penetration of the effective potential barrier (which resembles that of a Schottky barrier raised at the interface of a metal - semi-conductor junction). Thus, a number of carriers escape and flow through the PANI environment leading to a lowering of the density of charges in the interior of RGO as temperature increases. Subsequently,  $d\tau(T)/dT > 0$ , or,  $df_{max}(T)/dT < 0$ , then  $f_{max}$  slowdown on increasing temperature.

The scenario of electric charge de-trapping from the RGO inclusions at elevated temperatures is further supported by the reduction of the intensity  $\Delta\varepsilon$  with temperature (Figure 84), which is a measure of how the relaxing charge population decreases on heating. Note that the values of  $\Delta\varepsilon$  increase upon RGO loadings, in agreement with another prediction of the Sillars model (equation 51) [232] (i.e.,  $\Delta\varepsilon$  is proportional to the volume fraction of RGO in the host matrix).



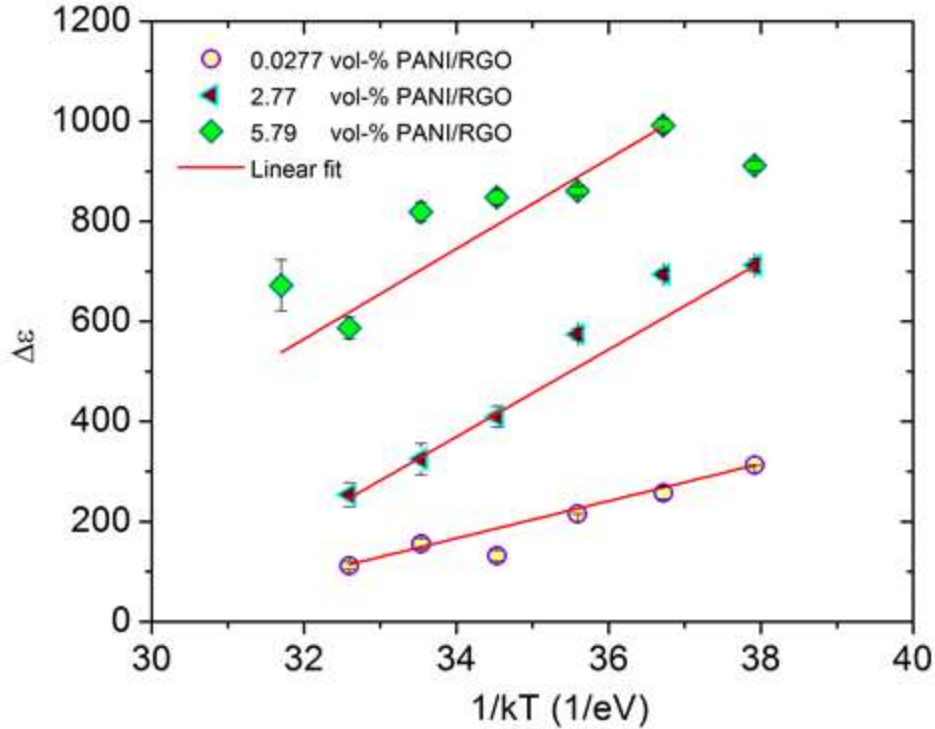


**Figure 84.** The peak intensity  $\Delta\varepsilon$  against  $1/kT$ . The decrease of  $\Delta\varepsilon$  upon temperature implies a reduction of the density of relaxing electric charges inside the RGO inclusions.

Charge liberation from the inclusions augments the concentration of free charges participating to the DC conductivity. While  $\Delta\varepsilon$  decreases on temperature by a factor of 100, the (total) DC-conductivity increases less (by a factor of 2) because, recalling that  $\sigma = n\mu q$ , (where  $n$  is the concentration of charge participating to conductivity,  $\mu$  is the charge mobility and  $q$  denotes the net charge) the mobility of the liberated charges is reduced when moving within a semi-conducting environment. The DC conductivity (reduced to the value measured at 306K) vs temperature plot for PANI reaches a maximum value above room temperature (Figure 85). It is noteworthy that the monotony of conductivity-temperature curves in conducting polymers depends strongly on their doping level [233]. Higher RGO concentrations provide more charge-trapping interfaces and more pinned charges are likely to be liberated towards the semi-conducting PANI matrix. The latter mechanism is intensified at higher RGO loading, as can be seen in Figure 85 in which the right-hand tail of the conductivity curves shifts systematically upward.

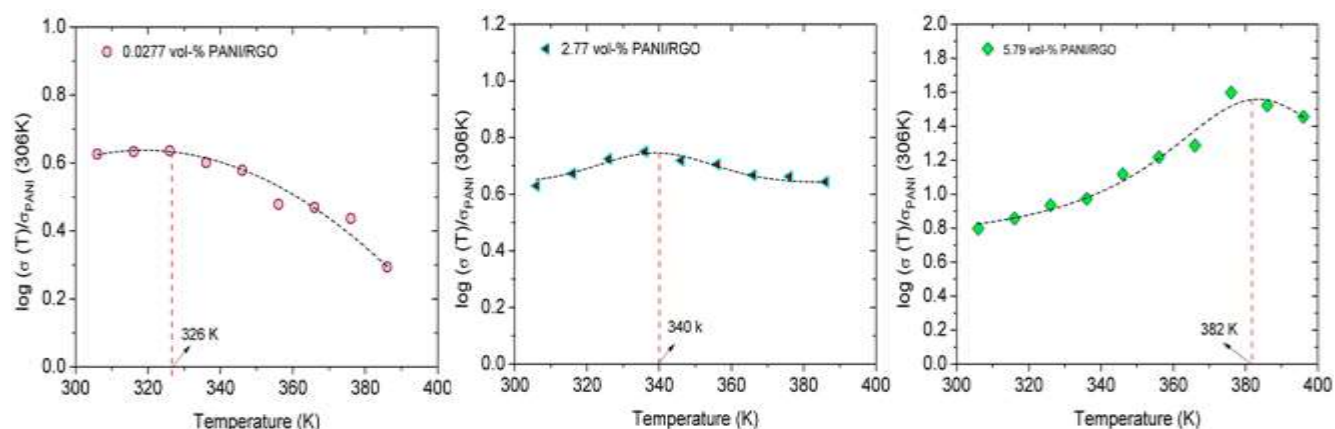


**Figure 85.** The logarithm of the DC conductivity reduced to the corresponding one measured at 306 K of PANI vs temperature for (a) 0.0277 vol-%, (b) 2.77 vol-%, (c) 5.79 vol-% PANI/RGO composites.

#### 4.3.3.3.3. Conclusion

In summary, complex permittivity measurements above room temperature on PANI/RGO nanocomposites of varying RGO contents reveal an interfacial relaxation mechanism characterized by decreased  $f_{max}$  values. This behavior is interpreted by revisiting the basic concepts of the Sillars model for interfacial polarization occurring in an insulator comprising dispersed conducting platelets. The semi-conducting PANI matrix provides a leakage resistance to the polarized RGO inclusions and enhances the DC conductivity of the composites at the expense of the intensity of the relaxation process. This is evidenced by the decrease in intensity of the relaxation peak on increasing temperatures which favors phonon-assisted charge detrapping in RGO platelets. This phenomenon corroborates with our experimental findings as reflected in decreased values of  $f_{max}$ . The heat-induced charge liberation contributes to DC conductivity and affects the shape of the DC conductivity - temperature curves for different weight fractions of RGO which can be explained through the Sillars model.

#### 4.3.4. Thermal properties

In the present section, we present the thermal properties the PANI/RGO composites. In order to determine the thermal conductivity of the composites, two different techniques, the laser flash method and DSC, and photothermal radiometry, have been employed.

##### 4.3.4.1 Thermal properties investigated by laser flash method and DSC

In this method, to obtain the thermal conductivity two different instruments have been used for two different samples. Thermal diffusivity of the pellets of the composites was carried out on laser flash method while DSC was used to investigate heat capacity of the powder of the composites.

###### 4.3.4.1.1. Thermal diffusivity and Volumetric heat capacity

Figure **86(a)** presents the thermal diffusivity of PANI/RGO composites as function RGO loading. As shown in Figure **86 (a)**, thermal diffusivity increases with the inclusion of RGO. The maximum thermal diffusivity  $1.88 \times 10^{-7} \text{ m}^2/\text{s}$  is obtained at 12.76 vol-% RGO content. As we know, thermal conductivity of RGO is more than thermal conductivity of PANI. Thus, the enhancement of the thermal diffusivity of the composites can be induced due to induced thermal conducting paths in the nanocomposites.

The volumetric heat capacity ( $\rho C$ ) of PANI/RGO composites as function RGO loading is displayed in Figure **86(b)**. It shows that the volumetric heat capacity increases with adding of RGO content in comparison with pure PANI ( $\rho C = 1.04 \pm 0.07 \text{ MJm}^{-3}\text{K}^{-1}$ ). The experimental data reveals that the volumetric heat capacity of the nanocomposites is almost constant ( $\sim 1.7 \text{ MJm}^{-3}\text{K}^{-1}$ ) at low RGO nano-fillers loading (up to 2.77 vol-%), where the volumetric heat capacity slightly increases over high RGO nano-fillers loading (beyond 2.77 vol-%). As shown in Figure **86(b)**, it can be seen that like PANI/MWCNT composites, the volumetric heat suddenly

decreases at 12.76 vol-% RGO content. But we have just one value and it can be related to experimental errors. So, it is neglected for further interpretation. The maximum value reaches up to  $1.93 \pm 0.06 \text{ MJm}^{-3}\text{K}^{-1}$  for the PANI/RGO composites with 10.57 vol-% RGO content. The obtained maximum value is almost two times larger than that of pure PANI. The result suggests that due to the enhancement of volumetric heat capacity, PANI/RGO composites can be used as heat storage materials.

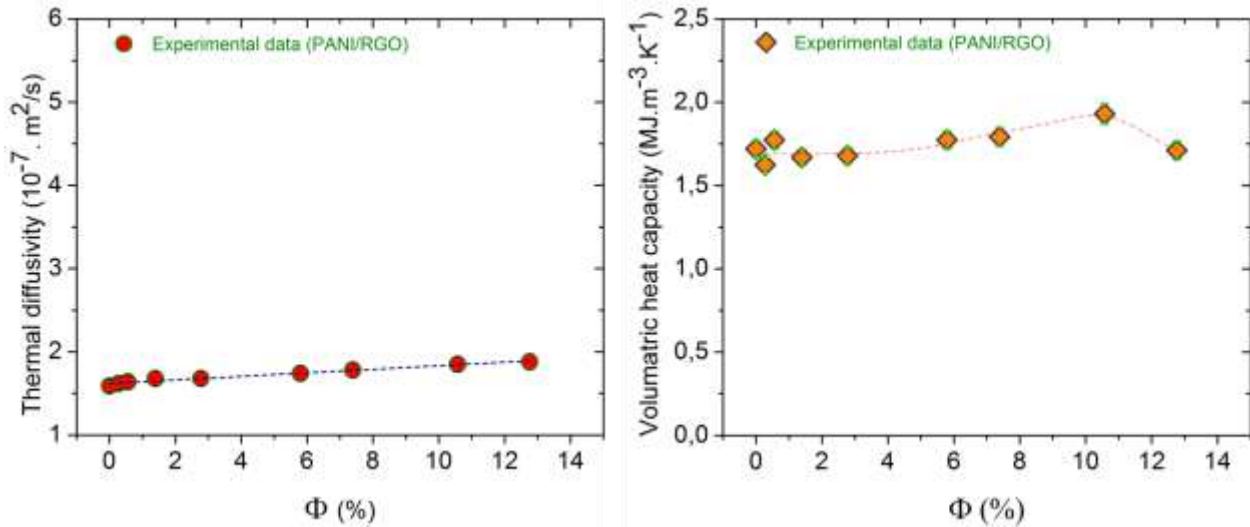


**Figure 86.** (a) Thermal diffusivity ( $\alpha$ ) and (b) volumetric heat capacity ( $\rho C$ ) of PANI/RGO nanocomposites as a function of RGO volume fraction. Dashed lines are guides to the eyes.

#### 4.3.4.1.2. Thermal conductivity

The thermal conductivity calculated by using equation 42 of the PANI/RGO composites is presented in Figure 87. As shown in Figure 87, the signature of thermal conductivity shows two different behaviors. Initially, the conductivity of the nanocomposites is barely changed or almost constant ( $\sim 0.28 \text{ W} \cdot \text{m}^{-1} \cdot \text{K}^{-1}$ ) at low RGO nano-fillers loading (up to 2.77 vol-%). But thermal conductivity slightly increases over high RGO nano-fillers loading (beyond 2.77 vol-%). The maximum value of thermal conductivity is  $\sim 0.28 \text{ W} \cdot \text{m}^{-1} \cdot \text{K}^{-1}$  for PANI/RGO composites with 10.57 vol-% RGO content. The observed phenomenon taking place at low vol-% RGO could be

ascribed to poor interactions between the filler and the matrix of the composites resulting in a large acoustic impedance mismatch. Since the acoustic speed is very much dependent on the density of the interfacial medium present between the two components of the nanocomposites [234]. It is likely that induced interfacial phonon scattering suppresses good thermal conductivity in the matrix with low filler contents. However, a reduction of acoustic impedance mismatch through the enhancement of interfacial interactions is achieved with higher RGO content leading to the observed rise of thermal conductivity.

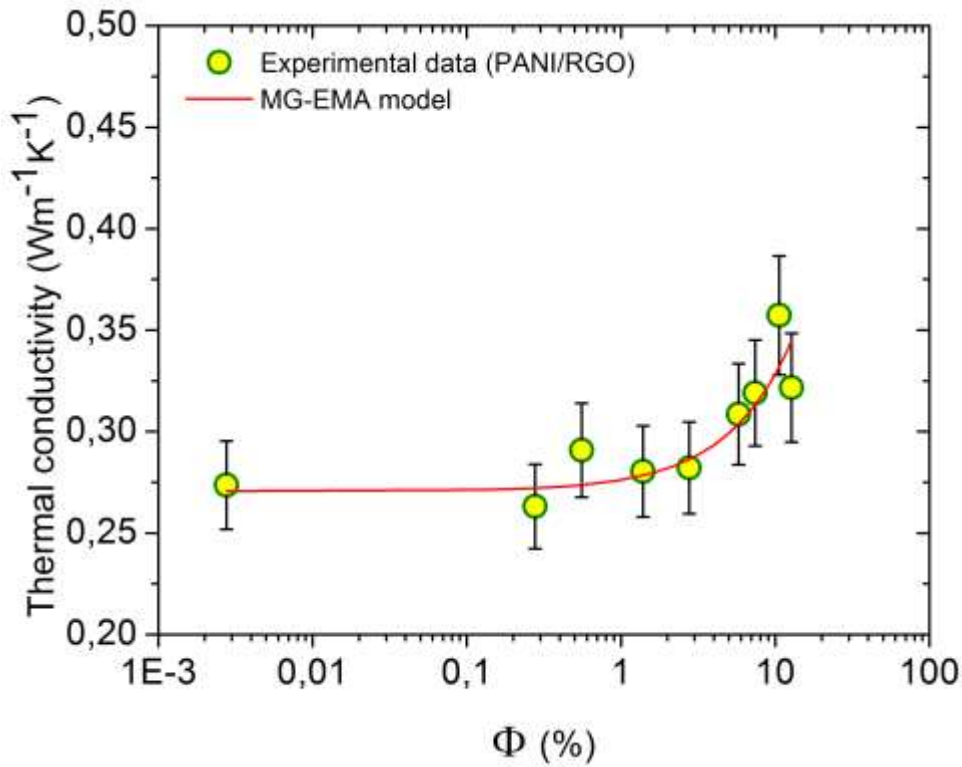


**Figure 87.** Thermal conductivity ( $k$ ) of PANI/RGO nanocomposites as a function of RGO volume fraction.

The thermal conductivity enhancement ( $\text{TCE}\% = ((k - k_{\text{PANI}}) \times 100 / k_{\text{PANI}})$ ) up to 89% is obtained for the composite with RGO content as high as 10.57 vol-% which is almost two orders of magnitude lower than that of epoxy/multilayer graphene composites with similar volume fraction of filler [235]. This finding may suggest that the thermal conductivity of RGO (multilayered) platelets is much lower compared to that of single layer graphene, which results in a limited rise of the effective thermal conductivity of the composites.

A Maxwell–Garnett type effective medium approximation (MG-EMA) which has presented in equation **19** is used in order to obtain interfacial thermal resistance. This model which is valid at low filler volume fractions in composites, is used to fit the dependence of  $k$  on volume fraction of RGO [235,236]. The fitting provides the value of interfacial thermal resistance (Kapitza),  $R_k$ , which is  $9.34 \times 10^{-10} \text{ m}^2\text{KW}^{-1}$ . The obtained  $R_k$  value is at least two orders of magnitude lower than that of polymer/carbon nanotubes composites [237]. Such a low  $R_k$  value can be attributed to good interactions between the planar geometry of RGO platelets and PANI aromatic rings through  $\pi$ - $\pi$  stackings (Figure **70**). This reduces the interfacial thermal resistance and suggests an improved coupling between some of the excited phonon modes in graphene sheets and the polymer matrix as predicted by Molecular Dynamics and Density Functional Theory simulations [148,149].

#### 4.3.4.2 Thermal properties investigated by photothermal radiometry (PTR)

In order to investigate the thermal conductivity in the same conditions, thermal properties of the PANI/RGO composites were characterized through photothermal radiometry (PTR) at room temperature.

##### 4.3.4.2.1. Thermal diffusivity and thermal effusivity

The changes of thermal diffusivity ( $\alpha$ ) and thermal effusivity ( $e$ ) of the nanocomposites as a function of RGO volume fraction are displayed in Figure **88**(a) and (b). These two parameters have been presented in the equation 36 and 37. In this study,  $\alpha$  and  $e$  are determined using the experimental evolution of the normalized phases of the corresponding PTR signals.

Figure **88**(a) exhibits thermal diffusivity values which are same order of magnitude of thermal diffusivity obtained via laser flash and DSC methods (see Figure **86**). Although the order of magnitude of thermal diffusivity is same, the values of thermal diffusivity of same sample obtained by two different methods (laser flash and DSC methods and PTR) are different. The significant differences between the results arise because of different natures of the experiments. Figure **88**(a) shows two different behaviors of  $\alpha$ , i.e., at low RGO fraction (<6 vol-%; average  $\alpha$

$\sim 2.38 \times 10^{-7} \text{ m}^2 \cdot \text{s}^{-1}$ ), the diffusivity does not change significantly. However, above that percentage a drop of  $\alpha$  with increasing RGO filler is conspicuous (lowest  $\alpha \sim 1.23 \times 10^{-7} \text{ m}^2 \cdot \text{s}^{-1}$ ). The “insensitivity” of  $\alpha$  at low RGO % could stem from the inhomogeneity of the composites brought about by the discontinuity of the embedded fillers. Thus, it is likely that upon increasing the amount of RGO (>6%) some effectual-thermal pathways are introduced which facilitate heat transfer, thereby decreasing the thermal diffusivity of the nanocomposites [238].

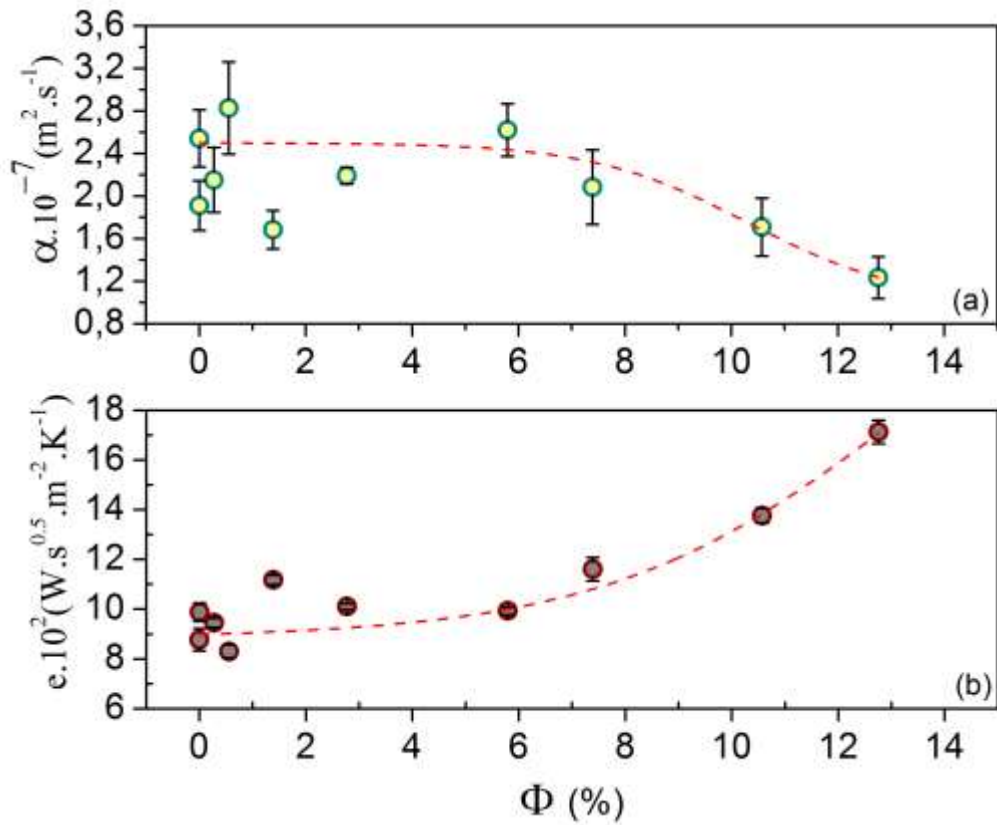


**Figure 88:** (a) Thermal diffusivity ( $\alpha$ ) and (b) thermal effusivity ( $e$ ) of PANI/RGO nanocomposites as a function of RGO volume fraction. Dashed lines are guides to the eyes.

The change of thermal effusivity ( $e$ ) as a function of RGO vol % (Figure 88(b)) shows that  $e$  is practically unaffected at low filler contents (< 6%; average  $e \sim 887 \text{ W} \cdot \text{s}^{0.5} \cdot \text{m}^{-2} \cdot \text{K}^{-1}$ ) but  $e$  clearly rises beyond that % (highest  $e \sim 1713 \text{ W} \cdot \text{s}^{0.5} \cdot \text{m}^{-2} \cdot \text{K}^{-1}$ ). Since thermal effusivity corresponds to the thermal impedance of a material and consequently its ability to exchange heat energy with

its environment it is likely that a rise in the volume fraction of RGO is accompanied with an enhancement of the overall “effective” heat exchange surface of the nanocomposites with its environment, thereby causing an increase in the thermal effusivity [239].

#### 4.3.4.2.2. Thermal conductivity

Next, a relationship between  $\alpha$ ,  $e$  and the thermal conductivity ( $k$ ) is obtained by solving equation **36** and **37**, that is:

$$k = e \times \sqrt{\alpha} \quad 53$$

Figure **89** displays the evolution of the thermal conductivity ( $k$ ) as a function of RGO vol- %. There is almost same trend relating thermal conductivity to vol-% RGO investigated by using laser flash and DSC methods (shown in Figure **87**). Although the trend relating thermal conductivity to vol-% RGO is same, the values of thermal conductivity for same sample obtained by two different methods (laser flash and DSC methods and PTR) are different. These differences are originated because of different natures of the experiments. Here, it can be seen that at low concentration of RGO,  $k$  remains essentially constant ( $\sim 0.44 \text{ W. m}^{-1} \cdot \text{K}^{-1}$ ) but registers a rise beyond that concentration with  $k$  value approaching  $\sim 0.60 \text{ W.m}^{-1} \cdot \text{K}^{-1}$  for a sample of 12.76 vol-% RGO.



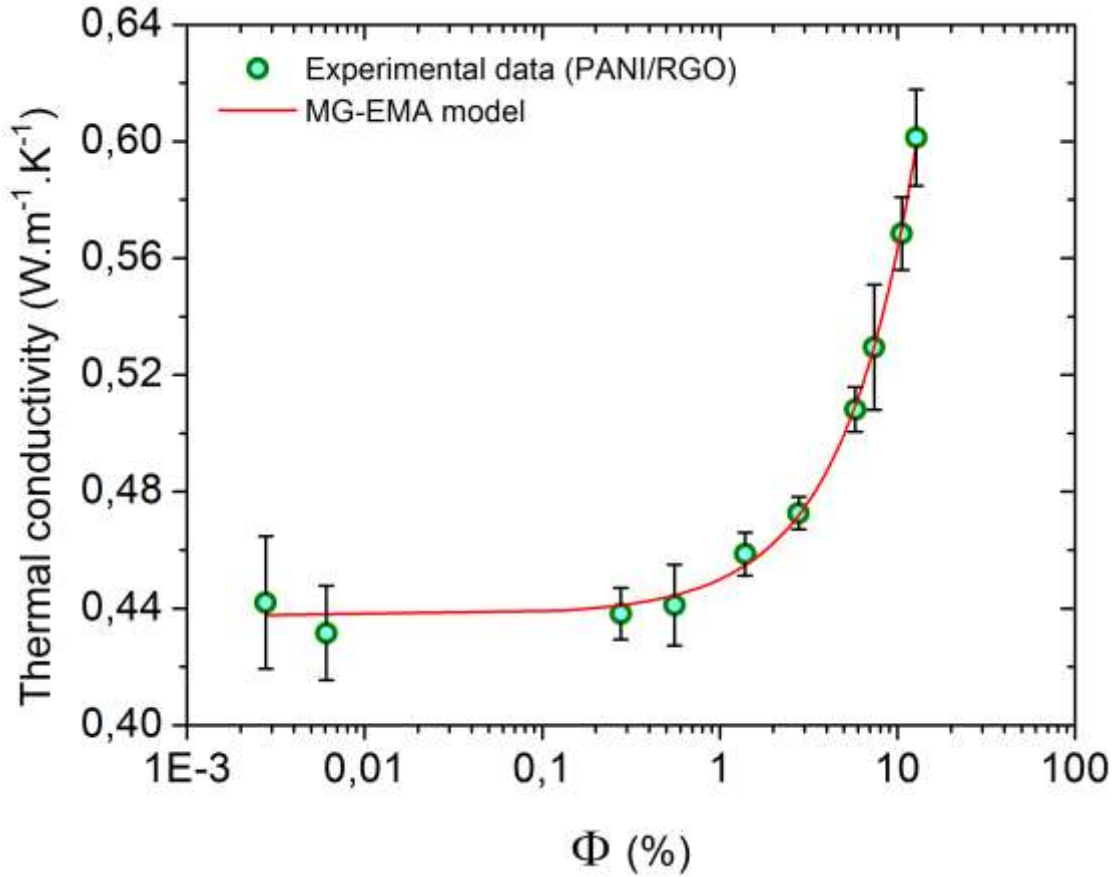


**Figure 89.** Evolution of the thermal conductivity ( $k$ ) as a function of RGO volume fraction.

In order to get further insights into thermal transport properties, we used a Maxwell–Garnett type effective medium approximation (MG-EMA) which has presented in equation 19. As shown in Figure 89, a good agreement is obtained between experimental data points and the fit (solid line) providing values of  $k_{\text{PANI}}=0.44 \text{ Wm}^{-1}\text{K}^{-1}$  and  $k_{\text{RGO}}=2.1 \text{ Wm}^{-1}\text{K}^{-1}$  which are in accord with data reported in the literature for PANI and RGO platelets [240–242]. In addition, it should be noted that thermal conductivity of layered materials like graphene or graphite is direction dependent. For example, in plane and through plane thermal conductivities in a graphene sheet with size of  $1\mu\text{m}$  and  $7\text{nm}$  thick, exhibit drastic differences, i.e.  $k_{\text{IP}}$  (in plane)  $\sim 0.6 \text{ Wm}^{-1}\text{K}^{-1}$  and  $k_{\text{TP}}$  (through plane)  $\sim 8.7 \text{ Wm}^{-1}\text{K}^{-1}$  [243]. The fact that our computed  $k_{\text{RGO}}$  lies in between the above values suggests that both in plane and through plane thermal transports could take place in the composites.

The value of interfacial thermal resistance (Kapitza) for PANI/RGO hybrids is found to be  $R_k = 4.9 \times 10^{-10} \text{ m}^2\text{K W}^{-1}$  which is at least two orders of magnitude lower than that of polymer/carbon nanotubes composites [237] and same order of magnitude of that of PANI/RGO composites investigated by laser flash and DSC methods. Recalling that the interlayer spacing between graphene sheets, estimated by X-Ray measurements, is  $d \sim 0.4 \text{ nm}$  and that the thickness  $t_h$  of RGO platelets retrieved from fitting (equation 19) is  $\sim 1.6 \text{ nm}$ , the number of layers  $n = t_h/d$  in RGO platelets is  $\sim 4$  which is consistent with the manufacturer's specifications.

Figure 90 shows that the ratio of the effective thermal conductivity over that of pure PANI vs. vol-% of RGO ( $k/k_{\text{PANI}}$ ) reaches 1.4 at  $\Phi = 12.76 \text{ vol-\% RGO}$ .

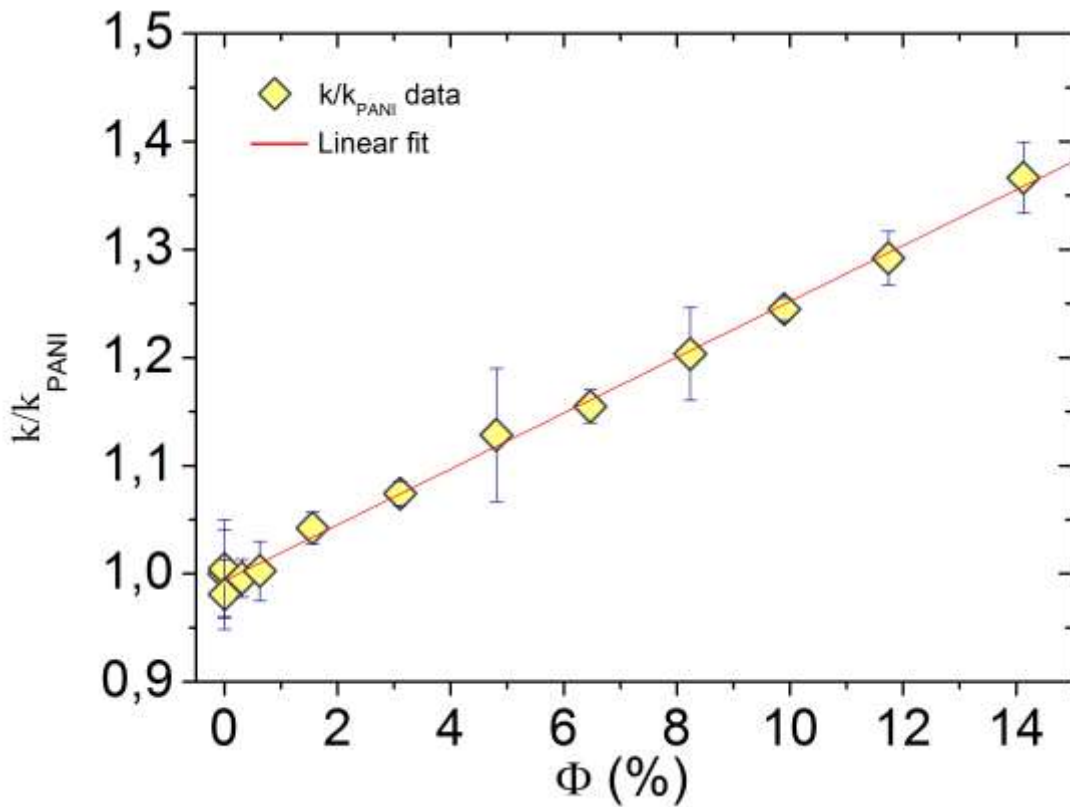


**Figure 90.** Plot of  $k/k_{\text{PANI}}$  vs vol-% RGO. Red solid line is linear fit.

Compared to simulated  $k/k_{\text{matrix}}$  ratios in ordered graphene composites whose values are as high as 360, that of the PANI/RGO composites is much lower suggesting that heat transport mostly occurs randomly through the samples [148]. Alternative explanations to the above-mentioned discrepancy in  $k/k_{\text{matrix}}$  ratios could come from the presence of void or air interfaces between PANI/RGO aggregates in the pressed pellets or a higher number of un-exfoliated graphene layers ( $n \geq 4$ ) in the RGO platelets which can significantly decrease their thermal conductivity [244]. The contribution of void fraction is investigated below.

#### 4.3.4.2.3. Contribution of void fraction in the thermal conductivity

It is interesting to point out that the thermal conductivity evolution of the PANI/RGO nanocomposites does not exhibit any thermal percolation which is in contrast to the behavior of other graphene-based nanocomposites as predicted by theoretical studies [245,246]. In addition, our results show that the effective thermal conductivity of the composites is much lower than that of their graphene-based counterparts. We believe that the thermal results are very much dependent on the density (Figure 91) of the nanocomposites. As shown in Figure 91 the result shows a quasi linear plot.

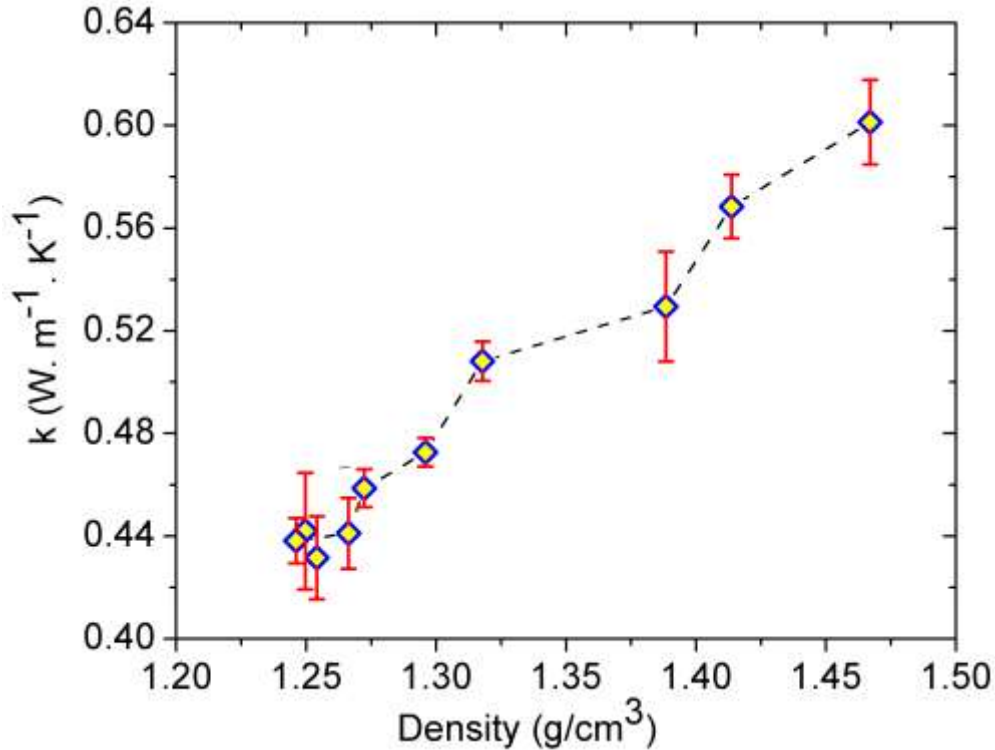


**Figure 91.** Thermal conductivity ( $k$ ) as a function of density of PANI/RGO composites.

Thus, the results indicate that the rise in thermal conductivity ( $k$ ) is directly correlated to an increase in density which in turn is “directly” proportional to the RGO loading. The increase in  $k$  values is, however, offset by the presence of air interfaces located in between PANI and RGO aggregates. Presumably, these voids arose from aromatic rings/ $\pi$ - $\pi$ , Van der Waals interactions between the high aspect ratio RGO platelet sheets [244] thereby lowering to some extent their interactions with the polymer host [24]. Figure 92 the void content in the nanocomposites which was determined from the experimental and theoretical densities using the following equation:

$$\text{Void fraction} = \frac{\rho_{\text{theoretical}} - \rho_{\text{experimental}}}{\rho_{\text{theoretical}}} \quad 54$$

where  $\rho_{experimental}$  and  $\rho_{theoretical}$  are the experimental and theoretical densities of the nanocomposites.

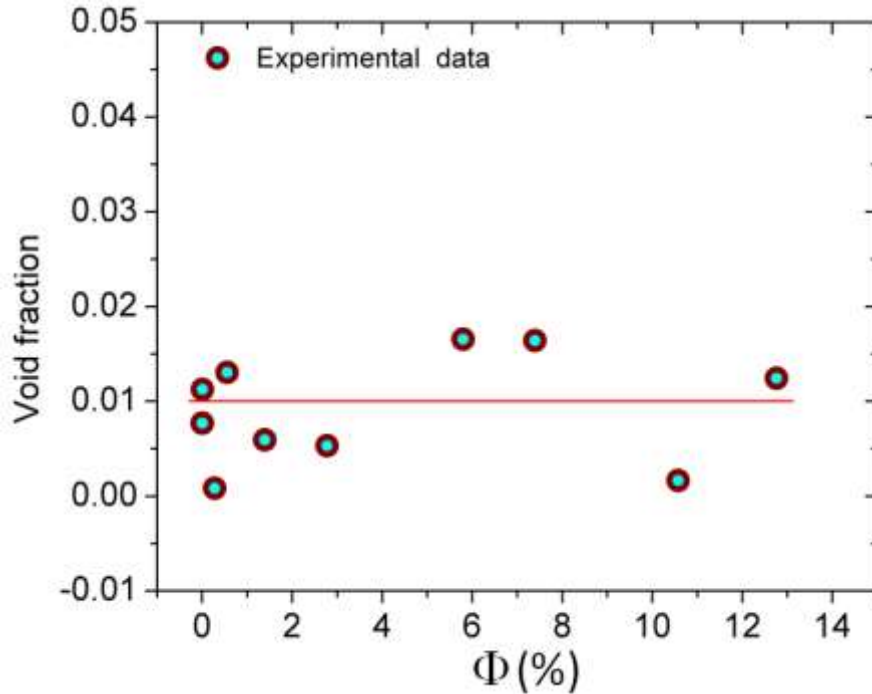


**Figure 92.** Void fraction of the nanocomposites as a function of RGO volume fraction and red solid line is for eye view.

Our computations provided a void fraction of  $\sim 1\%$  for all samples. This defect acts like an insulating layer which mitigates thermal transport phenomena, resulting in the observed lowered conductivity. Consequently, the measured thermal conductivity enhancement of PANI/RGO nanocomposites failed to match the theoretical prediction of the thermal conductivity enhancement of the graphene based polymer composites. And thus, the overall effective thermal conductivity of the nanocomposites can be contributed for the thermal conductivity of PANI ( $k_{PANI}$ ), RGO ( $k_{RGO}$ ), and void ( $k_{void}$ ). The finding indicates that the low thermal conductivity values are not only for 1% void but also it can be related to PANI/RGO interfacial contribution ( $k_{interface}$ ). But the lowered thermal conductivity of PANI/RGO nanocomposites could be exploited for the fabrication of thermoelectric materials for which thermal conductivity should be as much as minimum.

#### 4.3.4.3 Volumetric heat capacity

The thermal properties of the composites are further evaluated through their volumetric heat capacity ( $\rho C$ ) change as a function of RGO nano-fillers (equation **36** and **37**). The result, displayed in Figure **93**, leads to a trend similar to that of the corresponding volumetric heat capacity (Figure **86(b)**), i.e., the volumetric heat capacity of the nanocomposites barely changes at low RGO (<6%) content but increases beyond that percentage to reach a value as high as  $4.88 \pm 0.92 \text{ MJ.m}^{-3} \cdot \text{K}^{-1}$  for a 12.76 Vol-% RGO sample which is unexpected since reported values of binary composites are generally much lower [247]. But it can be seen that the values of volumetric heat capacity for same sample obtained by two different methods (laser flash and DSC methods and PTR) provides significant differences between two values. The nature of the experiments is responsible for these differences.

The obtained  $\rho C_{\text{PANI}}$  allows us to calculate the % volumetric heat capacity enhancement ( $\text{VHCE \%} = (\rho C - \rho C_{\text{PANI}}) \times 100 / \rho C_{\text{PANI}}$ ) for composites of lower % RGO to the highest 12.76 vol-% sample which provided a VHCE of 142%. It is of interest to point out that a) compared to the reported values of specific heat increments of other hybrid systems [247], our composites exhibits a remarkable HCE and b) in the present study, the VHCE is almost five times higher than that of the corresponding thermal conductivity enhancement (36% for the same sample).

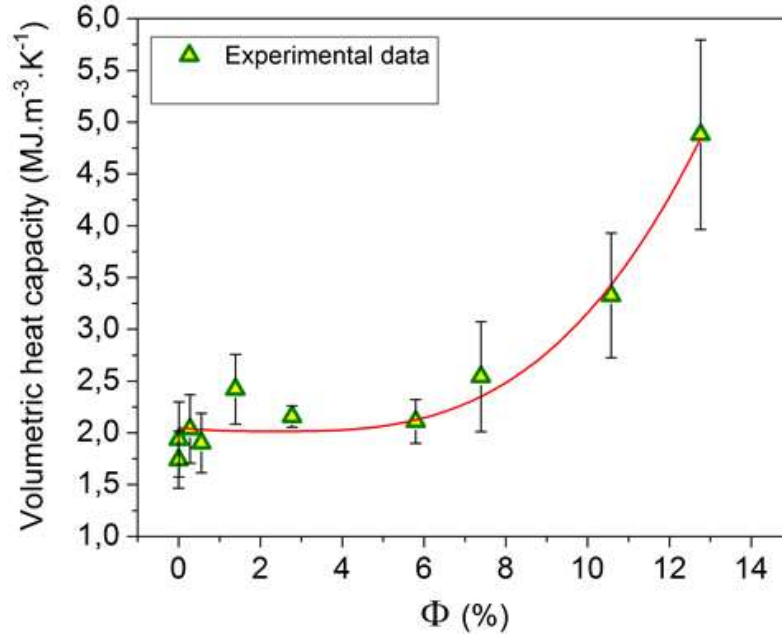


**Figure 93.** Volumetric heat capacity ( $\rho C$ ) of the nanocomposites as a function of RGO volume fraction.

A discussion on the overall thermal trend must include the topic of inhomogeneity of the composites and a block diagram featuring the host, filler and their interface is depicted in Figure 94 is proposed for this purpose. That is, heat transport is not only dependent on the morphology of the bulk composites, its propagation is intimately tied to the nature of the interface present in between RGO and PANI since polymerization produces some RGO (core)/PANI (shell) structures as supported by Figure 68 and 69 above. Thus, we believe that nano-confined structures are present within the PANI/RGO interfaces. Due to the large mismatch in the thermal conductivity of RGO and PANI, energy transfer from one component of the composite to the other is somewhat impeded by the above-mentioned confined features which could entrap and store heat. In a sense, these heat storage sites can be assimilated to nano-heat capacitors whose number increases with increasing RGO loading (Figure 95). Therefore, the observed drastic VHCE (Figure 93) could be attributed to the gradual increase in RGO%.

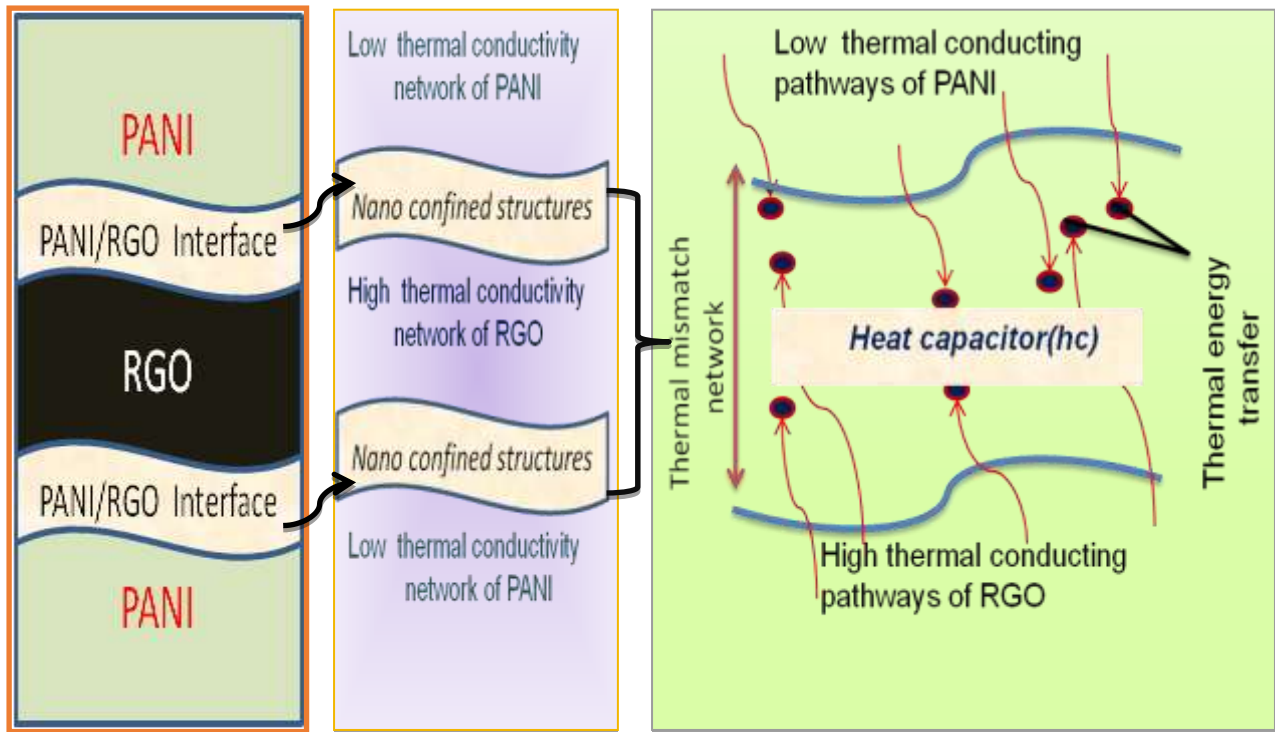


**Figure 94.** Block diagram of induced heat capacitor phenomena of PANI/RGO nanocomposite.

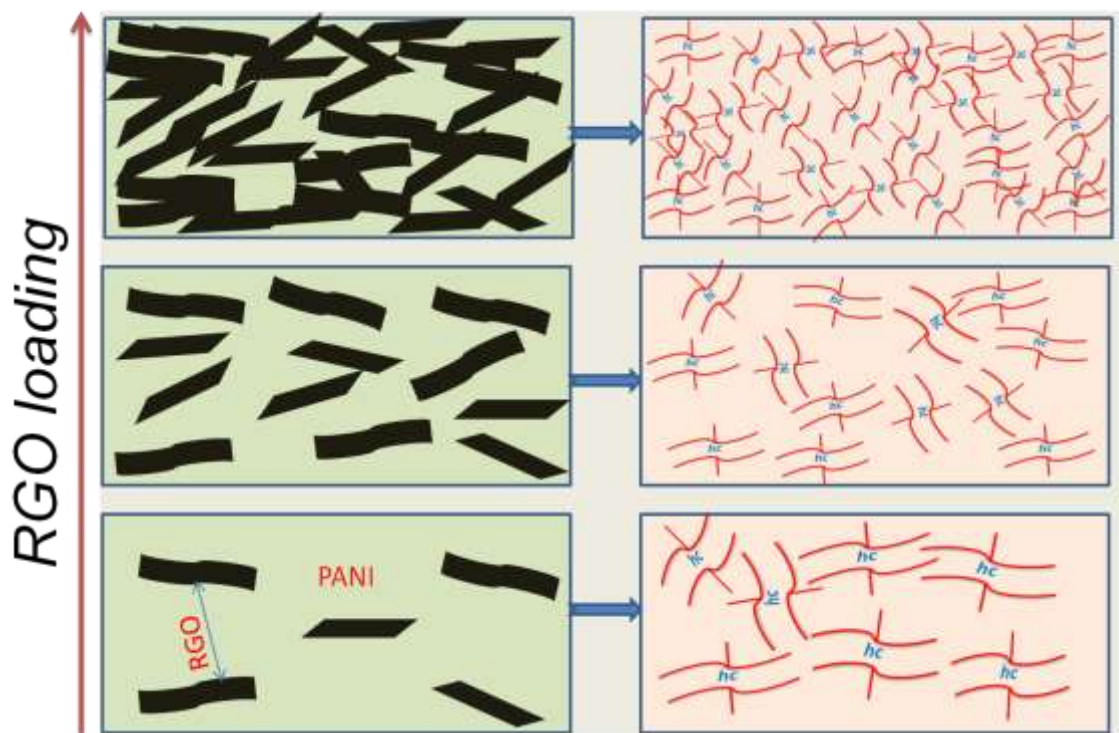


**Figure 95.** Schematic diagram of induced heat capacitor as a function of RGO volume fraction.



#### 4.3.4.4 Heat absorption capability

To gain further insights into the thermal properties of the composite, we have assessed its heat storage factor or heat absorption per unit area factor,  $Q$  ( $\text{J}/\text{m}^2$ ), which is defined as [248]:

$$Q = \rho C \times L_s \times T_m(x,t) \quad 55$$

where,  $\rho C$  is the volumetric heat capacity of the sample,  $L_s$  is thickness of the sample and  $T_m$  is the maximum temperature raised at the back surface of the sample which is a function of thickness ( $x$ ), where the maximum temperature is measured, and time ( $t$ ) required for the back surface to reach maximum temperature. If we consider a one-dimensional heat transport model, as shown in Figure 96 then  $T_m$  can be expressed as [249]:

$$T_m(x,t) = xt^{-3/2} \exp(-x^2/4\alpha t) \quad 56$$

where,  $\alpha$  is the thermal diffusivity of the sample.

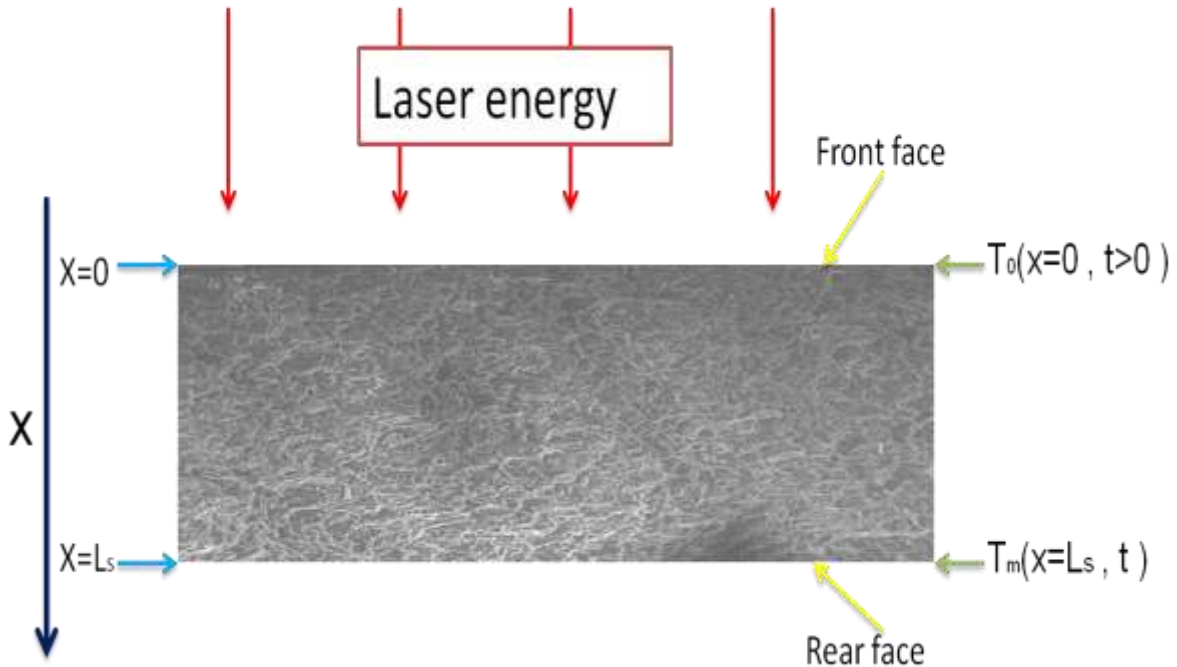


**Figure 96.** Schematic diagram of one dimensional geometry for heat conduction problem in a solid.

We also consider the following assumption:

$$T_m(x,t) = 0 \quad \text{for } x=0 \text{ and } t>0 \quad 57$$

The maximum temperature raised at the back surface can be calculated from the half maximum temperature raised as  $T_{m/2} = (T_m/2)$ . Inserting the values of thickness of the sample ( $L_s$ ) and  $t_{1/2}$  (which is the time required for the back surface to reach half maximum temperature rise) into equation **56**, the result leads to:

$$T_{m/2}(L_s, t_{1/2}) = L_s t_{1/2}^{-3/2} \exp(-L_s^2/4\alpha t_{1/2}) \quad 58$$

where,  $t_{1/2}$  is defined by the following equation [248]:

$$t_{1/2} = (1.38 L_s^2) / (\pi^2 \alpha) \quad 59$$

Thus, the heat storage factor or heat absorption per unit area factor,  $Q$  ( $J/m^2$ ) factor is obtained through the manipulations of the above equations.

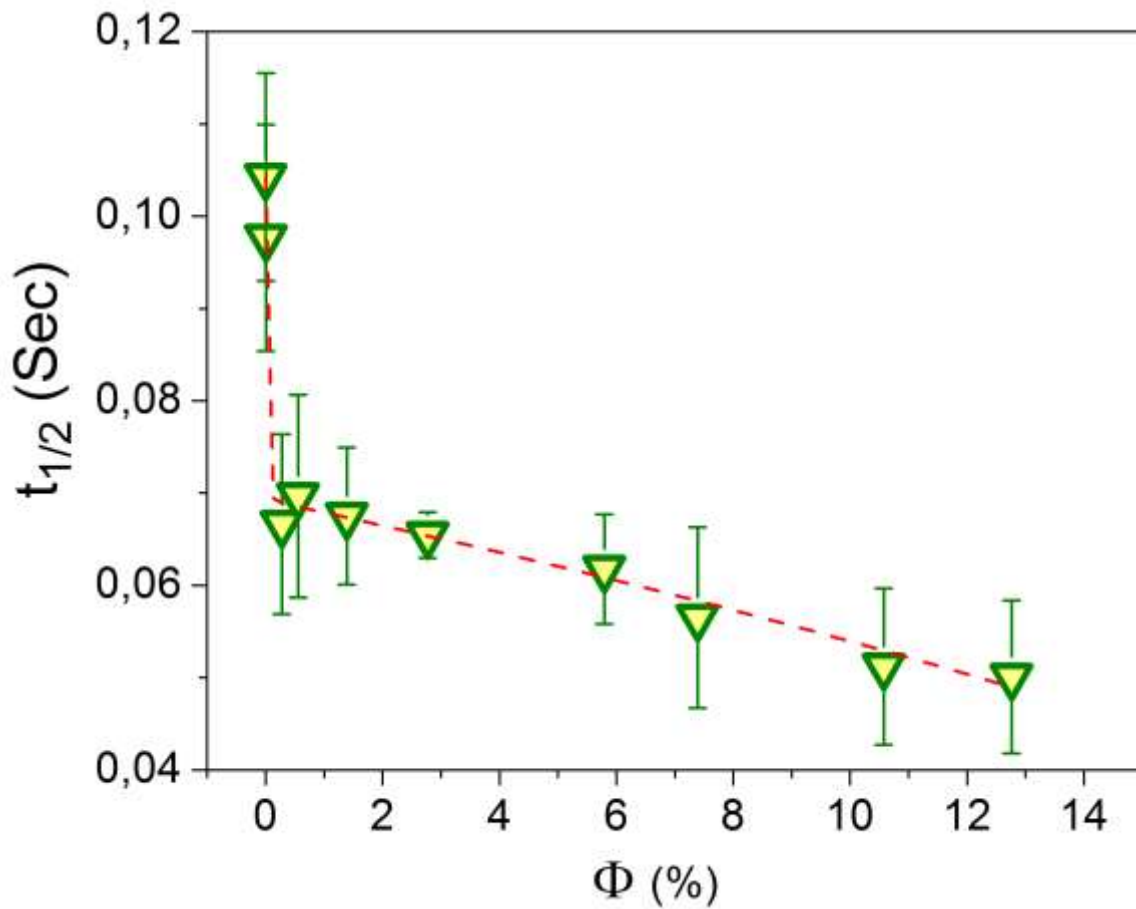


**Figure 97.** Time ( $t_{1/2}$ ) required for the back surface to reach half maximum temperature rise as a function of RGO volume fraction. Dashed line is guides to the eyes.

Figure 97 illustrates the calculated time ( $t_{1/2}$ ) required for the back surface to reach half maximum temperature rise as a function of volume fraction of RGO in nanocomposites. It can be observed that  $t_{1/2}$  is decreased with increasing volume fraction of RGO nano-fillers. We can infer that, in general, a higher content of RGO nano-fillers in the nanocomposites produces more thermal conducting pathways which reduce the time ( $t_{1/2}$ ) required for the back surface to reach half maximum temperature rise. We note that an amount of RGO as little as <1 vol-% is sufficient to cut the  $t_{1/2}$  by ~ 42%, additional RGO induces a less drastic time reduction.

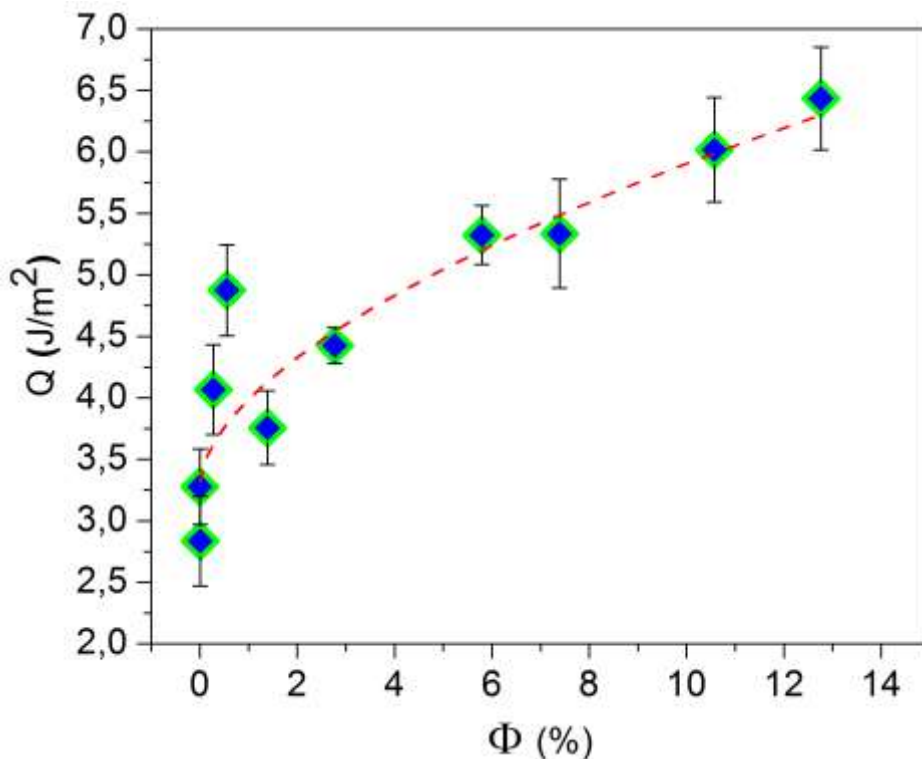


**Figure 98.** Heat storage factor or heat absorption per unit area or  $Q$  ( $\text{J}/\text{m}^2$ ) factor as a function of RGO volume fraction. Dashed line is guides to the eyes.

The data obtained from the previous computations allowed us to plot  $Q$  ( $\text{J}/\text{m}^2$ ) vs. RGO% (vol-%) as shown in Figure 98 which mirrors the trend displayed in Figure 98 i.e.  $Q$  factor rises with increasing vol-% of fillers. These results lend further support to our previous assumption that the presence of nano-confined structures, embedded into the composites, act as heat storage “nano-facilities” whose heat trapping capability is enhanced with higher RGO contents. The result further highlights the usefulness of PANI/RGO nanocomposites as critical components of heat storage/capacitive thermal management devices such lithium-ion batteries [250].

### 4.3.5. Seebeck coefficient(S) and power factor (PF)

The experimental evolution of Seebeck coefficient is presented in Figure 99(a). The S values obtained are all positive which is consistent with a p-type semiconductor like PANI, i.e., holes are the dominant contributors to electrical conductivity. Here it can be seen that Seebeck coefficient for low RGO loading composite is almost 22  $\mu$  V/K which is much greater than the Seebeck coefficients of low SWCNT and MWCNT loading composites. This different result can be due to the dimensionality effect since RGO is used as 2D nanofiller and SWCNT and MWCNT are used as a 1D nanofillers.

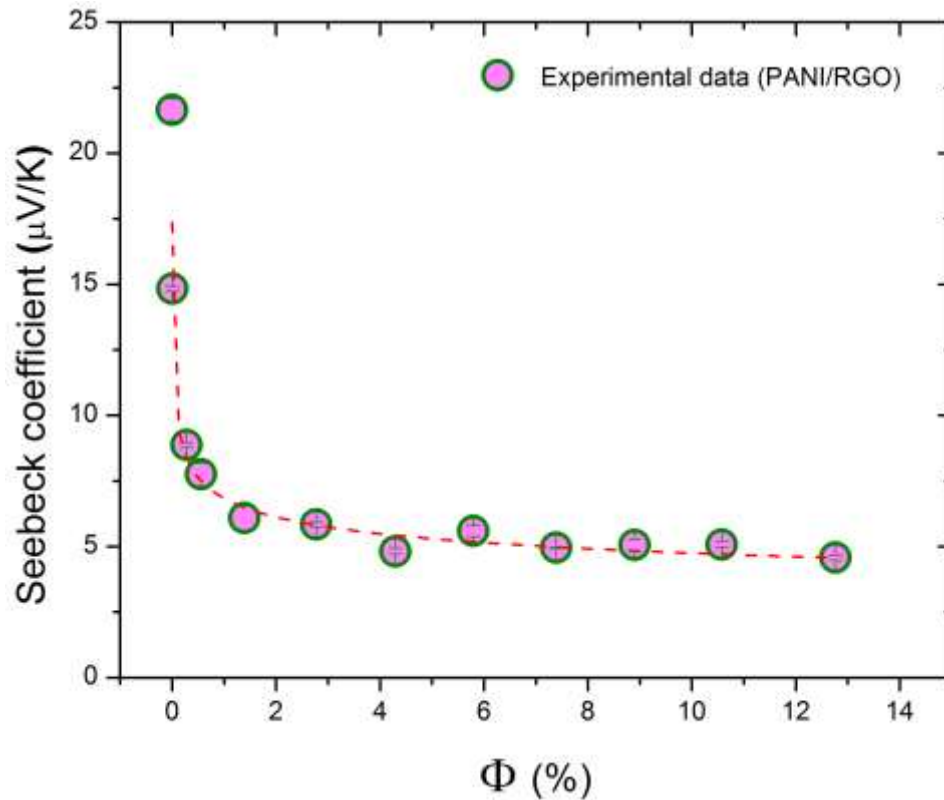


**Figure 99.** Experimental evolution of Seebeck coefficient (S) as function of vol-% RGO. Dashed line is guides to the eyes.

The behavior of the Seebeck coefficient can be interpreted by equation 22. The equation explains that Seebeck coefficient is inversely proportional to carrier concentration. Figure 100 depicts Seebeck coefficient decreases with increase electrical conductivity. Therefore,  $S$  decreases with increasing RGO content which can be related to an increase of the charge carrier concentration.

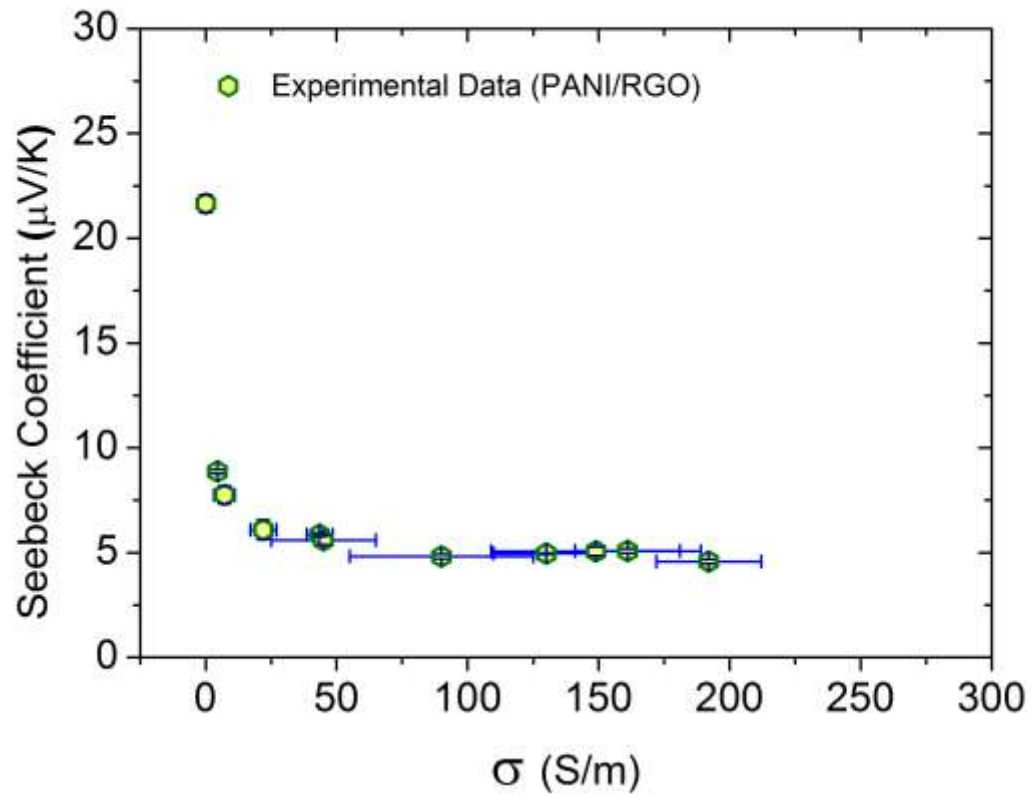


**Figure 100.** Experimental evaluation of Seebeck coefficient ( $S$ ) of PANI/RGO composites as function of electrical conductivity.

The TE power factor (PF) has been calculated using the equation 43. In contrast to  $S$ , PF increases sharply with RGO loading as displayed in Figure 101 evidencing that out of  $S^2$  and  $\sigma$ , the latter is the dominant parameter that significantly raises the PF values. As fillers of the PANI

matrix, RGO platelets may act like a “co-dopant” of PANI along with camphor sulfonic acid thereby enhancing significantly the overall electrical conductivity of the composites at the expense of  $\alpha$  as noted above. This conflicting trend is often attributed to an increase in charge carrier concentration taking place without any significant enhancement of their mobility. Such a phenomenon has also been observed in semi-conductor-based thermoelectric materials [165,167].

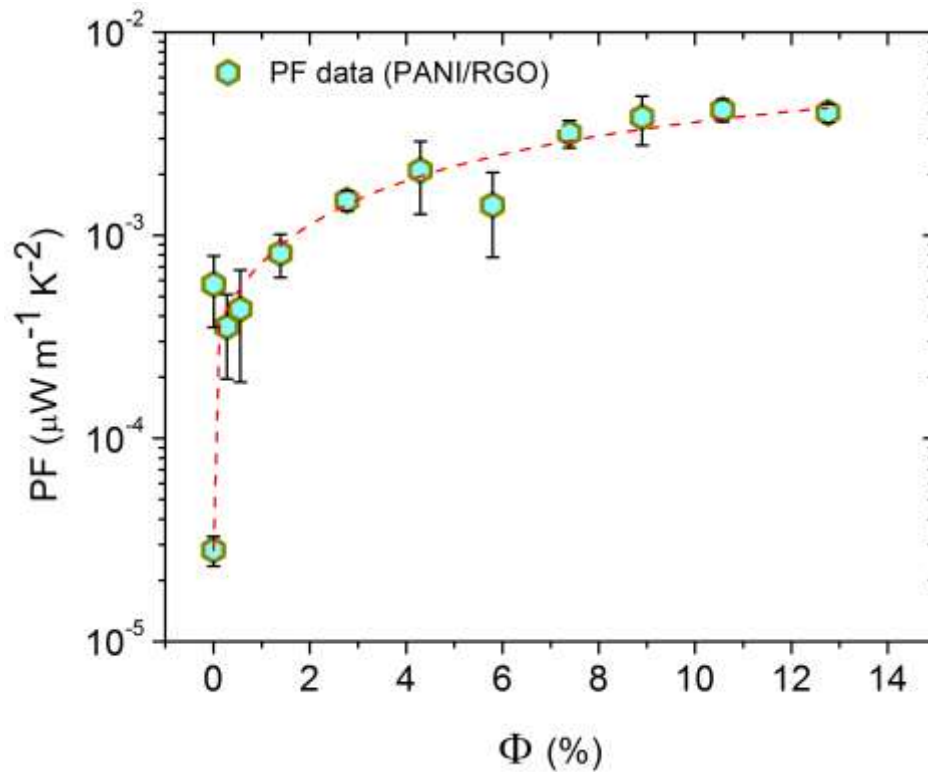


**Figure 101.** Power factor (PF) vs vol-% RGO. Dashed line is guides to the eyes.

### 4.3.6. Thermoelectric properties

As can be seen in Figure 102, ZT increases rapidly with increasing RGO content then levels off at a maximum value of ca.  $5 \times 10^{-6}$  which is two orders of magnitude higher than that of pure PANI. It is also interesting to note that the sharp rise in ZT occurs at low RGO loading (<3%). That is, the ZT enhancement relies mainly on the increase of the electrical conductivity “buffered” by a limited rise in thermal conductivity.

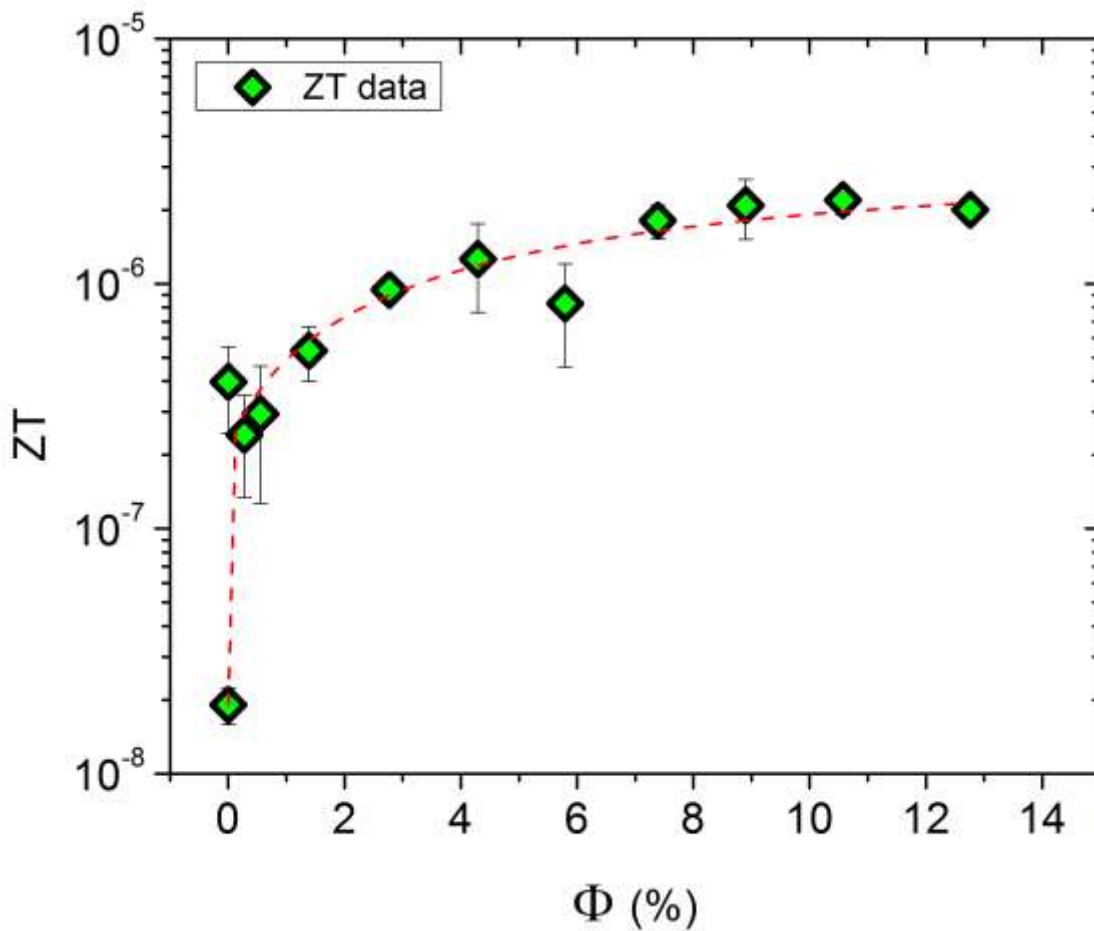


**Figure 102.** Thermoelectric performance (ZT) of PANI/RGO nanocomposites.





# CHAPTER 5 COMPARATIVE STUDY OF 1-D AND 2-D CARBONACEOUS NANO-FILLERS-BASED NANOSTRUCTURED COMPOSITES

Here we propose a comparative study of contributions of 1-D and 2-D carbonaceous nano-fillers in polyaniline composites. Carbonaceous materials with different dimensions such as, SWCNT (1-D), MWCNT (1-D), and RGO (2-D) were used as filler whereas polyaniline was used as common matrix to synthesize all nanostructured composites. It is also noticeable that the values of electrical conductivities of SWCNT (1-D), MWCNT (1-D), and RGO (2-D) are similar ( $10^2$  S/m). These three different composites, such as PANI/SWCNT, PANI/MWCNT, and PANI/RGO nanocomposites were prepared in the same conditions (i.e. same temperature, same environment, and same method etc.) as described in chapter 3. However, in the present chapter a comparative study based on the influences of different dimensions carbonaceous nano-fillers on morphological, electrical, thermal, Seebeck coefficient, thermoelectric, and interfacial properties of the polyaniline/carbonaceous nanostructured composites is conducted to highlight the dimensional effect in these properties of the composites.

## 5.1. Morphological study

The influence of carbonaceous nano-fillers with different sizes and shapes on morphology of polyaniline composites is being highlighted. 2-D RGO nanoplatelets are compared with 1-D rod-like carbon fillers such SWCNT and MWCNT for morphological investigation.

The morphology of PANI/SWCNT, PANI/MWCNT, and PANI/RGO nanocomposites have been presented in section 4.1.2, 4.2.2, and 4.3.2 respectively. A schematic diagram of the morphology of the PANI/SWCNT, PANI/MWCNT, and PANI/RGO nanocomposites as function of filler concentration is presented in Figure 103. Figure 103(a), (b) and (c), depict the morphology of pure PANI. It can be observed that the matrix used for three different composites follows the same morphology. At low filler loading, a rich domain of matrix (PANI) is shown for

all the three composites which are cartooned in Figure **103**(d), (e), and (f). Further inclusion of fillers favors the mixed morphology of matrix and core-shell structures of the nanocomposites which are schematically sketched in Figure **103**(g), (h), and (i). But, at high filler loading, resultant structures (core-shell structures) of fillers and matrix are dominated in the morphology of the nanocomposites, which is presented in Figure **103**(j), (k), and (l).

On TEM images, it is clearly visible that the filler surface was covered by the polymer layer resulted in core-shell structures in which filler is core whereas shell consists of polyaniline. These structures suggest good interaction between filler and matrix. Inclusion of 2-D nano-fillers into matrix makes layer like core-shell structures but addition of 1-D nano-fillers (SWCNT and MWCNT) into polyaniline gives rod-like core-shell structures. In the morphology of PANI/SWCNT, bundle of SWCNT is observed as core. In addition to the  $\pi$ - $\pi$  interaction, the Van der Waals one between fillers results in presence of significant agglomeration [251], and generally, Van der Waals interaction is more strong in SWCNT than MWCNT and RGO.

It can be seen that fillers keep their original diameter (for SWCNT and MWCNT) or thickness (for RGO) at all concentration loading. But the shell thickness as well as diameter of polyaniline fibers of the nanocomposites is reduced with fillers loading. Inclusion of all dimensions fillers gives almost same amount of reduction of the diameter of polyaniline fibers and thickness of the shell layer at same concentration loading. Thus, the change of the diameter of polyaniline fibers and thickness of the shell layer is almost insensitive to dimensionality of the fillers. In conclusion, it can be said that the structure of nanocomposites usually consists of the matrix material containing the nanosized reinforcement components in the form of nanotubes (1-D), nanoplatelets (2-D) etc.

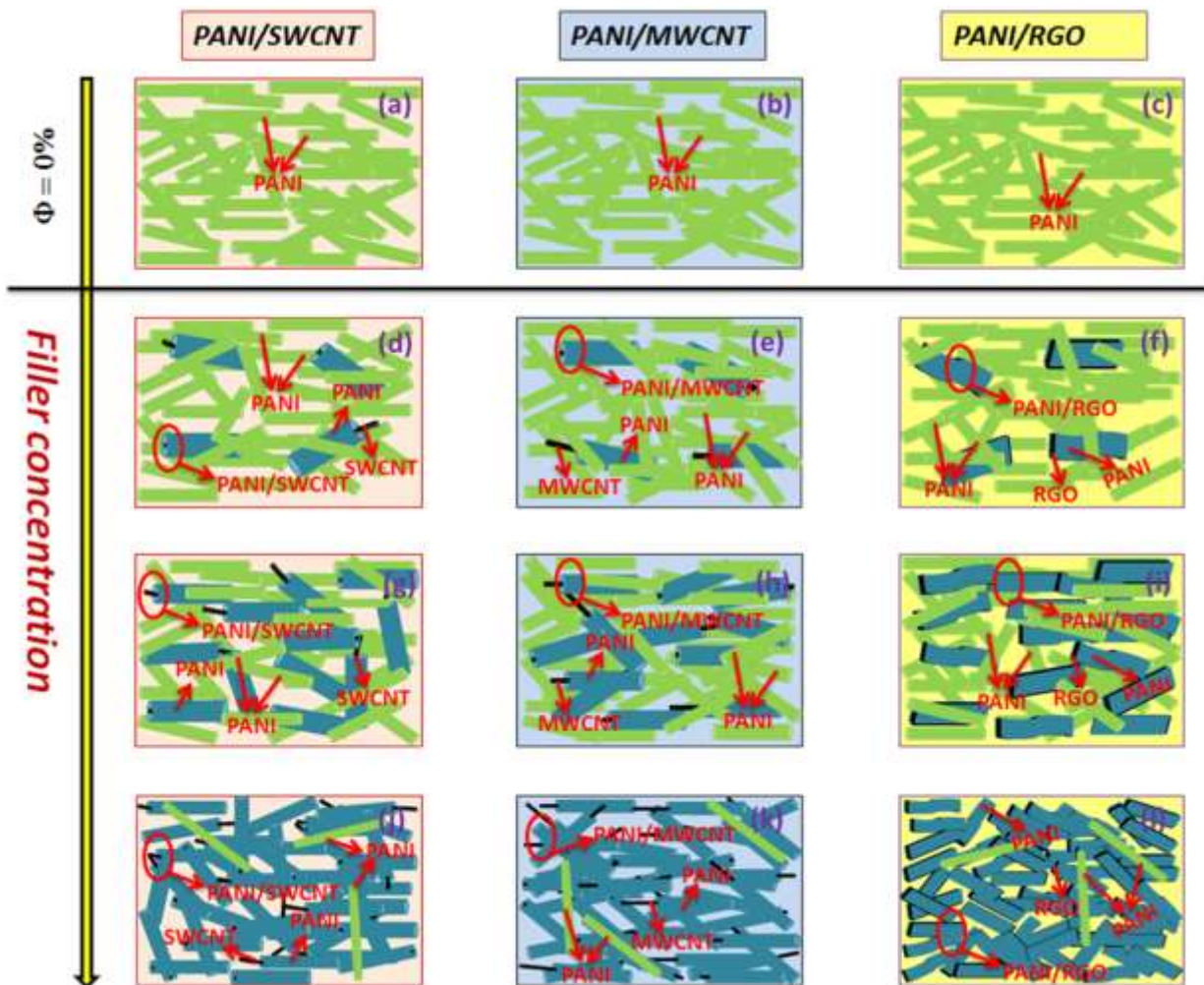


**Figure 103.** Schematic diagram of the morphology of the PANI/SWCNT, PANI/MWCNT, and PANI/RGO nanocomposites as function of filler concentration.

## 5.2. Electrical properties

A comparative study of the electrical phenomena in the different carbonaceous nano-fillers based polymer composites is discussed.

Carbonaceous fillers are employed in the production of polymer composites, to increase relatively electrical conductivity ( $>10$  S/m) , compared with that of common polymers of less than  $10^{-14}$  S/m, as well as to maintain light weight and corrosion resistance [28,29]. In the present work, the chosen conducting carbonaceous fillers included SWCNT, MWCNT, and RGO have similar conductivity ( $10^4$  S/m) whereas the synthesized pure PANI shows a conductivity of  $\sim 0.05$  S/m. As shown in Figure 104 the addition of SWCNT into polymer matrix leads to much larger electrical conductivity enhancement at same fillers content, than the addition of MWCNT and RGO. In Table 6, the highest values of electrical conductivity enhancement for PANI/SWCNT, PANI/MWCNT and PANI/RGO nanocomposites, are found to be  $2.8 \times 10^3$  at 12.25 vol-% ,  $4.7 \times 10^2$  at 12.01 vol-% and  $1.9 \times 10^2$  at 12.76 vol-% filler loading respectively.

**Table 6.** The maximum values of electrical conductivity of the composites.

| Samples    | maximum electrical conductivity enhancement $[(\sigma - \sigma_{\text{PANI}}) / \sigma_{\text{PANI}}]$ | $\Phi$ (%) for maximum electrical conductivity enhancement |
|------------|--|--|
| PANI/SWCNT | $2.8 \times 10^3$  | 12.25  |
| PANI/MWCNT | $4.7 \times 10^2$  | 12.01  |
| PANI/RGO   | $1.9 \times 10^2$  | 12.76  |

However, all three types of fillers are randomly distributed in polymer matrix, but SWCNT fillers contribute more to the formation of conductive network. Thus, PANI/SWCNT composite exhibits higher electrical conductivity than PANI/MWCNT and PANI/RGO composites. It can be seen that the geometrical shape of the fillers has a significant effect on electrical properties of the composites. So enhancement in electrical conductivity of the composites not only depends on the conductivity of the fillers but also depends on other factors such as dimensionality of the filler.

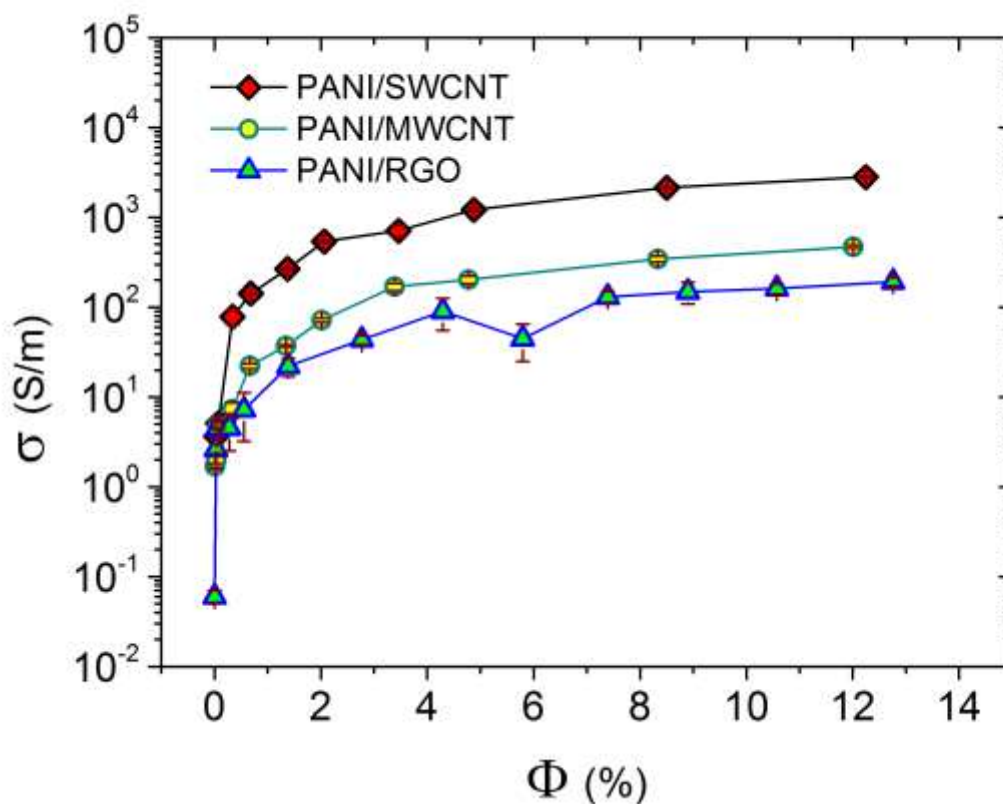


**Figure 104.** Electrical conductivity of all fillers based nanocomposites as function of volume loading of the fillers.

The volume fraction dependent electrical conductivity of all three composites have been interpreted by using mixing rule (upper bond) which were presented in section 4.1.3, 4.2.3, and 4.3.3. The results reveals that the conductivity values of matrix and fillers as used in the composites differ from the values of pure PANI (0.05 S/m) and fillers ( $10^4$  S/m). But the electrical conductivity value ( $\sigma_{\text{filler}} = 21288$  S/m) of SWCNT as used in nanocomposites is greater than MWCNT and RGO as used in the composites suggesting the dimensionality effect on conducting network in composites. However, the result reveals the modification of conducting state of matrix and fillers. In all three composites, this modification can be interpreted through the concept of charge transfer mechanism between matrix and fillers.

Also the construction of the conductive network in the composites has been analyzed with regard to the critical concentration of fillers by a percolation scaling law (section 4.1.3, 4.2.3, and 4.3.3). The values of all parameters such as  $\Phi_c$  (the volume percolation threshold),  $t$  (the critical exponent), and  $\sigma_0$  (the electrical conductivity prefactor) are tabled in Table 7.

**Table 7.** Percolation ( $\Phi_c$ , and  $t$ ) parameters of the composites reinforced with different fillers

| Samples    | $\Phi_c$ (%) | $t$  |
|------------|--------------|------|
| PANI/SWCNT | 0.004        | 1.04 |
| PANI/MWCNT | 0.07         | 1.11 |
| PANI/RGO   | 0.098        | 0.98 |

The results reveal the percolation threshold  $\Phi_c$  of 0.004, 0.07, and 0.098 vol-% for PANI/SWCNT, PANI/MWCNT, and PANI/RGO composites respectively. These values imply that PANI/SWCNT composites have much lower percolation threshold and higher electrical conductivity than PANI/MWCNT and PANI/RGO composites. By using the fitting with percolation scaling law, the values of critical exponent ( $t$ ) for PANI/SWCNT, PANI/MWCNT, and PANI/RGO composites have been obtained to be 1.04, 1.11, and 0.98 respectively. It can be seen that although different fillers based composites have different electrical conductivities as well as percolation threshold, there are almost same  $t$  values. The low  $t$  values for PANI/SWCNT, PANI/MWCNT can be correlated to the aggregation process which can influence the effective conductive network. Actually low  $t$  values for 1D fillers based composites do not really in adequation with conventional percolation behavior. But  $t$  value for PANI/RGO composites represents two-dimensional (2-D) conductive system which is evidenced by nanoplatelets morphology of the nanocomposites. Thus the conductive system of the all nanocomposites can be explained by the morphology of the composites. It also can be observed that the impact of charge transfer on electrical transport can affect the percolation network.

S. H. Xie et.al. [252] showed in a theoretical study that 2-D fillers (nanosheets) filled composites have slightly lower percolation threshold and higher electrical conductivity and critical exponent, and can form conductive networks more easily than 1-D fillers (CNT) filled composites at the same volume fraction of fillers. In this regard, it can be seen that our result shows contradiction of those theoretical results. These completely contrary results can be explained by the following reasons:

- (i) 1-D (SWCNT and MWCNT) fillers can be more easily dispersed in the polymer matrix than 2-D (RGO) because RGO fillers are apt to wrinkling and crimping, and even rolling into a tube-like structure which usually has a larger diameter than MWCNT and SWCNT [32] which is evidenced in morphological study of PANI/RGO composites
- (ii) Because of extremely larger surface area of RGO, many types of contact area such as plane-plane, edge-plane, edge-edge, and RGO surface-surface contact area are formed which can create more resistivity in the composites (as we know only plane-to-plane contact is helpful for charge transfer) while overlapping contact among SWCNTs and MWCNTs helps to build conducting network because overlapping behavior of SWCNTs and MWCNTs is the main way in charge transfer in these composites.
- (iii) In general, 2-D filler- matrix contact area is more than 1-D filler- matrix contact area. Thus, the presence of electrical mismatch network formed between filler and matrix because of high electrical conductivity of filler and low electrical conductivity of matrix is more in PANI/RGO composites than PANI/SWCNT and PANI/MWCNT composites. This electrical mismatch network can reduce the electrical conductivity in the composites.
- (iv) The presence of interconnected network is more in the composites filled with 1-D fillers than the composites filled with 2-D fillers. This network results in a dramatic increase in electrical conductivity of the composites.



- (v) The another important point is that charge transfer effect which can strongly modify the conducting behavior of matrix is different in 1-D fillers based composites than 2-D fillers based composites at same volume fraction because of different interfacial spaces. This phenomenon influences the formation of conductive network in the composites which significantly enhances the electrical conductivity of the composites.

As a consequence, based on above factors it can be said that the practical electrical conductivity of PANI/RGO composites is lower and their percolation threshold is higher than that of PANI/SWCNT and PANI/MWCNT composites. The above studied factors can influence the critical exponent as well as the conduction mechanism.

In summary, it is observed that in the three different kinds of carbonaceous nano-fillers based composites, three important processes influence the electrical conductivity in the composites. These are: (i) the electrical conductivity of the fillers, (ii) the formation of conductive network in the composites in which charge carriers move within the conductive framework, and (iii) charge transfer mechanism in composites. In addition, the electrical phenomena, the changes of electrical conductivities with different filler's type, and the mechanism of electron transport in these carbonaceous polymer composites are directly influenced by the dimensionality of the fillers dispersed in the polymer matrix. However, all three types of fillers are generally randomly dispersed in polymer matrix, but SWCNT fillers contribute more to the formation of conductive network.

### 5.3. Thermal properties

The effect of adding various carbonaceous nano-fillers on thermal properties of the three nanocomposites has been carried out in the previous chapter. More specifically, thermal diffusivity, volumetric heat capacity, and thermal conductivity of the nanocomposites have been investigated. The maximum thermal diffusivity values of the composites are presented in Table 8. It is shown that with respect to pure PANI ( $1.79 \times 10^{-7} \text{ m}^2/\text{s}$ ), the presence of the nano-fillers increases the thermal diffusivity of the nanocomposites. This result suggests that in comparison with MWCNT, and RGO, inclusion of SWCNT into PANI introduces more thermal conducting path resulting in the high thermal diffusivity at same concentration.

**Table 8.** The maximum thermal diffusivity values of the composites.

| Samples    | Maximum thermal diffusivity values ( $\text{m}^2/\text{s}$ ) | $\Phi$ (%) for the maximum values |
|------------|--|-----------------------------------|
| PANI/SWCNT | $4.50 \times 10^{-7}$  | 12.25                             |
| PANI/MWCNT | $2.65 \times 10^{-7}$  | 12.01                             |
| PANI/RGO   | $1.88 \times 10^{-7}$  | 12.76                             |

Furthermore, maximum volumetric heat capacity enhancement of the samples is displayed in Table 9.

**Table 9.** The maximum volumetric heat capacity enhancement of the composites.

| Samples    | maximum relative volumetric enhancement $[(\rho C - \rho C_{\text{PANI}}) / \rho C_{\text{PANI}}]$ (%) | $\Phi$ (%) for maximum relative volumetric enhancement |
|------------|--|--|
| PANI/SWCNT | 82   | 02.06  |
| PANI/MWCNT | 77   | 08.33  |
| PANI/RGO   | 85   | 10.57  |

It can be observed that inclusion of nano-fillers into PANI enhances the volumetric heat capacity of the composites. This result indicates that core-shell nanostructured materials provide a potential pathway for enhancing the heat storage capacity. This signature of volumetric heat capacity can be very useful in the application of thermal energy storage. In addition, dispersion of RGO nano-fillers into PANI matrix provides highest value (85%) of volumetric heat capacity enhancement in comparison with SWCNT (82%) and MWCNT (77%). Generally, large surface area can provide maximum interfacial area of matrix/fillers composites [22]. Heat storage can occur in that of interfacial area due to phonon mismatch at the interface of filler and matrix [22]. Here, RGO has a larger surface area than SWCNT, MWCNT. So, more interfacial area in PANI/RGO composites can provide maximum volumetric heat capacity. Thus, in comparison with 1-D fillers, 2-D fillers can create more storage density and can provide good heat storage materials.

To get further information on thermal properties, thermal conductivity of the nanocomposites has been studied as a function of fillers by using the values of thermal diffusivity and volumetric heat capacity. In previous chapter, the investigation of thermal conductivity of the three nanocomposites suggests that the observed enhancement in thermal conductivity is due to the introduction of the nano-fillers into PANI matrix. The values of the maximum thermal conductivity enhancement (%)  $[(k - k_{\text{PANI}}) \times 100 / k_{\text{PANI}}]$  of the three nanocomposites are listed in Table 10. It reaches up to 323% for PANI/SWCNT composites with 12.24 vol-% SWCNT content. In comparison with MWCNT (110%) and RGO (92%), the presence of SWCNT exhibits more thermal conductivity enhancement. It can be concluded that dispersion of SWCNT can form more continued thermally conductive pathways which allow heat transfer in the composites. This result also shows that PANI/RGO composites have low thermal conductivity enhancement. This behavior can arise due to high interfaces density limiting to the heat to flow in the nanocomposites. However, the dimensionality of the nano-fillers is found to have a significant effect on thermal conductivity enhancement. In this study, SWCNT is recognized as the best thermal conductive fillers because of its good thermal conductivity enhancement.

**Table 10.** The maximum relative thermal conductivity enhancement of the composites.

| Samples    | maximum relative thermal conductivity enhancement $[(k - k_{\text{PANI}}) / k_{\text{PANI}}]$ (%) | $\Phi$ (%) for maximum relative thermal conductivity enhancement |
|------------|---|--|
| PANI/SWCNT | 323   | 12.25  |
| PANI/MWCNT | 110   | 08.33  |
| PANI/RGO   | 89  | 10.58  |

Unlike electrical conductivity, thermal conductivity follows no percolation behavior. Several reasons can be proposed for this behavior:

- (i) The nano-fillers network is not sufficiently connected to allow heat transfer. Also it can be said that the thermal resistance between two adjacent nano-fillers is too high to transfer efficient direct heat in the composites.
- (ii) Another possibility can be that the heat transfer between adjacent PANI chains is not good enough to build a thermal percolation network.
- (iii) In the nanocomposites, there is also a poor heat transfer between PANI matrix and the nano-fillers. In general, at the interface of PANI matrix and the nano-fillers, thermal mismatch network is induced because of low thermal conductive pathways of PANI and high thermal conductive pathways of conductive nano-fillers. This can be related to interfacial thermal resistance which leads to several phonon scattering. So, heat transfer can be confined at the interface due to the thermal mismatch.

As a consequence, due to the above reasons, the enhancement of thermal conductivity in the nanocomposites cannot be described within the framework of percolation concepts. Thus, the enhancement of all three nanocomposites can be explained by making use of effective medium approaches.

## 5.4. Seebeck effect

Figure 105 represents the Seebeck coefficient of three composites as a function of filler content. It is shown that inclusion of the three different kinds of fillers into polymer matrix exhibits three different types of behavior. Seebeck coefficient of PANI/SWCNT increases with addition of filler whereas PANI/RGO shows the opposite trend. In the case of PANI/MWCNT composites, Seebeck coefficient decreases up to 3.39 vol-% MWCNT loading, but it increases at high concentration of MWCNT (>3.39 vol-%) as a function of volume fraction.

These results can be interpreted by the formula (equation 22) which indicates that Seebeck coefficient is directly proportional to carrier mobility and inversely proportional to effective electrical conductivity.

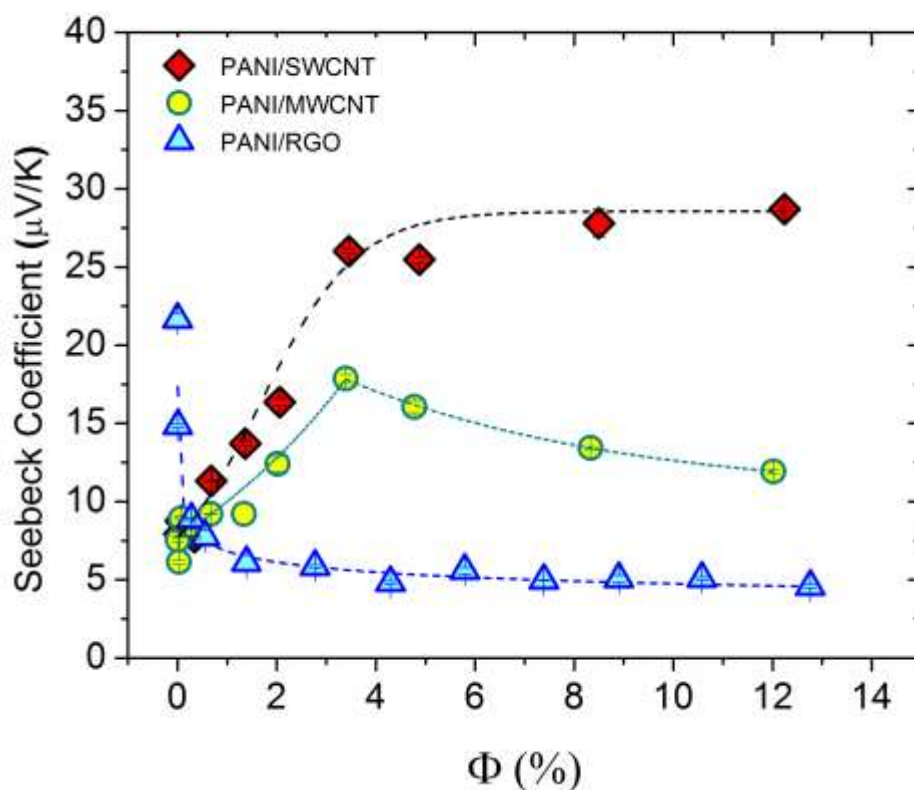


**Figure 105.** Seebeck coefficient (S) of PANI/SWCNT, PANI/MWCNT, and PANI/RGO composites

In PANI/SWCNT composites, although the charge carriers concentration is increased with high conducting SWCNT fillers loading, the Seebeck coefficient is increased as a function of the fillers concentration. Here, the study suggests that carrier mobility increases with the fillers loading, which strongly dominates the Seebeck coefficient behavior of those composites.

But PANI/RGO shows an opposite tendency which implies the reduction of carrier mobility in the composites. This reduced carrier mobility can be explained by a conventional model based on the band theory or scattering effect [126]. Especially, in 2-D heterogenous system, interfacial space plays a significant role which makes the surface roughness scattering in the composites. This scattering is on short range which limits the mobility of charge carrier at the interface. Due to this reduction of charge carrier mobility in the composites, the Seebeck coefficient decreases with RGO loading.

Furthermore, in PANI/MWCNT composites, charge carriers concentration is preponderant in Seebeck coefficient of the composites up to 3.39 vol-% MWCNT loading, but at higher concentration of MWCNT (>3.39 vol-%) carrier mobility actively handle the signature of Seebeck coefficient. It is very interesting to point out that at lower concentration MWCNT fillers play as 1-D filler whereas at higher concentration it plays as 2-D fillers in the behavior of Seebeck coefficient.

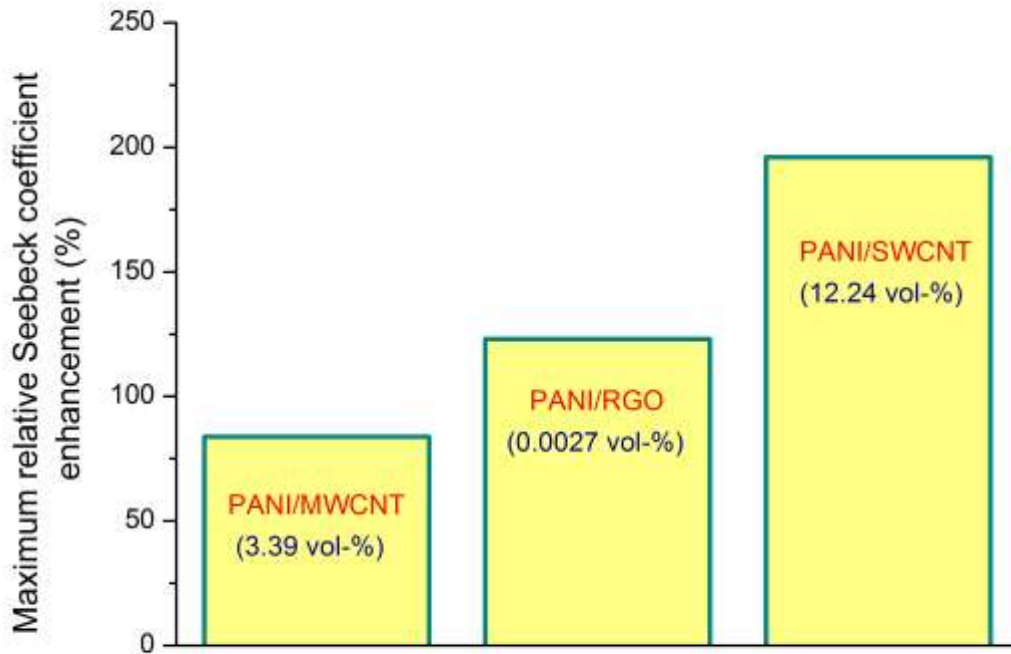


**Figure 106.** The maximum relative Seebeck coefficient enhancement (%) of the nanocomposites.

Figure 106 presents the maximum relative Seebeck coefficient enhancement (%)  $[(S - S_{\text{PANI}}) \times 100 / S_{\text{PANI}}]$  of the 3 different fillers based composites. It can be observed that the maximum relative Seebeck coefficient enhancement in PANI/SWCNT, PANI/MWCNT, and PANI/RGO composites are found to be 196%, 83%, and 123% at 12.25 vol-%, 3.39 vol-%, and 0.0027 vol-% respectively. This result insures that the enhancement in PANI/SWCNT is larger than in PANI/MWCNT and PANI/RGO composites. It also can be seen that the maximum enhancement in the PANI/SWCNT is achieved at higher concentration (12.25 vol-%) of SWCNT whereas in PANI/RGO, it is shown at lower concentration (0.0027 vol-%) of RGO. And in PANI/MWCNT composites, this value is in between the value of PANI/SWCNT and PANI/RGO composites. In conclusion, in comparison with MWCNT, and RGO filler, SWCNT filler is the good candidate for achieving the good Seebeck coefficient of the composites.

## 5.5. Power factor

If the thermal conductivity of the samples is almost unchanged, the power factor exhibits the performance of thermoelectric materials. The power factor enhancement as a function of volume fraction of PANI/SWCNT, PANI/MWCNT and PANI/RGO nanocomposites are displayed in Figure 107.

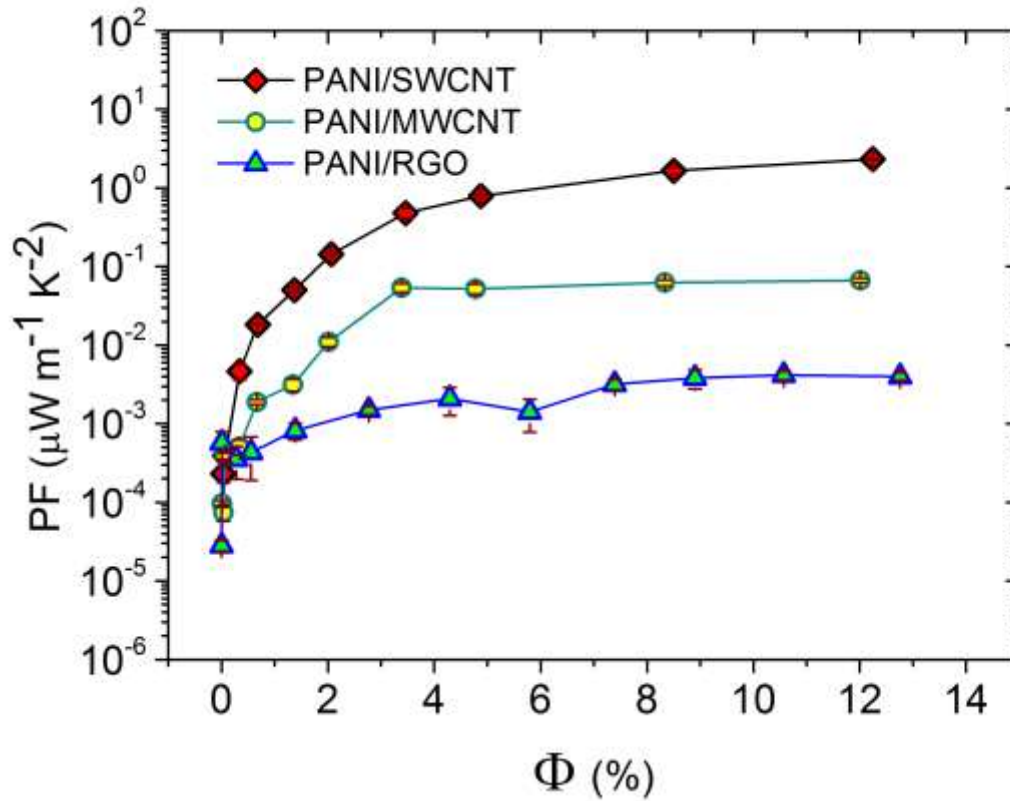


**Figure 107.** Power factor (PF) enhancement of all composites.

It shows that the power factors increases as a function of filler concentration since the value of pure PANI is almost  $\sim 4.77 \times 10^{-6} \mu\text{W m}^{-1} \text{K}^{-2}$ . As shown in Table 11, the maximum value of power factor reaches up to  $\sim 2.32 \mu\text{W m}^{-1} \text{K}^{-2}$  for PANI/SWCNT composites at 12.25 vol-%,  $\sim$



0.067  $\mu\text{Wm}^{-1}\text{K}^{-2}$  for PANI/MWCNT composites at 12.01 vol-% and  $\sim 0.004 \mu\text{Wm}^{-1}\text{K}^{-2}$  for PANI/RGO composites at 12.76 vol-%. In comparison with PANI/MWCNT and PANI/RGO composites, the power factor enhancement of PANI/SWCNT composites is larger.

**Table 11.** The maximum relative power factor enhancement of the composites.

| Samples    | maximum value of power factor<br>( $\mu\text{Wm}^{-1}\text{K}^{-2}$ ) | $\Phi$ (%) for maximum power factor value |
|------------|---|---|
| PANI/SWCNT | 2.32  | 12.25                                     |
| PANI/MWCNT | 0.067   | 12.01                                     |
| PANI/RGO   | 0.004   | 12.76                                     |

As shown in Figure 107, it can be seen that the power factor enhancement of PANI/MWCNT and PANI/RGO composites is slightly changed at higher loading of the fillers. This behavior can be attributed to Seebeck coefficient of the composites. Although the electrical conductivity of the composites increases at higher concentration of fillers, Seebeck coefficient decreases significantly. Thus, due to these different behaviors, the resultant factor ( $S^2\sigma$ ) hardly changes at higher concentration. In addition, in PANI/SWCNT the electrical conductivity and Seebeck coefficient simultaneously increase at high SWCNT content. Thus, the power factor is significantly enhanced at higher concentration of SWCNT. In conclusion, to achieve the high enhancement of the power factor, inclusion of 1-D fillers into polymer matrix is better than that of 2-D fillers.

## 5.6. Thermoelectric performance (ZT)

The ZT value of pure PANI is  $7.71 \times 10^{-9}$  which is very low as thermoelectric organic material. In order to enhance the performance, fillers with different dimensions such as 1-D (SWCNT, and MWCNT) and 2-D (RGO) have been dispersed in PANI matrix. The figure of merit (ZT) of PANI/SWCNT, PANI/MWCNT and PANI/RGO nanocomposites are displayed in Figure 108.

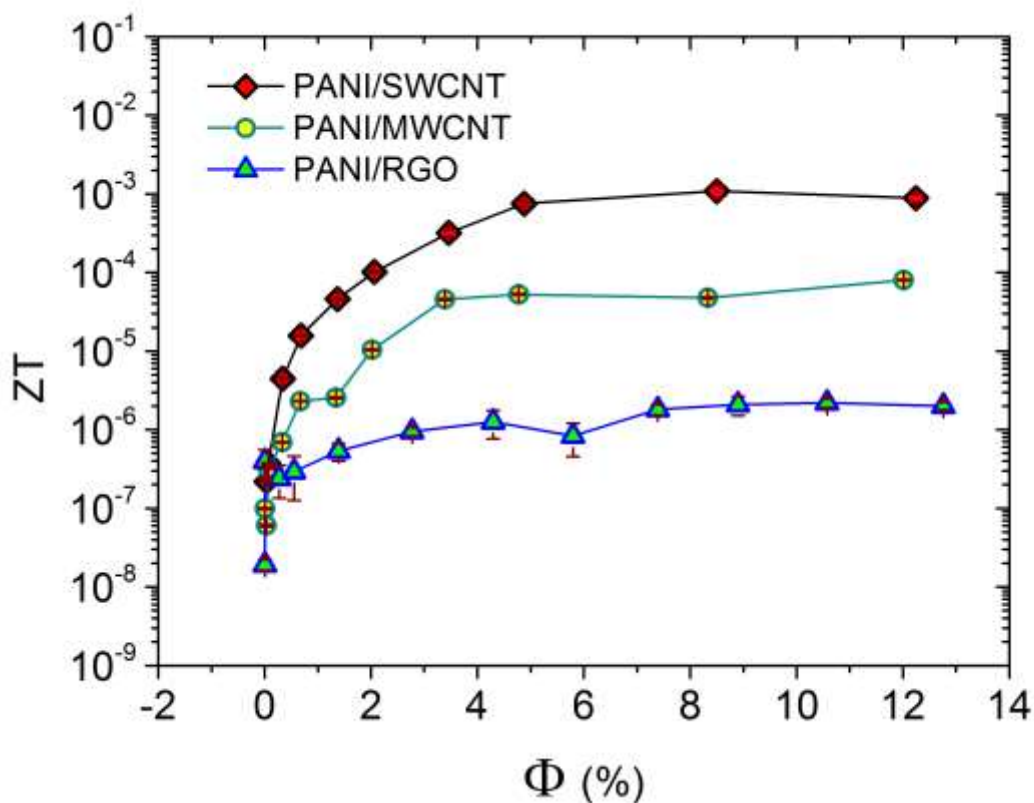


**Figure 108.** Figure of merit (ZT) enhancement of all composites.

As shown in Figure 108, the ZT value of PANI/SWCNT composites increases with the SWCNT content. As shown in Table 12, a maximum value of 0.0011 is reached for PANI/SWCNT composite for 8.50 vol-% SWCNT content. Like SWCNT, ZT increases with inclusion of MWCNT and RGO nanofillers. The maximum values of  $8.01 \times 10^{-5}$  and  $3.75 \times 10^{-6}$

are determined for PANI/MWCNT and PAN/RGO composites for 12.01 vol-% and 12.76 vol-% fillers content respectively.

**Table 12.** The maximum relative power factor enhancement of the composites.

| Samples    | Maximum ZT            | $\Phi(\%)$ for maximum ZT |
|------------|-----------------------|---------------------------|
| PANI/SWCNT | 0.0011                | 8.50                      |
| PANI/MWCNT | $8.01 \times 10^{-5}$ | 12.01                     |
| PANI/RGO   | $3.75 \times 10^{-6}$ | 12.76                     |

The thermoelectric performance is inversely proportional to thermal conductivity of the samples. Even although thermal conductivity of the composites is increased, ZT is enhanced with filler concentration. Moreover, thermal conductivity values of all the nanocomposites are quit low ( $< 1 \text{ W/m}\cdot\text{K}$ ) which is almost insensitive to the ZT enhancement. Thus, this signature of ZT enhancement in all the nanocomposites suggests that significant increased power factor of the composites with low thermal conductivity can contribute strongly to make the thermoelectric performance better. In addition, it can be observed that the thermoelectric performance is better in PANI/SWCNT than PANI/MWCNT and PANI/RGO composites. However, low thermal conductivity value of the composites can be very useful to achieve the good thermoelectric performance. The above study insures that in comparison with 2-D fillers, 1-D filler based polymer nanocomposites can be the best candidates for next generation organic thermoelectric materials.

## GENERAL CONCLUSION

In the present study, the thermoelectric properties of conducting polymer based nanocomposites are discussed. Generally, pure polymers exhibits very poor thermoelectric performance which is defined by figure of merit ( $ZT=S^2\sigma/k$ , where  $S$ ,  $\sigma$  and  $k$  are the Seebeck coefficient, electrical conductivity and thermal conductivity of the sample respectively). Thus, 1-D (SWCNT and MWCNT) and 2-D (RGO) carbonaceous nanofillers with high electrical conductivity ( $10^4$  S/m) have been dispersed into polyaniline (PANI) matrix, with low thermal conductivity ( $\sim 0.2$  W.m<sup>-1</sup>.K<sup>-1</sup>) in order to enhance the thermoelectric performance. It seems that a combination of low thermal conductivity (for polyaniline) and high electrical conductivity (for carbonaceous nanofillers) can show promise of favourable development of thermoelectric performance. From  $ZT=S^2\sigma/k$ , it can be identified that the best possible idea to improve the thermoelectric properties is to keep the thermal conductivity value as low as possible. However, it can be seen that efficient electrical and thermal behaviors of the polymer nanocomposites are the key properties to address the excellence of thermoelectric properties. In general, electrical and thermal transport mechanism in the materials play an important role in the performance. For this reason, a well-defined material is required to investigate these properties.

In order to address the above demand, PANI/SWCNT, PANI/MWCNT, and PANI/RGO nanocomposites with various weight fraction of nano-fillers ranging from 0-21 wt-% have been synthesized via in situ polymerization at same conditions. Furthermore, the morphology of the composites has been characterized by using SEM, and TEM. The images show that the targeted core-shell (where nano-fillers as core and matrix as shell)structured composites have been successfully synthesized. XRD and Raman spectroscopy have been employed to investigate structural properties as well as nano-filler contribution in the composites. Also, the electrical conductivities of the composites have been carried out on 4-probe method whereas thermal conductivities have been performed by Laser flash method, and DSC. Finally, to study the thermoelectric performance of the composites, Seebeck coefficient measurements have been carried out on a homemade setup.

The details investigations on electrical and thermal properties of the all three sets of nanocomposites are discussed in this thesis. It can be seen that the signature of the electrical properties of PANI/SWCNT composites shows a maximum enhancement in electrical conductivity by at least five orders of magnitude with inclusion of SWCNT into PANI. The enhancement of the electrical conductivity is interpreted by using mixing rule and percolation models. A great dispersion is observed between the value of pure PANI and low loading PANI/SWCNT composite. Where the mixing rule indicates the modification of conducting state of PANI, the percolation study reveals that the formation of conducting networks is not a true statistical percolation process based on the random distribution of individual high aspect ratio fillers, but rather is attributed to the mutual attraction of the nanotubes in the composites. The signature of the electrical conductivity is correlated to the morphology of the composite. The result also exhibits the contribution of charge transfer between PANI and SWCNT through  $\pi$ - $\pi$  interaction on electrical conductivity. The thermal conductivity of the composites does not show a percolation behavior. Also it can be observe that thermal conductivity value remains constant up to certain SWCNT volume loading (< 6 vol%) which fulfils the demand of the study. Further, in order to interpret the experimental data of thermal conductivity, effective mass approximation (EMA) model which was proposed by Nan *et. al* is used to fit the data. By using this model, the interfacial thermal resistance ( $R_k$ ) between PANI and SWCNT is determined. Seebeck coefficient of the composites increases significantly with SWCNT content which is explained by an existing physical model. The TE performance or figure of merit  $ZT$  of PANI/SWCNT composites shows a maximum value of 0.0001 which is almost five orders of magnitude larger than pure PANI.

Next, the electrical properties of the PANI/MWCNT composites have been presented. Like PANI/SWCNT, the signature of the electrical conductivity is interpreted by using mixing rule and percolation model. The modification of conducting state of PANI is explained through mixing rule. Also, the percolation study shows that the formation of conducting networks is not a true statistical percolation process. The behavior is evidenced by the morphology of the composites. It also explains that charge transfer between PANI and SWCNT through  $\pi$ - $\pi$  interaction is contributed to electrical conductivity network. The almost constant and low thermal conductivity values meet the idea to improve the thermoelectric performance. The Seebeck coefficient of the composites shows two different types of Seebeck coefficient behavior

(increasing and decreasing) as a function of MWCNT volume loading. Here, the Seebeck coefficient enhances with addition of MWCNT (up to 3.39 vol-%) whereas the opposite trend is observed at high concentration (>3.39 vol-%). The ZT of PANI/MWCNT shows an improvement of four orders of magnitude in comparison with pure PANI.

Furthermore, electrical and thermal transport properties of PANI/RGO composites are discussed. Here the electrical properties of the composites have been characterized by two different methods. First, like PANI/SWCNT and PANI/MWCNT, in plane electrical conductivity is determined by using 4-probe method. The experimental data are analyzed by using mixing rule and percolation model. The result shows that electrical transport phenomena exhibit a 2-D percolation behaviour which is evidenced by SEM and TEM images. The study indicates that the modification of conducting state of PANI and charge transfer which is occurred through  $\pi$ - $\pi$  interaction influence the effective conducting network. Second, in order to investigate the through plane electrical conductivity of PANI/RGO nanocomposites, Broadband Dielectric Spectroscopy (BDS) has been used. The imaginary part of the complex permittivity of the PANI/RGO nanocomposites has been recorded to extrapolate the through plane electrical conductivity. The imaginary part of complex permittivity is analyzed within the framework of Kohlrausch-Williams-Watts (KWW) model. The results reveal that the in plane electrical conductivity is greater than through plane electrical conductivity. This behavior is explained by using the concept of charge trapping which takes place at PANI/RGO interfaces. In addition, the through plane electrical conductivity result shows that the decrease of the DC-conductivity with increasing RGO content is linked to the increase of the intensity of a dielectric relaxation mechanism. On increasing RGO, the nano-composite becomes rich interfaces and, as a result, more charges are trapped; in this way the concentration of charges that are favoured to percolate is decreased in excess of the pinned charge concentration, enhancing capacitance effects. While this happens, the analysis of the dielectric relaxation peak evidences that mean dielectric relaxation time is roughly constant. The latter is in accordance with previous SEM studies, whereas the RGO sheets keep an average size of 0.5-3  $\mu\text{m}$  on increasing RGO component. Capacitance effects depend on the quantity of RGO sheets but the relaxation time does not, as being proportional to the mean size of these sheets. Our finding is that the mean dielectric relaxation time is practically constant for the studied RGO composition range, while the strength of the dielectric relaxation mechanism is concentration-dependent which is in accordance with

the predictions of the Sillars model for oblate conducting discs into an insulating matrix, for low concentration values. Also, complex permittivity measurements above room temperature on PANI/RGO nanocomposites reveal an interfacial relaxation mechanism characterized by negative activation energy values. This behavior is interpreted by revisiting the basic concepts of the Sillars model for interfacial polarization occurring in an insulator comprising dispersed conducting platelets. The semi-conducting PANI matrix provides a leakage resistance to the polarized RGO inclusions and enhances the DC conductivity of the composites at the expense of the intensity of the relaxation process. This is evidenced by the decrease in intensity of the relaxation peak with increasing temperatures, which favors phonon-assisted charge de-trapping in RGO platelets. This phenomenon corroborates with our experimental findings as reflected in the decreased frequency as a function of temperature. The heat-induced charge liberation contributes to DC conductivity and affects the shape of the DC conductivity versus temperature curves for different weight fractions of RGO, which can be explained through the Sillars model.

Like electrical properties of the composites, the thermal properties have been characterized by two different methods. First, Laser flash method, and DSC have been employed to determine the thermal conductivity ( $k$ ) like PANI/SWCNT and PANI/MWCNT composites. The result shows at low concentration of RGO,  $k$  remains essentially constant ( $\sim 0.44 \text{ W} \cdot \text{m}^{-1} \cdot \text{K}^{-1}$ ) which meets the demand of this study. The trend of thermal conductivity of the composites is modelled with a MG-EMA evidencing i) a quite low interfacial resistance between PANI and RGO and ii) a likely random mechanism of heat transport. These results suggest that electrical percolation has no significant effect on the thermal conductivity, i.e., the topology of the electrical conducting network is not the dominant parameter that controls the thermal transport. Such results imply that the effective channel for electric transport is along the 2-D percolating RGO platelets network whereas the dominant channels of the heat flow always involve the polymer media surrounding RGO. Second, same series of chemically prepared RGO/PANI nanocomposites have been characterized via photothermal radiometry (PTR) to study the thermal transport properties (diffusivity, effusivity, conductivity and volumetric heat capacity) as a function of RGO loading. Our results indicate that the above parameters remain essentially unchanged at low filler contents but observable changes occur above a certain % RGO threshold. The study also reveals that although the order of magnitude of thermal diffusivity and thermal conductivity are same for same PANI/RGO composites, the values are different. This difference

can arise for nature of the experiment. In addition, we found that as a function of RGO% i) thermal conductivity can be correlated to the density of nanocomposites and ii) volumetric heat capacity exhibits thermal percolation behavior. We believe that the overall observed evolutions of thermal properties as a function of RGO loading are closely related to the morphology of the composites. In particular, the chemical/physical interactions between the polymer host and its fillers and the resulting morphology are the critical factors that need to be taken into account. That is, the presence of inter-PANI/RGO features such as air “pockets” (acting as insulator layers, though a minor factor) and interfacial spacing/nano-confined structures (acting as nano heat capacitors, a major factor) are instrumental in controlling the thermal characteristics. Owing to their relatively low thermal conductivity (as compared to that of pristine graphene or carbon nanotubes counterparts) and their good heat storage capability, we can envision the use of these composites as the critical component of thermal management devices or their potential applications in the next generation of thermoelectrics. In addition, the practical usefulness of the proposed model should not be overlooked since it allows a fast determination of heat absorption or  $Q$  of nanohybrid composites which may not be readily accessible via the corresponding  $T_m$  when their values are in the mK range unless expensive instrumentation is available. Although Seebeck coefficient decreases with RGO loading, the TE performances of PANI/RGO composites exhibit an enhancement of the figure of merit  $ZT$  up to two orders of magnitude as compared to that of pure PANI.

Finally, a comparative study on electrical transport, thermal transport and thermoelectric properties has been conducted in order to investigate the dimensionality effect on these properties. Inclusion of 2-D nano-fillers into matrix makes layer like core-shell structured but addition of 1-D nano-fillers (SWCNT and MWCNT) gives rod-like core-shell structured. The electrical properties show that although nano-fillers have different dimensions, the electrical conductivity increases as a function of nano-filler loading. But there is significant dimensionality effect on electrical conductivity enhancement, and percolation threshold. It can be seen that inclusion of 1-D nano-fillers induces better conducting network than 2-D nano-fillers. Thermal conductivity and volumetric heat capacity depend also on the dimensions of the fillers. Due to the large interfacial spaces, inclusion 2-D nano-fillers shows lower thermal conductivity enhancement than 1-D nano-fillers. This result favors as good thermoelectric materials. The



results show the three different signatures of the Seebeck coefficient for three different fillers. In the evolution of Seebeck coefficient, MWCNT fillers behave at lower concentration as 1-D fillers and at higher concentration as 2-D fillers. Nevertheless, the present work has its advantages in that the preparation of samples and their processing are inexpensive and straight forward. The thermoelectric performance ZT is associated with the dimension of the fillers. The study shows that PANI/SWCNT provides better TE behavior ( $ZT = 0.001$ ) than PANI/MWCNT ( $8.01 \times 10^{-5}$ ) and PANI/RGO ( $3.75 \times 10^{-6}$ ). But results also show that PANI/RGO composites are better in energy storage than PANI/SWCNT and PANI/MWCNT.

All in all, there are numerous directions in which the research on polymer nanostructured composites can potentially progress. More specifically, due to the constantly growing need in energy, the research on organic thermoelectric and energy storage devices can lead over the coming years. In that research field, a broad and extensive research works are being conducted by various research groups around the world in order to achieve high efficiency. As extension of our work on that, we would like to investigate the same properties presented in this thesis, of 0-D nano-filler (Fullerene or  $C_{60}$ ) based polymer nanostructured composites. The electrical and thermal properties of the studied materials must be investigated at different temperatures in order to achieve their highest efficiency. Further studies on electrical and thermal transport are need to develop the performance of the materials. Finally, it can be conclude that at the point of view on renewable energy the research on carbonaceous based polymer nanostructured composites as thermoelectric and energy storage materials shall not be overlooked.



# BIBLIOGRAPHY

- [1] International Energy Outlook 2010. [www.eia.gov/oiaf/ieo/index.html](http://www.eia.gov/oiaf/ieo/index.html). (July 2010).
- [2] L. Sakhabakhsh and M. Yarmohammadi, *International Journal of Energy Science* **2**, 59 (2012).
- [3] A. Dey, O. Prakash, A. K. Sikder, S. Chattopadhyay, and A. Shafeeuulla, *Renew. Sustain. Energy Rev.* **53**, 653 (2016).
- [4] J. Z. Xu, G. J. Zhong, B. S. Hsiao, Q. Fu, and Z. M. Li, *Prog. Polym. Sci.* **39**, 555 (2014).
- [5] K. Zhang, M. Davis, J. Qiu, L. Hope-Weeks, and S. Wang, *Nanotechnology* **23**, 385701 (2012).
- [6] M. Kim and Y. C. Kim, *Synth. Met.* **198**, 31 (2014).
- [7] R. Chan Yu King, F. Roussel, J. F. Brun, and C. Gors, *Synth. Met.* **162**, 1348 (2012).
- [8] R. Gangopadhyay and A. De, *Chem. Mater.* **12**, 608 (2000).
- [9] Y. Huang and D. R. Paul, *J. Polym. Sci. Part B Polym. Phys.* **45**, 1390 (2007).
- [10] Y. Z. Meng and S. C. Tjong, *Polymer*. **39**, 99 (1998).
- [11] J. Y. Choi, S. W. Kim, and K. Y. Cho, *Compos. Sci. Technol.* **94**, 147 (2014).
- [12] R. A. Vaia and H. D. Wagner, *Mater. Today* **7**, 32 (2004).
- [13] R. Verdejo, M. M. Bernal, L. J. Romasanta, and M. a. Lopez-Manchado, *J. Mater. Chem.* **21**, 3301 (2011).
- [14] M. Supová, G. S. Martynková, and K. Barabaszová, *Sci. Adv. Mater.* **3**, 1 (2011).
- [15] G. Mittal, V. Dhand, K. Y. Rhee, S.-J. Park, and W. R. Lee, *J. Ind. Eng. Chem.* **21**, 11 (2015).
- [16] T. Kim, J. Park, J. Sohn, D. Cho, and S. Jeon, *ACS Nano* **10**, 4770 (2016).
- [17] S. C. Tjong, *Mater. Sci. Eng. R Reports* **74**, 281 (2013).
- [18] S. Stankovich, D. A. Dikin, G. H. B. Dommett, K. M. Kohlhaas, E. J. Zimney, E. A. Stach, R. D. Piner, S. T. Nguyen, and R. S. Ruoff, *Nature* **442**, 282 (2006).
- [19] J. K. W. Sandler, J. E. Kirk, I. A. Kinloch, M. S. P. Shaffer, and A. H. Windle, *Polymer*. **44**, 5893 (2003).
- [20] L. Hu, D. S. Hecht, and G. Grüner, *Nano Lett.* **4**, 2513 (2004).
- [21] P. Bonnet, D. Sireude, B. Garnier, O. Chauvet, P. Bonnet, D. Sireude, B. Garnier, and O.

- Chauvet, Appl. Phys. Lett. **91**, 201910(2007).
- [22] K. M. F. Shahil and A. A. Balandin, Solid State Commun. **152**, 1331 (2012).
- [23] Z. Han and A. Fina, Prog. Polym. Sci. **36**, 914 (2011).
- [24] S. Y. Kwon, I. M. Kwon, Y. G. Kim, S. Lee, and Y. S. Seo, Carbon. **55**, 285 (2013).
- [25] Y. Zhao, G.-S. Tang, Z.-Z. Yu, and J.-S. Qi, Carbon. **50**, 3064 (2012).
- [26] R. Atif, J. Wei, I. Shyha, and F. Inam, RSC Adv. **6**, 1351 (2016).
- [27] N. M. Barkoula, B. Alcock, N. O. Cabrera, and T. Peijs, Polym. Polym. Compos. **16**, 101 (2008).
- [28] I. Balberg, Carbon. **40**, 139 (2002).
- [29] D. Zhu, Y. Bin, and M. Matsuo, J. Polym. Sci. Part B Polym. Phys. **45**, 1037 (2007).
- [30] J. Y. Oh, G. H. Jun, S. Jin, H. J. Ryu, and S. H. Hong, ACS Appl. Mater. Interfaces **8**, 3319 (2016).
- [31] S. H. Xie, Y. Y. Liu, and J. Y. Li, Appl. Phys. Lett. **92**, 18 (2008).
- [32] J. Du, L. Zhao, Y. Zeng, L. Zhang, F. Li, P. Liu, and C. Liu, Carbon. **49**, 1094 (2011).
- [33] R. M. Mutiso and K. I. Winey, Prog. Polym. Sci. **40**, 63 (2014).
- [34] K. Miyasaka, K. Watanabe, E. Jojima, H. Aida, M. Sumita, and K. Ishikawa, J. Mater. Sci. **17**, 1610 (1982).
- [35] D. G. Cahill, P. V Braun, G. Chen, D. R. Clarke, S. Fan, K. E. Goodson, W. P. King, G. D. Mahan, A. Majumdar, H. J. Maris, S. R. Phillpot, E. Pop, and L. Shi, Appl. Phys. Rev. **1**, 011305, (2014).
- [36] S. Heo, S. Y. Cho, H. Kim do, Y. Choi, H. H. Park, and H. J. Jin, J Nanosci Nanotechnol **12**, 5990 (2012).
- [37] Y. Wang, A. K. Vallabhaneni, B. Qiu, and X. Ruan, Nanoscale Microscale Thermophys. Eng. **18**, 155 (2014).
- [38] C. A. Hewitt, A. B. Kaiser, S. Roth, M. Craps, R. Czerw, and D. L. Carroll, Nano Lett. **12**, 1307 (2012).
- [39] D. Kim, Y. Kim, K. Choi, J. C. Grunlan, and C. Yu, ACS Nano **4**, 513 (2010).
- [40] A. J. Minnich, M. S. Dresselhaus, Z. F. Ren, and G. Chen, Energy Environ. Sci. **2**, 466 (2009).
- [41] O. Bubnova and X. Crispin, Energy Environ. Sci. **5**, 9345 (2012).
- [42] N. Dubey and M. Leclerc, J. Polym. Sci. Part B Polym. Phys. **49**, 467 (2011).

- [43] N. Toshima, M. Imai, and S. Ichikawa, *J. Electron. Mater.* **pp.** 898 (2011).
- [44] C. Liu, F. Jiang, M. Huang, B. Lu, R. Yue, and J. Xu, *J. Electron. Mater.* **40**, 948 (2011).
- [45] M. Zebarjadi, K. Esfarjani, M. S. Dresselhaus, Z. F. Ren, and G. Chen, *Energy Environ. Sci.* **5**, 5147 (2012).
- [46] Y. Du, S. Z. Shen, K. Cai, and P. S. Casey, *Prog. Polym. Sci.* **37**, 820 (2012).
- [47] C. Yu, Y. S. Kim, D. Kim, and J. C. Grunlan, *Nano Lett.* **8**, 4428 (2008).
- [48] W. Lee, N. Park, J. Hong, S. Yoon, J. Koh, and S. Lee, *J. Alloys Compd.* **620**, 120 (2015).
- [49] K. Xiong, R. C. Longo, W. Wang, R. P. Gupta, B. E. Gnade, and K. Cho, *Comput. Mater. Sci.* **97**, 159 (2015).
- [50] K. K. Jung and J. S. Ko, *Curr. Appl. Phys.* **14**, 1788 (2014).
- [51] K. Biswas, J. He, Q. Zhang, G. Wang, C. Uher, V. P. Dravid, and M. G. Kanatzidis, *Nat Chem* **3**, 160 (2011).
- [52] Q. Zhang, C. D. Malliakas, and M. G. Kanatzidis, **2**, 10910 (2009).
- [53] N. Toshima, *Macromol. Symp.* **86**, 81 (2002).
- [54] R. Venkatasubramanian, E. Siivola, T. Colpitts, and B. O'Quinn, *Nature* **413**, 597 (2001).
- [55] B. Poudel, Q. Hao, Y. Ma, Y. Lan, A. Minnich, B. Yu, X. Yan, D. Wang, A. Muto, D. Vashaee, X. Chen, J. Liu, M. S. Dresselhaus, G. Chen, and Z. Ren, *Science* . **320**, 634 LP (2008).
- [56] H. Alam and S. Ramakrishna, *Nano Energy* **2**, 190 (2013).
- [57] H. Shirakawa, E. J. Louis, A. G. MacDiarmid, C. K. Chiang, and A. J. Heeger, *J. Chem. Soc.Chem. Commun.* **16**, 578 (1977).
- [58] Liming Dai, *Intelligent Macromolecules for Smart Devices:From Materials Synthesis to Device Applications*, 1st ed. (Springer-Verlag London, 2004).
- [59] R. Balint, N. J. Cassidy, and S. H. Cartmell, *Acta Biomater.* **10**, 2341 (2014).
- [60] T. Wang, Y. Qi, J. Xu, X. Hu, and P. Chen, *Appl. Surf. Sci.* **250**, 188 (2005).
- [61] S. H. Eom, S. Senthilarasu, P. Uthirakumar, S. C. Yoon, J. Lim, C. Lee, H. S. Lim, J. Lee, and S. H. Lee, *Org. Electron. Physics, Mater. Appl.* **10**, 536 (2009).
- [62] W. W. Focke and G. E. Wnek, **256**, 343 (1988).
- [63] D. Vachon, R. O. Angus Jr., F. L. Lu, M. Nowak, Z. X. Liu, H. Schaffer, F. Wudl and A. J. Heeger, *Synth. Metals*, **18**, 297 (1987)..
- [64] A.G. Macdiarmid, J. C. Chiang, and A. F. Richter, *Synth. Met.* **18**, 285 (1987).

- [65] A. G. MacDiarmid and A. J. Epstein, *Faraday Discuss. Chem. Soc.* **88**, 317 (1989).
- [66] J. Stejskal, P. Kratochvíl, and A. D. Jenkins, *Polymer*. **37**, 367 (1996).
- [67] V. J. Babu, S. Vempati, and S. Ramakrishna, *Mater. Sci. Appl.* **4**, 1 (2013).
- [68] J. Stejskal and R. G. Gilbert, *Pure Appl. Chem.* **74**, 857 (2002).
- [69] O. Kanoun, C. Muller, A. Benchirouf, A. Sanli, T. N. Dinh, A. Al-Hamry, L. Bu, C. Gerlach, and A. Bouhamed, *Sensors* **14**, 10042 (2014).
- [70] S. Iijima, *Nature* **354**, 56 (1991).
- [71] <http://www.lawandenvironment.com>, (March 2016).
- [72] A. Kuznetsov, *J. Mod. Phys.* **4**, 418 (2013).
- [73] <http://www-cpg.ch.cam.ac.uk/Images/CNT1.jp>, (March 2016).
- [74] A. Aqel, K. M. M. A. El-nour, R. A. A. Ammar, and A. Al-warthan, *Arab. J. Chem.* **5**, 1 (2012).
- [75] O. V Kharissova and B. I. Kharisov, *RSC Adv.* **4**, 30807 (2014).
- [76] L. Shao, Y. Bai, X. Huang, Z. Gao, L. Meng, Y. Huang, and J. Ma, *Mater. Chem. Phys.* **116**, 323 (2009).
- [77] <http://www.azonano.com/article.aspx/ArticleID=3469>, (April 2016).
- [78] <http://www.azonano.com/article.aspx/ArticleID=4041>. (April 2016).
- [79] [www.utu.fi](http://www.utu.fi), (April 2016).
- [80] S. Pei and H.-M. Cheng, *Carbon*. **50**, 3210 (2012).
- [81] [Http://www.graphenea.com/pages/reduced-graphene-oxide.VqnogBw4RBc](http://www.graphenea.com/pages/reduced-graphene-oxide.VqnogBw4RBc), (April 2016).
- [82] M. Lundie, Z. Sljivancanin, and S. Tomic, *J. Mater. Chem. C* **3**, 7632 (2015).
- [83] W. Lu, P. Soukiassian, and J. Boeckl, *MRS Bull.* **37**, 1119 (2012).
- [84] G. Eda, Y.-Y. Lin, C. Mattevi, H. Yamaguchi, H.-A. Chen, I.-S. Chen, C.-W. Chen, and M. Chhowalla, *Adv. Mater.* **22**, 505 (2010).
- [85] K. S. Novoselov, V. I. Falko, L. Colombo, P. R. Gellert, M. G. Schwab, and K. Kim, *Nature* **490**, 192 (2012).
- [86] Y. Mai and Z. Yu, *Polymer Nanocomposites*, 1st Editio (Woodhead Publishing, New York, 2006).
- [87] and M. S. S. S. Thomas , K. Joseph, S. K. Malhotra, K. Goda, *Polymer Composites*, Volume 1, Macro- and Microcomposites, 1 st (2012).

- [88] C. Lekakou and M. G. Bader, *Compos. Part A Appl. Sci. Manuf.* **29**, 29 (1998).
- [89] Y. Kojima, A. Usuki, M. Kawasumi, A. Okada, T. Kurauchi, and O. Kamigaito, *J. Polym. Sci. Part A Polym. Chem.* **31**, 983 (1993).
- [90] J. Coleman, S. Curran, a. Dalton, a. Davey, B. McCarthy, W. Blau, and R. Barklie, *Phys. Rev. B* **58**, R7492 (1998).
- [91] M. Depriester, P. Hus, A. H. Sahraoui, and F. Roussel, *J. Appl. Phys.* **109**,074902 (2011).
- [92] M. Depriester, A. Hadj Sahraoui, P. Hus, and F. Roussel, *Appl. Phys. Lett.* **94**, 1 (2009).
- [93] M. Baibarac and P. Gómez-Romero, *J. Nanosci. Nanotechnol.* **6**, 289 (2006).
- [94] C. Oueiny, S. Berlioz, and F. X. Perrin, *Prog. Polym. Sci.* **39**, 707 (2014).
- [95] C. Peng, S. Zhang, D. Jewell, and G. Z. Chen, *Prog. Nat. Sci.* **18**, 777 (2008).
- [96] R. Y. Suckeveriene, E. Zelikman, G. Mechrez, and M. Narkis, *Rev. Chem. Eng.* **27**, 15 (2011).
- [97] G. Ć iric-Marjanovic´ Marjanovic, *Synth. Met.* **170**, 31 (2013).
- [98] W. K. Maser, A. M. Benito, M. A. Callejas, T. Seeger, M. T. Martínez, J. Schreiber, J. Muszynski, O. Chauvet, Z. Osváth, A. A. Koós, and L. P. Biró, *Mater. Sci. Eng. C* **23**, 87 (2003).
- [99] H. Nakamatsu, E. Itoh, and K. Miyairi, *Mol. Cryst. Liq. Cryst.* **472**, 485, (2007).
- [100] M. Ginic-Markovic, J. G. Matisons, R. Cervini, G. P. Simon, and P. M. Fredericks, *Chem. Mater.* **18**, 6258 (2006).
- [101] S. G. Vaidya, S. Rastogi, and A. Aguirre, *Synth. Met.* **160**, 134 (2010).
- [102] R. A. Vaia and H. D. Wagner, *Mater. Today* **7**, 32 (2004).
- [103] E. N. Konyushenko, J. Stejskal, M. Trchov, J. Hradil, J. Kov, J. Proke, M. Cieslar, J. Y. Hwang, K. H. Chen, and I. Sapurina, *Polymer.* **47**, 5715 (2006).
- [104] Y. Long, Z. Chen, X. Zhang, J. Zhang, and Z. Liu, *J. Phys. D. Appl. Phys.* **37**, 1965 (2004).
- [105] A. Mekki, S. Samanta, A. Singh, Z. Salmi, R. Mahmoud, M. M. Chehimi, and D. K. Aswal, *J. Colloid Interface Sci.* **418**, 185 (2014).
- [106] B. Valter, M. K. Ram, and C. Nicolini, *Langmuir* **18**, 1535 (2002).
- [107] H. Zengin, W. Zhou, J. Jin, R. Czerw, D. W. Smith, L. Echegoyen, D. L. Carroll, S. H. Foulger, and J. Ballato, *Adv. Mater.* **14**, 1480 (2002).
- [108] M. Cochet, W. K. Maser, A. M. Benito, M. A. Callejas, M. T. Martinez, J.-M. Benoit, J. Schreiber, and O. Chauvet, *Chem. Commun.* **16**, 1450 (2001).

- [109] P. Saini, V. Choudhary, B. P. Singh, R. B. Mathur, and S. K. Dhawan, *Mater. Chem. Phys.* **113**, 919 (2009).
- [110] Y. Han, X. Gao, T. Wang, M. He, T. Li, and W. Li, *Synth. Met.* **217**, 288 (2016).
- [111] N. A. Ogurtsov, Y. V. Noskov, V. N. Bliznyuk, V. G. Ilyin, J. Wojkiewicz, E. A. Fedorenko, and A. A. Pud, *J. Phys. Chem. C* **120**, 230 (2016).
- [112] A. Rashid bin Mohd Yusoff, *Graphene-Based Energy Device* (Wiley-VCH Verlag GmbH & Co. KGaA, 2015).
- [113] N. Wu, X. She, D. Yang, X. Wu, F. Su, and Y. Chen, *J. Mater. Chem.* **22**, 17254 (2012).
- [114] W. Park, J. Hu, L. A. Jauregui, X. Ruan, and Y. P. Chen, *Appl. Phys. Lett.* **104**, 2012 (2014).
- [115] Z. Chen, H. Yan, T. Liu, and S. Niu, *Compos. Sci. Technol.* **125**, 47 (2016).
- [116] T. K. Bindu Sharmila, J. V. Antony, M. P. Jayakrishnan, P. M. Sabura Beegum, and E. T. Thachil, *Mater. Des.* **90**, 66 (2016).
- [117] N. Soin, S. S. Roy, S. K. Mitra, T. Thundat, and J. A. McLaughlin, *J. Mater. Chem.* **22**, 14944 (2012).
- [118] J. Zhang, J. Gao, Q. Song, Z. Guo, A. Chen, G. Chen, and S. Zhou, *Electrochim. Acta* **199**, 70 (2016).
- [119] Q. Wu, M. Chen, S. Wang, X. Zhang, L. Huan, and G. Diao, *Chem. Eng. J.* **304**, 29 (2016).
- [120] Y. M. Shulga, N. Y. Shulga, and Y. N. Parkhomenko, *Mod. Electron. Mater.* **1**, 1 (2015).
- [121] R. Rohini, P. Katti, and S. Bose, *Polymer.* **70**, A17 (2015).
- [122] P. Modak, S. B. Kondawar, and D. V. Nandanwar, *Procedia Mater. Sci.* **10**, 588 (2015).
- [123] J. Fournier, G. Boiteux, G. Seytre, and G. Marichy, *Synth. Met.* **84**, 839 (1997).
- [124] H. Gibson and J. Pochan, *Macromolecules* **15**, 242 (1982).
- [125] M. Shiraishi and M. Ata, *Synth. Met.* **128**, 235 (2002).
- [126] L. Chico, V. H. Crespi, L. X. Benedict, S. G. Louie, and M. L. Cohen, *Phys. Rev. Lett.* **76**, 971 (1996).
- [127] Z. Yao, H. W. C. Postma, L. Balents, and C. Dekker, *Nature* **402**, 273 (1999).
- [128] J. E. Fischer, H. Dai, A. Thess, R. Lee, N. M. Hanjani, D. L. Dehaas, and R. E. Smalley, *Phys. Rev. B* **55**, R4921 (1997).
- [129] Y. Yosida and I. Oguro, *J. Appl. Phys.* **86**, 999 (1999).



- [130] Z. K. Tang, H. D. Sun, and J. Wang, *Phys. B Condens. Matter* **279**, 200 (2000).
- [131] B. Liu, T. Wågberg, E. Olsson, R. Yang, H. Li, S. Zhang, H. Yang, G. Zou, and B. Sundqvist, *Chem. Phys. Lett.* **320**, 365 (2000).
- [132] C. Y. C. and C. G.-N. and L. C. J. and A. B. Kaiser, *J. Phys. Condens. Matter* **25**, 465303 (2013).
- [133] D. Joung and S. I. Khondaker, *Phys. Rev. B* **86**, 235423 (2012).
- [134] R. Negishi, M. Akabori, T. Ito, Y. Watanabe, and Y. Kobayashi, *Sci. Rep.* **6**, 28936 (2016).
- [135] A. Stauffer, D. & Aharony, *Introduction to Percolation Theory*, 2nd ed. (Taylor & Francis, London, 1994).
- [136] F. Lux, *J. Mater. Sci.* **28**, 285 (1993).
- [137] S. R. Broadbent and J. M. Hammersley, *Proc. Camb. Phil. Soc.* **53**, 629 (1957).
- [138] N. F. Mott, *Philos. Mag.* **19**, 835 (1969).
- [139] G. S. Fulcher, *J. Am. Ceram. Soc.* **8**, 339 (1925).
- [140] N. Binesh and S. V Bhat, *J. Polym. Sci. Part B Polym. Phys.* **36**, 1201 (1998).
- [141] P. Sheng, E. K. Sichel, and J. I. Gittleman, *Phys. Rev. Lett.* **40**, 1197 (1978).
- [142] P. Sheng, *Phys. Rev. B* **21**, 2180 (1980).
- [143] C. Kittel, *Introduction to Solid State Physics*, 8th ed. (2004).
- [144] M. Depriester, P. Hus, A. H. Sahraoui, F. Roussel, M. Depriester, P. Hus, and A. H. Sahraoui, *J. Appl. Phys.* **109**, 074902, (2013).
- [145] H. Im and J. Kim, *Carbon.* **50**, 5429 (2012).
- [146] A. Balandin, *Nano Lett.* 861 (2012).
- [147] C.-W. Nan, G. Liu, Y. Lin, and M. Li, *Appl. Phys. Lett.* **85**, 3549 (2004).
- [148] D. Konatham, K. N. D. Bui, D. V. Papavassiliou, and A. Striolo, *Mol. Phys.* **109**, 97 (2011).
- [149] D. Konatham and A. Striolo, *Appl. Phys. Lett.* **95**, 163105 (2009).
- [150] Z. Han and A. Fina, *Prog. Polym. Sci.* **36**, 914 (2011).
- [151] R. J. Warzoha, R. M. Weigand, and A. S. Fleischer, *Appl. Energy* **137**, 716 (2015).
- [152] C. W. Nan, Z. Shi, and Y. Lin, *Chem. Phys. Lett.* **375**, 666 (2003).
- [153] C. W. Nan, R. Birringer, D. R. Clarke, and H. Gleiter, *J. Appl. Phys.* **81**, 6692 (1997).

- [154] Th. J. Seebeck, *Magnetische Polarisation Der Metalle Und Erze Durch Temperatur-Differenz (1822-1823)* (Leipzig, Engelmann, Leipzig, 1895).
- [155] G. Magnus, *Poggendorff's Ann. Der Phys.* **83**, 469 (1851).
- [156] W. Thomson, *Trans. R. Soc.* **3**, 91 (1851).
- [157] E. Altenkirch, *Phys. Zeitschrift* **10**, 560 (1909).
- [158] E. Altenkirch, *Phys. Zeitschrift* **12**, 920 (1911).
- [159] A F Ioffe, *Semiconductor Thermoelements, and Thermoelectric Cooling* (Infosearch, London, 1957).
- [160] M. V Vedernikov and E. K. Iordanishvili, *Seventeenth Int. Conf. Thermoelectr. Proc. ICT98* (Cat. No.98TH8365) 37 (1998).
- [161] H. J. Goldsmid and R. W. Douglas, *Br. J. Appl. Phys.* **5**, 386 (1954).
- [162] Glen Slack, *CRC Handbook of Thermoelectrics* (CRC Press, 1995).
- [163] L. D. Hicks and M. S. Dresselhaus, *Phys. Rev. B* **47**, 12727 (1993).
- [164] L. D. Hicks, T. C. Harman, X. Sun, and M. S. Dresselhaus, *Phys. Rev. B* **53**, R10493 (1996).
- [165] M. S. Dresselhaus, G. Chen, M. Y. Tang, R. Yang, H. Lee, D. Wang, Z. Ren, J. P. Fleurial, and P. Gogna, *Adv. Mater.* **19**, 1043 (2007).
- [166] M. G. Kanatzidis, *Chem. Mater.* **22**, 648 (2010).
- [167] G. J. Snyder and E. S. Toberer, *Nat. Mater.* **7**, 105 (2008).
- [168] R. H. Tarkhanyan and D. G. Niarchos, *J. Mater. Res.* **28**, 2316 (2013).
- [169] Clemens J. M. Lasance, *Electronics-Cooling*, 4 (2006).
- [170] K. A. Borup, J. de Boor, H. Wang, F. Drymiotis, F. Gascoin, X. Shi, L. Chen, M. I. Fedorov, E. Müller, B. B. Iversen, and G. J. Snyder, *Energy Environ. Sci.* **8**, 423 (2015).
- [171] V. H. Guerrero, S. Wang, S. Wen, and D. D. L. Chung, *J. Mater. Sci.* **37**, 4127 (2002).
- [172] Shigeji Fujita and Akira Suzuki, *Quantum Theory of Thermoelectric Power (Seebeck Coefficient)* (2011).
- [173] M. Cutler and N. F. Mott, *Phys. Rev.* **181**, 1336 (1969).
- [174] J. P. Heremans, *ACTA Phys. Pol. A* **108**, 609 (2005).
- [175] C. Meng, C. Liu, and S. Fan, *Adv. Mater.* **22**, 535 (2010).
- [176] Y. Du, S. Z. Shen, W. Yang, R. Donelson, K. Cai, and P. S. Casey, *Synth. Met.* **161**, 2688 (2012).

- [177] F. Kremer and A. Schonhals, *Broadband Dielectric Spectroscopy*, 1st ed. (Springer-Verlag Berlin Heidelberg, 2003).
- [178] <http://www.cemhti.cnrs-orleans.fr/pot/software/focus.html>, (May 2016).
- [179] F. M. Smits, *Bell Syst. Tech. J.* **37**, 711 (1958).
- [180] Sir William Thomson, *Reprint of Papers on Electrostatics and Magnetism* (Macmillian, London, 1884).
- [181] I. Naik and A. K. Rastogi, *J. Control Instrum.* **5**, 24 (2016).
- [182] K. A. Borup, J. de Boor, H. Wang, F. Drymiotis, F. Gascoin, X. Shi, L. Chen, M. I. Fedorov, E. Müller, B. B. Iversen, and G. J. Snyder, *Energy Environ. Sci.* **8**, 423 (2015).
- [183] R. D. Tom, E. P. O'Hara, and D. Benin, *J. Appl. Phys.* **53**, 5392 (1982).
- [184] M. Depriester, P. Hus, S. Delenclos, and A. H. Sahraoui, *Rev. Sci. Instrum.* **76**, 074902 (2005).
- [185] M. Depriester, P. Hus, S. Delenclos, and A. H. Sahraoui, *Rev. Sci. Instrum.* **78**, 036101 (2007).
- [186] Graf. Softw. Is Available <http://www.grafitylabs.com> (May 2016).
- [187] B. Abad, I. Alda, P. Díaz-Chao, H. Kawakami, A. Almarza, D. Amantia, D. Gutierrez, L. Aubouy, and M. S. Martín-González, *J. Mater. Chem. A* **1**, 10450 (2013).
- [188] M. D. Camejo, D. R. Espeso, and L. L. Bonilla, *Phys. Rev. E* **90**, 12306 (2014).
- [189] K. Datta, P. Ghosh, M. a More, M. D. Shirsat, and a Mulchandani, *J. Phys. D. Appl. Phys.* **45**, 355305 (2012).
- [190] S. He, J. Wei, F. Guo, R. Xu, C. Li, X. Cui, H. Zhu, K. Wang, and D. Wu, *J. Mater. Chem. A* **2**, 5898 (2014).
- [191] V. Lordi and N. Yao, *J. Mater. Res.* **15**, 2770 (2000).
- [192] S. J. V Frankland, A. Caglar, D. W. Brenner, and M. Griebel, *J. Phys. Chem. B* **106**, 3046 (2002).
- [193] S. S. Tallury and M. A. Pasquinelli, *J. Phys. Chem. B* **114**, 4122 (2010).
- [194] G. B. Blanchet, C. R. Fincher, and F. Gao, *Appl. Phys. Lett.* **82**, 1290 (2003).
- [195] W. Bauhofer and J. Z. Kovacs, *Compos. Sci. Technol.* **69**, 1486 (2009).
- [196] B. Kim, J. Lee, and I. Yu, *J. Appl. Phys.* **94**, 1 (2003).
- [197] A. Yu, M. E. Itkis, E. Bekyarova, and R. C. Haddon, *Appl. Phys. Lett.* **89**, 2004 (2006).
- [198] R. Haggemueller, C. Guthy, J. R. Lukes, J. E. Fischer, and K. I. Winey, *Macromolecules*

- 40**, 2417 (2007).
- [199] T. A. El-Brollosy and S. S. Ibrahim, *Phys. Scr* **89**, 105701 (2014).
- [200] F. Deng, Q.-S. Zheng, L.-F. Wang, and C.-W. Nan, *Appl. Phys. Lett.* **90**, 021914 (2007).
- [201] T. C. Tsai, H. C. Chang, C. H. Chen, and W. T. Whang, *Org. Electron. Physics, Mater. Appl.* **12**, 2159 (2011).
- [202] T.-M. Wu, Y.-W. Lin, and C.-S. Liao, *Carbon*. **43**, 734 (2005).
- [203] Y. Han, X. Gao, T. Wang, M. He, T. Li, and W. Li, *Synth. Met.* **217**, 288 (2016).
- [204] V. Gupta and N. Miura, *J. Power Sources* **157**, 616 (2006).
- [205] Y. Han, M. Shen, X. Lin, B. Ding, L. Zhang, H. Tong, and X. Zhang, *Synth. Met.* **162**, 753 (2012).
- [206] B. E. Kilbride, J. N. Coleman, J. Fraysse, P. Fournet, M. Cadek, A. Drury, S. Hutzler, S. Roth, and W. J. Blau, *J. Appl. Phys.* **92**, 4024 (2002).
- [207] S. Quillard, G. Louarn, S. Lefrant, and A. G. Macdiarmid, *Phys. Rev. B* **50**, 12496 (1994).
- [208] S. Stankovich, D. A. Dikin, R. D. Piner, K. A. Kohlhaas, A. Kleinhammes, Y. Jia, Y. Wu, S. T. Nguyen, and R. S. Ruoff, *Carbon N. Y.* **45**, 1558 (2007).
- [209] H. Wang, D. He, Y. Wang, Z. Liu, H. Wu, and J. Wang, *Phys. Status Solidi Appl. Mater. Sci.* **208**, 2339 (2011).
- [210] R. Voggu, B. Das, C. S. Rout, and C. N. R. Rao, *J. Phys. Condens. Matter* **20**, 472204 (2008).
- [211] X. F. Zhang and Q. Xi, *Carbon N. Y.* **49**, 3842 (2011).
- [212] T. Tojo, K. Fujisawa, H. Muramatsu, T. Hayashi, Y. A. Kim, M. Endo, M. Terrones, and M. S. Dresselhaus, *RSC Adv.* **3**, 4161 (2013).
- [213] R. Chan Yu King and F. Roussel, *Synth. Met.* **159**, 2512 (2009).
- [214] J. P. Pouget, M. E. Jozefowicz, a. J. Epstein, X. Tang, and a. G. MacDiarmid, *Macromolecules* **24**, 779 (1991).
- [215] A. Guinier. *Théorie et Technique de La Radio-Cristallographie, Troisième* (DUNOD, Paris, 1964).
- [216] J. Li and J. K. Kim, *Compos. Sci. Technol.* **67**, 2114 (2007).
- [217] E. J. Garboczi, K. A. Snyder, J. F. Douglas, and M. F. Thorpe, *Phys. Rev. E* **52**, 819 (1995).
- [218] A. N. Papathanassiou, I. Sakellis, J. Grammatikakis, E. Vitoratos, and S. Sakkopoulos, *Appl. Phys. Lett.* **103**, (2013).

- [219] A. N. Papathanassiou, I. Sakellis, and J. Grammatikakis, *Appl. Phys. Lett.* **91**, 12291 (2007).
- [220] G. Williams and D. C. Watts, *Trans. Faraday Soc.* **66**, 80 (1970).
- [221] B. Marinho, M. Ghislandi, E. Tkalya, C. E. Koning, and G. de With, *Powder Technol.* **221**, 351 (2012).
- [222] X. Tian, M. E. Itkis, E. B. Bekyarova, and R. C. Haddon, *1* (2013).
- [223] L.K.H. van Beek, *Dielectric Behavior of Heterogeneous Systems in Progress in Dielectrics*, vol. 7 (Heywood, London, 1967).
- [224] H. Namikawa, *J. Non. Cryst. Solids* **18**, 173 (1975).
- [225] N. Bogris, J. Grammatikakis, and A. N. Papathanassiou, *Phys. Rev. B* **58**, 10319 (1998).
- [226] A. N. Papathanassiou and J. Grammatikakis, *Phys. Rev. B* **61**, 16514 (2000).
- [227] A. N. Papathanassiou, *J. Phys. Condens. Matter* **12**, 5789 (2000).
- [228] A. N. Papathanassiou, *J. Phys. Condens. Matter* **13**, L791 (2001).
- [229] V. Skákalová, A. B. Kaiser, J. S. Yoo, D. Oberfell, and S. Roth, *Phys. Rev. B* **80**, 153404 (2009).
- [230] A. B. Kaiser and V. Skakalova, *Chem. Soc. Rev.* **40**, 3786 (2011).
- [231] K. I. Bolotin, K. J. Sikes, J. Hone, H. L. Stormer, and P. Kim, *Phys. Rev. Lett.* **101**, 96802 (2008).
- [232] L. K. H. Van Beek, in *Prog. Dielectr.*, pp. 71–114 (1967).
- [233] A. B. Kaiser, *Reports Prog. Phys.* **64**, 1 (2001).
- [234] S. Ganguli, A. K. Roy, and D. P. Anderson, *Carbon* . **46**, 806 (2008).
- [235] K. M. F. Shahil and A. A. Balandin, *Nano Lett.* **12**, 861 (2012).
- [236] C.-W. Nan, R. Birringer, D. R. Clarke, and H. Gleiter, *J. Appl. Phys.* **81**, 6692 (1997).
- [237] S. T. Huxtable, D. G. Cahill, S. Shenogin, L. Xue, R. Ozisik, P. Barone, M. Usrey, M. S. Strano, G. Siddons, M. Shim, and P. Keblinski, *Nat. Mater.* **2**, 731 (2003).
- [238] M. Tanimoto, T. Yamagata, K. Miyata, and S. Ando, *ACS Appl. Mater. Interfaces* **5**, 4374 (2013).
- [239] A. R. Sadrolhosseini, A. S. M. Noor, K. Shameli, A. Kharazmi, N. M. Huang, and M. A. Mahdi, *J. Nanomater.* **2013**,1 (2013).
- [240] J. Jin, M. P. Manoharan, Q. Wang, and M. A. Haque, *Appl. Phys. Lett.* **95**, (2009).
- [241] H. Yan, N. Sada, and N. Toshima, *J. Therm. Anal. Calorim.* **69**, 881 (2002).

- [242] M. Kuriakose, M. Depriester, R. Chan Yu King, F. Roussel, and A. Hadj Sahraoui, *J. Appl. Phys.* **113**, 044502 (2013).
- [243] J. Xiang and L. T. Drzal, *Carbon*. **49**, 773 (2011).
- [244] A. A. Balandin, *Nat. Mater.* **10**, 569 (2011).
- [245] K. Chu, W. Li, H. Dong, and F. Tang, *EPL (Europhysics Lett.)* **100**, 36001 (2012).
- [246] L. Hu, T. Desai, and P. Keblinski, *J. Appl. Phys.* **110**, (2011).
- [247] I. M. Shahrul, I. M. Mahbulul, S. S. Khaleduzzaman, R. Saidur, and M. F. M. Sabri, *Renew. Sustain. Energy Rev.* **38**, 88 (2014).
- [248] W. J. Parker, R. J. Jenkins, C. P. Butler, and G. L. Abbott, *J. Appl. Phys.* **32**, 1679 (1961).
- [249] H.S. Carslaw and J.C. Jaeger, *Conduction of Heat in Solids*, 2nd ed. (Oxford University Press, 1959).
- [250] P. Goli, S. Legedza, A. Dhar, R. Salgado, J. Renteria, and A. A. Balandin, *J. Power Sources* **248**, 37 (2014).
- [251] S. Abdulla, T. L. Mathew, and B. Pullithadathil, *Sensors Actuators, B Chem.* **221**, 1523 (2015).
- [252] S. H. Xie, Y. Y. Liu, and J. Y. Li, *Appl. Phys. Lett.* **92**, 243121 (2008).

# ABSTRACT

Over the last decade, the polymer nanocomposites have attracted tremendous interests in both academic and industry research, especially regarding the conducting polymers, whose properties are expected to be considerably improved and tunable thanks to nano-fillers introduction. These composites exhibit for instance interesting thermoelectric properties which make them a promising, inexpensive, clean and efficient solution for heat waste harvesting. Thus a good understanding of the link between their micro/nanostructure and their macroscopic properties appears vital. Today one of the most important conducting polymers is polyaniline (PANI). This thesis reports on properties of PANI nanostructured composites as a function of various carbonaceous nano-fillers content such as one dimensional (1-D) carbon nanotubes (single walled and multiple walled), and two dimensional (2-D) reduced graphene oxide RGO. SEM, TEM, X-ray diffraction, and Raman spectroscopy have been employed to investigate their structure and morphology. Electrical and thermal conductivity, and the volumetric heat capacity have been systematically measured as a function of the filler content. To evaluate the thermoelectric performance, Seebeck coefficient measurements have also been carried out on a homemade system. An important increase of electrical conductivity has been observed with increasing filler fraction whereas thermal conductivity only slightly increases, which enhances the thermoelectric figure of merit  $ZT$  of several orders of magnitude. Fillers dimension effect is evidenced, but, whatever this dimension, it is shown that, in contrast with thermal conductivity, electrical conductivity follows a percolation behavior through 2D conduction process. This behavior is also observed in the case of the volumetric heat capacity of PANI/RGO nanohybrids which make them potential candidates for applications in high heat capacitive materials. For the first time their heat storage factor is assessed with a new analytical model proposed in this study. The PANI/RGO samples have also been investigated by Broadband Dielectric Spectroscopy at different temperatures. Results evidence an interesting charge trapping phenomenon occurring at the PANI/RGO interface which might find promising applications in supercapacitors or gate memory devices.

## RÉSUMÉ

Durant la dernière décennie, les polymères nanocomposites ont suscité un vif intérêt, aussi bien en recherche académique qu'industrielle, spécialement en ce qui concerne les polymères conducteurs, dont les propriétés sont susceptibles d'être considérablement améliorées et ajustables grâce à l'ajout de nanoobjets. Ces composites présentent notamment des propriétés thermoélectriques particulièrement intéressantes ce qui en fait une solution prometteuse, peu coûteuse, propre et efficace pour la récupération de pertes de chaleur. Il est donc essentiel de bien comprendre le lien entre leur micro/nanostructure et leurs propriétés macroscopiques. Aujourd'hui l'un des polymères conducteurs les plus courants est la polyaniline (PANI). Ce travail de thèse concerne l'étude des propriétés de composites nanostructurés à base de PANI en fonction de la concentration en nanoobjets tels que des nanotubes de carbone à une dimension (1-D) (simple feuillet et multi feuillets) et de l'oxyde de graphène réduit (RGO) à 2 dimensions (2-D). Les techniques de MEB, MET, diffraction des rayons X et de diffusion Raman ont été utilisées pour étudier leur structure et morphologie. La conductivité électrique, thermique ainsi que la capacité thermique volumique ont été systématiquement mesurées en fonction de la concentration en nanoobjets. Pour estimer les performances thermoélectriques, des mesures de coefficient Seebeck ont également été effectuées sur un système développé au laboratoire. On a pu observer une augmentation importante de la conductivité électrique avec la concentration en nanoobjets alors que la conductivité thermique ne croît que légèrement, ce qui améliore la figure de mérite thermoélectrique  $ZT$  de plusieurs ordres de grandeur. L'effet de la dimensionnalité des nanoobjets a été mis en évidence, mais, quelle que soit cette dimension, il a pu être montré que, contrairement à la conductivité thermique, la conductivité électrique suivait un comportement de percolation à travers un processus de conduction à 2 dimensions. Ce comportement a été également observé pour la capacité thermique volumique des nanohybrides PANI/RGO ce qui en fait des candidats potentiels dans le domaine des matériaux à haute capacité thermique. Pour la première fois leur facteur de stockage de la chaleur est traité avec un nouveau modèle analytique proposé dans ce travail. Les échantillons de PANI/RGO ont également été étudiés par spectroscopie diélectrique large bande à différentes températures. Les résultats font apparaître un phénomène intéressant de piégeage de charge à l'interface PANI/RGO qui pourrait trouver des applications dans les supercondensateurs et les mémoires électroniques.



